HAL
open science

Search for chargino and neutralino pair production in final states with one lepton, two b-jets consistent with a Higgs boson and missing transverse momentum with the ATLAS detector at the LHC Run2

Rima El Kosseifi

To cite this version:

Rima El Kosseifi. Search for chargino and neutralino pair production in final states with one lepton, two b-jets consistent with a Higgs boson and missing transverse momentum with the ATLAS detector at the LHC Run2. High Energy Physics - Experiment [hep-ex]. Aix Marseille Université, Ecole doctorale N°352 : Physique et Sciences de la Matière, 2018. English. NNT : . tel-01998851

HAL Id: tel-01998851

https://hal.science/tel-01998851v1

Submitted on 6 Feb 2019

HAL is a multi-disciplinary open access archive for the deposit and dissemination of scientific research documents, whether they are published or not. The documents may come from teaching and research institutions in France or abroad, or from public or private research centers.

L'archive ouverte pluridisciplinaire **HAL**, est destinée au dépôt et à la diffusion de documents scientifiques de niveau recherche, publiés ou non, émanant des établissements d'enseignement et de recherche français ou étrangers, des laboratoires publics ou privés.

AIX-MARSEILLE UNIVERSITÉ
Ecole Doctorale 352 : Physique et Sciences de la Matière
Faculté Des Sciences de Luminy
Centre de Physique des Particules de Marseille

Thèse présentée pour obtenir le grade universitaire de docteur

Discipline : Physique et Sciences de la Matière
Spécialité : Physique des Particules et Astroparticules

Rima EL KOSSEIFI

Search for chargino and neutralino pair production in final states with one lepton, two b-jets consistent with a Higgs boson and missing transverse momentum with the ATLAS detector at the LHC Run2

Soutenue le 28/11/2018 devant le jury :

Iacopo VIVARELLI	University of Sussex, England	Rapporteur
Barbara CLERBAUX	Université Libre de Bruxelles, Belgium	Rapporteur
Sara STRANDBERG	University of Stockholm, Sweden	Examinateur
Cristinel DIACONU	CPPM, Marseille, France	Examinateur
Mossadek TALBY	CPPM, Marseille, France	Examinateur
Steve MUANZA	CPPM, Marseille, France	Directeur de thèse
Jean-Loic KNEUR	L2C, Montpellier, France	Co-Directeur de thèse

Cette oeuvre est mise à disposition selon les termes de la Licence Creative Commons Attribution - Pas d'Utilisation Commerciale - Pas de Modification 3.0 France.

Acknowledgements

This part is dedicated to thank all who, in one way or another, contributed in the completion of this thesis. Firstly, I would like to express my sincere gratitude to my advisors, Steve and Jean-Loic, for their continuous support, their patience and motivation. Their guidance helped me throughout this research and writing of this thesis. Besides my advisors, I would like to thank the rest of my thesis committee, especially my two referees, Iacopo and Barbara, for their encouragement and insightful comments which incented me to widen my research from various perspectives.

Many thanks and appreciations also go to Arnaud Duperrin, Eric Kajfasz and Laurent Vacavant who provided me an opportunity to join the ATLAS CPPM team. A special thanks to Gilbert Moultaka for all the help provided to the SuSpect3 project, to Farès Djama for providing necessary information regarding my ATLAS authorship project and to Emmanuel Le Guirriec for his help and expertise in IT. A big thank you to Georges Aad for providing a lot of answers to my often annoying and technical questions and for giving me feedback on the thesis report. The discussions with you have been uplifting for me!

I would like to express my sincere thankfulness to the members of the b-tagging and the SUSY electroweak one lepton teams in the ATLAS collaboration, working in such a large experiment gave me the chance to collaborate with scientists around the world. I am also so thankful to my fellow student Wenlong li whoes challenges have provided new ideas to the work. Thanks to the CPPM PhD students for their sense of humour and for the happy times we spent together: Alessandro Morda, Royer, Pierre, Kevin, Nihal, Nghia, Cedric, Grigore, Dawid and all the others ;) I also thank Thomas and Robert for the good moments we shared in the office.

My special and heartfelt thanks go to my family: my parents, my brothers and sister for supporting me spiritually throughout writing this thesis and in my life in general. Last but not least, I thank God for giving me his protection and the ability to accomplish this thesis.

Abstract

Keywords : Chargino, Neutralino, b-tagging, Higgs boson, LHC, ATLAS

La Supersymétrie conservant la R-parité est l'une des théories les plus populaires au-delà du modèle standard. De nombreuses recherches ont été consacrées aux signatures de ce modèle supersymétrique depuis la première phase de l'exploitation du LHC, le Run1, qui a fourni des données à 7 et 8 TeV. Parmi ceux-ci, la recherche du chargino et du neutralino ($\tilde{\chi}_1^{\pm}$, $\tilde{\chi}_2^0$) dans les états finals avec un lepton, deux jets de b compatibles avec un boson de Higgs et une énergie transverse manquante. Cette analyse des données collectées par ATLAS à 8 TeV en 2012 a permis d'exclure certains modèles simplifiés pour lesquels le neutralino le plus léger ($\tilde{\chi}_1^0$) est non massif. Dans ces scénarios, les $\tilde{\chi}_1^{\pm}$, $\tilde{\chi}_2^0$ de moins de 250 GeV sont exclus à 95% C.L.. La présente analyse utilise les données collectées par ATLAS en 2015 et en 2016. Cette recherche montre une meilleure sensibilité au signal due à l'augmentation de l'énergie des collisions au Run 2 jusqu'à 13 TeV qui cause un gain dans la section efficace du signal supérieur au gain de la section efficace du bruit de fond dominant, ttbar. Par conséquent, le Run2 offre une sensibilité sans précédent à la production de $\tilde{\chi}_1^{\pm}$, $\tilde{\chi}_2^0$ à des masses elevée. Cependant, les résultats sont compatibles avec les prédictions du modèle standard et il n'y a pas de la nouvelle physique observée ainsi les limites inférieures sur les masses de $\tilde{\chi}_1^{\pm}$, $\tilde{\chi}_2^0$ sont élevées significativement et permettent d'exclure a 95% C.L. les modèles avec $\tilde{\chi}_1^{\pm}$, $\tilde{\chi}_2^0$ de moins de 680 GeV pour un $\tilde{\chi}_1^0$ non massif.

L'identification des jets contenant des hadrons B, dite "b-tagging", joue un rôle important dans cette analyse et dans plusieurs autres analyses au LHC, en particulier dans les mesures des bosons de Higgs, car h$\rightarrow$ bb domine les désintégrations de ce boson (58%). Les algorithmes d'étiquetage de saveurs d'ATLAS reposent sur les propriétés du hadron B (longue durée de vie, masse élevée) et sur les propriétés des trajectoires de particules associées aux jets. Dans cette thèse, une étude sur l'optimisation des algorithmes d'identification des jets dans ATLAS est présentée, ainsi que des études sur la robustesse des performances du b-tagging avec diverses conditions de détection pour le détecteur a pixels, le plus important pour l'étiquetage de saveur des jets.

Comme la plupart des recherches SUSY au LHC, cette analyse est effectuée en utilisant un modèle simplifié, ainsi le spectre de masse est choisi manuellement et les désintégrations SUSY considérées sont forcées (à un taux d'embranchement de 100%). De cette façon, la sensibilité expérimentale au signal peut être factorisée de l'interprétation réelle du résultat de la recherche dans des modèles SUSY réalistes. Suspect3 est l'un des outils théoriques utilisés pour interpréter les résultats de la recherche en modèles SUSY réalistes. Il s'agit d'un calculateur de spectre SUSY qui calcule les spectres de masse et les couplages SUSY. Cette thèse présente la version SuSpect3 post-découverte du Higgs que nous développons. Cette version utilise la nouvelle entrée de masse très importante du boson de Higgs pour contraindre les autres paramètres de modèle de base, généralement les plus importants, l'un des parametres libres de rupture SUSY, le couplage trilinéaire du top, actuellement donné en entrée. La même idée s'applique également aux limites de masse des particules SUSY résultant des recherches SUSY au LHC. Cette nouvelle version de Suspect3 facilitera la génération de spectres SUSY compatibles avec les contraintes expérimentales et sera également plus naturelle compte tenu de la nouvelle entrée fondamentale désormais disponible avec la masse du boson de Higgs, déterminée par ailleurs avec une bonne précision.

The R-parity conserving SUSY is one of the most motivated theories beyond the Standard Model. During the LHC 8 TeV Run1, many searches were dedicated to this model. Among those, the search for the lightest chargino and next-to-lightest neutralino ($\tilde{\chi}_1^{\pm}$, $\tilde{\chi}_2^0$) pair production in final states with

one lepton, two b-jets consistent with a Higgs boson and missing transverse energy. This search had negative outcome resulting in excluding $\tilde{\chi}_1^{\pm}$, $\tilde{\chi}_2^0$ masses up to 250 GeV for a massless lightest neutralino ($\tilde{\chi}_1^0$) at 95% C.L.. The Run1 search used 20.3 fb^{-1} of 8 TeV ATLAS data collected in 2012. In this thesis, this search with ATLAS at LHC 13 TeV Run2 is presented, it uses 36.1 fb^{-1} ATLAS data collected in 2015 and 2016. This Run 2 search takes advantage of the sensitivity enhancement as the gain in the signal cross section is higher than the gain in the cross section of the main background, ttbar. Therefore, it provides an unprecedented sensitivity to high mass $\tilde{\chi}_1^{\pm}$, $\tilde{\chi}_2^0$ production. However, no evidence of new physics is observed and tighter new limits are placed on the $\tilde{\chi}_1^{\pm}$, $\tilde{\chi}_2^0$ production, with significant improvements over previous searches: $\tilde{\chi}_1^{\pm}$, $\tilde{\chi}_2^0$ masses up to 680 GeV for a massless neutralino $\tilde{\chi}_1^0$ are excluded at 95% C.L.

The identification of jets containing B-hadrons, called b-tagging, plays a significant role in this and many other analyses at the LHC, in particular in the Higgs measurements, as h→bb dominates the total width (58%). The ATLAS b-tagging algorithms rely on B-hadron properties (long lifetime, high mass) and they are based on jets-associated tracks properties. In this thesis, a study on the optimisation of b-jet identification algorithms in ATLAS is presented as well as studies of the robustness of b-tagging performance with various conditions of the pixel detector, being the most important sub-detector for b-tagging.

As most SUSY searches at the LHC, this analysis is carried out using Simplified Model of SUSY, i.e. the mass spectrum is chosen by hand and the considered SUSY decays are forced (branching fractions of 100%). This way, the experimental sensitivity to the signal can be factorized out of the actual interpretation of the search result within realistic SUSY models. Suspect3 is one of the theory tools utilized to map the search result into realistic SUSY models, it is a SUSY spectrum calculator which calculates SUSY mass spectra and couplings. This thesis presents the post Higgs discovery SuSpect3 version we have been working on. This version takes advantage of the very important new Higgs boson mass input to constrain other basic model parameter typically most important one of the soft SUSY-breaking parameters, the top trilinear coupling, currently given as an input. The same idea also applies to the SUSY particles mass limits resulting from the SUSY searches at the LHC. This new Suspect3 version will facilitate generating SUSY spectra compatible with the experimental constraints, and is also more natural given the new fundamental input now available with the Higgs boson mass, which is moreover determined with a good accuracy.

Synthèse en français

Introduction

Notre compréhension du monde de l'infiniment petit s'appuie aujourd'hui sur le Modèle Standard de la physique des particules: une théorie quantique de champs relativistes qui englobe toutes les particules connues ainsi que les trois interactions (électromagnétique, forte et faible) ayant un effet à l'échelle des particules. Ce modèle explique que tout ce qui nous entoure est constitué à partir des fermions: les leptons (i.e. électrons, neutrinos, ...) et les quarks (i.e. up, bottom, ...). Chaque groupe compte six particules et pour chaque particule existe aussi une anti-particule. Les fermions se regroupent en 3 "générations": les particules les plus légères et plus stables appartiennent à la première génération, tandis que les plus lourdes et plus instables constituent la deuxième et la troisième génération. Toute la matière stable de l'Univers est composée de particules faisant partie de la première génération, car les autres particules se désintégrent rapidement pour se transformer en une particule plus stable. Les fermions interagissent entre eux en échangeant d'autres particules les "bosons de jauge" associés aux forces fondamentales. Chaque force vient avec un ou plusieurs bosons: la force forte vient avec les gluons et lie les quarks dans le proton et le neutron. Le photon est associé à la force électromagnétique. L'interaction faible est responsable de la radioactivité β. Elle est portée par les bosons Z et W. Les noms de ces deux classes, fermions et bosons, réfèrent à leur spin: les fermions ont des valeurs de spin de demi-entières tandis que les bosons ont des valeurs entières.

Le Modèle Standard contient deux interactions distinctes: l'interaction forte expliquée par QCD et l'interaction électrofaible qui est une unification partielle de l'interaction faible et de l'électromagnétisme, dont la théorie (QED) est incluse dans cette interaction. Le modèle contient aussi le boson de Higgs, une particule prédite dès 1964 par Peter Higgs, Robert Brout et François Englert. Cette particule permet de donner une masse aux autres particules de la théorie, les bosons et les fermions. Le boson de Higgs était la dérnière pièce manquante du Modèle Standard jusqu'au 4 juillet 2012 quand les collaborations ATLAS et CMS ont annoncé la découverte d'un boson scalaire d'une masse de 125.09 $\pm$ 0.21 (stat.) $\pm$ 0.11 (syst.) GeV se désintégrant en di-photons et en 4 $\ell^{\pm}$. Bien que le Modèle Standard ait eu beaucoup de succès en fournissant des prédictions expérimentales au cours des cinq dernières décennies: les mesures de précision en collisionneur e^+e^- au LEP et SLC et les mesures en collisionneurs hadroniques au Tevatron et au LHC, toutes ont accord avec les valeurs prévues (si on tient compte des marges d'erreur expérimentales), il n'y a aucun doute qu'il ne constitue qu'une approximation à "basses" énergies d'une réalité plus complexe qui ne se manifestera qu'à des énergies plus élevées. En effet, un grand nombre de questions restent encore sans réponses, telles que:

- Pourquoi la gravitation n'est pas décrite dans la théorie?
- Pourquoi n'y a-t-il que trois générations de fermions?
- Pourquoi l'Univers a-t-il plus de matière que d'antimatière?
- Quelle est l'origine et la nature de la matière noire dont serait composé une grande partie de l'Univers?
- Comment les neutrinos acquièrent une masse?
- Le Modèle standard contient 19 paramètres libres i.e. m_h, G_F, α_s ...

Ensuite il y a les questions théoriques liées au boson de Higgs:

- Potentiel du Higgs: bien que le mécanisme Brout-Englert-Higgs semble décrire parfaitement la phénoménologie observée en collisionneur, le potentiel du Higgs est une addition ad-hoc au Modèle Standard.
- Instabilité de la masse du Higgs: dans le Modèle Standard, la masse du Higgs est sujette à des corrections radiatives très importantes du fait de la présence de particules virtuelles, principalement des quarks top et les bosons W et Z virtuels. Ces corrections sont beaucoup plus grandes que la masse nue du Higgs. Ceci signifie que le paramètre de masse du Higgs dans le Modèle Standard doit être finement ajusté de façon à annuler presque complètement les corrections quantiques. Ce niveau d'ajustement, necessaire a chaque ordre du développement perturbatif, est estimé par de nombreux théoriciens comme non-naturel.

La supersymétrie (SUSY) est une extension prometteuse du Modèle Standard qui permet de répondre à plusieurs des questions posées ci-dessus. L'hypothèse fondatrice de la SUSY est qu'à chaque fermion (boson) du Modèle Standard est associé un superpartenaire bosonique (fermionique) portant les mêmes nombres quantiques à l'exception du spin qui diffère d'une demi-unité de $\hbar$. Par sa construction même, la SUSY permet de garder sous contrôle les corrections radiatives apportées à la masse du boson de Higgs. En effet, le signe de ces corrections dépend du caractère fermionique ou bosonique des particules intervenant dans les boucles virtuelles. La théorie contenant autant de fermions que de bosons, ceci permet donc d'annuler les corrections radiatives dans le cas où les particules et leur superpartenaire ont la même masse et des couplages identiques. Or aucune des particules supersymmetriques n'est observée (même le sélectron supposé avoir la même masse que l'électron), donc l'égalité des masses n'est pas observée ainsi SUSY est brisée et les corrections ne s'annulent pas exactement. L'introduction de la SUSY conduit cependant à des corrections radiatives de plus petites amplitudes. SUSY mène aussi de manière naturelle à l'explication de la matière noire. Les théories SUSY prédisent, sous certaines conditions (conservation de la R-parité), que la particule supersymétrique la plus légère est stable bien que massive. Cela en fait un très bon candidat pour expliquer la matière noire. D'autre part, l'introduction de la SUSY permet aux extrapolations des constantes de couplages des interactions du Modèle Standard de converger en une valeur unique à haute énergie. Enfin, SUSY peut générer dynamiquement la forme brisée du potentiel scalaire nécessaire au mécanisme BEH.

La recherche de nouvelles particules fondamentales et les mesures de précisions en physique des particules requièrent de grands accélérateurs et détécteurs de hautes performances. Le grand collisioneur de hadron (LHC) est l'accélérateur le plus puissant construit à ce jour. Après une première période d'exploitation en 2009-2012 (Run 1) couronnée par la découverte du boson de Higgs, le LHC a redémarré en 2015 pour le Run 2 et a permit des collisions de paquets de $\approx 10^{11}$ protons toutes les 25 ns (50 ns en 2015) correspondant à une énergie dans le centre de masse de 13 TeV. L'augmentation de l'énergie des faisceaux de 60% par rapport à celle au Run 1 a pour but d'élever les sections efficaces de production et d'étendre l'espace de phase disponible pour mettre en évidence de nouvelles particules. Le Run 2 s'est achevé, un mois avant la fin de cette thèse sur un excellent bilan: $\approx$ 150 fb^{-1} de données (des collisions de protons) accumulées depuis début 2015. Plusieurs détecteurs sont installés sur l'anneau de 26.7 km que forme le LHC. Les données sur lesquelles s'appuient les études de cette thèse ont été colléctées par le détecteur ATLAS en 2015 et 2016, correspondant à une luminosité intégrée de 36.1 fb^{-1}. Ce gigantesque détecteur cylindrique, 44 m de long pour 25 m de diamètre est conçu pour détecter un maximum de particules afin de satisfaire un vaste programme de recherche, allant des mesures de précision du Modéle Standard à la recherche de nouvelle physique,

et en passant par des mesures des propriétés du boson de Higgs. ATLAS est un puzzle technologique géant, constitué essentiellement de 3 couches concentriques. De l'intérieur vers l'extérieur, on trouve le détecteur interne, dont le but est de reconstruire les traces et mesurer l'impulsion des particules chargées, il est composé, au centre, d'un détecteur à pixels puis du SCT ("semiconductor tracker") et le TRT ("transition radiation tracker"). Ensuite on trouve les calorimètres, dont le but est de mesurer l'énergie des électrons, photons et hadrons. Enfin il y a le spectromètre à muon, qui permet de mesurer l'impulsion des muons. Les neutrinos ne sont pas détectés mais on peut calculer leur fuite en mesurant l'impulsion transverse manquante (E_T^{miss}) dans les événements reconstruits en comparant la somme des impulsions des différentes particules (principe de la conservation de l'impulsion). Ce détecteur a été conçu et est utilisé par la collaboration ATLAS de laquelle je fais partie, une collaboration internationale impliquant 3000 physiciens appartenant à 181 instituts répartis au sein de 38 pays.
Cette thèse, qui s'est déroulée entre 2015 et 2018, couvre à la fois la phénoménologie des théories supersymétriques et la recherche expérimentale des signaux prédits par ces théories, sous la supervision du Dr Muanza du Centre de Physique des Particules de Marseille et Dr Kneur du Laboratoire Charles Coulomb de Montpellier. Au cours de ces trois années j'ai développé la version SuSpect3 post-découverte du Higgs, un programme permettant de calculer le spectre de masse des théories supersymétriques. En parallèle, j'ai participé à l'évaluation des performances d'identification des jets de quarks b dans l'expérience ATLAS, pour laquelle j'ai étudié la robustesse des performances du b-tagging avec diverses conditions de détection pour le détecteur a pixels. Enfin, j'ai utilisé les données collectées par ATLAS dans les collisions protons-protons à $\sqrt{s} = 13$ TeV fournies par le LHC afin de rechercher les particules supersymétriques chargino et neutralino ($\tilde{\chi}_1^{\pm}$, $\tilde{\chi}_2^0$) dans les états finals avec un lepton, deux jets de b compatibles avec un boson de Higgs et de l'énergie transverse manquante. La première partie de cette thèse introduira le contexte théorique en motivant l'intérêt d'une recherche de SUSY et présentera la version SuSpect3 post-découverte du Higgs. Ensuite le cadre expérimental sera décrit en détail dans la deuxième partie. La troisième partie expliquera l'identification des b-jets dans ATLAS au Run2 et présentera mes études de robustesse des performances du b-tagging avec diverses conditions de détection pour le détecteur a pixel. La quatrième partie décrira la recherche de la production de paire chargino-neutralino. Enfin la dérnière partie contient la conclusion.

Etiquetage des jets de saveur b

L'étiquetage des b-jets, appelé "b-tagging", sert à différencier les jets issus des quarks b (b-jets) de ceux issus des quarks c (c-jets), des gluons ou des quarks légers, uds ("light-jets"). Les algorithmes de b-tagging se basent principlement sur les propriétés spécifiques des hadrons contenants un quark b (les B-hadrons): les B-hadrons emportent en moyenne 70% de l'impulsion du quarks b initial (fragmentation dure) et ont une grande masse ($\approx$ 5 GeV) et un temps de vie relativement long, de l'ordre de 1.5 ps (c$\tau = 450\ \mu m$). Ainsi un hadron B dans un jet (p_T=50GeV) vole $\approx$ 5mm dans le plan transverse avant de se désintégrer. Cette distance entre le vertex primaire (PV), le point de collision des protons, et le vertex secondaire (SV) de désintégration du B-hadron, mesurable avec le détecteur à pixels, permet ainsi de reconstruire un SV distinct du PV à partir des traces dans le jet. De plus, les traces de particules chargées issues de la désintégration des B-hadrons prennent leurs origines dans les vertex secondaires. L'incompatibilité des traces avec le vertex primaire se traduit par de relativement larges paramètres d'impact (IP), d_0 dans le plan transverse (voir figure 0.1(a)), et z_0 sur l'axe longitudinal. Il existe quatre classes principales d'algorithmes d'identification dans ATLAS, utilisant différentes reconstructions ou objets: IP, algorithmes basés sur les paramètres d'impact des traces dans les jets i.e. IP2D, IP3D; SV, algorithmes basés sur les propriétés d'un vertex secondaire reconstruit au sein du jet i.e. SV0, SV1; JetFitter, algorithme basé sur la reconstruction de la chaîne de désintégration

d'un B-hadron; BDT, algorithme basé sur une méthode dite "d'arbre de décision boosté" qui combine les variables ci-dessus. La distribution de sortie du BDT est nommée MV2 et est montrée en figure 0.1(b). Elle est utilisée comme variable discriminante finale pour identifier la saveur des jets. Les performances d'étiquetage sont évaluées dans une simulation Monte Carlo du processus $t\bar{t}$. On détermine ainsi dans la simulation la valeur de coupure sur la variable discriminante que les analyses utiliseront, et les efficacités et taux de rejet correspondants pour chaque saveur. Afin de corriger d'éventuelles imperfections de la simulation, ces efficacités et taux de rejet sont ensuite mesurés dans les données afin de fournir des facteurs correctifs. Par exemple, une coupure sur la variable MV2 de 0.8244 permet de conserver 70% des b-jets tout en rejetant 91.7% des c-jets et 99.7% des light-jets. L'étiquetage des

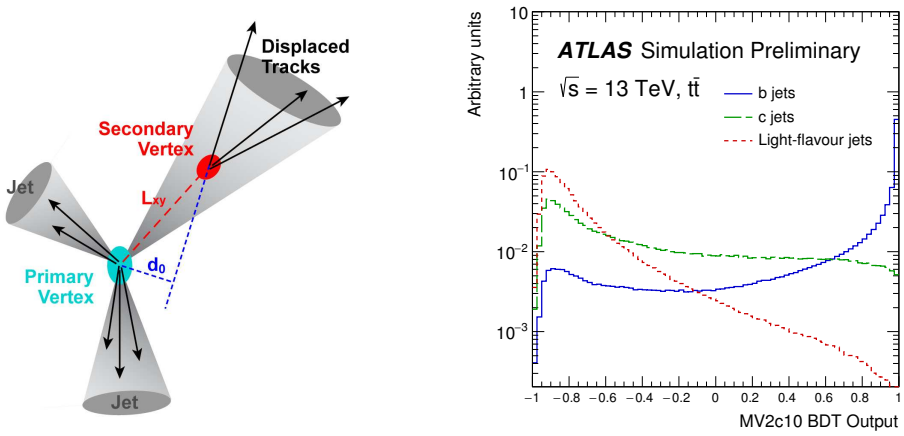

(a) (b)

Figure 0.1.: (a) Schéma représentant un b-jet accompagné de deux light-jets. (b) Discriminant final du b-tagging, MV2, pour la differentiation des b-jets contre les c-jets et light-jets [1].

jets issus de quarks b est un ingrédient majeur pour plusieurs recherche dans l'expérience ATLAS. Le b-tagging est en particulier primordial à ma recherche du signal supersymétrique chargino et neutralino: $\tilde{\chi}_1^{\pm}\ \tilde{\chi}_2^0 \to W^{\pm}(\to \ell^{\pm}\nu) + h(\to b\bar{b}) + E_T^{miss}$ qui possède deux quarks b dans son état final.

Robustesse des performances du b-tagging avec diverses conditions de détection pour le détecteur à pixels

Le rôle du détecteur à pixels d'ATLAS est de reconstruire précisément les vertex d'interaction primaire et secondaire dans le plan transverse et sur l'axe longitudinal, ce qui est primordial pour l'identification des b-jets. Il doit ainsi avoir une résolution spatiale très fine pour différencier les multiples traces et reconstruire le point d'impact associé. Le détecteur à pixels est composé de quatres cylindres concentriques autour de l'axe du faisceau avec des rayons de 30.25 mm (couche IBL), 50.5 mm (couche L0), 88.5 mm (couche L1) et 122.5 mm (couche L2) et pour les bouchons de trois disques centrés sur l'axe du faisceau et éloignés de 49.5, 58 et 65 cm de part et d'autre du centre du détecteur. Chaque cylindre ou disque consiste en un assemblage de modules de semi-conducteurs en silicium segmentés en pixels. Le détecteur à pixels contient ainsi 2192 modules pixels et il a une bonne résolution spatiale: 10 μm dans le plan transverse et 70 μm sur l'axe longitudinale, permettant une bonne précision sur la mesure des paramètres d'impact et une bonne reconstruction du vertex secondaire. La nouvelle couche IBL,

installée en 2014, a été étudiée pour fonctionner correctement jusqu'à une luminosité intégrée très élevée ≈ 550 fb^{-1} et avoir une bonne efficacité de lecture jusqu'à la luminosité instantanée de $\approx 3 \cdot 10^{34}$ cm^{-2} s^{-1}. Par contre, la conception des trois autres couches (L0, L1 et L2) est prévue pour une luminosité instantanée de $\approx 1 \cdot 10^{34}$ cm^{-2} s^{-1}. Au Run 2 ces couches surtout L0 (la plus proche du point d'interaction) devront faire face à une luminosité et à un taux de radiation très élevés. Leurs performances seront peut être dégradées, en raison du fort taux de radiation accumulé, de la limitation de la chaîne de lecture et du fort taux d'occupation. Une des solutions proposées pour réduire le taux d'occupation de la couche L0 est d'augmenter la coupure sur le "time-over-threshold" (ToT) pour réduire le nombre de "hits" enregistrées. Une autre inquiétude vient de la mortalité des modules pixels qui a atteint 5% à la fin du Run 1. Les couches les plus concernées était L0 et L2. Après les 2 ans de réparation, ATLAS a redémaré en 2015 avec 2% de modules inactifs.

Pour mieux controler l'acquisition des données durant le Run 2, j'ai étudié la robustesse des performances du b-tagging avec ces diverses conditions de détection pour le détecteur à pixels: l'augmentation de la fraction des modules pixel inactifs et l'augmentation de la coupure ToT au niveau de la couche L0. Ainsi, j'ai simulé plusieurs scénarios en faisant varier la fraction de modules pixels inactifs de 6% à 35% localisés sur l'une des couches: l'IBL, L0, L1 ou L2. Des scénarios avec une couche entière désactivée ont également été produits pour estimer l'effet maximal. Pour couvrir toutes les gammes des p_T des jets, deux échantillons différents sont utilisés: $t\bar{t}$ où des b-jets de $\langle p_T \rangle = 57$ GeV proviennent de la désintégration du top quark et "Z' mix": un mélange de $Z'(\rightarrow b\bar{b}) + Z'(\rightarrow q\bar{q})$ avec differentes masses de Z' de 1, 2 et 5 TeV, où les b-jets sont boostés de p_T: 25-2000 GeV. De même j'ai simulé des scénarios avec différentes coupures de ToT (exprimée en BC) en L0: 6, 7, 8, 10, 13. Les différences observées en comparant les scénarios par rapport à la base (avec les 2 % de modules inactifs et ToT= 4 BC comme au démarage du Run 2) concernent notamment la résolution des paramètres d'impact des traces, la multiplicité des traces en jet, ... Par conséquent, les distributions discriminantes varient pour chaque scénario et ainsi la performance des algorithmes de b-tagging qui est généralement illustrée par les courbes de rejet des jets légers en fonction des efficacités de b-tagging. Les figures 0.2(a), 0.2(c) présentent la performance de l'algorithme MV2c10 pour les scénarios produits avec l'´´echantillon $t\bar{t}$ avec différentes fractions de modules pixels morts sur la couche L0, L1 ou L2. Ces figures montrent que pour les jets avec des p_T moyens, la couche L0 la plus proche du point d'interaction est la plus affectée par la mortalité des modules: la dégradation relative de la réjection des light-jets pour une efficacité de b-tagging de 75% est de l'ordre de 10% pour le scénario avec 15% de modules inactifs sur la L0. Par contre, comme le montre la figure 0.2(b), pour les jets boostés l'effet est plus important dans le cas où la mortalité des modules est au niveau des couches lointaines L1 et L2. Et ça revient au fait que quand les B-hadrons sont plus boostés ils volent au-delà des couches centrales avant de se désintégrée. Finalement, comme le montre la figure 0.2(d), l'augmentation de la coupure de ToT jusqu'à 7 BC n'a pas d'effet visible sur la performance de l'algorithme MV2. Par conséquent cette nouvelle valeur de ToT a été utilisée pour la prise de données en 2016.

Recherche de Chargino et Neutralino ($\tilde{\chi}_1^{\pm}$, $\tilde{\chi}_2^0$) dans les états finals avec un lepton, deux jets de b compatibles avec un boson de Higgs et de l'énergie transverse manquante

Dans les collisionneurs hadroniques, les partenaires supersymétriques sont produits par paire via l'interaction de partons: soit par QCD, avec la production de paires de squarks ou de gluinos ou par interaction électrofaible, avec la production par paires de sleptons, de charginos et de neutralinos. La composition du proton et l'intensité relative de QCD par rapport à la force électrofaible résulte en

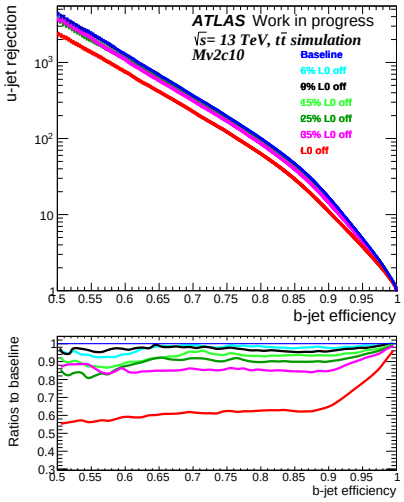

(a) Scénarios avec différentes fractions de modules pixels morts sur la couche L0 avec l'échantillon $t\bar{t}$

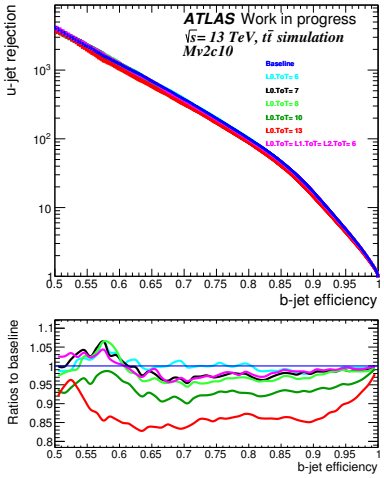

(b) Scénarios avec différentes coupures de ToT pour les pixels sur la couche L0 avec l'échantillon $t\bar{t}$

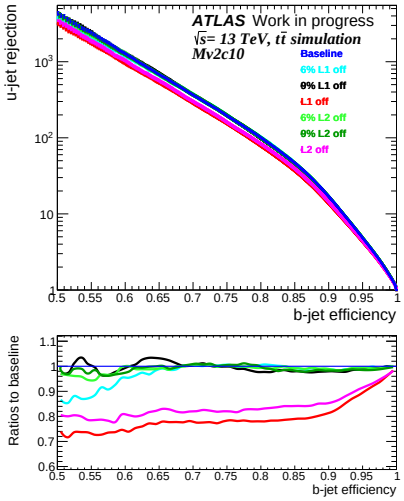

(c) scénarios avec différentes fractions de modules pixels morts sur la couche L1 ou L2 avec l'échantillon $t\bar{t}$

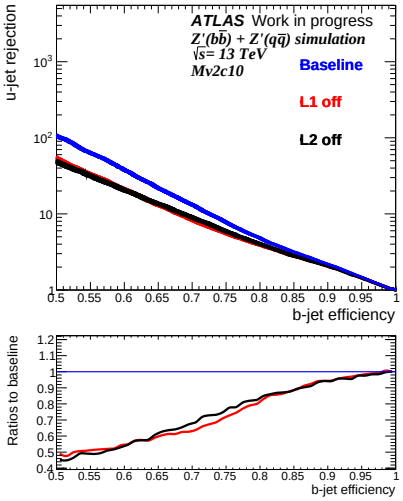

(d) scénarios avec différentes fractions de modules pixels morts sur la couche L1 ou L2 avec l'échantillon "Z' mix"

Figure 0.2.: La performance de l'algorithme MV2c10 pour les scénarios produits avec l'échantillon (a), (b), (c) $t\bar{t}$ et (d) "Z' mix".

une hiérarchie claire des sections efficaces de production des partenaires supersymétriques. La figure 0.3(c) présente les sections efficaces de paires de partenaire supersymétriques en fonction de la masse des particules produites. Cette figure montre que la production de squarks et gluinos est dominante pour une masse donnée. Par contre, les analyses d'ATLAS et CMS de 36.1 fb^{-1} de collisions de protons à $\sqrt{s} = 13$ TeV ont exclut une partie significative de l'espace des paramètres et ont imposé des limites d'exclusion sur les masses des squarks et gluino de l'ordre de 1-1.8 TeV pour un $\tilde{\chi}_1^0$ de masse nulle. Cela motive à rechercher SUSY dans le secteur électrofaible. De point de vue pratique la production par paire de charginos, neutralinos et sleptons peut être recherchée dans des états finaux multileptons qui sont plus clairs (avec un meilleur rapport signal/bruit) que les signatures dans le secteur QCD qui contiennent plutôt de jets. On s'intéresse dans cette thèse à la production de paire chargino-neutralino ($\tilde{\chi}_1^\pm$, $\tilde{\chi}_2^0$). Les états physiques de masse charginos sont des combinaisons linéaires des winos et Higgsinos chargés (super-partenaires des bosons W et H), les etats neutres Bino et wino se mélangent aux higgsinos neutres pour former les etats physiques de masse neutralino. Les charginos et neutralinos sont au nombre de six et par convention : $M_{\tilde{\chi}_1^\pm} < M_{\tilde{\chi}_2^\pm}$ et $M_{\tilde{\chi}_1^0} < M_{\tilde{\chi}_2^0} < M_{\tilde{\chi}_3^0} < M_{\tilde{\chi}_4^0}$. Pour cette analyse on recherche un $\tilde{\chi}_1^\pm$ se désintégrant en $\tilde{\chi}_1^0$ et un boson et un $\tilde{\chi}_2^0$ se désintégrant en $\tilde{\chi}_1^0$ et un boson de Higgs. Cette analyse vise au Run 2, cinq canaux qui diffèrent par le mode de désintégration des bosons W et Higgs:

- 4 canaux avec un boson W leptonique et différents modes de désintégration du Higgs: $1\ell^\pm b\bar{b}$, $1\ell^\pm\gamma\gamma$, $\ell^\pm\ell^\pm$, 3ℓ. Ces canaux faisaient partit de l'analyse faite pas ATLAS au Run 1 avec 20.3 fb^{-1} de collisions de protons à $\sqrt{s} = 8$ TeV enregistrés en 2012: la combinaison de ces canaux a permit d'exclure les $\tilde{\chi}_2^0$ et $\tilde{\chi}_1^\pm$ de moins de 250 GeV dans l'hypothèse d'un $\tilde{\chi}_1^0$ non massif. Ainsi que la contribution dominante à grande masse de $\tilde{\chi}_2^0$ venait de l'état final $1\ell^\pm b\bar{b}$ dont le diagramme de Feyman est montré en figure 0.3(a). Dans cette thèse l'analyse de ce canal intéressant au Run 2 à laquelle j'ai contribué est décrite.

- 1 canal "tout hadronic" recherché pour la première fois où le boson W se désintégre hadroniquement et le Higgs en $b\bar{b}$.

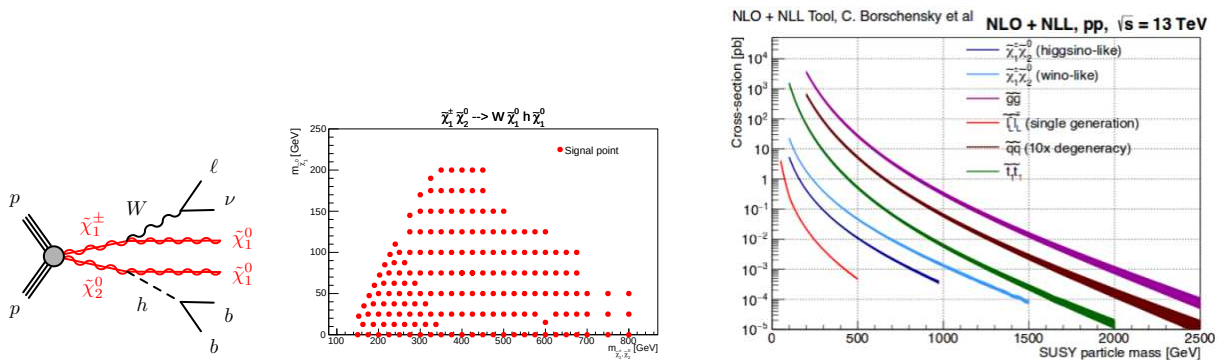

(a) (b) (c)

Figure 0.3.: (a)Diagrammes de Feynman illustrant l'état final $1\ell^\pm b\bar{b} + E_T^{miss}$ de la production Wh par désintégration de la paire $\tilde{\chi}_1^\pm$, $\tilde{\chi}_2^0$. (b) La grille montrant les points de signal recherchés dans le plan ($m_{\tilde{\chi}_1^0}$, $m_{\tilde{\chi}_1^\pm}$). (c) Hiérarchie des sections efficaces NLO+NLL de production des partenaires supersymétriques au LHC à $\sqrt{s} = 13$ TeV.

La recherche SUSY électrofaible Wh$\rightarrow 1\ell^{\pm}b\bar{b}+E_T^{miss}$ est basée sur un modèle dit “simplifié” qui repose sur plusieurs hypothèses parmi lesquelles: le Higgs recherché a les propriétés du Higgs du Modèle Standard, sa masse est fixée à 125 GeV et son rapport d'embranchement est celui attendu dans le Modèle Standard BR(h $\rightarrow$ bb)=0.58. De même pour le W le BR(W$\rightarrow$lv)= 0.33. Dans ce modèle on fixe les BR($\tilde{\chi}_1^{\pm} \rightarrow$ W +$\tilde{\chi}_1^0$) et BR($\tilde{\chi}_2^0 \rightarrow$ h+ $\tilde{\chi}_1^0$) à 1. On choisit de fixer $m_{\tilde{\chi}_1^{\pm}} = m_{\tilde{\chi}_2^0}$, réduisant alors le nombre de paramètres libres de ce modèle simplifié à deux: $m_{\tilde{\chi}_1^{\pm}}$ et $m_{\tilde{\chi}_1^0}$. Enfin, on ne s'intéresse qu'au cas où Δm= $m_{\tilde{\chi}_1^{\pm}} - m_{\tilde{\chi}_1^0}$ > 125 GeV afin de s'assurer que le Higgs sera produit sur couche de masse. Les fonds dominants dans cette analyse sont les paires de $t\bar{t}$, la production associée d'un boson W et de jets, la production single-top ainsi que des contributions plus petites de la production WH Modèle Standard. Afin d'isoler les événements de signal des processus du Modèle Standard, on utilise 4 variables principales, leurs distributions sont montrées en figure 0.4.

- L'énergie transverse manquante: la distribution E_T^{miss} du signal montre une plus longue queue que dans les fonds.
- La masse invariante de $b\bar{b}$: le signal montre une résonance $b\bar{b}$ issue de la désintégration du Higgs.
- La mass contransverse, m_{CT} ayant un point d'arrêt vers 160 GeV pour le $t\bar{t}$.
- La masse transverse, m_T ayant une limite supérieure vers m_W = 80.4 GeV pour le processus W+$b\bar{b}$.

Comme le montre la figure 0.3(b), sur toute la grille de signal, le Δm varie de 130 à 800 GeV. Ces différences de masse affectent la sensibilité de l'analyse: la réjection du fond est meilleur à grand Δm car augmenter le Δm élargie l'espace de phase du Higgs et du W. D'autre part la sensibilité dépend aussi de la masse du $\tilde{\chi}_1^{\pm}$: elle se dégrade à grand $\tilde{\chi}_1^{\pm}$ masses à cause de la décroissance exponentielle de la section efficace du signal montrée à la figure 0.3(c). Aussi augmenter la masse de $\tilde{\chi}_1^{\pm}$, élargit l'espace de phase du Higgs, W et le $\tilde{\chi}_1^0$ mais cet effet est négligeable comparé à la décroissance de la section efficace. Ainsi, l'optimisation du signal a été faite en 3 regions orthogonales qui visent 3 intervales de Δm: SR-Low ($\Delta m = [125, 150]$ GeV), SR-Medium ($\Delta m = [150, 250]$ GeV) et SR-High ($\Delta m > 250$ GeV). La séparation de ces 3 régions se fait grâce à la variable m_T qui montre une corrélation linéaire par rapport au Δm. En plus des coupures sur m_T les 3 SRs sont définies avec des coupures fixes sur les variables: m_{CT}> 160 GeV: le point d'arrêt du processus $t\bar{t}$, m_{bb}: [105, 135] GeV à cause de la résonnance bb, E_T^{miss}> 200 GeV. Les coupures sur m_T et E_T^{miss} ont été obtenues après l'optimisation de la valeur de Z_n qui est utilisée pour estimer la sensibilité su signal. En plus des régions de signal préalablement définies, on définit 5 régions de contrôle (3 enrichies en $t\bar{t}$, 1 pour W+jets et 1 pour le single-top) et 6 régions de validation. Les régions de contrôle sont utilisées pour contraindre la normalisation des fonds. Les régions de validation sont des régions situées entre les régions de contrôle et de signal, et servent à vérifier la qualité de l'extrapolation des fonds vers les régions de signal. Les définitions des différentes régions sont schématisées sur la figure 0.5.

La normalisation des fonds dominants est mesurée dans les données et estimée grâce au logiciel HistFitter développé au sein du groupe SUSY de la collaboration ATLAS. Ainsi on cherche à évaluer une éventuelle contribution du signal aux données observées. Pour ce faire on utilise HistFitter pour maximiser la fonction de vraisemblance (signal compris) dans les données, simultanément dans les régions de contrôle et de signal. La figure 0.6(c) montre pour les 5 canaux recherchés les limites obtenues par la méthode CLs sur la force du signal (μ) observée à 95% de niveau de confiance en fonction de la masse du $\tilde{\chi}_1^{\pm}$, pour l'hypothèses de $\tilde{\chi}_1^0$ de masse nulle. La limite observée est compatible avec les limites attendues dans la simulation. Les limites observées sont proches de μ= 1 à 95%CL,

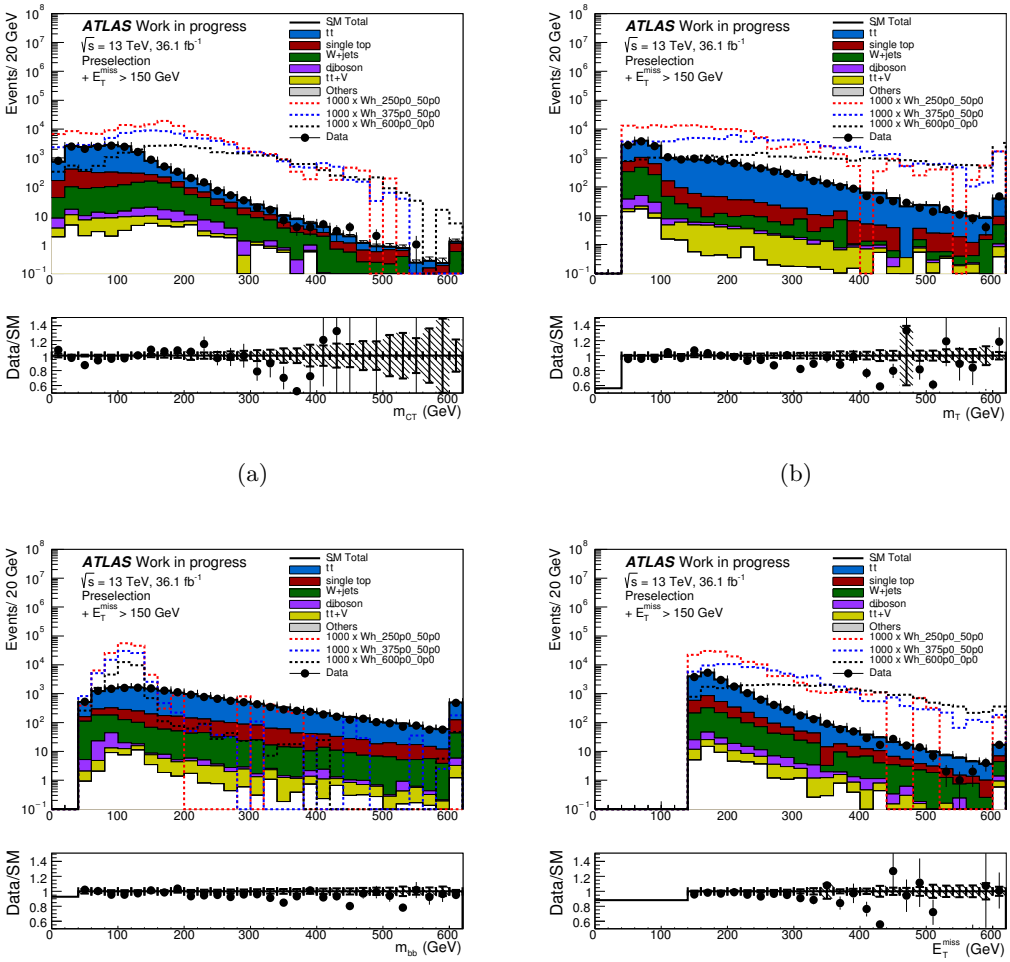

(a) (b)

(c) (d)

Figure 0.4.: Les distributions de (a) m_{CT}, (b) m_{T}^{W}, (c) $m_{b\bar{b}}$ and (d) $\mathrm{E}_{\mathrm{T}}^{\mathrm{miss}}$montrant les événements des données et du fond attendu après les selections: 1 lepton (avec $p_T > 25$ GeV), 2 ou 3 jets (avec $p_T > 25$ GeV) dont 2 sont b-jets, $m_T >$ 40 GeV $\mathrm{E}_{\mathrm{T}}^{\mathrm{miss}} >$ 150 GeV et $m_{bb} > 50$ GeV (coupure imposé pour reduire le fond QCD). Les lignes pointillées en rouges, bleu et noir correspondent au points de signal avec $(\mathrm{m}_{\tilde{\chi}_1^{\pm},\tilde{\chi}_2^0}, \mathrm{m}_{\tilde{\chi}_1^0})$= (250, 50), (375, 50) and (600, 0) GeV respectivement.

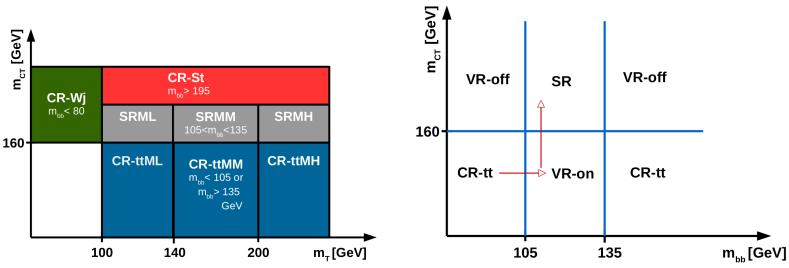

(a) (b)

Figure 0.5.: Schémas représentant (a) les 3 régions de signal, 5 régions de contrôle dans le plan (m_T , m_{CT}), (b) les régions de signal, de contrôles et de validations dans le plan (m_{bb} , m_{CT}).

c'est-à-dire proche de la possibilité d'exclure le modèle simplifié considéré. La figure 0.6(b) présente les limites dans le plan ($m_{\tilde{\chi}_1^0}$, $m_{\tilde{\chi}_1^\pm}$) de l'analyse $1\ell^\pm b\bar{b} + E_T^{miss}$. Les limites observées, ainsi que les contours à $\pm 1\sigma$ présentés sur cette figure correspondent à l'intersection de μ 95%CL avec 1 dans la figure 0.6(c). Pour un $\tilde{\chi}_1^0$ non-massif, cette analyse permet d'exclure à 95% CL les $\tilde{\chi}_1^\pm$ et $\tilde{\chi}_2^0$ de moins de 540 GeV. L'analyse "toute hadronique" qui a l'avantage des plus haut embranchement du Higgs et du W permet d'exclure à 95% CL les $\tilde{\chi}_1^\pm$ et $\tilde{\chi}_2^0$ de moins de 680 GeV pour un $\tilde{\chi}_1^0$ non-massif.

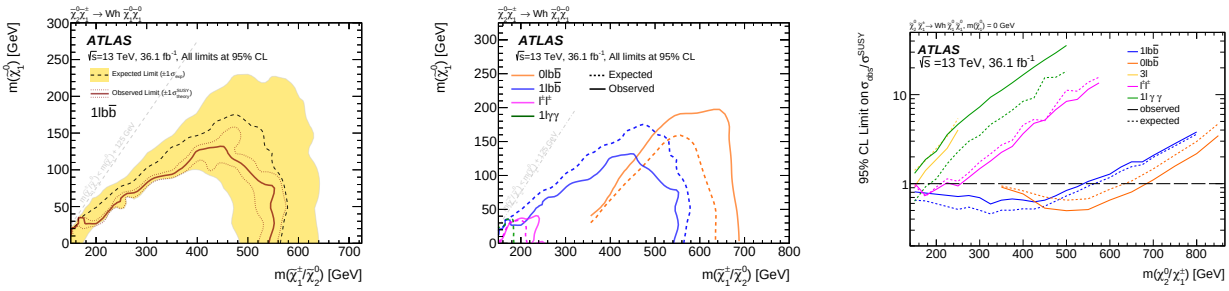

(a) (b) (c)

Figure 0.6.: Les limites sur la force du signal à 95%CL en fonction des masses du $\tilde{\chi}_2^0/\tilde{\chi}_1^\pm$ et du $\tilde{\chi}_1^0$ pour (a) le canal $1\ell^\pm b\bar{b}$, (b) les 5 canaux de l'analyse. En noir, la limite attendue dans la simulation, avec en jaune l'incertitude à 1σ. En rouge, la limite observée dans les données. Les traits rouges pointillés correspondent à l'incertitude théorique (PDF, α_s , les échelles de factorisation et de renormalisation) sur la limite observée. (c) Limites en fonction de la masse du $\tilde{\chi}_1^\pm$, pour l'hypothèses de $\tilde{\chi}_1^0$ de masse nulle pour les 5 canaux de l'analyse.

Au LHC les analyses basées sur les 36.1 fb^{-1} de collisions de protons à $\sqrt{s} = 13$ TeV enregistrées en 2015 et 2016 n'ont pas permis de trouver de la nouvelle physique en particulier SUSY, mais les recherches futures pourraient la révéler. Les analyses de l'ensemble des données 150 fb^{-1} enregistrées au Run 2 (2015-2018) sont en cours. D'autre part le LHC se prépare pour un Run 3 à $\sqrt{s} = 14$ TeV de 2021 jusqu'au 2023 et 300 fb^{-1} sont attendus. Ensuite on passe au LHC à haute luminosité, qui vise une luminosité intégrée totale de 3000 fb^{-1}. Collecter plus de données permet évidemment d'étendre l'espace des phases disponible pour mettre en évidence de nouvelles particules. Une extrapolation

préliminaire de l'analyse $\tilde{\chi}_1^{\pm}\tilde{\chi}_2^0 \rightarrow W(\rightarrow \ell\nu) + h(\rightarrow bb) + \tilde{\chi}_1^0$ pour 3000 fb^{-1} permet d'espérer une découverte potentielle de $\tilde{\chi}_1^{\pm}$ jusqu'à une masse de 950 GeV et $\tilde{\chi}_1^0$ jusqu'à une masse de 250 GeV ou durcir les limites d'exclusion sur le $\tilde{\chi}_1^{\pm}$ jusqu'à 1300 GeV et $\tilde{\chi}_1^0$ jusqu'à 650 GeV.

SuSpect 3: l'outil théorique calculateur de spectres de masse et de couplages SUSY

Au choix des termes de brisure près, SUSY fournit tous les éléments nécessaires pour calculer le spectre de masse de la théorie. Les trois principaux calculateurs de spectres SUSY sont SPHENO, SOFTSUSY et SuSpect3. Chacun prend en charge un jeu de modèles et possède ses spécificités. Une partie de cette thèse a été dédiée au développement d'une nouvelle version de SuSpect3, "SuSpect3 post-découverte du boson de Higgs". SuSpect originellement est un code Fortran proposé par A.Djouadi, J-L. Kneur, G.Moultaka en 2002 permettant de calculer les spectres pMSSM en appliquant éventuellement les conditions de brisures mSUGRA, AMSB et GMSB. SuSpect3, la version C++ de SuSpect, implémente l'ensemble des corrections radiatives à une boucle pour les masses, ainsi que les corrections dominantes à deux boucles pour le Higgs. La version actuelle calcule la masse du boson du Higgs comme paramètre de sortie bien que grâce à la découverte du boson de Higgs annoncée par ATLAS et CMS au LHC en 2012, ce paramètre est aujourd'hui connue avec une bonne precision. Ainsi le but de la nouvelle version SuSpect3 que nous dévéllopons est de se servir de cette nouvelle très importante entrée pour contraindre les termes de brisure douce, i.e. le couplage trilinèaire du top "A_t", le terme de masse des Higgsinos "μ".

La version SuSpect3 post-découverte du boson de Higgs

Dans cette thèse on s'interesse à contraindre le terme A_t en se servant de la formule des corrections radiative à la masse du Higgs, on procède en 3 étapes:

- En utilisant la formule simplifiée des corrections à une boucle: On a ré-écrit cette formule en fonction de A_t, ainsi on a obtenu une équation quartique en A_t mais qui contient aussi un terme en $\ln(A_t)$. Cette équation ne peut pas être resolue analytiquement, pour la résoudre en utilise la méthode de point fixe. À chaque itération on calcule le terme logarithmique grâce au A_t de l'itération précédente A_t^{i-1}. On itère jusqu'à ce que la solution A_t se stabilise. Cette procédure converge rapidement après $\approx$ 4 itérations et fournit au maximum 4 solutions.

- En utilisant la formule complète des corrections à une boucle: on a exprimé cette formule en terme de A_t ainsi on a obtenu la fonction $g(A_t)$. Le m_h, le nouveau paramètre d'entrée est caché derrière les coefficients C_i et R_i de cette fonction.

$$g(A_t) = C_3 {A_t}^3 + C_2 {A_t}^2 + C_1 A_t + C_0 + (R_2 {A_t}^2 + R_1 A_t + R_0)\sqrt{as{A_t}^2 + bsA_t + cs}$$

  $g(A_t)$ s'annule pour les valeurs de A_t qui correspondent au m_h d'entrée. La méthode de point fixe est encore une fois utilisée pour résoudre $g(A_t) = 0$ en se servant comme premier essai des 4 solutions A_t de la routine avec la formule des corrections simplifiées.

- En utilisant l'ensemble des corrections radiatives à une boucle ainsi que les corrections dominantes à deux boucle: on suit la même stratégie que pour le cas précédent sauf que à ce stade les coefficients C_i et R_i contiennent en plus que les corrections à une boucle, les corrections à deux boucles.

Cette stratégie qui est une sorte d'inversion du code qui permet de calculer A_t pour une masse de Higgs donnée a été éprouvées pour 3 points de référence comme le montre le tableau 0.1.

Table 0.1.: Trois exemples numériques du calcul de A_t à partir de la nouvelle entrée $m_h^{Deux\ boucles}$, en utilisant l'ensemble des corrections radiatives à une boucle ainsi que les corrections dominantes à deux boucles.

Benchmark ($m_h^{Two-Loop}$, A_t) [GeV]	A_t^{Guess} [GeV]	τ	$A_t^{Solution}$ [GeV]	$m_{\tilde{t}_1}$ [GeV]	$m_{\tilde{t}_2}$ [GeV]
(125.5, 3976.3)	-11187.7	-10	-10434.8	$2.6202\cdot 10^3$	$3.7318\cdot 10^3$
	1392.7	-10	**3976.3**	$2.7392\cdot 10^3$	$3.9519\cdot 10^3$
	11224.8	1	9923.9	$2.6199\cdot 10^3$	$3.7149\cdot 10^3$
(124.4, -3431.8)	1967.1	10	**-3431.8**	$1.8814\cdot 10^3$	$2.7548\cdot 10^3$
(123.0, -3616.4)	-912.0	10	**-3616.4**	$1.6965\cdot 10^3$	$4.0221\cdot 10^3$
	1279.6	-10	5016.3	$1.6936\cdot 10^3$	$4.0108\cdot 10^3$
	8795.3	1	7864.8	$1.6583\cdot 10^3$	$3.9756\cdot 10^3$

Cette nouvelle version de SuSpect3 est avantageuse pour les phénoménologues et aussi pour les expérimentateurs parce que ça facilite la génération de spectres supersymétriques qui sont compatibles avec les résultats experimentaux.

Introduction

After a successful LHC first Run, the Run2 is probaly the most exciting period in the physics program of the LHC as it almost doubles the energy of the Run1, thus we will have a significant increase in the mass reach compared to Run1. There are reasonable hopes to get new insights on fundamental questions like Naturalness at the electroweak scale, physics beyond the SM including the dark matter. Specially with the ATLAS software and detector improvement mainly tracking improvements following the installation of the new IBL layer (b-tagging, ...). This thesis took place during this challenging Run2 phase in 2015-2018 and it contains two parts: experimental and phenomenology.

On the phenomenology side, I worked with Dr. Jean Loic Kneur from L2C Montpellier on a new version of the SUSY spectrum calculator "Suspect 3" motivated by the discovery of the Higgs boson at Run1. Currently, Suspect3 uses inputs at the EW scale (i.e.: M_Z , M_t, the top trilinear coupling A_t, ...) to calculate the SUSY masses and couplings. My task on this front was to add an option trading-off some free soft-SUSY breaking parameters from the Higgs and stop sectors (i.e. A_t) for the well measured Higgs boson mass.

On the experimental side, my ATLAS authorship project concerned the optimisation of b-jets identification in Run2 data taking. More specifically, I studied the impact of several modifications related to the pixel tracker of ATLAS (Run2 conditions) on b-tagging performance. Namely, varying the fraction of inactive modules and the pixel time over threshold.

Last, I contributed to the search for the Supersymmetry electroweak pair production of Chargino-Neutralino with ATLAS using data collected in 2015-2016 at $\sqrt{s} = 13$ TeV. I mainly worked on the production of the MC samples, the SR, CR and VR definition, truth studies and signal theory uncertainties.

Contents

List of Figures 23

List of Tables 30

I Theoretical overview 33

1 The Standard Model of Particle Physics 34
- 1.1 Free Fields and Gauge interactions 34
- 1.2 The Higgs mechanism 37
- 1.3 The Standard Model constituents 38
  - 1.3.1 Electroweak interactions 39
  - 1.3.2 Electroweak symmetry breaking 41
  - 1.3.3 Quantum chromodynamics 42
- 1.4 Higgs boson searches and discovery 43
- 1.5 Limitations of the Standard Model 47

2 Supersymmetric extension of the SM 48
- 2.1 Basics of Supersymmetry 48
  - 2.1.1 Supersymmetric transformations 48
  - 2.1.2 Chiral and vector supermultiplets components 49
  - 2.1.3 Wess-Zumino model 51
  - 2.1.4 Chiral supermultiplet interactions 51
  - 2.1.5 Vector supermultiplet interactions 51
- 2.2 Soft Supersymmetry breaking 52
- 2.3 Minimal Supersymmetric Standard Model - MSSM 52
  - 2.3.1 R-Parity conservation and its consequences 53
  - 2.3.2 Soft Supersymmetry breaking in the MSSM 53
  - 2.3.3 The mass spectrum of the MSSM 54
    - 2.3.3.1 The Higgs boson and the electroweak symmetry breaking 54
    - 2.3.3.2 Neutralinos and charginos sector 56
- 2.4 SUSY simplified model searches and their interpretation 57

3 The SuSpect3 tool for the calculation of the supersymmetric particle spectrum 61
- 3.1 Overview of the SuSpect3 algorithm 61
- 3.2 SuSpect3 calculation of the MSSM parameters 65
  - 3.2.1 Treatment of the SM inputs 65
  - 3.2.2 SUSY breaking 66
  - 3.2.3 Electroweak symmetry breaking 67
- 3.3 Suspect3 calculation of the physical particle masses 67
  - 3.3.1 Sfermion sector 68
  - 3.3.2 Higgs sector 69
- 3.4 The post Higgs discovery SuSpect3 69
- 3.5 From the Higgs boson physical mass to the trilinear top coupling 70
  - 3.5.1 Using the approximate one-loop correction to the Higgs boson mass 71

3.5.2 Including the full one-loop correction 73
3.5.3 Adding the full one-loop plus leading two-loop correction 78
3.6 Conclusion and outlook 81

II Experimental apparatus 82

4 The Large Hadron Collider 83
4.1 LHC and the accelerator chain 83
4.2 LHC parameters 85
4.3 High luminosity LHC 86

5 The ATLAS detector 88
5.1 Magnet system 89
5.2 Inner detector 89
5.2.1 Particles interactions in the pixel detector 90
5.2.2 Pixel sensors and Front-Ends electronics 93
5.2.3 ToT calibration measurements 96
5.3 Calorimeters 97
5.4 Muon spectrometer 98
5.5 Forward detectors 99
5.6 Trigger and data acquisition 100

6 Objects reconstruction 101
6.1 Tracks and primary vertex 101
6.2 Jets 101
6.3 Electrons and photons 102
6.4 Taus 102
6.5 Muons 103
6.6 Missing Transverse Energy 104

7 Production of Monte Carlo samples 105
7.1 Introduction 105
7.2 Monte Carlo production steps 105
7.2.1 Event generation 105
7.2.2 Detector simulation 106
7.2.3 Digitization and reconstruction 106
7.3 Production campaign 107

III Identification of b-flavoured-jets 108

8 b-tagging in ATLAS in Run2 109
8.1 B-hadrons properties 109
8.2 b-tagging ingredients 110
8.2.1 Tracks association to jet 110
8.2.2 Events, jets and tracks selection 110
8.2.3 Jet truth labeling 111
8.2.4 Performance in simulation 111

8.2.5 Impact parameters definition 112
8.3 ATLAS Run 2 b-tagging algorithms 112
8.3.1 Impact parameter based algorithms 112
8.3.2 Secondary vertex based algorithms 113
8.3.3 MVX algorithms 115
8.4 V^0-tracks reconstruction in jets 116
8.4.1 Motivation 116
8.4.2 K_s^0-neutral-track reconstruction 117
8.4.3 K_s reconstruction efficiency 120
8.4.4 Impact on IP3D performance 121
8.4.5 Conclusion and outlook 121

9 Robustness of b-tagging performance with various conditions of the pixel detector 123
9.1 Introduction 123
9.2 Samples used 123
9.3 Baseline b-tagging performance 124
9.4 Configurations studied and impact on track categories 125
9.4.1 Dead pixel modules configurations 125
9.4.2 Pixel ToT configurations 128
9.5 b-tagging performance for the different layer configurations 130
9.5.1 IBL dead pixel modules configurations 130
9.5.1.1 Integrated performance (R_u vs ϵ_b) 130
9.5.1.2 Impact using fixed operating points 132
9.5.1.3 Study of the IBL role in multiple scattering and pattern recognition issues 134
9.5.2 b-layer dead pixel modules configurations 142
9.5.3 Layer-1 and Layer-2 dead pixel modules configurations 146
9.5.4 b-layer pixel ToT configurations 152
9.6 Conclusions and outlook 158

IV Search for electroweak production of chargino and neutralino in final states with 1 lepton, 2 b-jets and E_T^{miss} 160

10 Introduction 161
10.1 Search for Electroweak SUSY at LHC 161
10.2 Chargino-neutralino pair production leading to Wh states with E_T^{miss} 163

11 One lepton, two b-jets and E_T^{miss} channel 166
11.1 Data-set and Monte Carlo samples 166
11.1.1 Signal models 166
11.1.2 Standard model Monte Carlo 166
11.2 Object definiton and event pre-selection 167
11.2.1 Object definition 168
11.2.2 Event variables and pre-selection 169
11.3 Signal selection 171
11.4 Background estimation 175
11.4.1 Background control regions 176
11.4.2 Background validation regions 178

11.4.3 Truth composition of $t\bar{t}$ in CR/VR/SRs 180
11.5 Systematic uncertainties 180
11.5.1 Experimental uncertainties 182
11.5.2 Signal theoretical uncertainties 182
11.5.3 Background theoretical uncertainties 184
11.6 Fitting procedure 185
11.7 Results 185
11.8 Interpretation 188
11.9 Conclusion and outlook 188

V Conclusion 192

Bibliography 195

Auxiliary materials 208
J Data sets used for the study of the robustness of b-tagging performance with various conditions of the pixel detector 208
K Rate of tracks in the fourteen categories for the pixel configurations studied 209
L MC16a configuration 212
M Additional plots on b-tagging 214
N Signal Contamination in VR-offMM and VR-offMH 216
O Truth composition of $t\bar{t}$ in CR/VR/SRs 224

List of Figures

0.1 (a) Schéma représentant un b-jet accompagné de deux light-jets. (b) Discriminant final du b-tagging, MV2, pour la differentiation des b-jets contre les c-jets et light-jets [1]. 9

0.2 La performance de l'algorithme MV2c10 pour les scénarios produits avec l'échantillon (a), (b), (c) $t\bar{t}$ et (d) "Z' mix". 11

0.3 (a)Diagrammes de Feynman illustrant l'état final $1\ell^{\pm}b\bar{b} + E_T^{miss}$ de la production Wh par désintégration de la paire $\tilde{\chi}_1^{\pm}$, $\tilde{\chi}_2^0$. (b) La grille montrant les points de signal recherchés dans le plan ($m_{\tilde{\chi}_1^0}$, $m_{\tilde{\chi}_1^{\pm}}$). (c) Hiérarchie des sections efficaces NLO+NLL de production des partenaires supersymétriques au LHC à $\sqrt{s} = 13$ TeV. 12

0.4 Les distributions de (a) m_{CT}, (b) m_{T}^W, (c) $m_{b\bar{b}}$ and (d) $\mathrm{E_T^{miss}}$montrant les événements des données et du fond attendu après les selections: 1 lepton (avec $p_T > 25$ GeV), 2 ou 3 jets (avec $p_T > 25$ GeV) dont 2 sont b-jets, m_T> 40 GeV $\mathrm{E_T^{miss}}$> 150 GeV et $m_{bb} > 50$ GeV (coupure imposé pour reduire le fond QCD). Les lignes pointillées en rouges, bleu et noir correspondent au points de signal avec ($m_{\tilde{\chi}_1^{\pm},\tilde{\chi}_2^0}$, $m_{\tilde{\chi}_1^0}$)= (250, 50), (375, 50) and (600, 0) GeV respectivement. 14

0.5 Schémas représentant (a) les 3 régions de signal, 5 régions de contrôle dans le plan (m_T , m_{CT}), (b) les régions de signal, de contrôles et de validations dans le plan (m_{bb} , m_{CT}). 15

0.6 Les limites sur la force du signal à 95%CL en fonction des masses du $\tilde{\chi}_2^0/\tilde{\chi}_1^{\pm}$ et du $\tilde{\chi}_1^0$ pour (a) le canal $1\ell^{\pm}b\bar{b}$, (b) les 5 canaux de l'analyse. En noir, la limite attendue dans la simulation, avec en jaune l'incertitude à 1σ. En rouge, la limite observée dans les données. Les traits rouges pointillés correspondent à l'incertitude théorique (PDF, α_s , les échelles de factorisation et de renormalisation) sur la limite observée. (c) Limites en fonction de la masse du $\tilde{\chi}_1^{\pm}$, pour l'hypothèses de $\tilde{\chi}_1^0$ de masse nulle pour les 5 canaux de l'analyse. 15

1.1 The shape of the Higgs potential $V(\phi) = \mu^2\phi^*\phi + \lambda(\phi^*\phi)^2$, for positive and negative μ^2 with positive λ. 38

1.2 The SM particle content. 39

1.3 (a) Dominant production processes for the SM Higgs boson. These are the gluon-fusion , the Vector Boson Fusion , the Higgs strahlung and the t$\bar{t}$ associated production processes repectively, in descending order regarding their cross sections shown in (b) as function of the proton-proton collision energy [19]. (c) The Higgs boson decay rates as function of its mass [20]. 44

1.4 (a) Shows the invariant mass from pairs of photons selected in the Higgs to $\gamma\gamma$ analysis. The excess of events over the background prediction around 125 GeV is consistent with predictions for the Standard Model Higgs boson. (b) The distribution of candidate Higgs events from the H to ZZ to 4 leptons analysis [21]. (c) The distribution from VH analysis H decaying to bb, showing log(S/B), where S and B are the signal and background yields, respectively. The lower panel shows the "pull", i.e. the ratio of data minus background to the statistical uncertainty of the background [22]. 45

1.5 (a) Higgs boson mass measurements from the individual analyses of ATLAS and CMS and from the combined analysis. The systematic (narrower, magenta-shaded bands), statistical (wider, yellow-shaded bands), and total (black error bars) uncertainties are indicated. The (red) vertical line and corresponding (gray) shaded column indicate the central value and the total uncertainty of the combined measurement, respectively. (b) The coupling of the Higgs boson to fermions (μ, τ, b, t) and bosons (W, Z) as a function of the particle's mass, scaled under some theoretical assumptions. The diagonal line indicates the Standard Model prediction [23]. 46

3.1 The SuSpect3 iterative algorithm for the calculation of the SUSY particle spectrum starting from the choice of input and ending with the check of the spectrum [35]. 64
3.2 An example of spectra generated by SuSpect3. 68
3.3 The top and stop contributions at one-loop to (a) the Higgs boson self energy corrections and (b) the tadpole corrections. 70
3.4 The i-th (a) stop masses product, (b) c coefficient and (c) $X_t^{2,p}$ solution computed using the i-1-th $X_t^{2,p}$ versus the number of iteration, i, for the benchmark point ($m_h^{One-loop}$, A_t)= (117.1, -3431.8) GeV. 72
3.5 The i-th (a) stop masses product, (b) c coefficient and (c) $X_t^{2,m}$ solution computed using the i-1-th $X_t^{2,m}$ versus the number of iteration, i, for the benchmark point ($m_h^{One-loop}$, A_t)= (117.1, -3431.8) GeV. 72
3.6 The distribution of the function g(A_t) for the 3 benchmark points ($m_h^{one-loop}$, A_t): (119.5, 3976.3) GeV shown in blue, (117.1, -3431.8) GeV in red, (115.6, -3616.4) GeV in black. 75
3.7 The distributions of the coefficient (a) P_0 and (b) R_0 versus A_t for the 3 benchmark points ($m_h^{one-loop}$, A_t): (119.5, 3976.3) GeV shown in blue, (117.1, -3431.8) GeV in red, (115.6, -3616.4) GeV in black. 76
3.8 The distribution of the A_t relative error function versus A_t for the 3 benchmark points ($m_h^{one-loop}$, A_t): (119.5, 3976.3) GeV shown in blue, (117.1, -3431.8) GeV in red, (115.6, -3616.4) GeV in black. 77
3.9 The distribution of f(A_t) versus A_t for the benchmark points ($m_h^{one-loop}$, A_t): (a) (119.5, 3976.3) GeV, (b) (117.1, -3431.8) GeV, (c) (115.6, -3616.4) GeV. The 4 intersecting points between the violet line and each of the curve have f(A_t)=A_t. 77
3.10 Dependence of (a) $m_{11}^{two-loop}$, (b) $m_{12}^{two-loop}$ and (c) $m_{22}^{two-loop}$ in terms of A_t for the 3 benchmark points ($m_h^{two-loop}$, A_t): (125.5, 3976.3) GeV shown in blue, (124.4, -3431.8) GeV in red, (123.0, -3616.4) GeV in black. These benchmark points are the ones used in the previous section but the $m_h^{two-loop}$ denotes the Higgs mass value resulting from SuSpect3 using the full one–loop plus leading two-loop calculation. 79
3.11 The absolute values of the ratio of the one- over two-loop contribution to (a) m_{11}, (b) m_{12} and (c) m_{22} for the benchmark point ($m_h^{two-loop}$, A_t): (123.0, -3616.4) GeV. The distributions peaks are due to the zero value of the two-loop contributions to m_{ij} (see figure 3.10). 80
3.12 The distribution of f(A_t) versus A_t for the benchmark points ($m_h^{Two-loop}$, A_t): (a) (125.5, 3976.3) GeV, (b) (124.4, -3431.8) GeV, (c) (123.0, -3616.4) GeV. The intersecting points between the violet line and each of the curve have f(A_t)=A_t. 80

4.1 Illustration of the CERN accelerator complex and experiments [62]. 84

4.2 (a) The cumulative luminosity versus time delivered by the LHC (green) and recorded by ATLAS (yellow) during stable beams for pp collisions at 13 TeV centre-of-mass energy in 2016. (b) The peak instantaneous luminosity delivered to ATLAS during stable beams for each LHC fill as a function of time in 2016. (c) The luminosity-weighted distribution of the mean number of interactions per crossing for the 2016 pp collision data recorded from 16 April - 16 September [63]. 86
4.3 Time-line for the LHC and High-Luminosity LHC [64]. 87

5.1 Illustration of the ATLAS detector. The main parts of the inner detectors, Calorimeters, magnets, and muon spectrometer are highlighted [66]. 88
5.2 The layout of the ATLAS magnet system [67]. 89
5.3 The r-z cross-section view of the layout of a quadrant of the ATLAS inner detector for Run2. The top panel shows the whole inner detector, whereas the bottom-left panel shows a magnified view of the pixel detector region [66]. 90
5.4 dE/dx (stopping power or energy loss) for muons penetrating copper as a function of $\beta\gamma$ =p/(m_μc). The solid curve shows the total energy loss, with different components highlighted as dashed lines. The arrow labeled μ^- points to an effect that is specific to negatively charged particles [69]. 92
5.5 Landau distributions for various thickness of silicon. For reference the ATLAS Pixel Detector sensors are 250 μm, instead the IBL ones are 230 (3D) and 200 (Planars) μm thick [69]. 93
5.6 Diagram showing the pixel cell electronics [71]. 94
5.7 Illustration of cluster sizes in the transverse direction for selected scenarios: (a) a single charged particle crossing the silicon sensor with incident angle, ϕ, producing a cluster with a width of two pixels. The charge drifts due to the electric and magnetic field in the direction of the Lorentz angle $_L$ to the surface. (b) a merged cluster produced by two close-by particles (A1, A2) that both deposit charge in the second pixel. The fourth pixel is not read-out as the charge is below the read-out threshold. (c) a large cluster created from a single charged particle due to a δ-ray produced in the silicon [72]. 95
5.8 ToT mean values vs injected charge for a FE-I4 module [74]. The mean values are obtained from a ToT scan, the fit is performed with a second order polynomial given in equation 5.4. 96
5.9 Illustration of the ATLAS calorimeter system [66]. 98
5.10 Layout of the ATLAS muon spectrometer. The location of the barrel and end-cap Toroidal magnets is also show [66]. 99

6.1 Track reconstruction efficiency in 2015 [76]. 102
6.2 (a) Combined electron reconstruction and identification efficiency in Z→ee events as a function of the transverse energy E_T [79]. (b) Reconstruction efficiency of muons at the loose and medium identification working points as a function of η comparing Run2 data and simulations in Z→ $\mu\mu$ events [176]. 103

7.1 ATLAS Monte Carlo Simulation Flow [80]. 105

8.1 (a) The b-jet p_T as function of the B-hadron p_T. (b) A sketch of the b-jet decay products: displaced tracks and secondary vertex. Large impact parameter (d_0) tracks and a significant flight path length (L_{xy}) of the B-hadron are shown [89]. 110
8.2 (a) The transverse signed impact parameter significance of tracks for b- (solid green), c- (dashed blue) and light-flavour (dotted red) jets for the "Good category". (b) The log-likelihood ratio for IP3D for b- c- and light jets .The MC sample used is $t\bar{t}$ [92]. 113

8.3 Properties of secondary vertices reconstructed by the SV algorithm for b-, c- and light-flavour jets in $t\bar{t}$ events: (a) the 3D decay length significance, (b) the invariant mass of tracks associated wih the vertex [92]. 114
8.4 JetFitter secondary vertex reconstruction efficiency for b-jets, c-jets, and light-jets in $t\bar{t}$ simulated events at $\sqrt{s} = 13$ TeV as function of jet p_T (a) and jet $|\eta|$ (b) [1]. 115
8.5 (a) MV2c10 BDT output for b- (solid blue), c- (dashed green) and light-flavour (dotted red) jets evaluated with $t\bar{t}$ events. (b) A comparison between MV2c20 and MV1 light jet rejection at 70% b-jet efficiency as function of jet p_T [1]. 116
8.6 Feynman diagrams of K_s^0, Λ^0 weak decays. 117
8.7 Comparison between the reconstructed and the corresponding true K_s^0, p_T (a), radius (b) and d_0 (c). 118
8.8 The linear neutral K_s^0 'track' reconstructed using K_s^0 position and momentum vector. 118
8.9 The $d_0^{experimental}$ resolution as function of K_s^0 p_T (a), K_s^0 radius (b), and the angular separation between the K_s^0 daughters (c). 119
8.10 $\sigma(d_0)$ in % for the bins chosen in K_s^0 (p_T, Radius) (a). The IP significance of the reco-K_s^0-track: $\frac{d_0}{\sigma(d_0)}$ (b), $\frac{z_0}{\sigma(z_0)}$ (c). 120
8.11 The K_s^0 reconstruction efficiency as function of K_s^0 radius (a). Comparison between the true and the SV1 bad $\pi^{\pm}$ track from K_s^0 for the number of pixel hits (b) and for the p_T (c) 121
8.12 The light jet rejection as a function of b-jet efficiency for IP3D default configuration, in dark blue. The IP3D performance using the reco- (in light blue) or the true- (in red) K_s^0-track instead of the K_s^0 daughter tracks are shown as well. 122

9.1 p_T (a), $|\eta|$ (b) distributions of the b-jets and B-hadron decay radius distribution (c) in red for $t\bar{t}$, in blue for the Z' mix and in purple for all these samples merged together. 124
9.2 The light-jet rejection as a function of the b-tagging efficiency for the baseline configuration produced using (a) $t\bar{t}$, (b) the Z' mix and (c) all these samples merged together. IP3D performance is shown in black, SV1 in blue, JetFitter in purple and MV2c10 in red. 125
9.3 Rate of tracks in the mostly affected track categories, in blue for the baseline and in red for the scenario with 35% of inactive modules in IBL (a) and (d), 35% of inactive modules in L0 (b) and (e), L1 off and in black for L2 off scenarios (c) and (f). $t\bar{t}$ sample is used for the upper plots and the Z' mix samples for the lower plots. 127
9.4 Rate of tracks in the four mostly affected track categories, in blue for the baseline and in red for the scenario with the highest L0 ToT cut (a) for the $t\bar{t}$ sample and (b) for the Z' mix sample. 129
9.5 The light jet rejection as a function of b-jet efficiency for the IP3D (a), SV1 (b), JetFitter (c) and MV2c10 (d) algorithms for IBL failure scenarios compared with the baseline in blue for $t\bar{t}$ sample. 131
9.6 The light jet rejection as a function of b-jet efficiency for the IP3D (a), SV1 (b), JetFitter (c) and MV2c10 (d) algorithms for IBL failure scenarios compared with the baseline in blue for the Z' mix sample. 133
9.7 The relative degradation in the performance for the six IBL failure scenarios using the 20.7 operating points for the IP3D (a), the SV1 (b) and the JetFitter (c) taggers. Sample used is $t\bar{t}$. 135
9.8 The relative degradation in the performance for the six IBL failure scenarios using three different 20.7 operating points for the MV2c10 tagger. Sample used is $t\bar{t}$. 135
9.9 Absolute value of (a) d_0 and (c) z_0 resolutions of the track with lowest p_T and (b), (d) for the track with highest p_T in b-jets, for the baseline (blue) and the scenario without IBL (red). 136

9.10 The difference with and without IBL of the absolute value of d_0 resolution (a), z_0 resolution (b) and z_0 error (c) of track with lowest p_T (orange) and the track with highest p_T (green) in b-jets. 136
9.11 The IP3D individual track weight distribution for the lowest p_T track in a jet (a), (b), (c) and the maximal p_T track in a jet (d), (e), (f) in b- (black) and light- (brown) jets. 138
9.12 IP3D light jet rejection vs b-jet efficiency as a function of jet p_T for IBL off (red) and the baseline (blue): (a) concerns only jets with p_T in]25, 50 GeV[range, (b) for]100, 140 GeV[and (c) for jets with p_T> 300 GeV. 138
9.13 IP3D light jet rejection vs b-jet efficiency as a function of jet η for IBL off (red) and the baseline (blue): (a) concerns only jets with η in [0, 0.5[range, (b) for [0.5, 1[while (c) contain jets with $\eta \geq 1$. 139
9.14 (a) b-tagging quality track multiplicity, (b) p_T and (c) η distributions for b-jets conserving their tracks. 139
9.15 (a) b-tagging quality track multiplicity, (b) p_T and (c) η distributions for b-jets loosing tracks. 140
9.16 The IP3D weight of b- (black) and light- (brown) jets conserving their IP-tracks (a), (b), (c), loosing (d), (e), (f) and gaining (g), (h), (i) IP-tracks. Left plots show the jet IP3D weight distribution for the baseline, the middle plots for the scenario without IBL and the right plots show the difference with and without IBL. 141
9.17 The light jet rejection as a function of b-jet efficiency for the IP3D (a), SV1 (b), JetFitter (c) and MV2c10 (d) algorithms for L0 failure scenarios compared to the baseline in blue, for $t\bar{t}$ sample. 143
9.18 The light jet rejection as a function of b-jet efficiency for the IP3D (a), SV1 (b), JetFitter (c) and MV2c10 (d) algorithms for L0 failure scenarios compared to the baseline in blue, for Z' mix sample. 144
9.19 The relative degradation in the performance for the six L0 failure scenarios using 20.7 OP for IP3D (a), SV1 (b) and JetFitter (c). Sample used is $t\bar{t}$. 145
9.20 The relative degradation in the performance for the six L0 failure scenarios using three different 20.7 OP for MV2c10 algorithm. Sample used is $t\bar{t}$. 145
9.21 The light jet rejection as a function of b-jet efficiency for the IP3D (a), SV1 (b), JetFitter (c) and MV2c10 (d) algorithms for L1 failure scenarios compared with the baseline in blue, for $t\bar{t}$ sample. 147
9.22 The light jet rejection as a function of b-jet efficiency for the IP3D (a), SV1 (b), JetFitter (c) and MV2c10 (d) algorithms for L1 failure scenarios compared with the baseline in blue, for Z' mix sample. 148
9.23 (a) The SV1 performance for jets with p_T> 200 GeV for the scenario with L1 totally off (red) and the baseline (blue) for $t\bar{t}$ sample. (b) The radial distance distributions of the reconstructed secondary vertex (SV) in b- and (c) in light-jets 149
9.24 MV2c10 light jet rejection as a function of b-jet efficiency for extreme scenarios IBL off (purple), L0 off (red), L1 off (green), L2 off (black) compared with the baseline in blue, for B-hadrons decaying before IBL (a) and before L0 (b), before L1 (c) in Z' mix sample. 150
9.25 The degradation in the performance for L1 failure scenarios using 20.7 OP for IP3D (a), SV1 (b) and JetFitter (c). Sample used is $t\bar{t}$. 150
9.26 The degradation in the performance for L1 failure scenarios using three different 20.7 OP for MV2c10 algorithm. Sample used is $t\bar{t}$. 151
9.27 The relative degradation in the performance using 20.7 OP for IP3D (a), SV1 (b) and JetFitter (c) for scenarios produced with Z' mix sample. 151
9.28 The relative degradation in the performance using three different 20.7 OP for MV2c10 algorithm for scenarios produced with Z' mix sample. 151

9.29 The light jet rejection as a function of b-jet efficiency for the IP3D (a), SV1 (b), JetFitter (c) and MV2c10 (d) algorithms for MC15c L0 scenarios compared with the baseline in blue for $t\bar{t}$ sample. 153
9.30 The light jet rejection as a function of b-jet efficiency for the IP3D (a), SV1 (b), JetFitter (c) and MV2c10 (d) algorithms for L0 scenarios with ToT minimal cut at 13 BC, 10 BC compared with the baseline in blue for Z' mix sample. 154
9.31 The relative degradation in the performance for the five L0 scenarios using 20.7 OP for IP3D (a), SV1 (b) and JetFitter (c). The sample used is $t\bar{t}$. 155
9.32 The relative degradation in the performance for the five L0 scenarios using three different 20.7 OP for MV2c10 algorithm. The sample used is $t\bar{t}$. 155
9.33 The relative degradation in the performance for the L0 scenario with ToT cut at 10 using 20.7 OP as function of jet p_T, for IP3D using the OP corresponding to a baseline ϵ_b=70% (a), SV1 ϵ_b=60% (b) and MV2c10 at ϵ_b=85% (c). Sample used is $t\bar{t}$. 156
9.34 The relative degradation in the performance for the L0 scenario with ToT cut at 13 using 20.7 OP as function of jet p_T, for IP3D using the OP corresponding to a baseline ϵ_b=70% (a), SV1 ϵ_b=60% (b) and MV2c10 at ϵ_b=85% (c). Sample used is $t\bar{t}$. 157
9.35 The relative degradation in the performance for the L0 scenario with ToT cut at 10 using 20.7 OP as function of jet η, for IP3D using the OP corresponding to a baseline ϵ_b=70% (a), SV1 ϵ_b=60% (b) and MV2c10 at ϵ_b=85% (c). Sample used is $t\bar{t}$. 157
9.36 The relative degradation in the performance for the L0 scenario with ToT cut at 13 using 20.7 OP as function of jet η, for IP3D using the OP corresponding to a baseline ϵ_b=70% (a), SV1 ϵ_b=60% (b) and MV2c10 at ϵ_b=85% (c). Sample used is $t\bar{t}$. 158
9.37 Normalized p_T (a) and $|\eta|$ (b) distributions of tracks in category 6. (c) shows the Z size of L0 pixel clusters (in cells) as function of the $|\eta|$ of tracks. 158

10.1 NLO+NLL cross section for the production of sparticles at LHC at 13 TeV center-of-mass energy as a function of the average mass of the pair produced. 161
10.2 Exclusion contours on the scalar top (a) and gluino masses (b) for the final state with jets plus missing transverse momentum [97]. 162
10.3 Electroweak direct production with 2-leptons+ 0-jets, 2-leptons+ jets, 3-leptons decay topologies [98]. 162
10.4 Feynman diagrams for leading order (a) s-channel and (b) t-channel production of $\tilde{\chi}_1^{\pm}, \tilde{\chi}_2^0$. 163
10.5 The signal grid plotted in the (m$_{\tilde{\chi}_1^{\pm},\tilde{\chi}_2^0}$, m$_{\tilde{\chi}_1^0}$) plane [99]. 163
10.6 Feynman diagrams for the direct production of $\tilde{\chi}_1^{\pm}, \tilde{\chi}_2^0$ and the four modes studied at Run2: (a) hadronic, $0\ell b\bar{b}$, (b) $1\ell b\bar{b}$, (c) $1\ell\gamma\gamma$ and (d) $\ell^{\pm}\ell^{\pm}$, 3ℓ leptonic channels. Leptons are either electrons or muons. 164
10.7 (a) Exclusion limits for the signal at 95% CL. Dashed blue represents the limit expected using the combined four different Higgs boson decay channels simulation and in red observed limit from Run1 ATLAS data. (b) The expected and observed cross-section exclusion as a function of the $\tilde{\chi}_1^{\pm}/\tilde{\chi}_2^0$ masses assuming m($\tilde{\chi}_1^0$)= 0 GeV [101]. 165

11.1 Distributions of (a) m_{CT}, (b) m_{T}^{W}, (c) $m_{b\bar{b}}$ and (d) $\mathrm{E}_{\mathrm{T}}^{\mathrm{miss}}$for data and the expected background events passing the preselections with an increased lower $\mathrm{E}_{\mathrm{T}}^{\mathrm{miss}}$cut at 150 GeV. The lower panel shows the ratio between observed data and expected SM background processes. The red, blue and black dashed lines correspond to the bench mark signal model with (m$_{\tilde{\chi}_1^{\pm},\tilde{\chi}_2^0}$, m$_{\tilde{\chi}_1^0}$)= (250, 50), (375, 50) and (600, 0) GeV respectively, where cross-section are multipled by 1000 for shape illustration. Uncertainties are statistical only. 171

11.2 (a) The m_T mean values corresponding to ΔM of the signal points. For the points with equal ΔM, the m_T mean value of the highest $m_{\tilde{\chi}_1^\pm}$ point is shown. (b) The expected significance, Z_N, for SRLM, (c) SRMM and (d) SRMH regions. 173
11.3 Full m_{bb} distribution at preselection, for the signal point (450, 0) GeV fitted to a Crystal-ball function. 174
11.4 The m_T and E_T^{miss} N-1 distributions for the (250, 50), (375, 50) and (600, 0) signal points. The bottom pad shows a the expected significance when cutting on the value on the x-axis. 175
11.5 Shown are (a) the three SRs and the five CRs used in the analysis in the (m_T , m_{CT}) plan, (b) the SR, the $t\bar{t}$ CRs and the VRs in between in the (m_{bb} , m_{CT}) plan. A lower E_T^{miss} cut at 200 GeV is required for all these regions except for VR-off, where this cut is relaxed to 180 GeV. 176
11.6 Expected background compositions and the highest signal contamination in (a) CR-tt Low, Med and High, (b) CR-St and (c) CR-Wj control regions. 177
11.7 Distributions of (a) m_{CT} in the inclusive CR-tt and (b) m_{T}^{W}in CR-Wj, comparing data with the expected backgrounds from simulation. The lower panel shows the ratio between observed data and expected SM background. Uncertainties are statistical only. 178
11.8 Expected background compositions in (a) VR-onpeak and (b) VR-offpeak regions. 179
11.9 The signal contamination in % in the offpeak sideband validation regions: VR-offMM (a) and VR-offMH (b). 179
11.10 The truth number of heavy and light flavors jets as function of m_{CT}, m_{bb} of the $t\bar{t}$ events in control, validation and signal regions. 181
11.11 Data and SM predictions in SRs for (a) m_{CT} in SRMH and (b) $\mathrm{E_T^{miss}}$in SRMM. All SRs selections but the one on the quantity shown are applied. The statistical and systematic uncertainties are included in the uncertainty band. 187
11.12 Comparison of the predicted background with the observed numbers of events in the validation regions. The normalization of the background processes is obtained from the fit to the CRs. The upper panel shows the observed number of events and the predicted background yield. The statistical and systematic uncertainties are included in the uncertainty band. The lower panel shows the pulls in each VR. 187
11.13 The expected and observed exclusion limits as a function of the $\tilde{\chi}_2^0/\tilde{\chi}_1^\pm$ masses and $\tilde{\chi}_1^0$ mass for (a) $1\ell bb$ channel, (b) all channels. Only the expected exclusion is shown for the $1\ell\gamma\gamma$ channel since the observed exclusion does not appear due to the small excess observed. 189
11.14 Maximum mass reach of the ATLAS searches for SUSY [123]. 190
11.15 Expected 95% exclusion and discovery contours for the 3000 fb^{-1} luminosity scenario in the ($m_{\tilde{\chi}_1^\pm}$, $m_{\tilde{\chi}_1^0}$) plane for the Wh-mediated simplified model, comparing the cut and count and MVA approaches [124]. 190
11.16 Chargino-neutralino pair production via VBF process at the LHC (a) Feynman diagram where x1+, n1, n2 and h1 denote the $\tilde{\chi}_1^+$, $\tilde{\chi}_1^0$, $\tilde{\chi}_2^0$ and the SM higgs respectively, (b) cross section at LO at $\sqrt{s}$ =13 TeV. 191
0.17 The light jet rejection as a function of b-jet efficiency for the IP3D (a), SV1 (b), JetFitter (c) and MV2c10 (d) algorithms for MC16a configuration compared with the MC15c baseline in blue for $t\bar{t}$ sample. 213
0.18 p_T distribution of the track with lowest p_T (orange) and the track with highest p_T (green) in b-jets (a) and light jets (b). 214
0.19 (a) d_0 and (c) z_0 error distributions of the track with lowest p_T while (b) and (d) show the same for the track with highest p_T, in the b-jet in blue with IBL and in red fwithout IBL 215

0.20 The pull (a) d_0 and (b) z_0 distribution for the track with the lowest p_T in the b-jet, in blue with IBL and in red for scenario without IBL. 216
0.21 For the signal points having contamination in VRMMoff $>$ 15%: the expexted numbers of signal events in VRMMoff (a), their statistical uncertaities (b). 217
0.22 For the signal points having contamination in VRHMoff $>$ 15%: the expexted number of signal events in VRHMoff (a), their statistical uncertainties (b). 217
0.23 Signal points having contamination in VRHMoff $>$ 15%: Expexted number of signal in SRLM (a), Expexted number of signal in SRMM (b), Expexted number of signal in SRHM (c). 218
0.24 Signal points having contamination in VRHHoff $>$ 15%: Expexted number of signal in SRLM (a), Expexted number of signal in SRMM (b), Expexted number of signal in SRHM (c). 219
0.25 Full m_{bb} distributions, of the 3 signal points having the highest contamination in VRMMOff: Signal point (372, 12) GeV (a), Signal point (262, 62) GeV (b), Signal point (312, 12) GeV (c). 220
0.26 Full m_{bb} distributions at preselection, of the 3 signal points having the highest contamination in VRMMOff: Signal point (372, 12) GeV (c), Signal point (262, 62) GeV (b), Signal point (312, 12) GeV ??. 221
0.27 Full m_{bb} distributions, of the 3 signal points having the highest contamination in VRHMOff: Signal point (375, 25) GeV (a), Signal point (450, 0) GeV (b), Signal point (250, 0) GeV (c). 222
0.28 Full m_{bb} distributions at preselection, of the 3 signal points having the highest contamination in VRHMOff: Signal point (375, 25) GeV (a), Signal point (450, 0) GeV (b), Signal point (250, 0) GeV (c). 223
0.29 The truth number of heavy and light flavors jets of the $t\bar{t}$ events in control, validation and signal regions. 225

List of Tables

0.1 Trois exemples numériques du calcul de A_t à partir de la nouvelle entrée $m_h^{Deux\ boucles}$, en utilisant l'ensemble des corrections radiatives à une boucle ainsi que les corrections dominantes à deux boucles. 17

1.1 Gauge quantum numbers of the SM fermions (first family). 40

2.1 Chiral supermultiplets in the MSSM. 50
2.2 Gauge supermultiplets in the MSSM. 50
2.3 The ATLAS Run 1 scan ranges used for each of the 19 pMSSM parameters where "gen(s)" refers to generation(s) [34]. 59
2.4 Constraints on acceptable pMSSM points from considerations of precision electroweak and flavour results, dark matter relic density, and other collider measurements [34]. 60

3.1 The SM experimental input variables given at M_Z scale. 62
3.2 The 22 input parameters of the pMSSM. 63
3.3 The mSUGRA boundary conditions at M_Z, M_{EWSB} and M_{GUT} scales. 63
3.4 Numerical example of the A_t computation from m_h using the approximate one-loop correction. 73
3.5 The A_t computation from $m_h^{one-loop}$, using the full one-loop correction, for the 3 benchmark points. 78
3.6 The A_t computation from $m_h^{Two-loop}$, using the full one-loop plus leading two-loop correction, for the 3 benchmark points. 81

8.1 The Run 2 track selection criteria for the main b-tagging algorithms. 111
8.2 Description of the Run2 track categories used by IP2D and IP3D 113
8.3 V^0 mean life time and flight path. 116

9.1 Fraction of dead modules per layers at the start of Run2. 124
9.2 Configurations, produced from $t\bar{t}$ or Z' mix samples, with a fraction y of dead modules for the two innermost layers: (a) IBL, (b) L0. 125
9.3 Configurations, produced from $t\bar{t}$ or Z' mix samples, with a fraction y of dead modules for the two outermost layers: (a) L1, (b) L2. 126
9.4 The Pixel ToT configurations with x and y representing respectively the ToT cuts (in BC) for L0 (offline) and the two outermost layers for $t\bar{t}$ and Z' mix samples. The baseline configuration has (x, y)= (2, 4) BC. 128
9.5 Comparison between MC16a and MC15c configurations. 128
9.6 The mean and the RMS of the L0 pixel clusters Z and (r, ϕ) size distributions for MC16a and for MC15c: baseline (2, 4), (6,4), (10,4) and (13,4) configurations. 129
9.7 The fractions of tracks without any pixel cluster in L0 for MC16a and for MC15c: baseline (2, 4), (6,4), (10,4), (13,4) configurations. The fractions presented are within an error of 0.05% 129
9.8 The relative degradation in the light-jet rejection (%) for the IP3D and the MV2c10 taggers at a b-tagging efficiency of 75% for the six IBL scenarios produced using the $t\bar{t}$ sample. 132
9.9 The relative degradation in the light-jet rejection (%) for the SV1 and the JetFitter taggers at a b-tagging efficiency of 60% for the six IBL scenarios produced using the $t\bar{t}$ sample. 132
9.10 Release 20.7 operating points (for $t\bar{t}$ sample) checked. 134
9.11 The b-jet efficiency, light jet rejection and c-jet rejection using the MV2c10 tagger operating point of 0.6459 for the baseline and the IBL off scenario. 134
9.12 The relative degradation in the light-jet rejection (%) for the IP3D and the MV2c10 taggers at a b-tagging efficiency of 75% for the six L0 scenarios produced using $t\bar{t}$ sample. 142
9.13 The relative degradation in light-jet rejection (%) for the SV1 and the JetFitter taggers at a b-tagging efficiency of 60% for the six L0 scenarios produced using $t\bar{t}$ sample. 142
9.14 The relative degradation in the light-jet rejection (%) for the IP3D, the JetFitter and the MV2c10 taggers at 60% b-tagging efficiency for the scenario with L1 totally off produced using $t\bar{t}$ sample (second column) and Z' mix sample (last column). 146
9.15 The relative degradation in the light-jet rejection (%) for the IP3D, the JetFitter and the MV2c10 taggers at 60% b-tagging efficiency for the scenario with L2 totally off produced using $t\bar{t}$ sample (second column) and Z' mix sample (last column). 146
9.16 The relative degradation in the light-jet rejection (%) for the IP3D and the MV2c10 taggers at 75 % b-tagging efficiency for the six L0 scenarios produced using $t\bar{t}$ sample. The x and y represent respectively the ToT cuts for the L0 (offline) and the two outermost layers. 152
9.17 The relative degradation in the light-jet rejection (%) for the SV1 and the JetFitter taggers at 60 % b-tagging efficiency for the six L0 scenarios produced using $t\bar{t}$ sample. The x and y represent respectively the ToT cuts for L0 (offline) and the two outermost layers. 152
9.18 The b-jet efficiency degradation (in %) with respect to the baseline when increasing the L0 ToT minimal cut in function of jets p_T and $|\eta|$. 156

10.1 Comparison between Run1 and Run2 for the signal with $m_{\tilde{\chi}_1^\pm} = 250$ GeV and the main background process $t\bar{t}$ cross sections in pb. 165

11.1 List of generators used for the different processes. Information is given about the underlying-event tunes, the PDF sets and the pQCD highest-order accuracy (LO, NLO, next-to-next-to-leading order, NNLO, and next-to-next-to-leading-log, NNLL) used for the normalization of the different samples. 167
11.2 Cuts defining the baseline and signal electrons and muons. 168
11.3 Summary of the jet selection criteria. The signal selection requirements are applied on top of the preselection. 169
11.4 Summary of the event selection for signal regions of the $1\ell b\bar{b}$ channel. 176
11.5 The truth composition of the $t\bar{t}$ events in control, validation and signal regions. 180
11.6 The raw number of the signal ($m_{\tilde{\chi}^{\pm}}, m_{\tilde{\chi}_1^0}$)= (500, 0) GeV events in SRML corresponding to the 101 nominal PDF members. 183
11.7 The (Eff $\times$ Acc), mean$\pm$ Uncert$_{sys}$ in %, per signal region for 3 signal points. Second line of each signal region is showing the uncertainty as fraction(%) of the mean. 183
11.8 Background-only fit results for the SRML, SRMM and SRMH regions, for an integrated luminosity of 36.1 fb^{-1}. Nominal MC expectations (normalised to MC cross-sections) are given for comparison. The uncertainties shown are the statistical plus systematic. 186
11.9 The observed 95% CL upper limits on the visible cross sections σ_{vis}, the observed (S^{95}_{obs}) and expected (S^{95}_{exp}) 95% CL upper limits on the number of signal events with $\pm 1\sigma$ excursions of the expectation, and the discovery p-value (p_0), truncated at 0.5. 188
0.10 Z'($b\bar{b}$) dataSets names of the HITS samples for the different Z' masses values. 208
0.11 Z'($q\bar{q}$) dataSets names of the HITS samples for the different Z' masses values. 209
0.12 Rate (%) of tracks in the fourteen categories for the baseline and the IBL scenarios produced with $t\bar{t}$ sample. y represents the fraction of inactive module in IBL. 209
0.13 Rate (%) of tracks in the fourteen categories for the baseline and the L0 scenarios produced with $t\bar{t}$ sample. y represents the fraction of inactive module in L0. 210
0.14 Rate (%) of tracks in the fourteen categories for the baseline and the L1 (L2) scenarios produced with $t\bar{t}$ sample. y represents the fraction of inactive module in L1 (L2). 210
0.15 Rate (%) of tracks in the fourteen categories for the baseline and the scenarios produced with Z' mix sample. y represents the fraction of inactive module. 211
0.16 Rate (%) of tracks in the fourteen categories for the baseline and the scenarios with the highest L0 ToT cuts produced with $t\bar{t}$ sample. 211
0.17 Rate (%) of tracks in the fourteen categories for the baseline and the scenarios with the highest L0 ToT cuts produced with Z' mix sample. 212
0.18 Fraction (%) of events having mbb $\notin$ [95,145] for the 6 sig pts at Preselection, and with tighter m_T and E_T^{miss} cuts Errors shown are only stat errors. 223

Part I.

Theoretical overview

1. The Standard Model of Particle Physics

While there are several reasons to believe that the Standard Model (SM) is just the low energy limit of a more fundamental theory, the SM has been successfully tested at an impressive level of accuracy and provides at present our best fundamental understanding of the phenomenology of particle physics. It is (a model) a quantum field theory, that describes the fundamental particles currently experimentally known, as well as three of the four fundamental forces which are the electroweak force (including electromagnetic and weak forces) and the strong nuclear force. The main ingredient missing from the SM is the quantum version of the field of gravity.

This chapter intends to introduce the theoretical framework of the SM, while a more detailed discussion of this theory can be found in Ref [2]. In the first section several underlying concepts are introduced. Some of these concepts are based on the experimental observations that the elementary constituents of matter carry half-integer spins. Therefore they obey the Fermi–Dirac statistics and their wave functions change sign under parity transformations. Such particles are called fermions. In contrast, interactions among the fermions are mediated through the exchange of integer spin particles, called bosons. Those follow the rules of Bose-Einstein statistics. Section 1.1 introduces the gauge interactions which allow to define the SM constituents in section 1.3. The Higgs mechanism will be presented in section 1.2 which allows to introduce the SM Higgs and to discuss the significance of its discovery in section 1.4. Finally section 1.5 mentions the open problems of the SM.

1.1. Free Fields and Gauge interactions

The SM is first of all a quantum field theory (QFT). In QFT, particles are treated as excited states of an underlying field and are called field quanta, the interactions among these particles are described by interaction terms among the corresponding quantum fields. Those interactions are usually described in terms of Lagrangian ($\mathcal{L}$). The Lagrangian of a field is determined by its kinetic and potential energies T and V respectively:

$$\mathcal{L} = \mathrm{T} - \mathrm{V} \tag{1.1}$$

The most prominent examples of fields in QFT are: the fermionic field which is a quantum field whose quanta are fermions, they obey Fermi–Dirac statistics, also the scalar field which is associated with spin-0 particles such as the charged pions mediating the strong nuclear interaction. The Lagrangians for a free scalar field Φ or a free fermion field ψ both with masses m are:

$$\begin{aligned} \mathcal{L}_{\text{Klein-Gordon}} &= \frac{1}{2}\partial_\mu \Phi \partial^\mu \Phi^* - \frac{1}{2} m \Phi^* \Phi \\ \mathcal{L}_{\text{Dirac}} &= \bar{\Psi}\left(i\gamma_\mu \partial^\mu - m\right)\Psi \end{aligned} \tag{1.2}$$

where the field $\bar{\psi} = \psi^\dagger \gamma_0$ is the Dirac adjoint field, and the matrices γ_μ are the gamma or Dirac matrices defined in Ref [2]. Given these Lagrangians, the equations of motion can be obtained by applying the Euler–Lagrange equation:

$$\partial_\mu \left(\frac{\partial L}{\partial \left(\partial_\mu \Phi\right)} \right) - \frac{\partial L}{\partial \Phi} = 0 \tag{1.3}$$

Using the Lagrangians of equation 1.2, equation 1.4 shows the Klein–Gordon equation for the free

boson field and the Dirac equation for the free fermion field.

$$\begin{aligned}\left(\partial_\mu \partial^\mu + m^2\right)\Phi &= 0 \\ \left(i\gamma^\mu \partial_\mu - m\right)\Psi &= 0\end{aligned} \tag{1.4}$$

These equations can be thought of as relativistic generalisations of the Schrödinger equation. The simplest possible solutions are:

$$\begin{aligned}\Phi &= e^{\pm i P_\mu x^\mu} \\ \Psi &= u\left(\vec{p}\right) e^{\pm i P_\mu x^\mu}\end{aligned} \tag{1.5}$$

where $u(\vec{p})$ is a four-component Dirac spinor that depends on the momentum of the fermion field. These plane wave solutions form a basis for the Fourier components of any general fields that solve the equation 1.4. To describe the nature of weak interactions as will be discussed in section 1.3.1, a chirality projection operator can be defined as:

$$P = P_{R/L} = \frac{1}{2}\left(1 \pm \gamma^5\right) \tag{1.6}$$

where $\gamma_5 = \gamma_1\gamma_2\gamma_3\gamma_4$ is the product of the Dirac matrices γ_μ. With this operator a fermion field ψ can be split into a right- and a left-handed component:

$$\Psi = \frac{1}{2}\left(1 - \gamma^5\right)\Psi + \frac{1}{2}\left(1 + \gamma^5\right)\Psi = \Psi_L + \Psi_R \tag{1.7}$$

The definition of a projection operator to split the fields into these components is not needed if a particular representation of the Dirac matrices is chosen. In this so-called Weyl or chiral representation a four-component Dirac spinor field ψ can directly be written as a vector of two complex objects $\psi^T = (\xi_\alpha \chi^{\dagger\dot{\alpha}})$, where ξ_α is a two-component left-handed Weyl spinor and $\chi^{\dagger\dot{\alpha}}$ a two-component right-handed one. The spinor indices of the upper and lower components are usually labelled as greek symbols ($\alpha = 1, 2$) and as greek symbols with dots ($\dot{\alpha} = 1, 2$), respectively, to indicate the different behaviour of the upper and lower components of ψ with respect to electroweak interactions. Using this representation the Dirac Lagrangian can be written as:

$$\mathcal{L}_{\text{Dirac}} = i\xi^\dagger \bar{\sigma}^\mu \partial_\mu \xi + i\chi^\dagger \bar{\sigma}^\mu \partial_\mu \chi - m\left(\xi\chi + \xi^\dagger \chi^\dagger\right) \tag{1.8}$$

Here the σ-matrices are determined by the two-dimensional identity matrix I and the three Pauli matrices $\vec{\sigma}$ of the same dimension:

$$\bar{\sigma}^\mu = (\mathbf{1} - \vec{\sigma}) \tag{1.9}$$

In the Lagrangian formalism, interactions among fields are represented by terms that connect several fields and which are added to the free field Lagrangians of equation 1.2. Within the full Lagrangian, the interaction cross section σ of a given process can be derived by calculating the transition probability from the initial to the final state. In QFT, this probability can't be calculated exactly but instead a perturbation theory is used which gives a good approximation even when just taking lower orders of the perturbation series into account. In this approach the transition probability to a given order is then calculated as the square of the sum of all terms in the series up to that order. This square of sums is denoted as the Matrix element. Each of the terms in the perturbation series can be depicted by a Feynman diagram, named after their inventor R. P. Feynman [3]. These diagrams give a simple visualisation of complicated expressions and processes. However, if interaction terms are introduced by hand in an arbitrary way, higher order terms in the perturbation series, like those including loops

of virtual particles, usually lead to divergences in the calculations and therefore to unphysical expressions for measurable quantities. This problem can be solved by a reinterpretation of the parameters of the theory, like masses and couplings, as bare quantities and not as the physical quantities that can be measured in experiments. In this case the divergences can be absorbed in redefinitions of the bare parameters. Physical observables, however, will still remain finite since only differences to a given reference point, the renormalisation scale, can be measured. This renormalisation procedure does not only solve the issue with the divergences, it also implies that the coupling parameters of the theory are not constant. Instead they depend on the energy scale of a given process and therefore are usually denoted as running coupling constants.

Given the above considerations, the renormalisability of a theory is a necessary condition for a meaningful description of measurable quantities. In this context M.Veltman and G. 't Hooft showed that a quantum field theory is renormalisable if it is locally gauge invariant [4]. This principle of local gauge invariance is based on the concept that physical processes and their properties are preserved under transformations of certain symmetries. Transferred to the Lagrangian formalism, this means that the Lagrangian must be invariant (i.e. does not change) if the particle fields undergo local gauge transformations of the particular symmetry group. An example of the local gauge invariance is the invariance of the free fermion field Lagrangian of equation 1.2 under transformations of the symmetry group U(1). The elements of this group can be described as phase transformations of the fields:

$$\Psi \longmapsto \Psi e^{i\alpha(x)} \tag{1.10}$$

Local gauge invariance requires the transformation angle α to depend on the space-time coordinates x. Applying this transformation changes the derivative part of the kinetic term in the Lagrangian $\mathcal{L}_{Dirac}$ of equation 1.2 to:

$$\partial_\mu \Psi \longmapsto e^{i\alpha(x)} \partial_\mu \Psi + e^{i\alpha(x)}\ \Psi \partial_\mu \alpha\left(x\right). \tag{1.11}$$

As a consequence, the last term spoils the invariance under the local gauge transformation. Therefore, this Lagrangian is not locally gauge invariant and hence not renormalisable. To restore the local gauge invariance of the theory a new gauge field A_μ is introduced and its transformation properties are set to:

$$A_\mu \longmapsto A_\mu + \frac{1}{2}\partial_\mu \alpha\left(x\right), \tag{1.12}$$

Consequently, the ordinary derivative ∂_μ needs to be replaced by the covariant derivative D_μ, which is defined as:

$$D_\mu \longmapsto \partial_\mu - ieA_\mu \tag{1.13}$$

Using these definitions, the modified gauge invariant Lagrangian for a massless fermion field becomes:

$$\mathcal{L} = i\bar{\Psi}\gamma^\mu \partial_\mu \Psi - \frac{1}{4} F_{\mu\nu}\ F^{\mu\nu} - e\bar{\Psi}\gamma^\mu A_\mu \Psi \tag{1.14}$$

In equation 1.14, the kinetic term of the gauge field A_μ is expressed in terms of the field strength tensor $F_{\mu\nu}$. For a general gauge group with i generators and antisymmetric structure constants f^{ijk} this tensor is given by:

$$F_i^{\mu\nu} = \partial_\mu A_\nu^i - \partial_\nu A_\mu^i - g f^{ijk}\ A_\mu^j A_\nu^k \tag{1.15}$$

The last term in equation 1.14 shows that by requiring local gauge invariance, an interaction of the fermion fields with the gauge boson field with coupling strength e can be introduced in the Lagrangian in a renormalisable way.

1.2. The Higgs mechanism

An explicit mass term for the new gauge field is forbidden because it would violate the gauge invariance. Such a term would be of the form $\frac{1}{2}m^2 A^\mu A_\mu$. However, the gauge field masses can be generated dynamically by the Higgs mechanism that was initially proposed in 1964 by P. Higgs [5] [6] [7]. This mechanism adds an additional quantum field, the Higgs field, that all massive particles interact with. The physical mass eigenstate that is associated with the new field is the Higgs boson. The Higgs mechanism can be described using a model of a complex scalar field, $\phi = (\phi_1 + i\phi_2)/\sqrt{2}$, and its Lagrangian:

$$\mathcal{L} = (\partial_\mu \phi)^* \partial^\mu \phi - \mu^2 \phi^* \phi - \lambda (\phi^* \phi)^2 \tag{1.16}$$

where μ can be interpreted as the mass of the scalar field, if one assumes that $\mu^2 > 0$. The last term represents the self-interaction of the scalar field with coupling strength $\lambda > 0$. Following the discussion in the previous section, this Lagrangian can be made invariant under U(1) transformations of the Higgs field if the partial derivative is replaced by the covariant derivative of equation 1.13 and if a gauge field A_μ, satisfying equation 1.12, is introduced. In this case the Lagrangian of equation 1.16 becomes:

$$\mathcal{L} = (D_\mu \phi)^* D^\mu \phi - \frac{1}{4} F_{\mu\nu} F^{\mu\nu} - \mu^2 \phi^* \phi - \lambda (\phi^* \phi)^2 \tag{1.17}$$

The last two terms in equation 1.17 determine the scalar interaction potential $V = \mu^2 \phi^* \phi + \lambda (\phi^* \phi)^2$, that is denoted as the Higgs potential. To generate mass for the gauge field, the parameter μ^2 is taken as a bare parameter of the theory and not as the mass of the Higgs field. In that case the choice $\mu^2 < 0$ is valid. Figure 1.1 shows the shape of the Higgs potential for both cases, positive and negative μ^2. The case $\mu^2 < 0$ shows that the minimum of the potential is not at the origin anymore. Instead, there is a circle of minima in the ϕ_1-ϕ_2 plane, which is given by $\phi_1^2 + \phi_2^2 = v^2$, with $v^2 = -\mu^2/2\lambda$. The field ϕ can now be expanded around a minimum $v = v_0$ in terms of fields η and θ, which results in the expression:

$$\phi(x) = \sqrt{\frac{1}{2}} v_0 + \eta(x) + i\theta(x) \tag{1.18}$$

For this field the interaction potential is not symmetric anymore and the symmetry of the original model is spontaneously broken by the choice of the new ground state. Using the Taylor expansion for ϕ as given in equation 1.18, the Lagrangian of this theory can be written as:

$$\mathcal{L} = \frac{1}{2} (\partial_\mu \eta)^2 + \frac{1}{2} (\partial_\mu \theta)^2 - v_0^2 \lambda \eta + \frac{1}{2} e^2 v_0^2 A_\mu A^\mu - e v_0 A_\mu \partial^\mu \theta + ... \tag{1.19}$$

The fourth term in this equation represents an effective mass term with mass $m = ev_0$ for the field A that is generated by spontaneously breaking the symmetry. This is done in a way that preserves the local gauge invariance of the Lagrangian. Therefore, every theory in which the particles retrieve their masses by the Higgs mechanism will stay renormalisable. In addition to the generation of mass, the Higgs mechanism introduces a massive scalar field η, the Higgs boson, and a massless scalar field θ. Such massless scalars, denoted as "Goldstone bosons", are always created, when a symmetry is spontaneously broken. This is stated by the "Goldstone Theorem" that has been proven in Ref. [8]. However, within SM these additional bosons can be absorbed by appropriate gauge transformations and are interpreted as the longitudinal polarisation degrees of freedom of the massive gauge bosons.

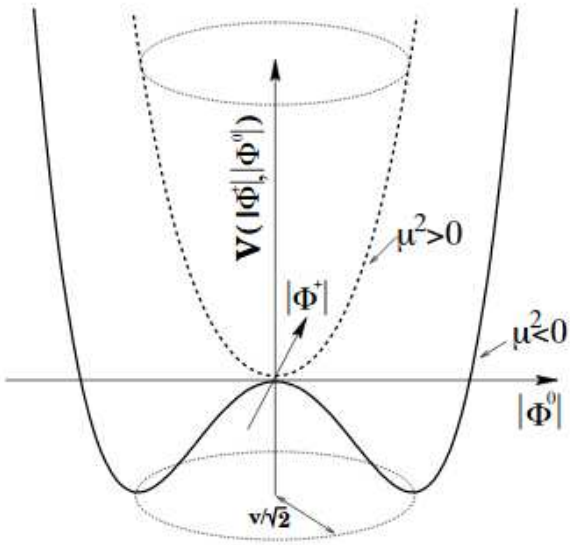

Figure 1.1.: The shape of the Higgs potential $V(\phi) = \mu^2\phi^*\phi + \lambda(\phi^*\phi)^2$, for positive and negative μ^2 with positive λ.

1.3. The Standard Model constituents

The SM of particle physics is based on the concepts discussed in the previous sections. The main ingredients of the SM are shown in figure 1.2. The particles involved are characterized by their spin, their mass, and the quantum numbers (charges) determining their interactions. The fermion content is organized in three families with identical quantum numbers and different masses. The heavier families are unstable and decay into the lightest one, which makes up most of the ordinary matter. The four fermions in each family are distinguished by their charges under strong and electromagnetic interactions. Two of them are quarks, which are charged under the strong interactions, and two are leptons, which are not. The two quarks have electromagnetic charges 2/3 ("up" quarks) and -1/3 ("down" quarks) respectively, and the two leptons have charges -1 (charged, or "down" leptons) and 0 (neutrinos, or "up" leptons), in units in which the electron charge is -1. The neutrinos are peculiar from two, they are neutral under both the strong and the electromagnetic interactions, but they feel weak interactions and they are at least six order of magnitudes lighter than all the other SM fermions. The masses of the SM fermions span a range going from the sub-eV neutrino masses to the $1.7 \cdot 10^2$ GeV top mass. Each fermion is associated to two so-called chiralities. Chirality is conserved for massless fermions, in which case the chirality coincides with the helicity. That is why the two possible chiralities are called left-handed and right-handed. Massive charged fermions are necessarily described by two components of different chiralities combined in a Dirac spinor. As for neutrinos, only the left-handed chirality has been observed so far.

The SM is a gauge field theory based on the symmetry group $U(1)_Y \otimes SU(2)_L \otimes SU(3)_C$: $U(1)_Y$ group with a quantum number called weak hypercharge Y, the group $SU(2)_L$ with quantum number weak isospin I_W and the $SU(3)_C$ group of strong interaction with colour charge C as quantum number. The mass eigenstates of the corresponding gauge bosons are the massive $W^{\pm}$ and Z bosons, the massless photon γ and eight massless gluons. In order to generate these masses and those of the fermions one massive Higgs boson is predicted by the Standard Model. The total Lagrangian of the Standard Model

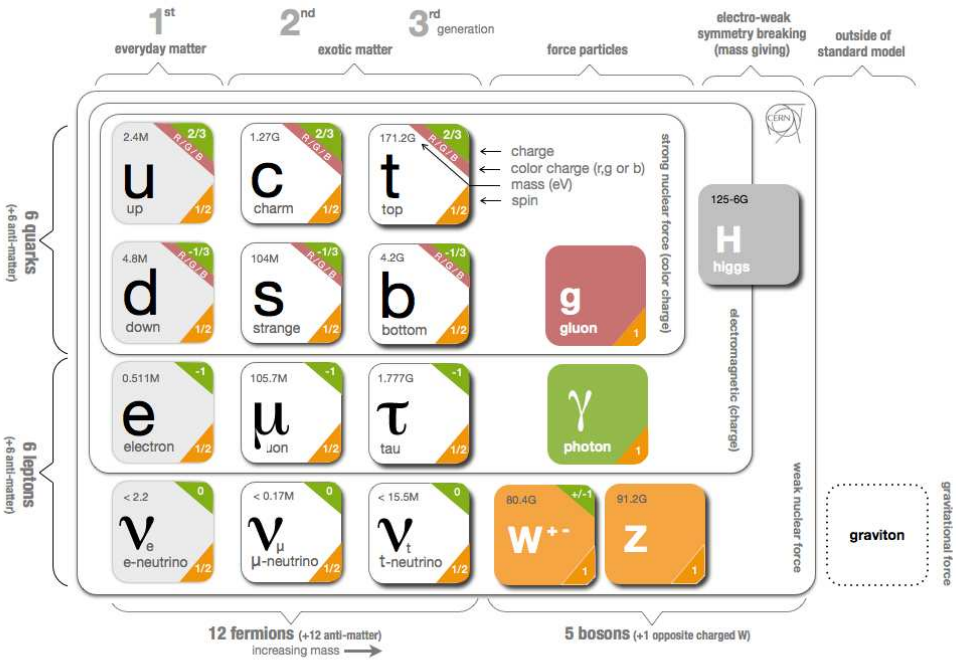

Figure 1.2.: The SM particle content.

can be written as:

$$\mathcal{L}_{\text{SM}} = \mathcal{L}_{\text{QCD}} + \mathcal{L}_{\text{EW}} + \mathcal{L}_{\text{Higgs}} + \mathcal{L}_{\text{Yukawa}} \tag{1.20}$$

In the next sections, each of the $\mathcal{L}_{SM}$ individual terms will be discussed.

1.3.1. Electroweak interactions

The electroweak interaction is the unified description of the electromagnetism and the weak interactions, the corresponding gauge symmetry group is $U(1)_Y \otimes SU(2)_L$. Although, these two forces appear very different at low energies, they are modeled as two different aspects of the same force. Above the unification energy, of the order of 246 GeV, they would merge into a single electroweak force. Sheldon Glashow, Abdus Salam, and Steven Weinberg were awarded the 1979 Nobel Prize for their contributions to this unification of the weak and electromagnetic interaction [9] [10].

The existence of the electroweak interactions was also experimentally established. Low-energy experiments have provided a lot of information about the dynamics underlying flavour-changing processes. The detailed analysis of the energy and angular distributions in β decays, such as $\mu^- \to e^-\bar{\nu}_e\nu_\mu$ or $n \to pe^-\bar{\nu}_e$, made clear that only the left-handed (right-handed) fermion (antifermion) chiralities participate in those charged weak transitions. Moreover, the strength of the interaction appears to be universal. This is further corroborated through the study of other processes like $\pi^- \to e^-\bar{\nu}_e$ or $\pi^- \to \mu^-\bar{\nu}_\mu$, which show that neutrinos have left-handed chiralities while anti-neutrinos are right-handed. From neutrino scattering data, we learnt the existence of different neutrino types ($\nu_e \neq \nu_\mu$) and that there are separately conserved lepton quantum numbers which distinguish neutrinos from antineutrinos.

Together with theoretical considerations related to unitarity and the absence of flavour-changing neutral-current transitions, the low-energy information was good enough to determine the structure of the modern electroweak theory. To describe the parity violating nature of weak interactions the left- and right-handed components of the fields, which can be projected out like shown in equation 1.6, are treated differently: only the left-handed components of the fields carry weak isospin charge and are arranged in doublets of the weak isospin symmetry group $SU(2)_L$. The right-handed fields do not carry weak isospin charge thus stay singlets under the $SU(2)_L$ symmetry transformations. Therefore, the electroweak theory is often called a chiral gauge theory. In addition to a possible weak isospin charge, all fermion fields except the right-handed neutrinos carry weak hypercharge of the $U(1)_Y$ gauge group. The arrangement of the first family of fermions into doublets and singlets of weak isospin is presented in table 1.1.

Table 1.1.: Gauge quantum numbers of the SM fermions (first family).

	$SU(3)_C$	$SU(2)_L$	$U(1)_Y$
L	1	2	-1/2
e_R	1	1	-1
Q	3	2	1/6
u_R	3	1	2/3
d_R	3	1	-1/3

$$L \equiv \begin{pmatrix} \nu_L \\ e_L \end{pmatrix} \qquad Q \equiv \begin{pmatrix} u_L \\ d_L \end{pmatrix}$$

The ordering of the leptons into the doublets of weak isospin is straightforward. In contrast, experiments demonstrated that weak interactions between quarks can proceed through flavour changing charged currents: not only transitions like u→d have been observed, but also transitions in between different generations, like u→s. Therefore, the quark eigenstates participating in electroweak interactions must be superpositions of their mass eigenstates. To describe this behaviour an additional mixing matrix for the quark fields denoted as the CKM matrix has been introduced by Cabibbo, Kobayashi and Maskawa [11]. With this matrix, labelled M_{CKM}, the quark field eigenstates of electroweak theory, q', can be related to their mass eigenstates, q, by:

$$\begin{bmatrix} d' \\ s' \\ b' \end{bmatrix} = M_{\text{CKM}} \cdot \begin{bmatrix} d \\ s \\ b \end{bmatrix} \tag{1.21}$$

Starting from the free field Lagrangian for the fermions, local gauge invariance under $SU(2)_L$ and $U(1)_Y$ transformations requires the introduction of a gauge boson triplet $W^{1,2,3}$ and one gauge field B, respectively, all with appropriate transformation properties. The covariant derivative of this theory is given by:

$$D_\mu = \partial_\mu + i\frac{g}{2}\tau_i W^i_\mu + i\frac{g'}{2} Y B_\mu \tag{1.22}$$

where the constants g' and g determine the coupling strengths of the fermions to the gauge bosons B and W^i, respectively. The Y and the τ_i in equation 1.22 denote the generators of the gauge groups $U(1)_Y$ and $SU(2)_L$, respectively. The τ_i are usually represented by the Pauli matrices σ_i. Given this covariant derivative the total Lagrangian of electroweak interactions can be written in terms of the weak isospin doublets of left-handed fields, represented by $(\text{ab})_L$, and the right-handed singlet fields,

a$_R$ and b$_R$:

$$\mathcal{L}_{\text{EW}} = i\left(\bar{a}\bar{b}\right)_L \gamma_\mu D^\mu \begin{pmatrix} a \\ b \end{pmatrix}_L + i\bar{a}_R\gamma_\mu D^\mu a_R \\ + i\bar{b}_R\gamma_\mu D^\mu b_R - \frac{1}{4}W^i_{\mu\nu}W_i^{\mu\nu} - \frac{1}{4}B_{\mu\nu}B^{\mu\nu} \tag{1.23}$$

Again the kinetic terms of the gauge fields W^i and B are expressed in terms of their field strength tensors $W^i_{\mu\nu}$ and $B_{\mu\nu}$. Their definition follows equation 1.15, given the appropriate structure constants f^{abc} of the gauge groups SU(2) and U(1).

1.3.2. Electroweak symmetry breaking

As discussed in section 1.2, explicit mass terms for the gauge bosons of electroweak theory are forbidden as these violate local gauge invariance. Instead the $U(1) \otimes SU(2)$ must be broken spontaneously to generate those masses. For this purpose a Higgs doublet of weak isospin, ϕ, is introduced:

$$\phi = \begin{pmatrix} \phi_\alpha \\ \phi_\beta \end{pmatrix} = \frac{1}{\sqrt{2}} \begin{pmatrix} \phi_1 + i\phi_2 \\ \phi_3 + i\phi_4 \end{pmatrix} \tag{1.24}$$

The Lagrangian of this Higgs doublet is given by:

$$\mathcal{L}_{Higgs} = D_\mu\phi^\dagger D^\mu\phi - \mu^2\phi^\dagger\phi - \lambda\left(\phi^\dagger\phi\right)^2 \tag{1.25}$$

According to section 1.2, the parameter μ^2 can be taken negative to spontaneously break the $U(1) \otimes SU(2)$ symmetry. This results in a non-trivial ground state for the Higgs doublet, which can be chosen as:

$$\phi_0 = \frac{1}{\sqrt{2}} \begin{pmatrix} 0 \\ v \end{pmatrix} \neq \begin{pmatrix} 0 \\ 0 \end{pmatrix} \tag{1.26}$$

The vacuum expectation value v of the Higgs boson is connected to the Fermi coupling G_F by $v = (\sqrt{2}G_F)^{-1/2}$ [2] [12]. As G_F was determined precisely from muon decay measurements [13] [14], the value of v could be predicted to $v \approx 246$ GeV. In contrast, the mass of the Higgs boson could not be predicted as the self interaction strength of the Higgs boson is not related to any quantity that could be measured. The choice of the new ground state as given in equation 1.26 generates the masses for the gauge bosons. Due to the SU(2) structure of weak isospin, the masses of the gauge bosons are described by a mass matrix for the fields W_i and B. The corresponding mass eigenstates can be obtained by diagonalising this matrix. However, the mass eigenstates already have been observed, they are the massive $W^\pm$ and Z bosons and the massless photon γ. To be in agreement with the experimental observations of a massless photon, the $U(1)_{em}$ symmetry of electromagnetic interactions must be preserved when the electroweak symmetry is broken. Hence, the quantum numbers of the Higgs doublet must be chosen appropriately. In that case the electromagnetic quantum number Q is connected to the third component of weak isospin I_3 and the weak hypercharge Y by the requirement $Q = I_3 - \frac{Y}{2}$, and the Higgs boson must be electrically neutral (Q=0). The resulting mixing of the fields B and W^i is parameterised by the weak mixing angle [2]:

$$\theta_W := \sin^{-1}\left(\frac{g'}{\sqrt{g^2 + g'^2}}\right) = \cos^{-1}\left(\frac{g}{\sqrt{g^2 + g'^2}}\right) \tag{1.27}$$

With this definition, the mass eigenstates are connected to the gauge boson by:

$$\begin{aligned} W_\mu^\pm &= -\frac{1}{\sqrt{2}}\left(W_\mu^1 \pm iW_\mu^2\right) \\ \begin{pmatrix} A_\mu \\ Z_\mu \end{pmatrix} &= \begin{pmatrix} \cos\theta_W & -\sin\theta_W \\ \sin\theta_W & \cos\theta_W \end{pmatrix} \begin{pmatrix} B_\mu \\ W_\mu^3 \end{pmatrix} \end{aligned} \tag{1.28}$$

The masses of the observed gauge bosons are determined by the coupling constants g and g' and the vacuum expectation value of the Higgs boson:

$$\begin{aligned} M_{W^\pm} &= \frac{1}{2}vg \\ M_Z &= \frac{1}{2}v\sqrt{g^2 + g'^2} \end{aligned} \tag{1.29}$$

The W and Z bosons were discovered experimentally at the UA1 and UA2 experiments in 1983 [15] [16] with measured values of $M_{W^\pm} \approx$ 80.4 GeV and $M_Z \approx$ 91.2 GeV [12].

On the other hand, to generate the masses of the fermions in a gauge invariant way, additional Yukawa coupling terms that connect the fermion fields to the Higgs field are introduced. For a fermion b, of which the left handed component is part of the weak isospin doublet $(\text{ab})_L$ and the right-handed component is the singlet b_R, the Yukawa term is given by:

$$\mathcal{L}_{\text{Yukawa}} = -G_b\left[\left(\bar{a}\bar{b}\right)_L \phi b_R + \bar{b}_R\phi^\dagger \begin{pmatrix} a \\ b \end{pmatrix}_L\right] \tag{1.30}$$

The masses of the upper components a of weak isospin doublets are generated as in equation 1.30 but with replacing ϕ by $-i\tau_2\phi^*$ and b_R by a_R. Following equation 1.30, in order to generate distinct masses for each fermion f, a new coupling constant G_f needs to be introduced.

1.3.3. Quantum chromodynamics

The strong interactions of quarks and gluons are described by Quantum Chromodynamics(QCD), which was developed in the 1970s. The symmetry of this theory is represented by the $\text{SU}(3)_C$ group of colour charge. The fermions that participate at strong interactions are the quarks, that either carry one of the three colours or anti-colours. Leptons do not interact strongly and therefore are not colour charged. The requirement of local gauge invariance under $\text{SU}(3)_C$ symmetry requires a covariant derivative of the form:

$$D_\mu = \partial_\mu + ig_s\lambda_i G_\mu^i \tag{1.31}$$

where λ_i are the eight generators of the $\text{SU}(3)_C$ symmetry group, which are usually represented by the Gell-Mann matrices defined in Ref. [2]. Eight gluon gauge fields G^i are required to ensure local gauge invariance. With the covariant derivative of equation 1.31 and by defining the quark colour triplets q_f for each of the six quark flavours f, the Lagrangian of the strong interactions for massless quarks can be written as:

$$\mathcal{L}_{\text{QCD}} = \sum_{\text{flavours f}} i\bar{q}_f\gamma_\mu D^\mu q_f - \frac{1}{4}G_{\mu\nu}^i G_i^{\mu\nu} \tag{1.32}$$

The tensor $G_{\mu\nu}^i$ is the gauge invariant gluonic field strength tensor as defined in equation 1.15, with the $\text{SU}(3)_C$ structure constants f_{ijk} and the coupling constant of strong interactions. The symmetry

group SU(3)$_C$ is non-abelian, their elements and generators do not commute. This leads to additional terms in the Lagrangian if a gauge transformation is applied to the fermion fields and the ordinary derivative is replaced by the covariant derivative. To compensate these terms the gluon fields G^i are defined to transform differently from the field in equation 1.12: an additional contribution $-f_{ijk}\alpha^j G^k_\mu$ is required to recover the gauge invariance of the Lagrangian. This transformation behaviour is reflected by the last term of the field strength tensor definition of equation 1.15, $-gf^{ijk}G^j_\mu G^k_\nu$, which represents a self-interaction term among the gluons. The corresponding coupling strength is given by the coupling constant of strong interactions. The interpretation of this self interaction is that gluons carry colour charge themselves(a colour and an anti-colour) and therefore allow for colour exchanges in between quarks. This has important consequences on the behaviour of the running coupling constant of Quantum Chromodynamics, α_s, which can be expressed at one-loop level as in equation 1.33 [2].

$$\alpha_s\left(Q^2\right) = \frac{1}{\beta_0 \ln\left(\frac{Q^2}{\Lambda^2}\right)} \tag{1.33}$$

In this equation, Q^2 denotes the energy scale of the interaction process, Λ the fundamental energy scale of strong interactions and β_0 a constant computed by Gross, Wilczek and Politzer [17] [18]. At short distances (high energies) the running coupling constant of strong interactions gets small and therefore quarks and gluons interact very weakly at these conditions. This is called the asymptotic freedom of quarks and gluons. However, the strong coupling constant gets very large at large distances (low energies). Therefore, if quarks get separated the potential energy between them increases up to some threshold at which it is energetically more favorable that a quark–anti-quark pair is created. For this reason quarks cannot be observed in isolation, instead they cluster to colour neutral groups of quarks, the hadrons. This phenomenon is known as colour confinement, the process of the creation of quark–anti-quark pairs and the clustering to hadrons is denoted as hadronisation or fragmentation. The resulting hadrons do not solely consist of the valence quarks that built up the hadron. In addition, there is an indefinite number of sea (anti-)quarks and gluons that carry parts of the momentum of the hadron and constantly exchange colour charge among themselves.

1.4. Higgs boson searches and discovery

Although many searches for the Higgs boson have been carried out since its prediction, it has remained elusive until 2012. About 10 years ago, searches at the CERN Large Electron Positron (LEP) collider indicated that the Higgs boson mass was greater than 114.4 GeV. On the other hand, after 25 years of collecting data, experiments at the Tevatron proton-antiproton collider at Fermilab excluded in 2011 the mass region 147 to 180 GeV at 95% C.L.. Then came the CERN Large Hadron Collider (LHC), which will be described in section 4, to observe the SM Higgs boson and measure its properties. In 2011, the LHC operated with a total proton-proton collision energy of 7 TeV. Both ATLAS and CMS experiments observed tantalizing hints of a new particle with mass in the region 124 to 126 GeV and compatible with a SM Higgs boson. The LHC's collision energy was raised to 8 TeV in 2012, increasing the predicted production rate of SM Higgs bosons and the sensitivity of the search.

The processes relevant for the production of a SM Higgs boson at the LHC are shown in figure 1.3(a). The corresponding cross sections of these processes are shown in figure 1.3(b) as a function of the proton-proton collision energy for a Higgs boson mass of 125 GeV. The most important SM Higgs boson production process in the energy range of the LHC is expected to be gluon fusion. Gluons do not directly produce the SM Higgs boson but rather do so indirectly through a quantum loop process involving mainly the heaviest (top) quark. Other processes are predicted to provide much clearer signals but at substantially reduced rates.

The production and decay rates shown in figure 1.4 are taken from theoretical predictions.

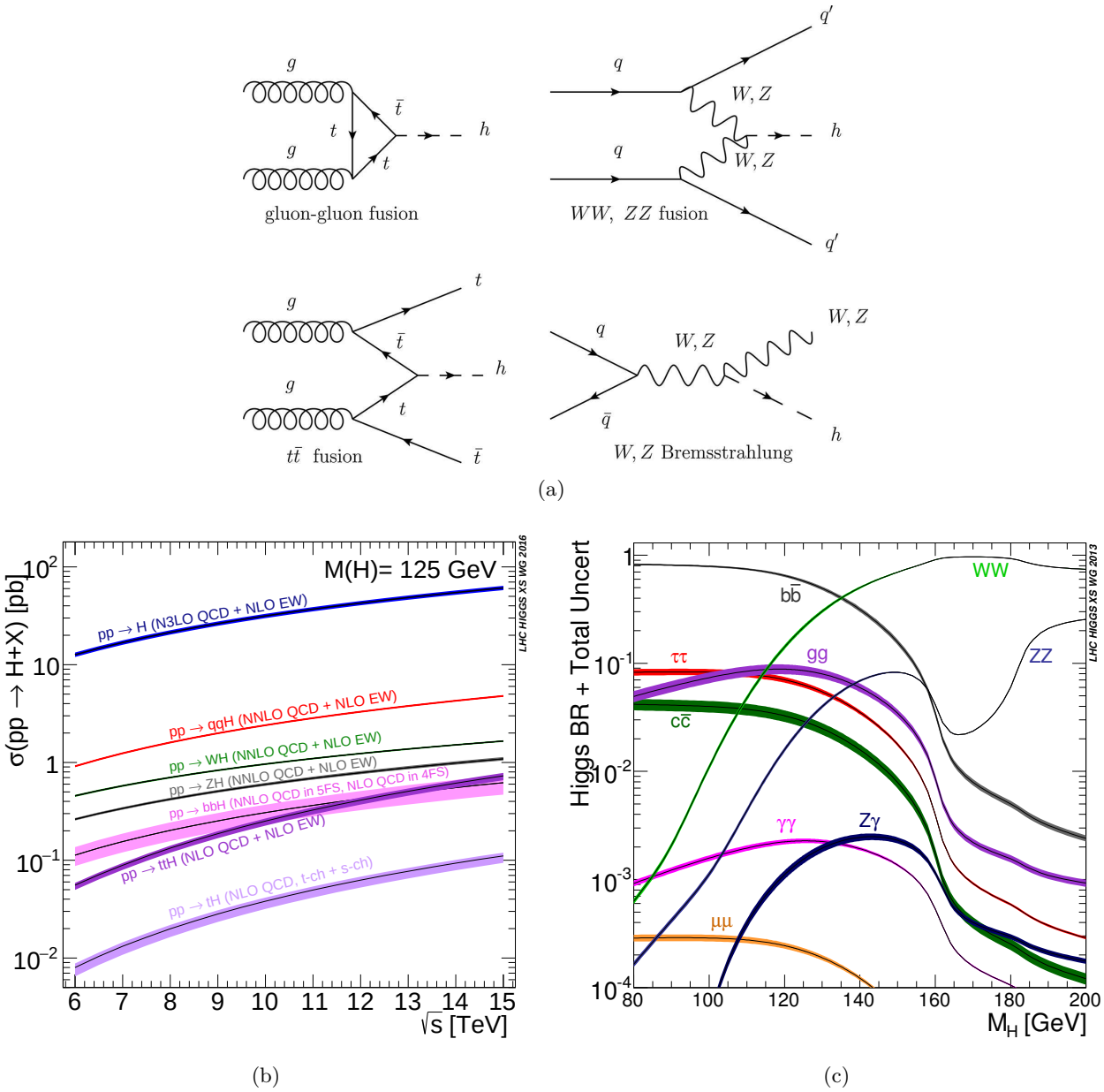

Figure 1.3.: (a) Dominant production processes for the SM Higgs boson. These are the gluon-fusion , the Vector Boson Fusion , the Higgs strahlung and the t$\bar{t}$ associated production processes repectively, in descending order regarding their cross sections shown in (b) as function of the proton-proton collision energy [19]. (c) The Higgs boson decay rates as function of its mass [20].

Detection of a Higgs boson required computing its mass from the total energy and momentum of all its decay particles. For a Higgs boson with a mass of $\approx$ 126 GeV, the Higgs boson would have five main experimentally accessible decay channels (H$\rightarrow$ $\gamma\gamma$, ZZ, WW, bb, or $\tau\tau$). Two of the most sensitive channels as shows figures 1.4(a) and 1.4(b), were the decay into two photons (denoted

the H→ $\gamma\gamma$ channel) and the decay into two Z bosons, which in turn each decay into an oppositely charged pair of electrons or muons (denoted the H→ZZ→ $\ell\ell\ell\ell$ channel). Both of these channels were examined in the data from 2011 and 2012. An additional sensitive decay mode involving two W bosons decaying to an electron, a muon, and two neutrinos (denoted the H→WW→ $e\nu\mu\nu$ channel) was included in the 2012 search. Additional channels in which the SM Higgs boson decays to pairs of b quarks (which dominates for low Higgs boson mass) or τ leptons, or alternative decay patterns for the W or Z bosons, have so far been studied in 2011 data having more complex signatures.

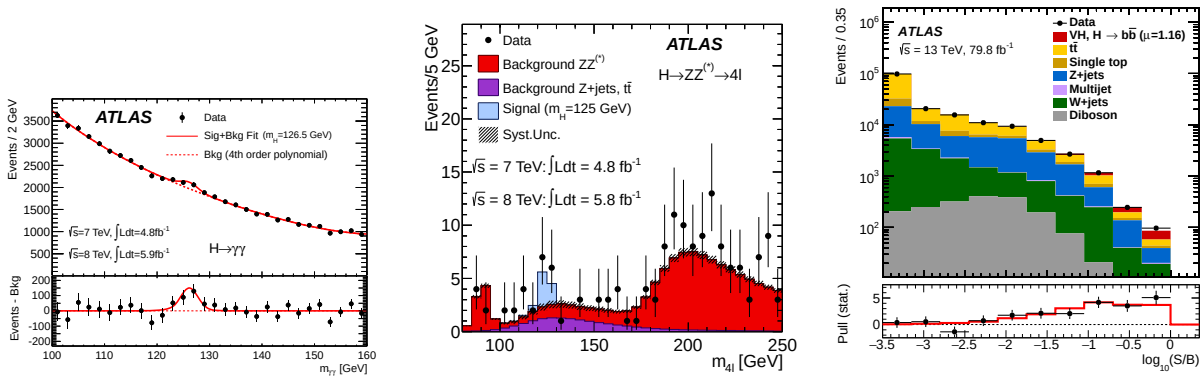

(a) (b) (c)

Figure 1.4.: (a) Shows the invariant mass from pairs of photons selected in the Higgs to $\gamma\gamma$ analysis. The excess of events over the background prediction around 125 GeV is consistent with predictions for the Standard Model Higgs boson. (b) The distribution of candidate Higgs events from the H to ZZ to 4 leptons analysis [21]. (c) The distribution from VH analysis H decaying to bb, showing log(S/B), where S and B are the signal and background yields, respectively. The lower panel shows the "pull", i.e. the ratio of data minus background to the statistical uncertainty of the background [22].

Evidence for Higgs boson production is inferred from statistically significant excesses of events above the background predictions. The significance is typically quoted as σ, or a number of standard deviations of the normal distribution. In particle physics, a significance of 3σ is referred to as evidence, while 5σ is referred to as an observation, corresponding to the probability of a statistical fluctuation from the background of less than 1 in a million. On 4 July 2012, the ATLAS and CMS Collaborations annouced that each experiment found an excess around 5σ at a Higgs boson mass of 125 GeV. On 8 October 2013 the Nobel prize in physics was awarded jointly to François Englert and Peter Higgs "for the theoretical discovery of a mechanism that contributes to our understanding of the origin of mass of subatomic particles, and which recently was confirmed through the discovery of the predicted fundamental particle, by the ATLAS and CMS experiments at CERN's Large Hadron Collider." As shown in figure 1.5(a), using LHC Run1 data combination of H→ $\gamma\gamma$ and H→ZZ*→4ℓ decay channels give $m_H = 125.36 \pm 0.37(stat.) \pm 0.18(syst.)$ GeV based on ATLAS data and $m_H = 125.09 \pm 0.21(stat.) \pm 0.11(syst.)GeV$ based on ATLAS and CMS data combined. ATLAS and CMS further verified SM coupling relationship of Higgs boson. In the SM, coupling of Higgs to fermions is $\propto m_f$ and for massive weak bosons is $\propto m_V^2$. Good agreement with expectation from SM across wide particle mass range was seen as shows figure 1.5(b). Also the two experiments measured the Higgs boson width. SM Higgs boson with $m_H = 125$ GeV has expected to have a width $\Gamma_H = 4.1$

MeV. The direct limits on Higgs boson width calculated by ATLAS and CMS are ≈2 GeV. However, indirect limits from measurement of off-shell coupling strength in high-mass tails result in Observed (expected) limit of $\Gamma_H < 22.7$ (33.0) MeV. The data also provide evidence for the spin-0 nature of the Higgs boson, with positive parity. During the LHC Run 2, the increase in the centre-of-mass energy to

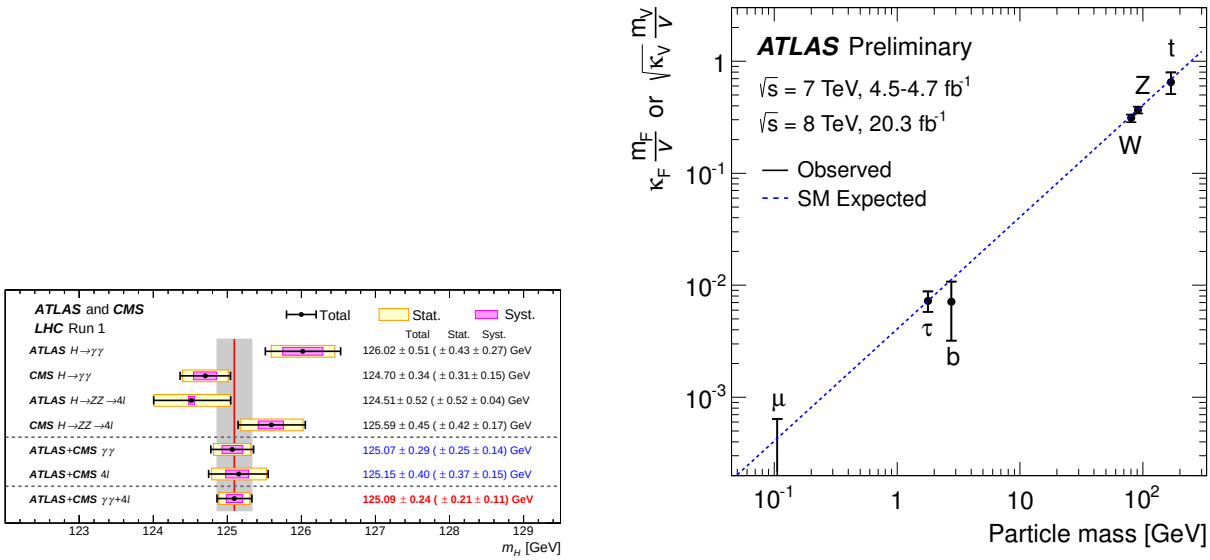

(a) (b)

Figure 1.5.: (a) Higgs boson mass measurements from the individual analyses of ATLAS and CMS and from the combined analysis. The systematic (narrower, magenta-shaded bands), statistical (wider, yellow-shaded bands), and total (black error bars) uncertainties are indicated. The (red) vertical line and corresponding (gray) shaded column indicate the central value and the total uncertainty of the combined measurement, respectively. (b) The coupling of the Higgs boson to fermions (μ, τ, b, t) and bosons (W, Z) as a function of the particle's mass, scaled under some theoretical assumptions. The diagonal line indicates the Standard Model prediction [23].

13 TeV and the larger dataset allowed further channels to be probed. Over the past year, the evidence for the Higgs decay to bottom quarks as figure 1.4(c) shows and the production of the Higgs boson together with top quarks has been observed. This means that the interaction of the Higgs boson to fermions has been clearly established.

The discovery of a SM Higgs-like boson may have identified the last missing piece of the SM but is also a motivation for further studies of the newly discovered boson, which might help to explore the physics beyond the SM. A relatively light Higgs boson suggests that new physical phenomena may exist at energies not far above the measured mass. Without new phenomena, quantum loop processes would drive the predicted Higgs boson mass far above the highest energy scale at which the SM is valid. For example, the supersymmetry model could provide a natural explanation for the light mass. Various models, including supersymmetry, suggest that at least five distinct types of Higgs bosons exist. Therefore, another key issue is whether the observed boson is the only Higgs boson.

1.5. Limitations of the Standard Model

Despite being a successful, thoroughly tested theory we know that there are problems the SM can't explain. These gaps in our understanding indicate that the SM is only an approximation, at low energies, of a more complete theory.

Here are currently the major unsolved problems within the standard model:

- Neutrino mass: the SM initially assumed neutrinos were massless, until it was experimentally determined that they had some tiny mass. Their exact masses and the mechanism behind is not yet understood and requires beyond standard model (BSM).
- Interaction unification: two of the four fundamental interactions have already been unified into the electroweak interaction. The next step is to try and unify this with the strong force, at an even higher unification energy. The ultimate aim would then be to unify this with gravity and have one fundamental unified interaction.
- Gravity: it is not explained within the SM. The properties of a graviton, the name coined for a potential force carrier, are still debated let alone observed by experiment.
- Dark matter and dark energy: Only about 5% of our universe consists of 'ordinary matter' as explained by the standard model. The rest is made up of completely unexplained kinds of matter and energy, which we currently call dark matter and dark energy.
- Matter-antimatter asymmetry: We observe that our universe is almost exclusively matter and the SM gives no reasons why antimatter and matter shouldn't be produced in equal amounts. Therefore, it is a question of cosmology and particle physics as to why our universe has developed into such an asymmetrical state.
- The hierarchy problem: Quantum corrections to the Higgs boson mass lead to divergent contributions. In the SM a stringent fine-tuning of several parameters is required to accomplish cancellations of the divergent terms. This need is denoted as the fine-tuning problem. Closely related to the fine-tuning problem it the hierarchy problem: given the measured value for the vacuum expectation value of the Higgs field and the cancellations of divergences due to the fine-tuning, the mass of the SM Higgs boson is very low compared to the Planck mass. There is no obvious reason for the large difference of these quantities.

To solve these issues several extensions to the Standard Model have been proposed. In the next chapter we will discuss one of these extensions, the class of Supersymmetric extensions (SUSY).

2. Supersymmetric extension of the SM

Supersymmetry (SUSY) is a well-motivated BSM theoretical framework which may solve multiple problems of the SM that were discussed in section 1.5: it provides the gauge coupling unification at a scale M_{GUT} of the order of 10^{16} GeV [24], moreover it can provide an explanation of the large hierarchy between the energy scale that characterizes the EWSB ($\approx$ 100 GeV) and the Planck energy scale ($M_P \approx 10^{19}$ GeV) where the gravitational interactions become comparable in magnitude to the gauge interactions. The stability of this large gauge hierarchy with respect to radiative quantum corrections is not possible to maintain in the SM without an unnatural fine-tuning of the parameters of the fundamental theory at the M_P, in contrast in a SUSY extension of the SM this unnatural fine-tuning is not needed anymore [24]. Since none of the superpartners predicted by SUSY have (yet) been observed, it must be a broken symmetry, nevertheless, the stability of the gauge hierarchy can still be maintained if the SUSY breaking is soft and the corresponding SUSY-breaking mass parameters are not larger than a few TeV.

This chapter intends to introduce some basic points about SUSY and the soft SUSY breaking in sections 2.1 and 2.2, while a more detailed discussion of SUSY theoretical framework can be found in Refs [24], [25]. Then, an overview of the Minimal Supersymmetric SM is presented in section 2.3 and finally the SUSY simplified models, widely used to search for SUSY at particle collider, are discussed in section 2.4.

2.1. Basics of Supersymmetry

2.1.1. Supersymmetric transformations

SUSY is a symmetry that connects bosons with fermions and is the only way space-time and internal symmetries can be combined consistently [26]. A SUSY transformation proceeds via a fermionic generator Q which shifts, upwards or downwards, the spin S by half a unit of $\hbar$ as equation 2.1 shows.

$$\begin{aligned} Q|S\rangle &= |S \pm 1/2\rangle \\ Q|boson\rangle &= |fermion\rangle \\ Q|fermion\rangle &= |boson\rangle \end{aligned} \tag{2.1}$$

The simplest scenario suggests only one fermionic generator Q and its conjugate $\bar{Q}$: expressed in terms of two Weyl spinors, Q acts on the left-handed spinor, $\bar{Q}$ acts on the right-handed spinor [26] and have the (anti) commutation relations presented in equation 2.2:

$$\begin{aligned} \left\{Q_\alpha, \bar{Q}_{\dot{\beta}}\right\} &= 2(\sigma^\mu)_{\alpha\dot{\beta}} P_\mu \\ [Q_\alpha, P_\mu] &= 0 \\ [Q_\alpha, B_r] &= b_r Q_\alpha \end{aligned} \tag{2.2}$$

where P_μ are the generators of translation, σ^μ are the Pauli matrices, B_r an internal symmetry generator and b_r its eigenvalue. The last two relations in equation 2.2 show that SUSY preserves the fields mass, quantum numbers and only affect the spin. The extension of the Poincaré algebra to incorporate SUSY is known as the super-Poincaré algebra [25]. Its elements are described in equation 2.3.

$$G(x^\mu, \theta, \bar{\theta}) = e^{ix^\mu P_\mu + i + i\bar{\theta}\bar{Q}} \tag{2.3}$$

This equation contains space-time coordinates x^μ and four extra fermionic coordinates $\theta^1, \theta^2, \bar{\theta}^1, \bar{\theta}^2$ transforming as a two-component Weyl spinor and its conjugate. The irreducible representations of this SUSY algebra are supermultiplets that contain fields with the same quantum numbers but different spins: the boson and fermion resulting from the SUSY transformation. The most commonly used supermultiplets are vector and chiral supermultiplets which will be described in section 2.1.2. All the SM fields and their SUSY partner fields fit in these 2 representations. One of the early idea was to form these supermultiplets with the known SM particles, i.e. neutrino as the fermionic partner of the photon, but it was then realized that this is impossible and that it is unavoidable to at least double all the SM particles by introducing a new bosonic partner for each SM fermion and a new fermionic partner for each SM boson [27] as equation 2.4 shows. Also, two Higgs doublets are needed in the SUSY version of the SM, not just one as it will be discussed in section 2.3.3.1.

$$\begin{aligned} Fermions(\psi_i) &\leftrightarrow Scalar\ Fermions\ (\phi_i) \\ Gauge\ Bosons(W^a) &\leftrightarrow Gauginos(\lambda^a) \\ Higgs(H) &\leftrightarrow Higgsino(\tilde{H}) \end{aligned} \tag{2.4}$$

2.1.2. Chiral and vector supermultiplets components

A chiral (also known as scalar) supermultiplet consists of a spin-1/2 Weyl fermion ψ_i with 2 degrees of freedom on-shell ($N_{dof}^{on-shell}$) and a complex spin-0 boson ϕ_i ($N_{dof}^{on-shell} = 2$), both with the same quantum numbers, except the spin. Such supermultiplets represent the leptons, quarks and their superpartners called sfermions ("scalar fermions"). Since the left- and right-handed components of a fermion field are separate two-component Weyl fermions that couple differently to the gauge bosons of electroweak interactions, two complex scalar superpartners are postulated for each fermion. Despite the fact that the sfermions are spin-0 particles, they are denoted as left- or right-handed fields to indicate their affiliation to the fermions. The gauge interactions for these sfermions are identical to those of their SM partners.

For SUSY to be preserved, equal masses and N_{dof} between fermions and scalars are needed. This is achieved in the on-shell case, however to always maintain $N_{dof}(\phi) = N_{dof}(\psi)$, in particular within loops where particles could be off-shell, an additional complex scalar field F is introduced having N_{dof}= 2. Its role is to compensates the $\Delta N_{dof} = 2$ in the off-shell case. F is not a physical field, it does not propagate (no kinetic term), it can be eliminated using its equation of motion. So the chiral supermultiplet content is: Ψ=(ϕ_i,ψ_i, F).

On the other hand, a vector (also known as gauge) massless supermultiplet contains a real vector field A_μ ($N_{dof}^{on-shell} = 2$) and a Weyl fermion λ ($N_{dof}^{on-shell} = 2$). These multiplets describe a massless SM gauge boson with spin-1 and a massless spin-1/2 Weyl fermion, the gaugino and take care of the gauge interactions. As for the chiral supermultiplet, an auxiliary real scalar field D is added and Φ= (λ, A_μ, D). The SM fields and their SUSY partner fields forming these supermultiplets are shown in tables 2.1 and 2.2.

Table 2.1.: Chiral supermultiplets in the MSSM.

Names		Spin 0	Spin 1/2	$SU(3)_C$	$SU(2)_L$	$U(1)_Y$
squarks, quarks	Q	$(\tilde{u}_L \tilde{d}_L)$	(u_L, d_L)	3	2	1/6
	$\bar{u}$	$\tilde{u}_R^*$	$u_R^\dagger$	$\bar{3}$	1	-2/3
	$\bar{d}$	$\tilde{d}_R^*$	$d_R^\dagger$	$\bar{3}$	1	1/3
sleptons, leptons	L	$(\tilde{\nu}\tilde{e}_L)$	(νe_L)	1	2	-1/2
	$\bar{e}$	$\tilde{e}_R^*$	$e_R^\dagger$	1	1	1
Higgs, higgsinos	H_u	$(H_u^+ H_u^0)$	$(\tilde{H}_u^+ \tilde{H}_u^0)$	1	2	+1/2
	H_d	$(H_d^0 H_d^-)$	$(\tilde{H}_d^0 \tilde{H}_d^-)$	1	2	-1/2

Table 2.2.: Gauge supermultiplets in the MSSM.

Names	Spin 1/2	Spin 1	$SU(3)_C$	$SU(2)_L$	$U(1)_Y$
gluino, gluon	$\tilde{g}$	g	8	1	0
winos, W bosons	$\tilde{W}^\pm, \tilde{W}^0$	$W^\pm, W^0$	1	3	0
bino, B boson	^{0}	B^0	1	1	0

2.1.3. Wess-Zumino model

In 1974, Julius Wess and Bruno Zumino studied the dynamics of a single chiral superfield composed of a complex scalar and a spinor fermion [28]. The simplest action we can write down for this chiral supermultiplet consists of kinetic energy terms for each of its components:

$$S = \int d^4x(\mathcal{L}_{scalar} + \mathcal{L}_{fermion} + \mathcal{L}_{auxiliary}) \tag{2.5}$$

where

$$\begin{aligned} \mathcal{L}_{scalar} &= -(\partial^\mu \phi)(\partial_\mu \phi^*) \\ \mathcal{L}_{fermion} &= -i(\psi^\dagger \bar{\partial}^\mu \partial_\mu \psi) \\ \mathcal{L}_{auxiliary} &= F^* F \end{aligned} \tag{2.6}$$

2.1.4. Chiral supermultiplet interactions

Hereafter, we introduce the interaction between the scalar and the fermion within the chiral supermultiplet.

$$\mathcal{L}_{int} = -\frac{1}{2} W^{ij}(\phi)\psi_i\psi_j + V(\phi, \phi^*) + h.c. \tag{2.7}$$

As equation 2.8 shows, W^{ij} is derived from the superpotential W(ϕ) expressed in terms of ϕ where M^{ij} and y^{ijk} represent the fermion mass matrix and the yukawa couplings between the scalar and the fermions respectively.

$$\begin{aligned} W^{ij} &= \frac{\partial^2 W(\phi)}{\partial\phi_i \partial\phi_j} \\ W(\phi) &= \frac{1}{2} M^{ij}\phi_i\phi_j + \frac{1}{6} y^{ijk}\phi_i\phi_j\phi_k \end{aligned} \tag{2.8}$$

The auxiliary fields F_i are connected to the superpotential via their equation of motion as shown in eqaution 2.9.

$$\begin{aligned} F_i &= -\frac{\partial W(\phi)}{\partial \phi^i} = -W_i^* \\ F^{*i} &= -\frac{\partial W(\phi)}{\partial \phi_i} = -W^i \end{aligned} \tag{2.9}$$

The scalar potential V can be expressed in terms of the superpotential as well, as equation 2.10 shows.

$$V = F_i F^{*i} = W_i^* W^i \tag{2.10}$$

2.1.5. Vector supermultiplet interactions

The Lagrangian density for a vector supermultiplet can be written as:

$$\mathcal{L}_{gauge} = -\frac{1}{4} F^a_{\mu\nu} F^{a\mu\nu} - i\lambda^{a\dagger}\bar{\partial}^\mu D_\mu \lambda^a + \frac{1}{2} D^a D_a - V \tag{2.11}$$

where $F^a_{\mu\nu}$ is the usual Yang-Mills field strength and $D_\mu\lambda^a$ the covariant derivative of the gaugino field given in equation 2.12.

$$
\begin{aligned}
F^a_{\mu\nu} &= \partial_\mu A^a_\nu - \partial_\nu A^a_\mu - g f^{abc} A^b_\mu A^c_\nu \\
D_\mu \lambda^a &= \partial_\mu \lambda^a - g f^{abc} A^b_\mu \lambda^c
\end{aligned}
\tag{2.12}
$$

The gauge auxiliary field equation of motion can be written as $D^a = -g\phi^* T^a \phi$. As equation 2.13 shows the full scalar potential contains the Yukawa interactions (F terms) and the gauge interactions (D terms).

$$
V = F_i F^{i*} + \frac{1}{2}\sum_a D^a D_a = W_i^* W^i + \frac{1}{2}\sum_a (g\phi^* T^a \phi)^2 \tag{2.13}
$$

2.2. Soft Supersymmetry breaking

If SUSY were an exact symmetry, the SM particles and their superpartners would have exactly the same masses, since no SUSY particles have been observed so far, SUSY must be broken if realised in nature. Several models of SUSY breaking have been proposed in the literature [29], [30]. A common feature of all the proposals is that the symmetry is broken in a soft way meaning that all additional contributions to the SUSY Lagrangian only contain mass terms and parameters with positive mass dimensions while the dimensionless terms in the Lagrangian remain unchanged. So the soft SUSY breaking give different masses to SM particles and their superpartners but preserves the structure of couplings of the theory. Within this requirement the quadratic divergences to the Higgs mass are not reintroduced and therefore soft SUSY breaking models still provide a solution to the hierarchy problem. A drawback of the softly breaking SUSY terms is that one introduces $\mathcal{O}(100)$ new free parameters (on top of the 19 of the SM), which decreases the predictivity of the theory. This number can be reduced to $\mathcal{O}(20)$ when assuming the absence of CPV phases and mixing of fermion generations and assuming the universality of the first and second generations of sfermions. Such models with restricted parameter space are easier to investigate and therefore are denoted as phenomenological models [31]. In addition to the explicit approach to just add soft SUSY breaking terms to the Lagrangian, different scenarios describing how SUSY might be broken spontaneously were proposed. Several models such as the minimal Supergravity model (mSUGRA) [32], introduce new interactions at high mass scales and further constraints on the masses and mixing angles are predicted reducing the number of free parameters to $\mathcal{O}(5)$.

2.3. Minimal Supersymmetric Standard Model - MSSM

The MSSM, originally proposed in 1981, is a supersymmetric extension of the SM with minimal particle content. It imposes R-parity conservation to explain the stability of the proton as will be discussed in section 2.3.1. It adds SUSY breaking by introducing explicit soft SUSY breaking operators into the Lagrangian resulting in 105 new free parameters. Using the supermultiplet definitions of tables 2.1 and 2.2, the superpotential of the MSSM is given by equation 2.14 [24]:

$$
W_{MSSM} = \tilde{\bar{u}} y_u \tilde{Q} H_u - \tilde{\bar{d}} y_d \tilde{Q} H_d - \tilde{\bar{e}} y_e \tilde{L} H_d + \mu H_u H_d \tag{2.14}
$$

where the y_i are the Yukawa coupling matrices in the 3x3 family space and the term proportional to μ represents the supersymmetric version of the SM Higgs boson mass. Other terms like $\tilde{\bar{u}} y_u \tilde{Q} H_d^*$ and $\tilde{\bar{d}} y_d \tilde{Q} H_u^*$ are not allowed, therefore two distinct Higgs doublets are needed to generate masses of up- and down-type fermions.

2.3.1. R-Parity conservation and its consequences

The most general gauge-invariant and renormalizable superpotential with chiral superfields of the MSSM would include not only the terms in equation 2.14, but also, the two additional terms appearing in the second and third lines of equation 2.15 [24], that introduce lepton number and baryon number violating interactions respectively.

$$\begin{aligned} W = & W_{MSSM} \\ & + \frac{1}{2}\lambda^{ijk} L_i L_j E_k + \lambda'^{ijk} L_i Q_j D_k + \mu'^{i} L_i H_u \\ & + \frac{1}{2}\lambda''^{ijk} U_i D_j D_k \end{aligned} \tag{2.15}$$

Having both lepton and baryon number violated allow the rapid proton decay, however since the measured lower limit on the proton lifetime is of order 10^{33} years [12], the corresponding couplings (λ, λ' and λ'') are either very weak or absent. In order to avoid the need for fine-tuning of those couplings, P.Fayet and G.R. Farrar proposed a discrete symmetry, called R-Parity, that protects the proton from decaying rapidly. The multiplicatively conserved quantum number P_R with respect to R-Parity is expressed as in equation 2.16 in terms of the particle spin quantum number S, lepton number L and baryon number B [24].

$$P_R = (-1)^{3\cdot(B-L)+2s} \tag{2.16}$$

As a consequence of this definition, the particles within the same supermultiplet have different R-Parity charges: sparticles have $P_R =$ -1, all particles of the SM and the scalar Higgs bosons have $P_R = +1$. Therefore, the conservation of R-Parity gives rise to particular features of a SUSY model:

- Sparticles do not mix with particles.
- Sparticles are always produced in pairs.
- The lightest sparticle, the LSP, is stable.
- Other instable sparticles decay into final states containing an odd number of LSPs. In several SUSY models, the LSP is taken as electrically neutral so it interacts only weakly with the SM particles and therefore the conservation of R-Parity results in a dark matter candidate in such models.

2.3.2. Soft Supersymmetry breaking in the MSSM

The most general soft SUSY breaking Lagrangian of the MSSM that conserves R-Parity and local gauge invariance is given by equation 2.17 [24]:

$$\begin{aligned} \mathcal{L}^{soft}_{MSSM} = & -\frac{1}{2}(M_3\tilde{g}\tilde{g} + M_2\tilde{W}\tilde{W} + M_1\tilde{B}\tilde{B} + c.c.) \\ & - (\tilde{\bar{u}} a_u \tilde{Q} H_u - \tilde{\bar{d}} a_d \tilde{Q} H_d - \tilde{\bar{e}} a_e \tilde{L} H_d + c.c.) \\ & - \tilde{Q}^\dagger m_Q^2 \tilde{Q} - \tilde{L}^\dagger m_L^2 \tilde{L} - \tilde{\bar{u}} m_{\bar{u}}^2 \tilde{\bar{u}}^\dagger - \tilde{\bar{d}} m_{\bar{d}}^2 \tilde{\bar{d}}^\dagger - \tilde{\bar{e}} m_{\bar{e}}^2 \tilde{\bar{e}}^\dagger \\ & - m_{H_u}^2 H_u^* H_u - m_{H_d}^2 H_d^* H_d - (b H_u H_d + c.c.) \end{aligned} \tag{2.17}$$

where the first three terms provide masses to the gluinos, winos and binos. The matrices $a_{u,d,e}$ are 3x3 matrices in family space that introduce trilinear couplings between the scalar fields. The matrices $m_{Q,L,\bar{u},\bar{d}}$ are 3x3 matrices in family space that explicitly provide masses to squarks and sleptons which might explain why the sparticles are heavier than their SM partners. A mixing between right- and left-handed sfermions might be realised if these mass matrices are non-diagonal. The last line of this equation contains the soft SUSY breaking scalar Higgs mass terms and the bilnear coupling between scalars, b. Adding $\mathcal{L}^{soft}_{MSSM}$ to the SUSY Lagrangian shown in equation 2.18 breaks explicitly SUSY, whilst $\mathcal{L}_{SUSY}$ preserves global SUSY.

$$\begin{aligned} \mathcal{L}_{SUSY} &= \mathcal{L}_{scalar} + \mathcal{L}_{fermion} + \mathcal{L}_{int} + \mathcal{L}_{gauge} \\ \mathcal{L}_{MSSM} &= \mathcal{L}_{SUSY} + \mathcal{L}^{soft}_{MSSM} \end{aligned} \tag{2.18}$$

2.3.3. The mass spectrum of the MSSM

2.3.3.1. The Higgs boson and the electroweak symmetry breaking

In the MSSM, two doublets of complex scalar fields of opposite hypercharge are needed to break electroweak symmetry: $H_u = (H_u^+, H_u^0)$, $Y_{H_u} = +1$ and $H_d = (H_d^0, H_d^-)$, $Y_{H_d} = -1$. The scalar potential of these two Higgs doublets, V_H, is shown in equation 2.19, it contains three terms V_D, V_F and V_{soft} from three different sources [24]:

- V_D is resulting from the D terms having the quartic Higgs interactions in equation 2.13.
- V_F is resulting from the Superpotential F-term in equation 2.14.
- V_{soft} is originating from the soft SUSY breaking scalar Higgs mass terms and the bilinear term in equation 2.17.

$$\begin{aligned} V_H &= V_D + V_F + V_{soft} \\ V_D &= \frac{g^2}{8}[|H_u|^2 - |H_d|^2] + \frac{g'^2}{8}[4|H_d^\dagger H_u|^2 - 2|H_d|^2|H_u|^2 + (|H_u|^2|H_d|^2)^2] \\ V_F &= \mu^2(|H_u|^2 + |H_d|^2) \\ V_{soft} &= M^2_{H_d} H_d^\dagger H_d + M^2_{H_u} H_u^\dagger H_u + b\mu(H_u + H_d + h.c.) \end{aligned} \tag{2.19}$$

The minimum of the potential, V_H^{min}, should break the SU(2)$_L$xU(1)$_Y$ group while preserving the electromagnetic symmetry U(1)$_Q$. Thus, the vacuum expectation values of the fields H_d^- and H_u^+ are chosen to be zero ($\langle H_d^- \rangle = 0$, $\langle H_u^+ \rangle = 0$) to avoid a breaking in the charged directions and to preserve the QED symmetry.

Similarly to the mass generation in the SM, the mass squared term of the scalar Higgs doublets field may be negative. This requires the two conditions of equation 2.20 which imply a close connection between electroweak symmetry breaking (EWSB) and SUSY-breaking.

$$\begin{aligned} \mu^2 &= \frac{1}{2}\left[\tan 2\beta \left(m^2_{H_u} \tan\beta - m^2_{H_d} \cot\beta\right) - M_Z^2\right] \\ b\mu &= \frac{1}{2}\sin 2\beta \left[m^2_{H_u} + m^2_{H_d} + 2\mu^2\right] \end{aligned} \tag{2.20}$$

Due to the EWSB, the two Higgs boson fields obtain the vacuum expectation values $v_u = \langle H_u^0 \rangle$ and $v_d = \langle H_d^0 \rangle$ which are related to the SM Higgs vev (v) by:

$$v^2 = v_u^2 + v_d^2 = \frac{2M_Z^2}{g^2 + g'^2} = (246 \text{ GeV})^2 \tag{2.21}$$

The ratio of v_u, v_d defines the angle β: $\tan\beta = \frac{v_u}{v_d}$, $0 < \beta < \frac{\pi}{2}$.

Using $\tan\beta$ and an additional mixing angle α the gauge-eigenstate fields of the Higgs boson doublets can be related to the mass eigenstates.

The two Higgs doublets of complex scalar fields represent N_{dof}=8, 3 are Goldstone bosons that are interpreted as the longitudinal polarisation degrees of freedom of the massive Z and W$^{\pm}$ bosons. Therefore, the MSSM spectrum has 5 physical Higgs bosons denoted as h, H, A and H$^{\pm}$: h and H are CP-even and electrically neutral scalars that result from the mixing of the fields H_u^0 and H_d^0 with mixing angle α, by convention their masses are chosen such that $m_h < m_H$, A is electrically neutral and CP-odd, $H^{\pm}$ are electrically charged with $H^- = H^{+*}$. To find these physical states, one needs to develop the Higgs fields components around V_{Higgs}^{min} into their real and imaginary parts: $H_u = \frac{1}{\sqrt{2}}(H_u^+, H_u^0 = v_u + H_u^0 + iP_u^0)$ and $H_d = \frac{1}{\sqrt{2}}(H_d^0 = v_d + H_d^0 + iP_d^0, H_d^-)$. Where the real parts correspond to the CP-even Higgs boson, while the CP-odd include the Goldstone bosons. Around V_{Higgs}^{min}, we obtain: $\langle H_u^0 \rangle = \frac{v_u}{\sqrt{2}}, \langle H_d^0 \rangle = \frac{v_d}{\sqrt{2}}$ and $\langle H_{u/d}^{\pm} \rangle = 0$. In these conditions, the Higgs mass matrices are defined by the V_{Higgs} second derivatives:

$$M^2 = \frac{1}{2}\left(\frac{\partial^2 V_{\text{Higgs}}}{\partial H_u^0 \partial H_d^0}\right)_{\text{Min. Cond}} \tag{2.22}$$

Equation 2.23 shows these matrices in the bases (Re(H_u)/$\sqrt{2}$, Re(H_d)/$\sqrt{2}$) and (Im(H_u)/$\sqrt{2}$, Im(H_d)/$\sqrt{2}$).

$$\begin{aligned} M_{Re}^2 &= \begin{pmatrix} -b\mu\tan\beta + m_Z^2\cos^2\beta & b\mu - m_Z^2\sin\beta\cos\beta \\ b\mu - m_Z^2\sin\beta\cos\beta & -b\mu\cot\beta + m_Z^2\sin^2\beta \end{pmatrix} \\ M_{Im}^2 &= \begin{pmatrix} -b\mu\tan\beta & b\mu \\ b\mu & -b\mu\cot\beta \end{pmatrix} \end{aligned} \tag{2.23}$$

The M_{Im}^2 matrix has a determinant $Det(M_{Im}^2) = 0$ with one null eigenvalue corresponding to the Goldstone boson and the other eigenvalue given by:

$$m_A^2 = 2b/\sin(2\beta) = 2\mu^2 + m_{H_u}^2 + m_{H_d}^2 \tag{2.24}$$

This inserted in M_{Re}^2 matrix, leads to its eigenvalues:

$$m_{H,h}^2 = \frac{1}{2}\left[m_A^2 + m_Z^2 \pm \sqrt{(m_A^2 + m_Z^2)^2 - 4m_Z^2 m_A^2\cos^2(2\beta)}\right] \tag{2.25}$$

The same development done with the charged components leads to the charged Higgses mass expressions:

$$m_{H^{\pm}}^2 = m_A^2 + m_W^2 \tag{2.26}$$

Equations 2.24 and 2.26 show that the masses m_A, m_H and $m_{H^{\pm}}$ increase with increasing the soft SUSY breaking parameter b, thus they are not constrained. However, using equation 2.25, one finds that the h mass is bounded from above and at tree level $m_h < m_Z$. Additional quantum

corrections add further important, sizeable contributions to the h mass and therefore increase this upper bound: especially contributions from stop and top loops.Assuming that all masses contributing to those loop corrections are less than 1 TeV, the upper limit on m_h is increased to $m_h \leq 135$GeV.

2.3.3.2. Neutralinos and charginos sector

Due to the EWSB the higgsinos and electroweak gauginos mix with each other, the mixing of the neutral gauginos ($\tilde{B}$, $\tilde{W}^0$) and neutral higgsinos ($\tilde{H}_u^0$ and $\tilde{H}_d^0$) is described, at tree-level, by M_N, a 4x4 complex symmetric mass matrix which can be written in the gauge-eigenstate basis ($\tilde{B}$, $\tilde{W}^0$, $\tilde{H}_d^0$, $\tilde{H}_u^0$) as in equation 2.27 [24]:

$$M_N \equiv \begin{pmatrix} M_1 & 0 & -\frac{1}{2}g'v_d & \frac{1}{2}g'v_u \\ 0 & M_2 & \frac{1}{2}gv_d & -\frac{1}{2}gv_u \\ -\frac{1}{2}g'v_d & \frac{1}{2}gv_d & 0 & -\mu \\ \frac{1}{2}g'v_u & -\frac{1}{2}gv_u & -\mu & 0 \end{pmatrix} \tag{2.27}$$

where M_1 and M_2 are the same terms used in equation 2.17, corresponding to the $U(1)_Y$ and SU(2)$_L$ soft SUSY breaking gaugino mass terms respectively, terms with $-\mu$ are the SUSY higgsino mass terms and the terms containing g, g' are the result of Higgs-higgsino-gaugino couplings. M_N can also be written as in equation 2.28, where θ_W is the weak mixing angle introduced previously in section 1.3.2.

$$M_N \equiv \begin{pmatrix} M_1 & 0 & -\cos\beta\ \sin\theta_W\ m_W & \sin\beta\ \sin\theta_W\ m_Z \\ 0 & M_2 & \cos\beta\ \cos\theta_W\ m_Z & -\sin\beta\ \cos\theta_W\ m_Z \\ -\cos\beta\ \sin\theta_W\ m_W & \cos\beta\ \cos\theta_W\ m_Z & 0 & -\mu \\ \sin\beta\ \sin\theta_W\ m_Z & -\sin\beta\ \cos\theta_W\ m_Z & -\mu & 0 \end{pmatrix} \tag{2.28}$$

To determine the physical neutralino states and their masses, we must perform a diagonalization of M_N as equation 2.29 shows:

$$N^* M_N N^{-1} = diag(M_{\tilde{\chi}_1^0}, M_{\tilde{\chi}_2^0}, M_{\tilde{\chi}_3^0}, M_{\tilde{\chi}_4^0}) \tag{2.29}$$

where N is a unitary matrix and the term in the right-hand side is the diagonal matrix of (real and positive) neutralino masses. The physical neutralino states are denoted by $\tilde{\chi}^0_{i=1,2,3,4}$, by convention, they are labeled in ascending order of mass from 1 to 4. The lightest neutralino, $\tilde{\chi}_1^0$, is usually assumed to be the LSP, unless there is a lighter gravitino or unless R-parity is not conserved, because it is the best MSSM particle that can make a good dark matter candidate. The $\tilde{\chi}_i^0$ are the linear combinations of the neutral gaugino and higgsino states determined by the matrix elements of N, their masses correspond to the singular values of M_N, i.e., the positive square roots of the eigenvalues of $M_N^\dagger M_N$. Exact formulae for these masses can be found in Ref [33].

On the other hand, the mixing of the charged gauginos ($\tilde{W}^\pm$) and charged Higgsinos ($\tilde{H}_u^+$, $\tilde{H}_d^-$) is described, at tree-level, by the 2x2 complex mass matrix, M_C, presented in equation 2.30 [24].

$$M_C \equiv \begin{pmatrix} M_2 & \frac{1}{\sqrt{2}}gv_u \\ \frac{1}{\sqrt{2}}gv_d & \mu \end{pmatrix} \equiv \begin{pmatrix} M_2 & \sqrt{2}\ \sin\beta\ m_W \\ \sqrt{2}\ \cos\beta\ m_W & \mu \end{pmatrix} \tag{2.30}$$

The mass eigenstates are related to the gauge eigenstates by two unitary 2x2 matrices U and V according to equation 2.31:

$$\begin{aligned} \begin{pmatrix} \tilde{\chi}_1^+ \\ \tilde{\chi}_2^+ \end{pmatrix} &= V \begin{pmatrix} \tilde{W}^+ \\ \tilde{H}_u^+ \end{pmatrix} \\ \begin{pmatrix} \tilde{\chi}_1^- \\ \tilde{\chi}_2^- \end{pmatrix} &= U \begin{pmatrix} \tilde{W}^- \\ \tilde{H}_d^- \end{pmatrix} \\ U^* M_C V^{-1} &= diag(M_{\tilde{\chi}_1^+}, M_{\tilde{\chi}_2^+}) \end{aligned} \tag{2.31}$$

where the term in the right-hand side is the diagonal matrix of (real positive) chargino masses. The physical chargino states are denoted by $\tilde{\chi}_1^\pm$ and $\tilde{\chi}_2^\pm$, they are linear combinations of the charged gaugino and higgsino states determined by the matrix elements of U and V. Their masses correspond to the singular values of M_C, i.e., the positive square roots of the eigenvalues of $M_C^\dagger M_C$:

$$\begin{aligned} M^2_{\tilde{\chi}_1^+, \tilde{\chi}_2^+} = &-\frac{1}{2}|\mu|^2 + |M_2|^2 + 2m_W^2 \pm [(|\mu|^2 + |M_2|^2 + 2m_W^2)^2 \\ &- 4|\mu|^2|M_2|^2 - 4m_W^4 \sin^2 2\beta + 8m_W^2 \sin 2\beta Re(\mu M_2)]^{1/2} \end{aligned} \tag{2.32}$$

Depending on the μ, M_1 and M_2 values, the chargino or neutralino state approximates a particular combination of gaugino or higgsino [24]:

- If M_1 and m_Z are small compared to M_2 and $|\mu|$, this results in $\tilde{\chi}_1^0$ nearly pure bino, $\tilde{B}$.
- If M_2 and m_Z are small compared to M_1 and $|\mu|$, then the lightest chargino pair and neutralino would constitute a triplet of roughly mass-degenerate pure winos, $\tilde{W}^\pm$, and $\tilde{W}_3^0$.
- If $|\mu|$ and m_Z are small compared to M_1 and M_2, then the $\tilde{\chi}_1^0$ would be nearly a pure higgsino.

Each of the above cases leads to a different phenomenology.

2.4. SUSY simplified model searches and their interpretation

As seen previously, the general MSSM has over a hundred free parameters that describe the pattern of sparticle masses and their couplings, this parameter space is too large to be scanned and compared to particle collider data, i.e. ATLAS and CMS data. Thus, several approaches are used in order to reduce the number of free parameters such as to assume specific breaking models at the GUT scale. The standard approach is to use the SUSY simplified models which attempt to capture the behaviour of a small number of kinematically accessible sparticles, assuming all others play no role. Such models focus on one or few specific SUSY production processes and decay chain with fixed branching ratio. Examples of simplified models used in ATLAS are models of gluino pair production with different assumptions about the gluino decay, models of squark-antisquark production with different assumptions on the type of squark or the pattern of squark decay, models of chargino and neutralino production and decay, etc. These models provide insight into the experimental constraints on the individual sparticle and decay mode but don't allow to study the complex effects that can result from large numbers of competing production and decay processes.

However, the results of these SUSY simplified models searches can be used to test a wide range of alternative models such as the phenomenological MSSM (pMSSM) [31] which is a 19-parameter

version of the MSSM with choices of weak scale parameters agnostic of what happens at GUT scale. This model is assumed to conserve R-parity, the parameters are assumed to be real so that new CP violation does not occur in the sparticle sector, also the parameters that would give rise to additional flavour-changing neutral currents are absent. The LSP provides a dark matter candidate being colourless and electrically neutral. The 19 free parameters of the pMSSM are shown in table 2.3. An overview of the pMSSM coverage using the ATLAS simplified SUSY searches at LHC run 1 is described hereafter while the full details of this pMSSM interpretation can be found in Ref. [34]. ATLAS generated around 500 million pMSSM model point SLHA with the 19 parameters randomly chosen according to table 2.3, a variety of ATLAS software packages are used to calculate the mass spectrum and couplings of each model point. The sparticle decays (BR) are calculated, again using a variety of codes and analytical techniques, the model points are furthermore required to have consistent electroweak symmetry breaking, a scalar potential that does not break colour or electric charge, and all particles mass-squared values must be positive. Further experimental constraints (shown in table 2.4) are applied.Then it is determined for the selected SLHA which, if any, of the ATLAS simplified searches are sensitive to it and whether it can be excluded or not by computing the production cross-sections for each SUSY simplified model.

Fixing the Higgs boson mass to its experimental mass of 125 GeV found in 2012 instead of computing it for each signal point, reject those with values non consitent with the 125 GeV, can constraint the triliniear top coupling A_t and can facilitate the pMSSM scans by avoiding generating large number of incompatible models. I worked on implementing such an A_t inversion in the SUSY spectrum calculator SuSpect3, this project will be detailed in the next chapter.

Table 2.3.: The ATLAS Run 1 scan ranges used for each of the 19 pMSSM parameters where "gen(s)" refers to generation(s) [34].

Parameter	Min value	Max value	Note
$m_{\tilde{L}_1}(= m_{\tilde{L}_2})$	90 GeV	4 TeV	Left-handed slepton (first two gens.) mass
$m_{\tilde{e}_1}(= m_{\tilde{e}_2})$	90 GeV	4 TeV	Right-handed slepton (first two gens.) mass
$m_{\tilde{L}_3}$	90 GeV	4 TeV	Left-handed stau doublet mass
$m_{\tilde{e}_3}$	90 GeV	4 TeV	Right-handed stau mass
$m_{\tilde{Q}_1}(= m_{\tilde{Q}_2})$	200 GeV	4 TeV	Left-handed squark (first two gens.) mass
$m_{\tilde{u}_1}(= m_{\tilde{u}_2})$	200 GeV	4 TeV	Right-handed up-type squark (first two gens.) mass
$m_{\tilde{d}_1}(= m_{\tilde{d}_2})$	200 GeV	4 TeV	Right-handed down-type squark (first two gens.) mass
$m_{\tilde{Q}_3}$	100 GeV	4 TeV	Left-handed squark (third gen.) mass
$m_{\tilde{u}_3}$	100 GeV	4 TeV	Right-handed top squark mass
$m_{\tilde{d}_3}$	100 GeV	4 TeV	Right-handed bottom squark mass
$\lvert M_1 \rvert$	0 GeV	4 TeV	Bino masss parameter
$\lvert M_2 \rvert$	70 GeV	4 TeV	Wino masss parameter
$\lvert \mu \rvert$	80 GeV	4 TeV	Bilinear Higgs mass parameter
M_3	200 GeV	4 TeV	Gluino masss parameter
A_t	0 GeV	8 TeV	Trilinear top coupling
A_b	0 GeV	4 TeV	Trilinear bottom coupling
A_τ	0 GeV	4 TeV	Trilinear τ lepton coupling
M_A	100 GeV	4 TeV	Pseudoscalar Higgs boson mass
$\tan\beta$	1	60	Ratio of the Higgs vaccum expectation values

Table 2.4.: Constraints on acceptable pMSSM points from considerations of precision electroweak and flavour results, dark matter relic density, and other collider measurements [34].

Parameter	Minimum value	Maximum value
$\Delta\rho$	-0.0005	0.0017
$\Delta(g-2)_\mu$	$-17.7 \cdot 10^{-10}$	$43.8 \cdot 10^{-10}$
BR(b→sγ)	$2.69 \cdot 10^{-4}$	$3.87 \cdot 10^{-4}$
BR($B_s \to \mu^+\mu^-$)	$1.6 \cdot 10^{-9}$	$4.2 \cdot 10^{-9}$
BR($B^+ \to \tau^+\nu_\tau$)	$66 \cdot 10^{-6}$	$161 \cdot 10^{-6}$
$\omega_{\tilde{\chi}_1^0} h^2$	—	0.1208
$\Gamma_{invisible(SUSY)}(Z)$	—	2 MeV
Masses of charged sparticles	100 GeV	—
$m(\tilde{\chi}_1^\pm)$	103 GeV	—
$m(\tilde{u}_{1,2}, \tilde{d}_{1,2}, \tilde{c}_{1,2}, \tilde{s}_{1,2})$	200 GeV	—
m(h)	124 GeV	128 GeV

3. The SuSpect3 tool for the calculation of the supersymmetric particle spectrum

To study the properties of the SUSY models, programs which numerically calculate the physical (pole) masses and couplings of the SUSY particles, given a set of theory input parameters, are needed. The output of these so-called spectrum generators can be transferred to programs which calculate further observables such as the branching ratios or the dark matter relic density.

In order to produce a spectrum, the SUSY model must be defined by specifying the gauge group, the field content, mixings, the superpotential and the soft-breaking terms. From this information, the mass matrices, radiative corrections and EWSB conditions can be derived.

In addition, as discussed previously in section 2.2, there are well motivated SUSY models which require boundary conditions for the model parameters at a low and a high scale. For example, in the constrained MSSM (CMSSM) mSUGRA, boundary conditions for the soft-breaking parameters are imposed at the gauge coupling unification scale. Furthermore, at the Z mass scale the CMSSM is matched to the SM, which implies conditions for the gauge and Yukawa couplings. Such models lead to the simplest situation where the entire spectrum of superparticles and Higgs bosons is determined by the values of only 5 free parameters. In this case, the low-energy parameters are derived from the high-energy input parameters through Renormalization Group Equations (RGE) which will be discussed in section 3.2.1.

There are several public spectrum generators such as SuSpect3 [35] [36], SOFTSUSY [37] and SPHENO [38] [39]. In sections 3.1, 3.2 and 3.3 of this chapter, we describe the present version of the SuSpect3 program which calculates the Susy Spectrum in the constrained and unconstrained MSSMs. Then in sections 3.4 and 3.5 we discuss the new version of SuSpect3, we have been working on, which will include a few options trading-off some free soft-SUSY breaking parameters (i.e. the trilinear top coupling A_t), using the measured Higgs boson mass and the SUSY particles masses limits resulting from the SUSY searches at the LHC.

3.1. Overview of the SuSpect3 algorithm

SuSpect3 deals with the general pMSSM with boundary conditions defined either at low (E_{low}) or high (E_{high}) energy scale. It treats as well the CMSSM with boundary conditions imposed at E_{high} such as mSUGRA [32], mGMSB [40] and mAMSB [41]. It requires as input the standard SUSY Les Houches Accord file, SLHA [42] [43], containing the experimental values of the SM variables listed in table 3.1 and it writes output file in the same format to facilitate interfacing with other codes such as SUSYHIT [44] used to compute the branching ratios of the SUSY particles. As will be discussed in section 3.2.1, the experimental values of the SM variables serve for computing boundary values for the 7 free parameters of the SM the gauge (g_1, g_2, g_3) and Yukawa couplings (y_t, y_b, y_τ) and the Higgs vev v. The program has several flags which allow to select the model to be studied, on top of the SM experimental variables, there are additional input variables needed depending on the selected model:

- For the pMSSM with boundary conditions: the 22 input variables shown in table 3.2 defined either at E_{low} or E_{high} are needed. The energy scale E_{Low} or E_{high} has also to be provided as well as input.

– For the CMSSM: the boundary conditions at E_{high} corresponding to the model parameters must be given as input. In case of the mSUGRA model, E_{high} corresponds to the M_{GUT}, the scale at which the electroweak gauge coupling constants unify, it can also be given as input while SuSpect3 takes $M_{GUT} = 2 \cdot 10^{16}$ GeV by default. For this model, the boundary conditions at M_{GUT} described in the last column of table 3.3, the ratio of the vevs of the two Higgs fields, $\tan\beta$, and the sign of μ which is the Higgs-Higgsino mass parameter are needed.

Given the above input parameters, $|\mu|$ and the soft SUSY-breaking bilinear Higgs term b can be determined through the EWSB conditions as will be discussed in section 3.2.3.

Since the trilinear sfermion couplings will be always multiplied by the fermion masses they are important only in the case of the third generation, this explains why in the pMSSM scan discussed in section 2.4 only the trilinear couplings of the third generation were used. Also, the pMSSM scanning strategy used the pseudoscalar Higgs boson mass M_A and $|\mu|$ instead of the $m^2_{H_u}$ and $m^2_{H_d}$, this is because one can trade the values of $m^2_{H_u}$ and $m^2_{H_d}$ given M_A and μ. Such an alternative is possible in SuSpect3 using appropriate setting of the input parameters.

The SuSpect3 diagram showing its main steps is presented in figure 3.1. It includes the implementation of the RGE, EWSB condition and the calculation of the pole masses. In the following sections we will discuss each of these steps for the example of the mSUGRA model having the boundary conditions at M_Z, M_{EWSB} and M_{GUT} as described in table 3.3.

Table 3.1.: The SM experimental input variables given at M_Z scale.

Parameters	Note
G_F	The Fermi constant
$\alpha_s(M_Z)$	The SM strong coupling at M_Z scale
$\alpha_{em}(M_Z)$	The SM electromagnetic coupling at M_Z scale
M_{top}, M_τ	The top quark and tau lepton pole masses
$m_b(m_b)^{\overline{MS}}$	The bottom quark running mass in the $\overline{MS}$ scheme
m_Z	The Z boson pole mass

Table 3.2.: The 22 input parameters of the pMSSM.

Parameters	Note
$m_{\tilde{q}}$, $m_{\tilde{u}_R}$, $m_{\tilde{d}_R}$, $m_{\tilde{l}}$, $m_{\tilde{e}_R}$	The first/second generation sfermion mass parameters
$m_{\tilde{Q}}$, $m_{\tilde{t}_R}$, $m_{\tilde{b}_R}$, $m_{\tilde{L}}$, $m_{\tilde{\tau}_R}$	The third generation sfermion mass parameters
M_1, M_2, M_3	The Bino, Wino and Gluino mass parameters
$m^2_{H_u}$, $m^2_{H_d}$	The Higgs mass parameters squared
A_u, A_d, A_e	The first/second generation trilinear couplings
A_t, A_b, A_τ	The third generation trilinear couplings
tanβ	The ratio of the vacuum expectation values of the two Higgs doublet fields

Table 3.3.: The mSUGRA boundary conditions at M_Z, M_{EWSB} and M_{GUT} scales.

Parameters	M_Z	M_{EWSB}	M_{GUT}
Gauge couplings	g_1, g_2, g_3	—	—
Vevs	$\tan\beta$, v	—	—
Yukawa couplings	y_t, y_b, y_τ	—	—
Common gauginos mass parameter	—	—	$m_{\frac{1}{2}}$
Common Sfermions mass parameter and Higgs bosons	—	—	m_0
Universal trilinear coupling	—	—	A_0
μ, b	—	EWSB conditions	—

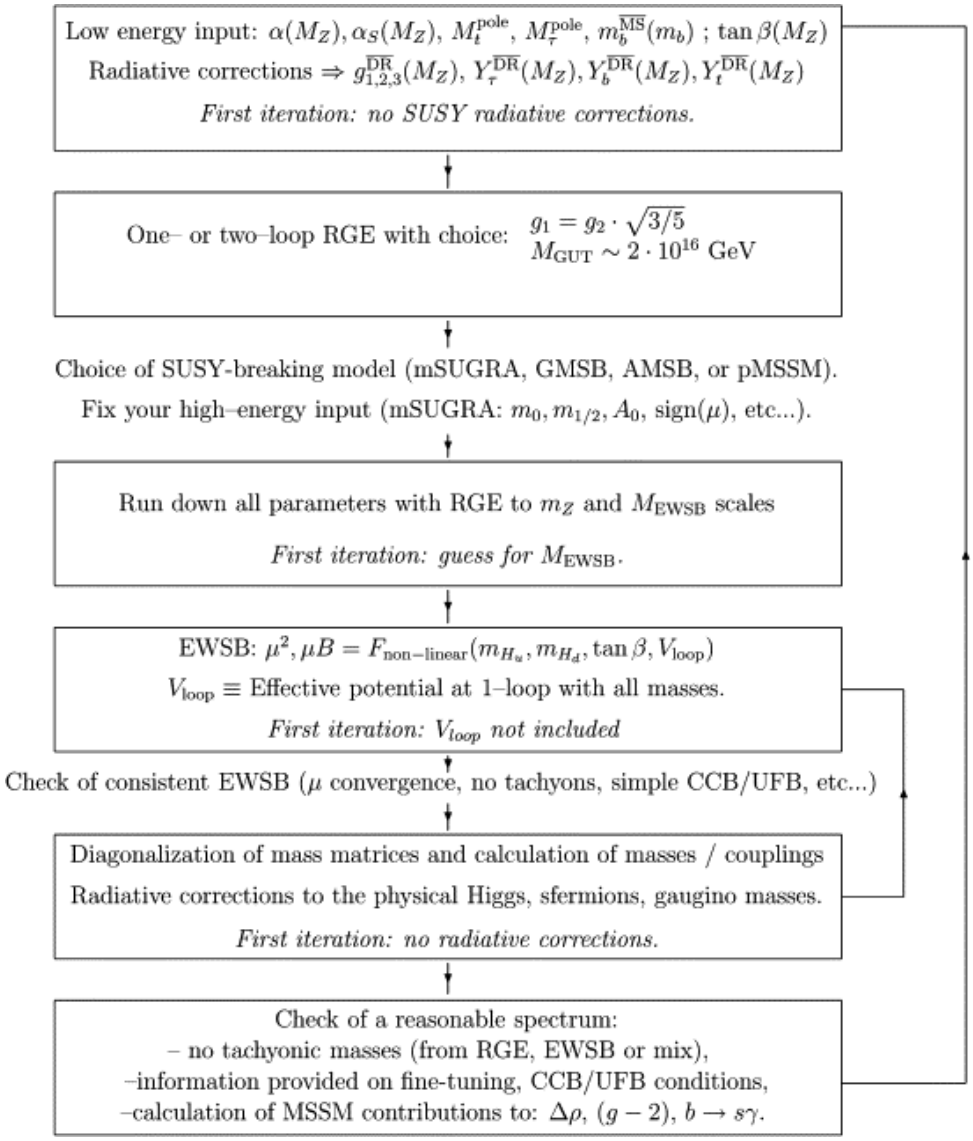

Figure 3.1.: The SuSpect3 iterative algorithm for the calculation of the SUSY particle spectrum starting from the choice of input and ending with the check of the spectrum [35].

3.2. SuSpect3 calculation of the MSSM parameters

3.2.1. Treatment of the SM inputs

As discussed in section 1.1, the renormalisability of a theory is a necessary condition for a meaningful description of the measurable quantities. Within a renormalizable theory, a renormalization scheme is used to absorb the infinities that arise in perturbative calculations beyond leading order. The renormalization scheme depends on the type of particles that are being considered, thus several schemes exist such as the minimal subtraction, $\overline{MS}$, scheme [45] and the dimensional reduction, $\overline{DR}$, scheme [46]. The values of the SM input parameters shown in table 3.1 are measured at Q= M_Z and usually the α_s, α_{em} and m_b parameters are given in a theory with five quark flavors, renormalized in the $\overline{MS}$ scheme. However, for SUSY, the dimensional reduction $\overline{DR}$ scheme is more appropriate [47]. Therefore, SuSpect3 translates these parameters at M_Z into $\overline{DR}$ values by subtracting the appropriate parts of the radiative corrections from the experimental data, taking into account the complete MSSM spectrum. Then using the formulas of Ref. [48], SuSpect3 computes, at Q= M_Z, the MSSM $\overline{DR}$ g_1 , g_2 , g_3 and v using the 4 experimental SM input parameters: G_F , M_Z , $\alpha_{em}(M_Z)$, $\alpha_s(M_Z)$. The equation 3.1 shows the SuSpect3 default values of these SM variables.

$$\begin{aligned} G_F &= 1.16639 \cdot 10^{-5}\ \text{GeV}^{-2} \\ M_Z &= 91.1876\ \text{GeV} \\ \alpha_{em}^{-1}(M_Z)^{\overline{MS}} &= 127.934 \\ \alpha_s(M_Z)^{\overline{MS}} &= 0.1172 \end{aligned} \tag{3.1}$$

SuSpect3 also calculates the third generation Yukawa couplings y_τ, y_t and y_b which can be determined in the $\overline{DR}$ scheme from the corresponding running fermion masses as shows equation 3.2:

$$\begin{aligned} y_t &= \frac{\sqrt{2}m_t}{v\sin\beta} \\ y_b &= \frac{\sqrt{2}m_b}{v\cos\beta} \\ y_\tau &= \frac{\sqrt{2}m_\tau}{v\cos\beta}, \end{aligned} \tag{3.2}$$

where the $\overline{DR}$ running fermion masses m_τ, m_t and m_b can be derived at the one–loop level from the corresponding pole masses, by subtracting the finite parts of the one–loop fermion self–energy. The top quark and τ pole masses are given as input, their present default values are shown in equation 3.3. Concerning the bottom quark, SuSpect3 follows Ref. [42] which prescribes to take as input the SM running mass in the $\overline{MS}$ scheme, $m_b(m_b)^{\overline{MS}}$, its default value is shown in the same equation.

$$\begin{aligned} M_t &= 173.5\ \text{GeV} \\ m_b(m_b)^{\overline{MS}} &= 4.21\ \text{GeV} \\ M_\tau &= 1.777\ \text{GeV} \end{aligned} \tag{3.3}$$

The renormalization procedure does not only solve the issue with the divergences, it also demonstrates that the coupling parameters of the theory are not constant. Instead they depend mainly logarithmically on the energy scale and therefore they are denoted as running coupling constants. This dependence of the coupling parameters on the energy scale (Q) is given by the RGEs [49] [50]. Thus, SuSpect3 extends the resulting values of the gauge and third generation Yukawa couplings at M_Z to the SUSY scale by using the (one- or two-loop) MSSM RGEs in the $\overline{DR}$ scheme. The one-loop RGE for the third generation Yukawa and gauge coupling parameters are non-linear coupled equations as shows equation 3.4.

$$\begin{aligned}
\frac{dg_1^2}{dt} &= \frac{1}{16\pi^2}\left(\frac{33}{5}\right)g_1^4, \quad t = ln(Q) \\
\frac{dg_2^2}{dt} &= \frac{1}{16\pi^2}g_2^4 \\
\frac{dg_3^2}{dt} &= \frac{1}{16\pi^2}(3)\,g_3^4 \\
\frac{dy_\tau}{dt} &= \frac{1}{16\pi^2}y_\tau\left(4y_\tau^2 + 3y_b^2 - \frac{9}{5}g_1^2 - 3g_2^2\right) \\
\frac{dy_b}{dt} &= \frac{1}{16\pi^2}y_b\left(6y_b^2 + y_\tau^2 + y_t^2 - \frac{7}{15}g_1^2 - 3g_2^2 - \frac{16}{3}g_3^2\right) \\
\frac{dy_t}{dt} &= \frac{1}{16\pi^2}y_t\left(6y_t^2 + y_b^2 - 13\frac{g_1^2}{15} - 3g_2^2 - \frac{16}{3}g_3^2\right)
\end{aligned} \tag{3.4}$$

SuSpect3 includes all the important SUSY radiative corrections to the gauge and Yukawa couplings. As the SUSY particle masses contribute to these corrections, an iterative procedure is required as shows figure 3.1 since the values of the SUSY particle spectrum depend on the precise values of the gauge and Yukawa couplings via the RGE. The iteration is to be performed until a sufficiently stable final SUSY spectrum is obtained.

3.2.2. SUSY breaking

In the case of mSUGRA (or the pMSSM with boundary conditions at E_{high}), using the boundary conditions of table 3.3 (or table 3.2), all the soft SUSY breaking parameters and couplings are evolved down to the M_{EWSB} and M_Z scales, using either the one– or full two–loop RGE options depending on the choice of the user.

The M_{EWSB} scale value can be entered as a free parameter input, while alternatively its default value is shown in equation 3.5. It represents the geometric mean of the two top squark running masses in the $\overline{DR}$ scheme as it minimizes the scale dependence of the one–loop effective Higgs potential Ref. [51]. At first iteration, as the stop masses have not yet been calculated SuSpect3 uses the geometric mean of the soft SUSY–breaking stop masses instead as a first guess.

$$M_{EWSB} = \sqrt{m_{\tilde{t}_1} m_{\tilde{t}_2}} \tag{3.5}$$

However, in the case of the pMSSM with boundary conditions at E_{low}, the code will perform RGE consistently between the scale M_Z and E_{low} as well as the RGE between E_{low} and the M_{EWSB}, while the RGE from a high scale E_{high} down to M_{EWSB} are not relevant in this case and are thus switched off.

3.2.3. Electroweak symmetry breaking

SuSpect3 requires that the electroweak symmetry is broken radiatively and use equation 2.20 to determine the parameters μ^2 (M_{EWSB}) and b(M_{EWSB}). It is well known that the one–loop radiative corrections to the Higgs potential play a major role in determining the values of these two parameters which at tree level are given in terms of the soft SUSY–breaking masses of the two Higgs doublet fields, m_{H_u} and m_{H_d}. SuSpect3 treats these corrections using the tadpole method [52]. In quantum field theory, a tadpole is a one-loop Feynman diagram with one external leg (as shows figure 3.3(b)) giving a contribution to the Higgs field's vacuum expectation value. The dominant tadpole contribution comes from the stops. At any given order in perturbation theory, minimizing the Higgs potential is equivalent to requiring that the tadpoles vanish. This requires to add the one–loop tadpole corrections t_u , t_d to the m_{H_u} and m_{H_d} as shows equation 3.6. The tadpole contributions used are taken from Ref. [48].

$$\begin{aligned} m_{H_u}^2 &\rightarrow m_{H_u}^2 - \frac{t_u}{v_u} \\ m_{H_d}^2 &\rightarrow m_{H_d}^2 - \frac{t_d}{v_d} \end{aligned} \tag{3.6}$$

Since $|\mu|$ and b affect the masses of some (s)particles contributing to these radiative corrections, this gives a non–linear equation for $|\mu|$ which is solved by a standard iteration algorithm (as shows figure 3.1) until stability is reached and a consistent value of μ is obtained. In the first iteration, the values of μ^2 is guessed by using the tree–level potential since no sparticle or Higgs mass has been calculated yet.

3.3. Suspect3 calculation of the physical particle masses

Once all the soft SUSY–breaking terms are obtained and eventually EWSB is radiatively realized SuSpect3 then calculates all the physical particle masses. The conventions for the mass matrices in the sfermion and Higgs sectors will be specified in sections 3.3.1 and 3.3.2 respectively. Figure 3.2 shows an example of spectra generated by SuSpect corresponding to the mSUGRA model with the boundary conditions at M_{GUT} scale: $m_0 =$ 100 GeV, $m_{1/2} =$ 250 GeV, $A_0 =$ -100 GeV, tan$\beta =$ 10 and sign (μ) = 10.

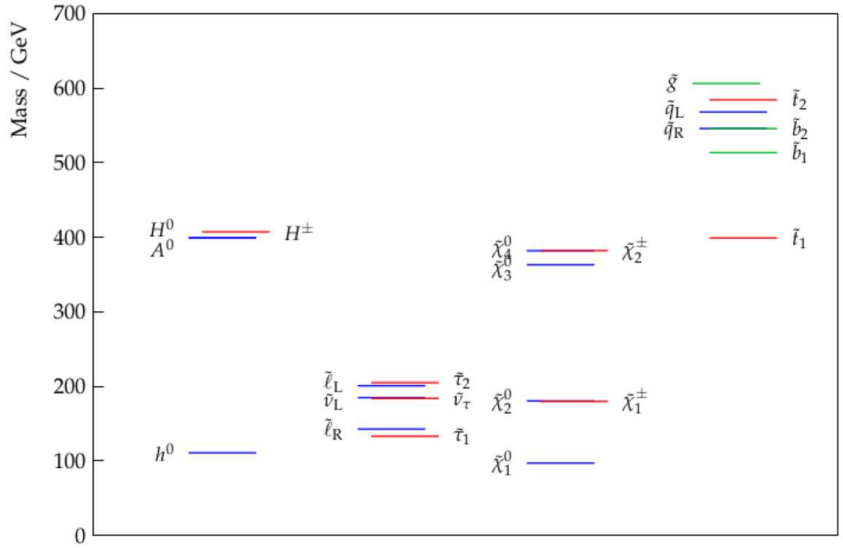

Figure 3.2.: An example of spectra generated by SuSpect3.

3.3.1. Sfermion sector

In the third generation sfermion sector, mixing between the "left" and "right" current eigenstates is included. The sfermion mass matrices are given by equation 3.7:

$$M_{\tilde{f}}^2 = \begin{pmatrix} m_{\tilde{f}_L}^2 + (I_f^3 - e_f s_W^2) M_Z^2 \cos 2\beta + m_f^2 & m_f(A_f - \mu r_f) \\ m_f(A_f - \mu r_f) & m_{\tilde{f}_R}^2 + (I_f^3 - e_f s_W^2) M_Z^2 \cos 2\beta + m_f^2 \end{pmatrix} \tag{3.7}$$

where $m_{\tilde{f}_{L,R}}$, A_f, μ and m_f are respectively, the $\overline{DR}$ soft SUSY scalar masses, trilinear couplings, higgsino mass parameter and running fermion masses at the scale M_{EWSB} and $r_b = r_\tau = 1/r_t = \tan\beta$. These matrices are diagonalized by orthogonal matrices, the mixing angles θ_f and the squark eigenstate masses are shown in equation 3.8. The masses are defined such that $m_{\tilde{f}_1}$ and $m_{\tilde{f}_2}$ correspond to the mass of respectively the lightest and the heaviest sfermion.

$$\begin{aligned} \tan 2\theta_f &= \frac{2m_f\,(A_f - \mu r_f)}{m_{\tilde{f}L}^2 - m_{\tilde{f}R}^2 + I_f^3 M_Z^2 \cos 2\beta} \\ \tan\theta_f &= \frac{m_{\tilde{f}1}^2 - m_{\tilde{f}2}^2 + m_{\tilde{f}R}^2 - m_{\tilde{f}L}^2 - I_f^3 M_Z^2 \cos 2\beta}{2m_f\,(A_f - \mu r_f)} \\ m_{\tilde{f}_{1,2}}^2 &= m_f^2 - \frac{1}{2}\left[m_{\tilde{f}_L}^2 + m_{\tilde{f}_R}^2 \pm \sqrt{(m_{\tilde{f}_L}^2 - m_{\tilde{f}_R}^2 + I_f^3 M_Z^2 \cos 2\beta)^2 + 4m_f^2(A_f - \mu r_f)^2}\right] \end{aligned} \tag{3.8}$$

The one-loop radiative corrections to the previous tree-level sfermion masses are included according to Ref [48].

3.3.2. Higgs sector

The running $\overline{DR}$ mass of the pseudoscalar Higgs boson at the scale M_{EWSB}, $\overline{M}_A$, is obtained from the soft SUSY–breaking Higgs mass terms evolved from RGE at the scale M_{EWSB} and including the loop tadpole corrections as shows equation 3.9.

$$\overline{m}_A^2(M_{EWSB}) = \frac{1}{\cos 2\beta}(m_{H_d}^2 - \frac{t_d}{v_d} - m_{H_u}^2 + \frac{t_u}{v_u}) - \overline{m}_Z^2 + \sin^2\beta\frac{t_d}{v_d} + \cos^2\beta\frac{t_u}{v_u} \tag{3.9}$$

This mass together with the running Z boson mass, $\overline{M}_Z$, at scale M_{EWSB}, are then used as inputs in the CP-even Higgs boson 2x2 mass matrix M^S discussed previously in section 2.3.3.1. Including all the loop contributions of the self–energies (some dominant contributions are shown in figure 3.3(a)) of the unrotated CP–even neutral Higgs fields H_u^0 and H_d^0 as well as the tadpole contributions, this matrix reads at a given scale q^2 as:

$$M^S(q^2) = \begin{pmatrix} \overline{m}_Z^2\cos^2\beta + \overline{m}_A^2\sin^2\beta - s_{11}(q^2) & -\frac{1}{2}(\overline{m}_Z^2 + \overline{m}_A^2)\sin 2\beta - s_{12}(q^2) \\ -\frac{1}{2}(\overline{m}_Z^2 + \overline{m}_A^2)\sin 2\beta - s_{12}(q^2) & \overline{m}_Z^2\sin^2\beta + \overline{m}_A^2\cos^2\beta - s_{22}(q^2) \end{pmatrix} \tag{3.10}$$

where the $s_{ij}(q^2)$ originates from the self-energies.

One can then obtain the running CP–even Higgs boson masses and the mixing angle α which rotates the fields H_u^0, H_d^0 into the physical CP–even Higgs boson fields h, H in terms of the matrix elements M_{ij}^S as shows equation 3.11. This equation also shows the running charged Higgs boson mass at the EWSB scale.

$$\begin{aligned} \overline{m}_{H,h}^2 &= \frac{1}{2}\left[M_{11}^s + M_{22}^s \pm \sqrt{(M_{11}^s - M_{22}^s)^2 + 4(M_{12}^s)^2}\right] \\ \overline{m}_{H^\pm}^2 &= \overline{m}_A^2 + \overline{m}_W^2 - \sin^2\beta\frac{t_d}{v_d} - \cos^2\beta\frac{t_u}{v_u} \\ \sin(2\alpha) &= \frac{2M_{12}^s}{\overline{m}_H^2 - \overline{m}_h^2} \qquad \left(-\frac{\pi}{2} < \alpha < \frac{\pi}{2}\right) \end{aligned} \tag{3.11}$$

The pole masses of all the Higgs bosons are then obtained by including the self–energy corrections evaluated at the masses of the Higgs bosons themselves. In the evolution of the radiative correction, SuSpect3 provides a full one-loop plus leading two-loop calculation controlled by the third generation Yukawa couplings and the strong gauge coupling, derived in Refs. [53] [54].

3.4. The post Higgs discovery SuSpect3

The observation at the LHC of the Higgs particle (discussed previously in section 1.4) fixed the mass of the MSSM lighter Higgs boson to $\approx$ 125 GeV, however as seen in section 3.3.2, the different spectrum generators in particular SuSpect3 still calculate m_h as output. In the new version of SuSpect3 we would like to take advantage of this very important new input to constrain other basic model parameter typically most important one of the free soft SUSY-breaking terms, the trilinear top coupling A_t, currently given as input. The same idea also applies to the SUSY particles masses limits resulting from the SUSY searches at the LHC:

– By fixing the two physical masses $m_{\tilde{\chi}_{1,2}^+}$ to their lower limits, two free parameters, the Higgsino mass parameter, μ, and the bino mass parameter M_2 can be calculated at tree

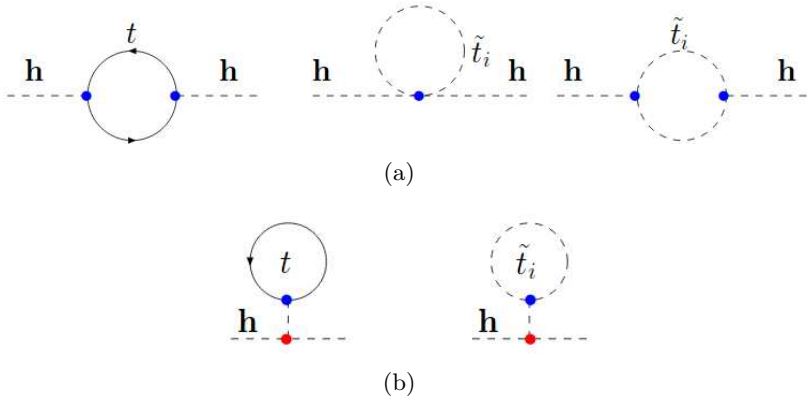

Figure 3.3.: The top and stop contributions at one-loop to (a) the Higgs boson self energy corrections and (b) the tadpole corrections.

level by diagonalizing the M_C matrix in equation 2.30.

- By fixing one of the 4 $\tilde{\chi}_i^0$ physical masses, the free wino mass parameter M_1 can be calculated at tree level by diagonalizing the M_N matrix in equation 2.28.
- By fixing the physical masses $m_{\tilde{t}_1}$, $m_{\tilde{t}_2}$, the free parameters m_Q and $m_{\tilde{t}_R}$ can be calculated at tree level by diagonalizing the matrix $M^2_{\tilde{f}}$ in equation 3.7.

More generally, the new version will include an inverted bottom up procedure from physical masses constraining some free SUSY parameters. This option will facilitate generating SUSY spectrums compatible with the experimental constraints, and is also more natural given the new fundamental input now available with the Higgs boson mass, moreover determined with a good accuracy.

In the following sections we discuss the inversion in the Higgs sector constraining the trilinear top coupling A_t. This inversion is the most complicated one as the radiative corrections to the Higgs boson mass play a very important role while the radiative corrections for the charginos, neutralinos and stops are less important.

3.5. From the Higgs boson physical mass to the trilinear top coupling

At tree level, the masses of the five MSSM Higgs particles and their mixings are described by only two parameters: the ratio of the vacuum expectation values of the two Higgs fields, tanβ, and the mass M_A of the pseudoscalar Higgs boson. However, the radiative corrections play a very important role as their dominant component depends on the top quark mass m_t and the stops masses $m_{\tilde{t}_1}$ and $m_{\tilde{t}_2}$, while the stop masses in turn depend on the trilinear top coupling A_t as seen in section 3.3.1. When the input $m_h = 125$ GeV is taken into account within some accuracy bands and by expressing the radiative corrections in terms of A_t one can constrain this free parameter. This is straightforward when using the simplified expression of the radiative corrections to the Higgs boson mass as will be discussed in section 3.5.1, however it becomes more complicated when using the exact full one-loop and leading two loop corrections as will

be discussed in sections 3.5.2 and 3.5.3. We emphasize that in the SuSpect3 new version, we will not use the simple but the full radiative corrections expression, which constitutes an original possibility...

3.5.1. Using the approximate one-loop correction to the Higgs boson mass

To test the Higgs mass inversion, we started by using the simple approximation for the radiative corrections, RC, given in equation 3.12 [55] where m_t is the running top mass and g_2 is the SU(2) gauge coupling.

$$\begin{aligned} RC = m_h^{pole,2} - \overline{m}_h^2 &= \frac{3g_2^2 m_t^4}{8\pi^2 m_w^2 \sin^2\beta}\left[ln\left(\frac{m_{\tilde{t_1}} m_{\tilde{t_2}}}{m_t^2}\right) + \frac{X_t^2}{M_S^2} - \frac{X_t^4}{12M_S^4}\right] \\ M_S^2 &= \sqrt{m_{\tilde{Q}}^2 m_{\tilde{t}_R}^2 + m_t^2\left(m_{\tilde{Q}}^2 + m_{\tilde{t}_R}^2\right) + m_t^4} \\ X_t &= A_t - \mu\cot\beta \\ m_{\tilde{t_1}} m_{\tilde{t_2}} &= \sqrt{M_S^4 - 4m_t^2 X_t^2} \end{aligned} \tag{3.12}$$

This expression has a quartic and quadratic A_t dependencies coming from the stop mixing parameter X_t and a logarithmic A_t dependence from the stop masses product $m_{\tilde{t_1}} m_{\tilde{t_2}}$. Given the input variables listed in the second line of table 3.4, one can compute at tree level the value of $\overline{m}_A$ needed to calculate $\overline{m}_h$ given in equation 3.13.

$$\begin{aligned} \overline{m}_A^2 &= m_{H_d}^2 + m_{H_u}^2 + 2\mu^2 \\ \overline{m}_h^2 &= \frac{1}{2}\left[\overline{m}_A^2 + m_Z^2 - \sqrt{(\overline{m}_A^2 + m_Z^2)^2 - 4\overline{m}_A^2 m_Z^2 \cos^2 2\beta}\right] \end{aligned} \tag{3.13}$$

Then by subtracting the squared pole Higgs boson mass from the squared tree Higgs boson mass one obtains the value of RC and transforms equation 3.12 to a quadratic equation on X_t^2 where the a and b coefficients multiplying the X_t^4 and X_t^2 respectively are constant, however the c coefficient is depending logarithmically on X_t as shows equation 3.14.

$$\begin{aligned} aX_t^4 + bX_t^2 + c &= 0 \\ a &= -\frac{1}{12M_S^4} \\ b &= \frac{1}{M_S^2} \\ c &= -\frac{RC\cdot 8\pi^2 m_w^2 \sin^2\beta}{3g_2^2 m_t^4} + ln\left(\frac{\sqrt{M_S^4 - 4m_t^2 X_t^2}}{m_t^2}\right) \end{aligned} \tag{3.14}$$

Since the logarithmic dependence on X_t is very moderate, to solve this equation we use a fixed-point iteration method, where the first X_t^2 guess is 0 and each step assume temporarily solving a true quadratic equation. This guess gives two X_t^2 solutions ($X_t^{2,p}$, $X_t^{2,m}$) which will be used separately in the next iteration to compute the stop mass products ($m_{\tilde{t_1}} m_{\tilde{t_2}}^p$, $m_{\tilde{t_1}} m_{\tilde{t_2}}^m$) and then give the c coefficients (c^p, c^m). The iteration stopping criteria is when the $X_t^{2,p}$ or $X_t^{2,m}$ stabilize. The convergence of this method is fast as shows the $X_t^{2,p}$ and $X_t^{2,m}$ versus the iteration number distributions in figures 3.4(c) and 3.5(c) respectively.

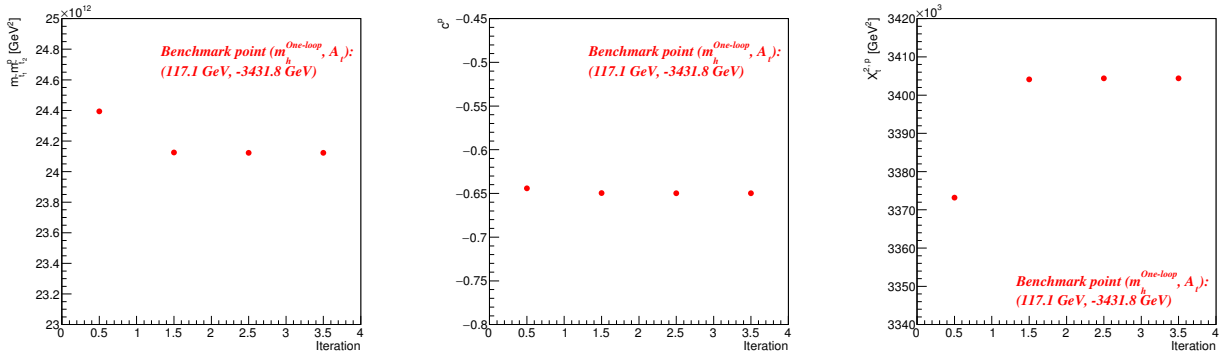

(a) (b) (c)

Figure 3.4.: The i-th (a) stop masses product, (b) c coefficient and (c) $X_t^{2,p}$ solution computed using the i-1-th $X_t^{2,p}$ versus the number of iteration, i, for the benchmark point ($m_h^{One-loop}$, A_t)= (117.1, -3431.8) GeV.

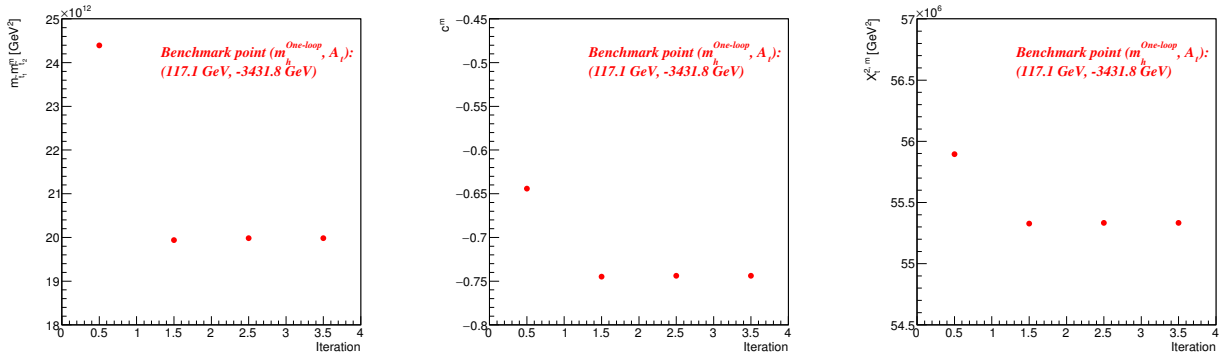

(a) (b) (c)

Figure 3.5.: The i-th (a) stop masses product, (b) c coefficient and (c) $X_t^{2,m}$ solution computed using the i-1-th $X_t^{2,m}$ versus the number of iteration, i, for the benchmark point ($m_h^{One-loop}$, A_t)= (117.1, -3431.8) GeV.

Some protection are mandatory to ensure the convergence of this iterative procedure:

- To avoid a complex $m_{\tilde{t}_1} m_{\tilde{t}_2}^m$, $M_S^4 - 4m_t^2 X_t^2$ must be always positive.
- If during the iterations X_t^2 became complex, the X_t^2 norm is used instead for the next iteration to avoid a complex X_t^2.
- If during the iterations X_t^2 became negative, the $-X_t^2$ is used instead for the next iteration to avoid a complex X_t.

Solving equation 3.14 gives multiple X_t solutions, typically 4 X_t corresponding to 4 A_t, the main difficulty here is to know if these solutions are all valid or some must be rejected.

A numerical example of A_t computation is presented in table 3.4 where the first and second column show the list of input used and their values respectively, while the third column represents the computation procedure and the A_t multiple solutions obtained as output.

Table 3.4.: Numerical example of the A_t computation from m_h using the approximate one-loop correction.

Parameters	Input	Output
g_c	0.64	
m_h^{pole} [GeV]	125	
m_{top} [GeV]	173	
m_W [GeV]	80.1	
m_Z [GeV]	90.1	
$\tan(\beta)$	10	
Signed μ	+1000	
m_{t_R} [GeV]	2000	
m_Q [GeV]	2000	
$m_{H_u}^2$ [GeV^2]	-984135 GeV	
$m_{H_d}^2$ [GeV^2]	-1.01164 $\cdot 10^6$	
$\overline{m}_A$ [GeV]		65
$\overline{m}_h$ [GeV]		62.5
RC [GeV^2]		11719.3
A_t solutions [GeV]		A_{t_1} : -2004.48
		A_{t_2} : 2204.48

3.5.2. Including the full one-loop correction

In this section we discuss the Higgs mass inversion newly developed as a part of this thesis work when replacing the simplified one-loop by the full one-loop correction as implemented in SuSpect3. Instead of using the very approximate RC expression as in the simplified case, the strategy is to use the squared Higgs boson mass from exact one-loop equation 3.11, which also

can be written as in equation 3.15:

$$m_h^4 - m_h^2(M_{11}^S + M_{22}^S) + M_{11}^S M_{22}^S = (M_{12}^S)^2 \tag{3.15}$$

where the matrix M^S including exact one-loop correction is given by equation 3.16,

$$M^S = \begin{pmatrix} M_Z^2 \cos^2\beta + M_A^2 \sin^2\beta + \pi_{11} - t_1 & -\frac{1}{2}\left(M_Z^2 + M_A^2\right)\sin 2\beta + \pi_{12} \\ -\frac{1}{2}\left(M_Z^2 + M_A^2\right)\sin 2\beta + \pi_{21} & M_Z^2 \sin^2\beta + M_A^2 \cos^2\beta + \pi_{22} - t_2 \end{pmatrix} \tag{3.16}$$

and the full one-loop Higgs boson self-energies, π_{ij}, and the tadpoles, t_i, are taken from Ref. [48]. These are complicated expressions including fermionic and scalars contributions as discussed previously in section 3.3.2. They contain different kind of A_t dependencies which have to be extracted being not obvious and rather non linear. In particular the A_0 tadpole loop function (given by equation 3.17) has a rather involved A_t dependence through the stop mass (see equation 3.7).

$$A_0(m_{\tilde{t}_i}) = m_{\tilde{t}_i}^2 \left(1 - ln\left(\frac{m_{\tilde{t}_i}^2}{\mu^2}\right)\right) \tag{3.17}$$

Thus we had to devise an iterative procedure following typically a fixed-point algorithm such that at a given step exactly solvable equations are obtained (quite similarly to previous approximation). In equation 3.19 we decompose the different A_t dependencies we considered for each of the π_{ij} and t_i, the terms with:

- an upper index "1" are terms with a linear A_t dependence originating from the h-$\tilde{t}$-$\tilde{t}$ couplings: g_{s2t1t1}, g_{s2t2t2} and g_{s2t1t2} given in equation 3.18.

$$\begin{aligned} g_{s2t1t1} &= \cos^2\theta \text{ s2tLtL} + 2\cos\theta\sin\theta \text{ s2tLtR} + \sin^2\theta \text{ s2tRtR} \\ g_{s2t2t2} &= \sin^2\theta \text{ s2tLtL} - 2\cos\theta\sin\theta \text{ s2tLtR} + \cos^2\theta \text{ s2tRtR} \\ g_{s2t1t2} &= \sin\theta\cos\theta \text{ (s2tRtR- s2tLtL)} + (\cos^2\theta - \sin^2\theta) \text{ s2tLtR} \\ \text{s2tLtR} &= \frac{y_t}{\sqrt{2}} A_t \end{aligned} \tag{3.18}$$

- an upper index "2" are terms with A_t^2 dependence coming from the h-$\tilde{t}$-$\tilde{t}$ couplings squared.
- an upper index "s" are terms depending on the $\sqrt{asA_t^2 + bsA_t + cs}$ term originating from the $A_0(m_{\tilde{t}_i})$ function.
- an upper index "1s" are terms containing $A_t \cdot \sqrt{asA_t^2 + bsA_t + cs}$ resulting from the product $g_{s2t1t1} \cdot A_0(mst1)$.
- finally an upper index "0" means all remnant contributions that do not depend at all on A_t.

$$\begin{aligned} t_1 &= t_1^s + t_1^0 \\ t_2 &= t_2^{1s} + t_2^0 \\ \pi_{11} &= \pi_{11}^s + \pi_{11}^0 \\ \pi_{12} &= \pi_{12}^1 + \pi_{12}^0 \\ \pi_{22} &= \pi_{22}^s + \pi_{22}^1 + \pi_{22}^2 + \pi_{22}^0 \end{aligned} \tag{3.19}$$

Next, by replacing these π_{ij} and t_i expressions in equation 3.15 we obtain the function $g(A_t)$ shown in equation 3.20 which should consistently vanish at any A_t solution.

$$g(A_t) = C_3 A_t^3 + C_2 A_t^2 + C_1 A_t + C_0 + (R_2 A_t^2 + R_1 A_t + R_0)\sqrt{asA_t^2 + bsA_t + cs} = 0 \qquad (3.20)$$

Figure 3.6 shows the distributions of g(A_t) versus A_t for 3 benchmark points ($m_h^{one-loop}$, A_t): (119.5, 3976.3) GeV, (117.1, -3431.8) GeV and (115.6, -3616.4) GeV. In this notation the $m_h^{one-loop}$ stands for the Higgs boson mass input value which is used to compute the C_i and R_i coefficients, while the A_t represents the correct A_t value corresponding to this m_h.

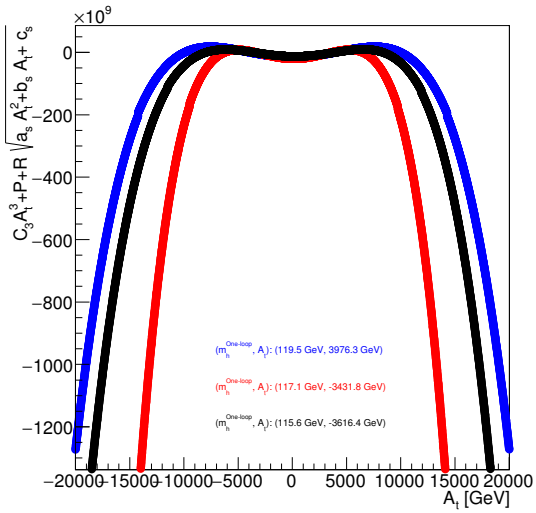

Figure 3.6.: The distribution of the function g(A_t) for the 3 benchmark points ($m_h^{one-loop}$, A_t): (119.5, 3976.3) GeV shown in blue, (117.1, -3431.8) GeV in red, (115.6, -3616.4) GeV in black.

The cubic term, dominating the g(A_t) behavior, results from the product $M_{11}^S \cdot M_{22}^S$, more precisely from the terms $\pi_{11}^s t_2^{1s}$ and $t_1^s \cdot t_2^{1s}$. Equation 3.21 shows the C_3 coefficient expression while the other C_i and R_i coefficients are not shown being more complicated.

$$\begin{aligned} C_3 &= -as \cdot C_{\pi_{11}^s} C_{t_2^{1s}} + as \cdot C_{t_1^s} \cdot C_{t_2^{1s}} \\ C_{\pi_{11}^s} &= \frac{\pi_{11}^s}{\sqrt{asA_t^2 + bsA_t + cs}} \\ C_{t_1^s} &= \frac{t_1^s}{\sqrt{asA_t^2 + bsA_t + cs}} \\ C_{t_2^{1s}} &= \frac{t_2^{1s}}{A_t \cdot \sqrt{asA_t^2 + bsA_t + cs}} \end{aligned} \qquad (3.21)$$

Concerning the 7 coefficients, one should note that they are actually not constant in terms of A_t,

as the π_{ij} and t_i listed in equation 3.19 also have a logarithmic A_t dependence coming from the A_0 and B_0 functions which we didn't develop to reduce the complexity of the g(A_t) function, therefore C_i and R_i are re-computed iteratively for each A_t. Figure 3.7 shows the distributions of the coefficients R_0 and C_0 versus A_t for the 3 benchmark points.

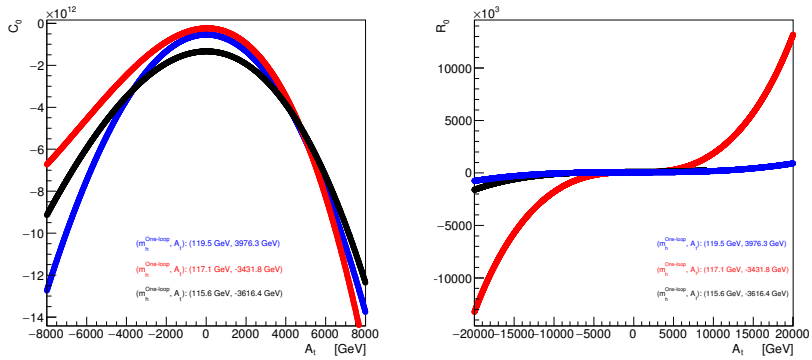

(a) (b)

Figure 3.7.: The distributions of the coefficient (a) P_0 and (b) R_0 versus A_t for the 3 benchmark points ($m_h^{one-loop}$, A_t): (119.5, 3976.3) GeV shown in blue, (117.1, -3431.8) GeV in red, (115.6, -3616.4) GeV in black.

To solve the $g(A_t) = 0$ equation we thus use the fixed point iterative method, $A_{t,i+1} = f(A_{t_i})$, where the function f(A_t) is given in equation 3.22. The iteration stopping criteria is based on the A_t relative error shown in figure 3.8. More explicitly the solution at a given step is given by equation 3.22.

$$\begin{aligned} P &= C_2 A_t^2 + C_1 A_t + C_0 \\ R &= R_2 A_t^2 + R_1 A_t + R_0 \\ A_{t,i+1}^3 &= -\frac{1}{C_3}[P + R\sqrt{asA_{t,i}^2 + bsA_{t,i} + cs}] \\ A_{t,i+1} = f(A_{t_i}) &= \begin{cases} (A_{t,i+1}^3)^{\frac{1}{3}} & if(A_{t,i+1}^3 > 0) \\ -(|A_{t,i+1}^3|)^{\frac{1}{3}} & else \end{cases} \end{aligned} \tag{3.22}$$

As figure 3.9 shows, the function $f(A_t)$ behaves in roughly the same way for the 3 benchmark points and it has 4 intersecting points with the bisector. These are the fixed points of f(A_t), thus they represent the 4 A_t solutions denoted as s_0, s_1, s_2, s_3 in ascending order.

Figure 3.9 shows that s_3 is an attractive fixed point meaning that starting from an A_t guess that is close enough to s_3 and iterating it always leads to convergence to s_3. However, s_0 and s_2 are repulsive fixed points as they push away a nearby A_t guess; while s_1 shows a mixed behavior. Knowing that the fixed point iteration $A_{t,i+1} = f(A_{t_i})$ will only work with the attractive point s_3 and not for the 3 other points, we use a more general sequence given in equation 3.23 depending on three parameters $A_{t,i}$, $A_{t,i+1} = f(A_{t_i})$ and an extra arbitrary parameter, τ.

$$A_t^{i+1\prime} = \frac{A_t^i * (\tau - 1) + A_t^{i+1}}{\tau} \qquad \tau \neq 0 \tag{3.23}$$

The advantage of this sequence is that it can converge to a non attractive fixed point for an

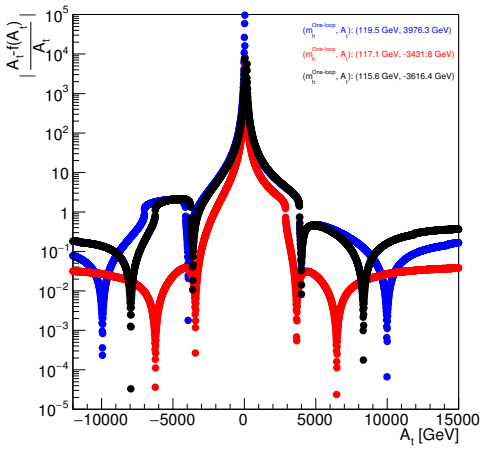

Figure 3.8.: The distribution of the A_t relative error function versus A_t for the 3 benchmark points ($m_h^{one-loop}$, A_t): (119.5, 3976.3) GeV shown in blue, (117.1, -3431.8) GeV in red, (115.6, -3616.4) GeV in black.

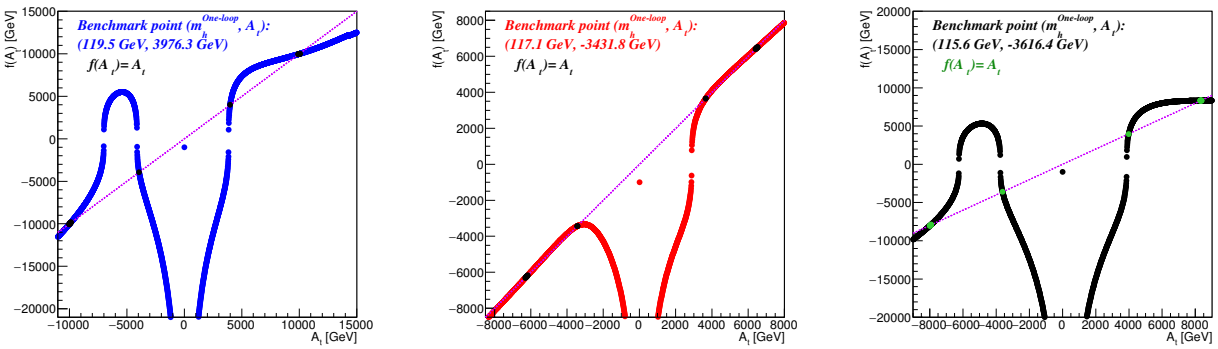

(a) (b) (c)

Figure 3.9.: The distribution of f(A_t) versus A_t for the benchmark points ($m_h^{one-loop}$, A_t): (a) (119.5, 3976.3) GeV, (b) (117.1, -3431.8) GeV, (c) (115.6, -3616.4) GeV. The 4 intersecting points between the violet line and each of the curve have f(A_t)=A_t.

adequate choice of the sign and value of the τ parameter. This choice is determined by the behavior of the function f(A_t) close to that point: when f(A_t) is an increasing function (i.e. at s_0 and s_2) a negated τ with $|\tau|$ >>1 is needed, however when it is decreasing (i.e. at s_1), a positive τ with $|\tau|$ >>1 is needed. In case of an attractive point, $\tau = 1$ is used and so one obtains $A_t^{i+1\prime} = f(A_t^i)$, receiving the more standard fixed point method.

This strategy was tested for the 3 benchmark points described above, the results are shown in table 3.5. The A_t first guesses used are the 4 A_t solutions resulting from the simplified algorithm described in section 3.5.1 , denoted as $A_t^{guess,i}$ and sorted in ascending order to facilitate the choice of τ:

- For $A_t^{guess,0}$, $A_t^{guess,2}$, expected to be near solution s_0 and s_2 respectively, τ = -10 is used.
- For $A_t^{guess,1}$, expected to be close to solution s_1, $\tau = 10$ is used.
- For $A_t^{guess,3}$ expected to be close to s_3, $\tau = 1$ is used.

So using these 4 A_t guesses with their corresponding τ and after iterating we obtained the correct A_t plus 3 additional A_t solutions. To cross check the validity of these additional solutions they are re-implemented in the stop mass calculation.

Table 3.5.: The A_t computation from $m_h^{one-loop}$, using the full one-loop correction, for the 3 benchmark points.

Benchmark ($m_h^{One-Loop}$, A_t) [GeV]	A_t^{Guess} [GeV]	τ	$A_t^{Solution}$ [GeV]	$m_{\tilde{t}_1}$ [GeV]	$m_{\tilde{t}_2}$ [GeV]
(119.5, 3976.3)	-11187.7	-10	-9944.0	$2.6334\cdot 10^3$	$3.7559\cdot 10^3$
	-1355.6	10	-3939.2	$2.7387\cdot 10^3$	$3.9563\cdot 10^3$
	1392.7	-10	**3976.3**	$2.7392\cdot 10^3$	$3.9519\cdot 10^3$
	11224.8	1	9981.1	$2.6187\cdot 10^3$	$3.7120\cdot 10^3$
(117.1, -3431.8)	-1743.4	-10	3655.5	$1.8825\cdot 10^3$	$2.7521\cdot 10^3$
	1967.1	10	**-3431.8**	$1.8814\cdot 10^3$	$2.7549\cdot 10^3$
(115.6, -3616.4)	-912.0	10	**-3616.4**	$1.6964\cdot 10^3$	$4.0221\cdot 10^3$
	1279.6	-10	3983.6	$1.7016\cdot 10^3$	$4.0186\cdot 10^3$

3.5.3. Adding the full one-loop plus leading two-loop correction

As discussed in section 3.3.2, SuSpect3 implements the two-loop corrections to the Higgs boson mass as calculated in Ref [53] [54]. These corrections depend on the strong, weak and the third generation Yukawa couplings and lead to terms of $\mathcal{O}(\alpha_s)\times\mathcal{O}$(One-loop). These terms are added to the M^S matrix which enter the squared Higgs boson mass equation shown in equation 3.15, their dependence in terms of A_t is shown in figure 3.10.

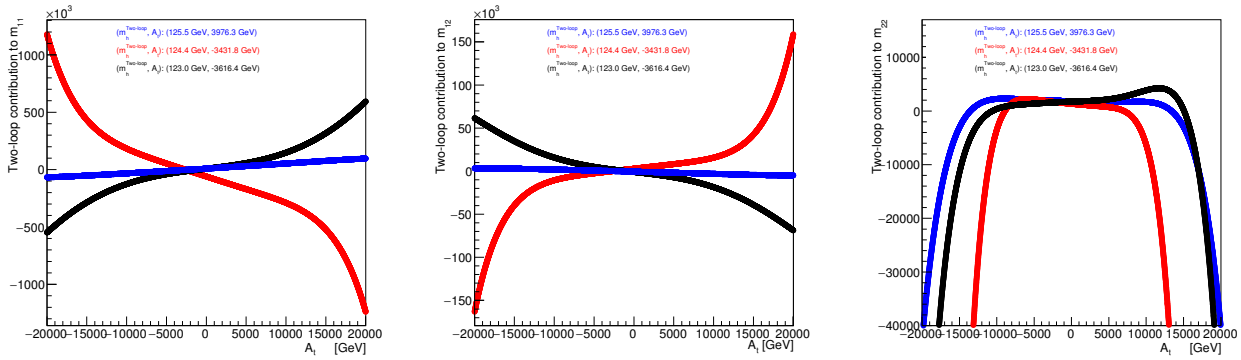

Figure 3.10.: Dependence of (a) $m_{11}^{two-loop}$, (b) $m_{12}^{two-loop}$ and (c) $m_{22}^{two-loop}$ in terms of A_t for the 3 benchmark points ($m_h^{two-loop}$, A_t): (125.5, 3976.3) GeV shown in blue, (124.4, -3431.8) GeV in red, (123.0, -3616.4) GeV in black. These benchmark points are the ones used in the previous section but the $m_h^{two-loop}$ denotes the Higgs mass value resulting from SuSpect3 using the full one–loop plus leading two-loop calculation.

Being of $\mathcal{O}(\alpha_s)\times\mathcal{O}$(One-loop), the two-loop are much less important than the one-loop contributions. This can be seen in figure 3.11 showing the absolute values of the ratio of the one- over two-loop contributions versus A_t, clearly the one-loop contributions is often 3-10 times more than the two-loop contributions. This factor can also be obtained by comparing how much the one- or two-loop contributions affect finally the Higgs boson mass value, in case of the two-loop contribution it is about 3-5 GeV, while for the one-loop it is 30-50 GeV [56]. Thus, for the Higgs mass inversion, we chose to not decompose the different A_t dependencies for the two-loop contributions, instead, they are treated as independent of A_t similarly to the π_{ij}^0 in equation 3.19.

Then, similarly to the one-loop Higgs mass inversion the 7 coefficients entering the g(A_t) function of equation 3.20 are computed but using consistently now the $m_h^{Two-loop}$ input instead of the $m_h^{One-loop}$. The resulting function f(A_t), given in equation 3.22, is shown in figure 3.12 for the three benchmark points described in the previous section here denoted as ($m_h^{Two-loop}$, A_t): (125.5, 3976.3) GeV, (124.4, -3431.8) GeV, (123.0, -3616.4) GeV. The two-loop inversion was tested for the 3 benchmark points described above, the results are shown in table 3.6. The A_t first guesses used are the 4 A_t solutions resulting from the simplified algorithm as described in section 3.5.1 and the τ values used are the same used for the one-loop inversion, as the added two-loop contributions did not affect much the f(A_t) behavior.

So using these 4 A_t guesses with their corresponding τ and after iterating we obtained the correct A_t solution, plus additional A_t solutions in some cases. To cross check the validity of these additional solutions they are re-implemented in the stop mass calculation.

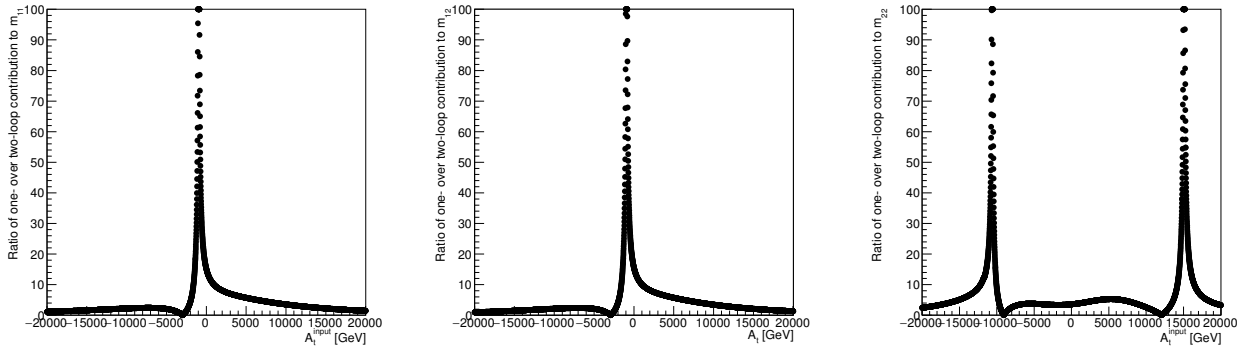

(a) (b) (c)

Figure 3.11.: The absolute values of the ratio of the one- over two-loop contribution to (a) m_{11}, (b) m_{12} and (c) m_{22} for the benchmark point ($m_h^{two-loop}$, A_t): (123.0, -3616.4) GeV. The distributions peaks are due to the zero value of the two-loop contributions to m_{ij} (see figure 3.10).

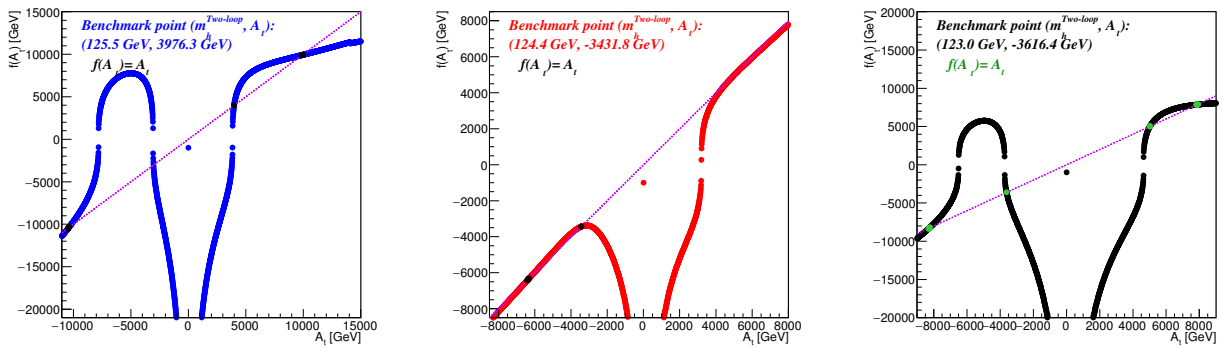

(a) (b) (c)

Figure 3.12.: The distribution of f(A_t) versus A_t for the benchmark points ($m_h^{Two-loop}$, A_t): (a) (125.5, 3976.3) GeV, (b) (124.4, -3431.8) GeV, (c) (123.0, -3616.4) GeV. The intersecting points between the violet line and each of the curve have f(A_t)=A_t.

Table 3.6.: The A_t computation from $m_h^{Two-loop}$, using the full one-loop plus leading two-loop correction, for the 3 benchmark points.

Benchmark ($m_h^{Two-Loop}$, A_t) [GeV]	A_t^{Guess} [GeV]	τ	$A_t^{Solution}$ [GeV]	$m_{\tilde{t}_1}$ [GeV]	$m_{\tilde{t}_2}$ [GeV]
(125.5, 3976.3)	-11187.7	-10	-10434.8	$2.6202\cdot 10^3$	$3.7318\cdot 10^3$
	1392.7	-10	**3976.3**	$2.7392\cdot 10^3$	$3.9519\cdot 10^3$
	11224.8	1	9923.9	$2.6199\cdot 10^3$	$3.7149\cdot 10^3$
(124.4, -3431.8)	1967.1	10	**-3431.8**	$1.8814\cdot 10^3$	$2.7548\cdot 10^3$
(123.0, -3616.4)	-912.0	10	**-3616.4**	$1.6965\cdot 10^3$	$4.0221\cdot 10^3$
	1279.6	-10	5016.3	$1.6936\cdot 10^3$	$4.0108\cdot 10^3$
	8795.3	1	7864.8	$1.6583\cdot 10^3$	$3.9756\cdot 10^3$

3.6. Conclusion and outlook

As a part of this thesis work, we developed a new version of SuSpect3 which allow to directly determine the trilinear top coupling, A_t, using the measured Higgs boson mass. This was done using, first, the simplified expression of the radiative corrections to the Higgs boson mass and, next, the exact full one-loop with the leading two loop corrections. Further inversions from physical masses constraining other free SUSY parameters can be done in principle, such as μ, M_2, M_1,...

The Higgs mass inversion done is the first step in this bottom-up procedure and probably the most complicated one as the radiative corrections to the Higgs boson mass play a very important role and include complicated dependencies on A_t which are not negligeable.

Part II.

Experimental apparatus

4. The Large Hadron Collider

The world's largest and most complex particle accelerator is the Large Hadron Collider (LHC) [57]. It is a circular, synchrotron accelerator in which the particles are accelerated using the electromagnetic field. It operates by colliding two beams of protons obtained from ionization of hydrogen gas or, in alternative, lead ions ($^{208}_{82}\mathrm{Pb}^{82+}$).

The LHC was built to accelerate protons up to a center-of-mass energy of $\sqrt{s}$ =14 TeV and therefore provides a possibility to study the electroweak symmetry breaking and to search for new physics at the TeV scale. Searches for the Higgs boson and BSM physics were the main objectives of this machine.

The delivered energy was $\sqrt{s} = 7$ TeV during 2010 and 2011 and $\sqrt{s}$ =8 TeV during 2012, in 2015 it has been raised to $\sqrt{s} = 13$ TeV. The increase of the center-of-mass energy is well justified by the bigger increment in production cross section for heavy particles, such as those predicted by super-symmetry, over the increased background rates. In this thesis, the data recorded in 2015 and 2016 at $\sqrt{s}$ =13 TeV is analysed. This section is organized as follows: the LHC machine and its accelerator chain are described in subsection 4.1 and the LHC luminosity, LHC pileup conditions are described in subsection 4.2.

4.1. LHC and the accelerator chain

The LHC is located at CERN, the European Organization for Nuclear Research, near Geneva and across the border between France and Switzerland. Its storage ring is 27 km in circumference and installed about 100 m underground, in the old Large Electron Positron Collider (LEP) tunnel. However, the LHC storage ring cannot accelerate particles from rest. Instead, it relies on a chain of pre-accelerators that raise the kinetic energy of the particle beams before they are injected into the LHC. The simplified LHC accelerator chain is shown in figure 4.1. Several synchrotron and linear accelerators are supplying the LHC ring. The chain starts with a linear accelerator (LINAC 2) which is about 30 m long. The valence electrons are stripped off from the hydrogen atoms and the remaining protons are collected and accelerated up to 50 MeV kinetic energy at the end of the LINAC 2. The next step in the chain is the Proton Synchrotron Booster (PSB) which is composed of four superimposed synchrotron rings, each of them is about 150 m long. The PSB accelerates and squeezes the protons into a high-intensity proton beam which has a 1.4 GeV beam energy when it exits the PSB. This beam is passed on to the next accelerator, the Proton Synchrotron (PS), which has a circumference of 628 m, and it provides 25 GeV proton beams to the next accelerator, the Super Proton Synchrotron (SPS). The SPS is the second largest accelerator at CERN, it is nearly 7 km in circumference and it injects 450 GeV proton beams into the LHC ring, the final synchrotron accelerator in the chain.

The protons are organized in bunches containing $1.15 \cdot 10^{11}$ particles with a time spacing between two consecutive bunches down to 25 ns before being injected into the LHC ring where they are accelerated to the designed center-of-mass energy by sixteen 400MHz superconductive radio frequency (RF) cavities. This system accelerates the beams through oscillating electromagnetic fields, the cavities are operated at a temperature of 4.5K and a potential of 2 MV. The accelerating field within the cavities is 5 MV/m.

The LHC ring has two separate vacuum beam pipes, and the proton beams from the SPS are split into two sets that are injected in the two pipes. One proton beam circulates clockwise while the other one circulates anti-clockwise around the ring. The proton beams are kept confined in the LHC ring through the use of 1232 superconducting dipole magnets. Each magnet is kept at a temperature of 1.9K and is operated with a current nominally (for 14 TeV) of 11700 A, producing a magnetic field of 8.3 T. Additional 392 quadruple magnets are installed in order to stabilize and focus the particle beams.

The two beam pipes cross each other at four colliding points where the four complex particle detectors, ATLAS [58], CMS [59], ALICE [60], and LHCb [61] are placed in order to study the products of the collision. The ATLAS and CMS experiments are general-purpose detectors which are independently designed to investigate a broad range of physics phenomena. The ALICE experiment is designed to study heavy-ion collisions and the LHCb experiment is designed to study the decays of hadrons containing bottom quarks.

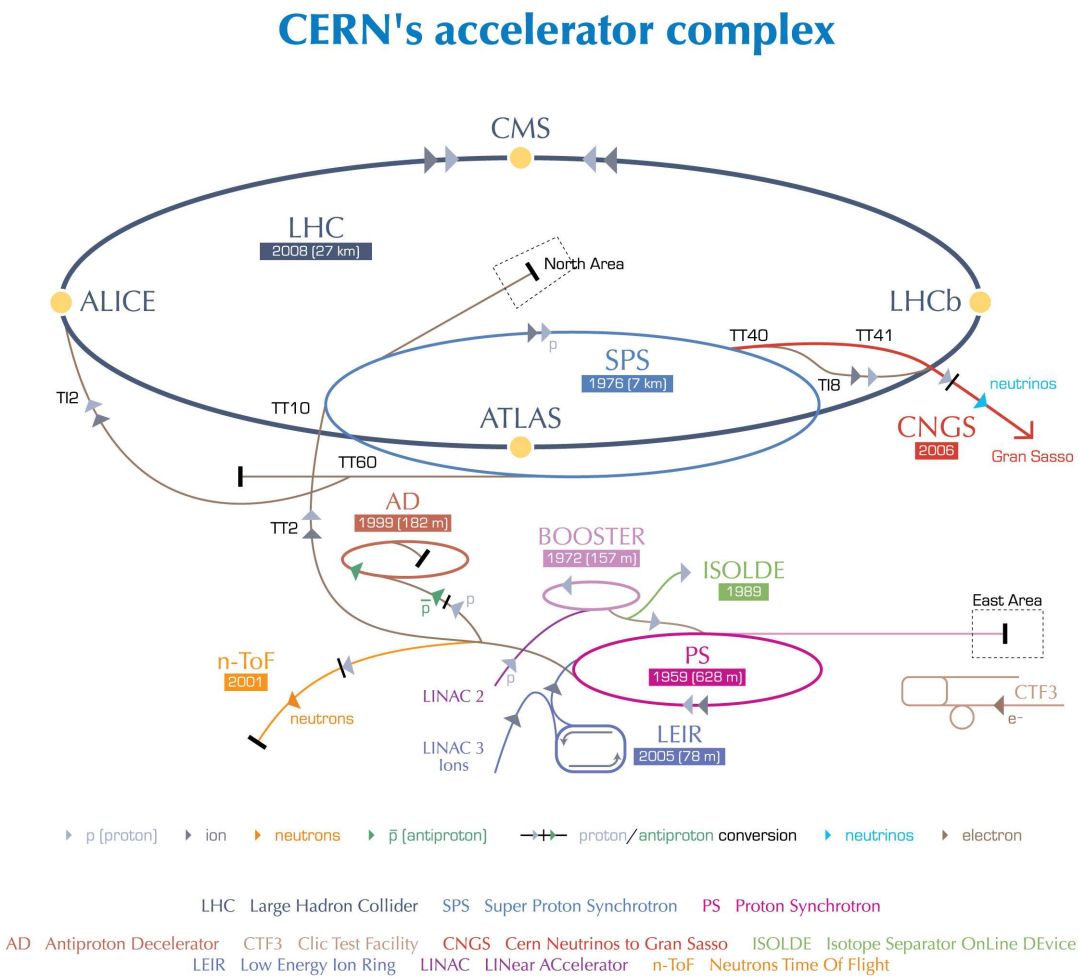

Figure 4.1.: Illustration of the CERN accelerator complex and experiments [62].

4.2. LHC parameters

The Luminosity is a key parameter of the LHC: the higher luminosity allows a larger accumulated data set which is essential to perform high precision measurements and study rare physics processes. The instantaneous luminosity (L) is a measure of the number of collisions that can be produced per cm^2 and second. The design value of L in the LHC is 10^{27} cm^{-2}s^{-1} at 5.5 TeV for the heavy ions and 10^{34} cm^{-2}s^{-1} for proton-proton collisions at 14 TeV. L corresponds to the peak luminosity that the LHC can reach when filled with proton bunches. The instantaneous luminosity decreases with the run time, after a certain amount of time the circulating beams will be dumped and new proton bunches will be injected in the LHC ring.

In terns of beam parameters the instantaneous luminosity can be expressed as in equation 4.1:

$$L = \frac{N_b^2 n_b f_r \gamma}{4\pi\epsilon_n \beta^*} F \tag{4.1}$$

where N_b is the number of particles per bunch, n_b is number of bunches per beam, f_r is the cycling frequency of the bunches, γ is the relativistic factor, ϵ_n is the transverse beam emittance and β^* is the β function at the interaction point and F is a geometrical reduction factor due to the introduced crossing angle at the interaction points.

The integrated luminosity, $L_{\text{int}} = \int L dt$, is the integral of the instantaneous luminosity over a certain time interval. In the LHC this generally corresponds to entire run periods, such as one or two years of data taking. Correspondingly, the number of expected events N for a physics process having a production cross section σ over a given time interval is related to the integrated luminosity, which is $N = L_{\text{int}}\sigma$. The unit of the integrated luminosity is normally inverse barn (b^{-1}), where 1 b=10^{-24} cm^2 and cross sections are analogously given in units of barn (b). During August 2016, in pp collisions LHC delivered $\approx$ 25 fb^{-1} reaching a peak luminosity of 1.55$\cdot$ 10^{34} cm^{-2}s^{-1}, as shown in figures 4.2(a) and 4.2(b).

If the number of bunches in the LHC beam is high, and therefore high luminosity is delivered, multiple collisions in the same bunch-crossing can occur. These proton-proton collisions in addition to the collision of interest (or primary interaction), referred to as "pile-up", present a serious challenge to physics analysis at the LHC. Many of the ATLAS detector subsystems have sensitivity windows longer than 25 ns, which is the interval between proton-proton bunch crossings. As a result, every physics object is affected by pile-up in some way, from additional energy contributions in jets to the mis-reconstruction of background as high-momentum muons. During 2011, the number of proton-proton collisions per bunch crossing increased from 5 to 15, and during 2012 the number increased from 10 to almost 35. Thus, understanding and modeling this background is critical for performing analysis. There are two main components of the pile-up background:

- In-time pile-up: additional proton-proton collisions occurring in the same bunch-crossing as the primary collision.
- Out-of-time pile-up: additional proton-proton collisions occurring in bunch-crossings just before and after the primary collision. When detectors are sensitive to several bunch-crossings or their electronics integrate over more than 25 ns, these collisions can affect the signal in the primary collision.

The in time pile-up is the more problematic of the two and is expressed by the mean number

of interactions per bunch crossing as in equation 4.2:

$$\langle\mu\rangle = \frac{L_{\text{bunch}} \cdot \sigma_{\text{inel}}}{f_{\text{rev}}} \tag{4.2}$$

where $L_{\text{bunch}} = \text{L}/n_b$ is the per bunch instantaneous luminosity and f_{rev} is the LHC revolution frequency of 11.245 kHz. This overlap is a real challenge for readout-electronics and the reconstruction algorithms where finding the correct vertex for each particle is really crucial to estimate the missing energy, p_T, invariant masses, etc . In figure 4.2(c), the average number of interactions for data, recorded from 16 April - 16 September, per bunch-crossing is shown.

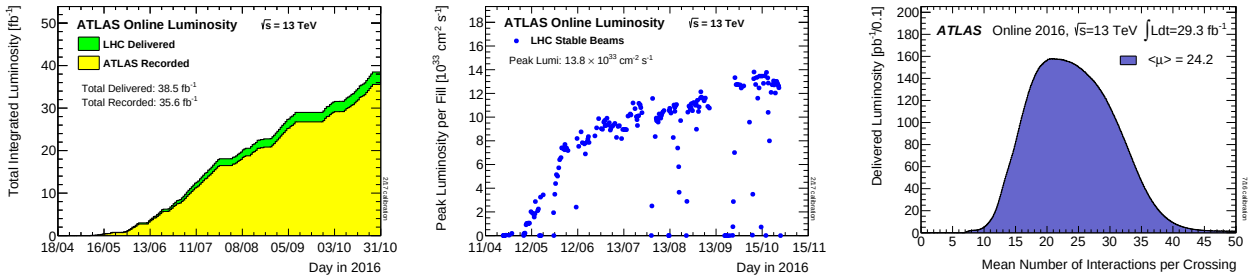

(a) (b) (c)

Figure 4.2.: (a) The cumulative luminosity versus time delivered by the LHC (green) and recorded by ATLAS (yellow) during stable beams for pp collisions at 13 TeV centre-of-mass energy in 2016. (b) The peak instantaneous luminosity delivered to ATLAS during stable beams for each LHC fill as a function of time in 2016. (c) The luminosity-weighted distribution of the mean number of interactions per crossing for the 2016 pp collision data recorded from 16 April - 16 September [63].

4.3. High luminosity LHC

Given that the center-of-mass energy achievable in a collider is constrained by the diameter of the accelerator ring for a given magnetic field strength, plans for upgrades of the LHC have been focused mostly on increases in luminosity as shows figure 4.3. The high-luminosity LHC (HL-LHC) project [64] consists of a series of upgrades to the accelerator that include more powerful focusing magnets and more precise radio-frequency cavities. The HL-LHC design luminosity is 10 times that of the LHC. Its goal is to deliver a total of 3000 fb^{-1} running over a decade starting in 2025. The HL-LHC aims to crank up the performance of the LHC in order to increase the potential for discoveries. It allow also precise studies of the new particles observed at the LHC, such as the Higgs boson [65]. As statistical uncertainties decrease roughly as the square root of the integrated luminosity, running the LHC at the current luminosity will result in diminishing statistical gains.

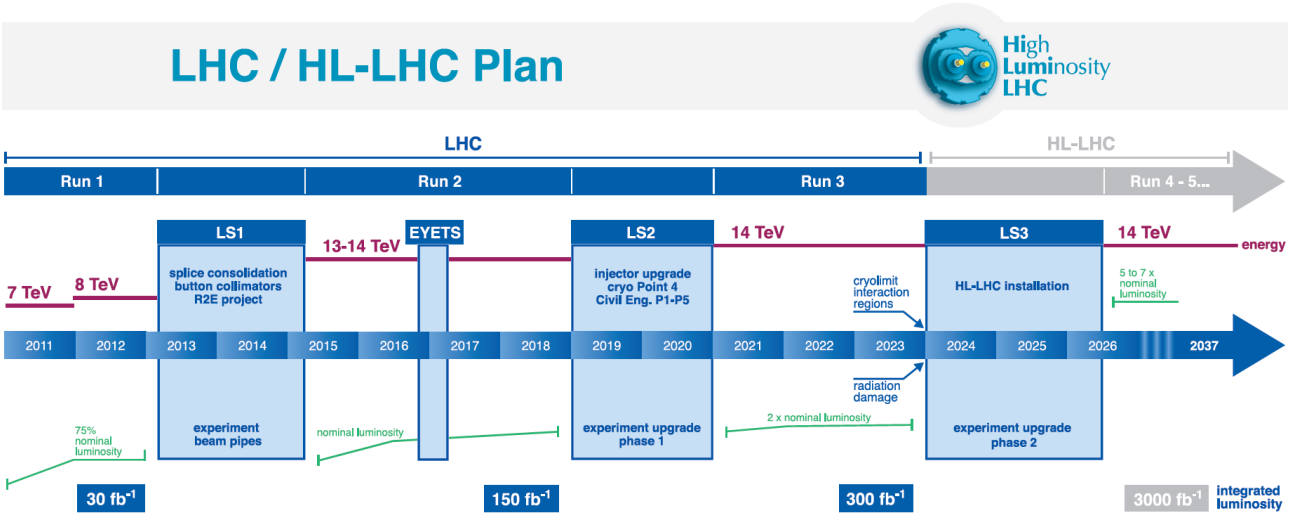

Figure 4.3.: Time-line for the LHC and High-Luminosity LHC [64].

The higher particle rate and harsher radiation environment expected at the HL-LHC pose stringent requirements on the detector technology and readout electronics used in the experiments. To cope with this, various ATLAS sub-detectors such as the muon spectrometer, the liquid-argon Calorimeters, and the inner detector will be upgraded.

5. The ATLAS detector

ATLAS [66] is a detector capable of measuring a wide variety of physics processes, its dimensions are 46 m long and 25 m high and is $\approx$ 7000 tons. It covers the full azimuth angle[a] and has a cylindrical symmetric geometry. As shows figure 5.1, the detector consists of several different sub-detectors, aiming to reconstruct tracks, measure momenta and energies of particles that interact with the detector material.

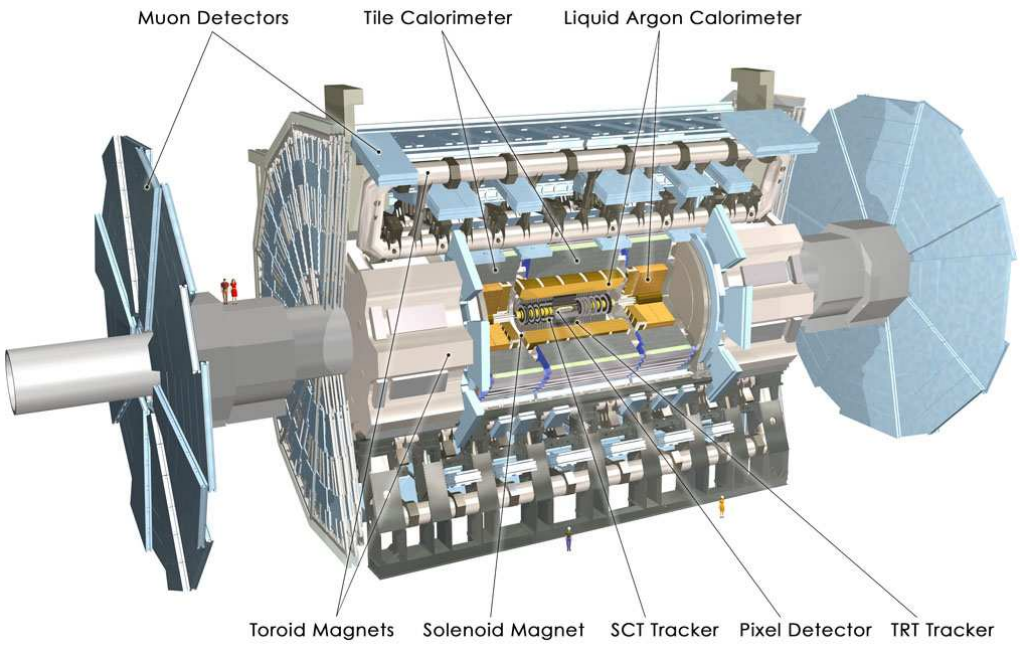

Figure 5.1.: Illustration of the ATLAS detector. The main parts of the inner detectors, Calorimeters, magnets, and muon spectrometer are highlighted [66].

The ATLAS detector is formed of: Inner detector (ID) which is surrounded by a superconducting solenoid magnet which provides a 2 T magnetic field and serves to measure the trajectories and the momenta of electrically charged particles. Outside the ID, electromagnetic Calorimeters and hadronic Calorimeters are installed to provide energy measurements. Muons escape from these Calorimeters since they interact very little with the detector material. Thus, momentum of a muon is measured in a dedicated sub-detector, the muon spectrometer (MS), which surrounds the calorimeter and operates in a 4 T Toroidal magnetic field. Neutrinos do not interact with the detector material meaning that they are invisible in all sub-detector systems and give rise to missing momentum in the transverse detector plane. The ATLAS main parts are described in this section with a special focus on the ATLAS pixel detector.

[a]The convention for the coordinate system adopted by the ATLAS collaboration is detailed in Ref [66]: "ATLAS uses a right-handed coordinate system with its origin at the nominal interaction point in the center of the detector and the z-axis along the beam pipe. The x-axis points from the interaction point (IP) to the center of the LHC ring, and the y-axis points upward. Cylindrical coordinates (r,ϕ) are used in the transverse plane, ϕ being the azimuthal angle around the beam pipe. The pseudo-rapidity is defined in terms of the polar angle *theta* as $\eta = -\ln[\tan(\theta/2)]$."

5.1. Magnet system

ATLAS magnet system consist of: an outer air-core toroid system and a 2 T superconducting solenoid surrounding the inner detector. Figure 5.2 shows the layout of the ATLAS magnet system. This choice of layout gives ATLAS (A Toroidal LHC Apparatus) its characteristic geometry. A strong magnetic field is crucial for momentum determination of charged particles, as the bending radius of a charged particle trajectory is proportional to the momentum perpendicular to the magnetic field direction. The solenoid and the beam axes being aligned, the bending radius serves to determine the p_T of the particle. The air-core toroid system generates a large magnetic field volume with strong bending power within an open structure to minimize Multiple-scattering effects. The toroid system is used for determining muon momentum with high precision and is arranged such that the field is mostly perpendicular to the muon trajectory to compensates the limitation of the solenoid especially at high η.

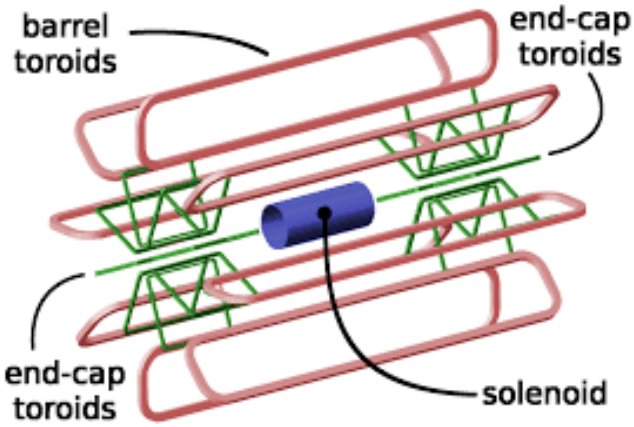

Figure 5.2.: The layout of the ATLAS magnet system [67].

5.2. Inner detector

The inner detector (ID) is designed to reconstruct the trajectories of charged particles, to measure their charge and momentum and it is crucial in the reconstruction of vertices. It occupies a cylindrical volume around the center of the interaction region and has a diameter of 2.1 m, a length of 6.2 m, and covers $|\theta| > 9.4°$ ($|\eta| < 2.5$). The momentum and vertex resolution requirements from physics call for high-precision measurements to be made given the very large track density expected at the LHC. Semiconductor tracking detectors, using silicon micro-strip and pixel technologies offer these features. Therefore, the ID is based on two main technologies: silicon detectors in the smaller radii and gas detectors in the larger radii. All these systems are immersed in a 2 T axial magnetic field produced by a superconducting magnet.

The ID is arranged in concentric cylindrical layers at the central section (barrel) and in disks perpendicular to the beam in the forward section (end-cap). As shows figure 5.3, the innermost part corresponds to the pixel detector system, which is surrounded by the semiconductor tracker (SCT), that is made of micro-strip detectors. The third sub-detector is the transition radiation tracker (TRT) that is based on gas-filled drift tubes.

The pixel system consists of four barrel layers and three end-cap disks on each side with a total of 2024 modules and ≈ 92 million readout channels (more details about this subdetector will be provided in the next subsections).
The SCT consists of four barrel layers and nine end-cap disks on each side with a total of 4088 modules and ≈ 6.2 million 80μm×12 cm channels.
The TRT consists of about 3×105 drift tubes of 4 mm diameter and 0.4-1.5 m length filled with a gas mixture containing xenon and carbon dioxide.
Typically, a charged particle produces 4 hits in the pixel system, 4 in the SCT, and 30 in the TRT. The silicon part of the inner detector has a resolution of about 15μm in the bending plane, whereas the TRT has a resolution of about 150μm. The inner detector vertex resolution, which depends on its number of charged particles, is about 80 (20)μm in the transverse plane and about 150 (40)μm in the longitudinal coordinate for vertices with 10 (80) charged particles.

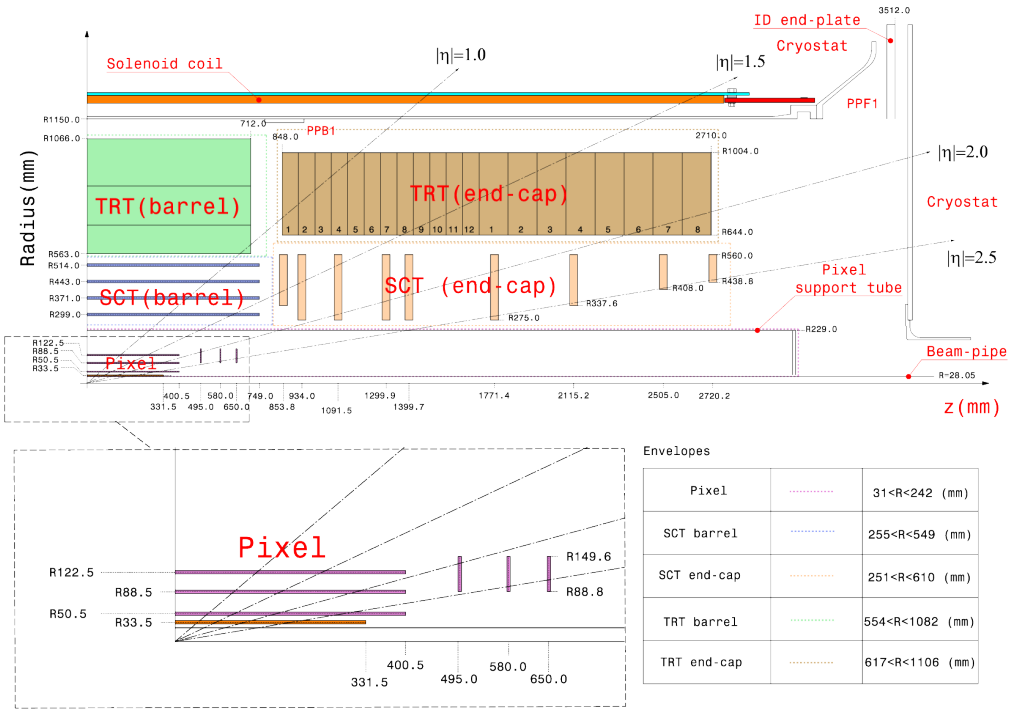

Figure 5.3.: The r-z cross-section view of the layout of a quadrant of the ATLAS inner detector for Run2. The top panel shows the whole inner detector, whereas the bottom-left panel shows a magnified view of the pixel detector region [66].

5.2.1. Particles interactions in the pixel detector

This section covers the interactions of charged particles with a surrounding medium, with a special focus on the most relevant interactions to the operation of the ATLAS pixel detector, the ionization and the related excitation of atoms.
Low-energy charged particles traversing the detector interact mainly with the atomic electrons of the detector material, and can either excite them into more energetic states, or ionize them, creating electron–ion pairs. Excited atoms can also create further ionization by

transferring their energy to other atoms. These processes depend strongly on the incident particle's momentum, which determines the maximum kinetic energy that can be transferred to the electrons of the medium. For particles other than electrons ($m_0 > m_e$) and energies low enough to satisfy $2\gamma m_e/m_0 << 1$ where γ is the Lorentz factor, this maximum energy can be approximated as in equation 5.1 [68]:

$$E_{kin}^{max} = 2m_e c^2 \beta^2 \gamma^2 \tag{5.1}$$

where β is v/c and γ is $1/\sqrt{1-\beta^2}$. Equation 5.1 only depends on $\beta\gamma$, not on the particle's mass. For the muon, the latter condition can be written as $\gamma << 424$, which should hold for muons up to a few GeV and all heavier particles with the same momentum.
The goal of all tracking devices is the detection of the free charges resulting from the ionization of a medium due to a passing charged particle. This dependence of the energy loss on $\beta\gamma$ is described by the Bethe–Bloch formula in equation 5.2.

$$-\langle\frac{dE}{dx}\rangle = Kz^2\frac{Z}{A\beta^2}(\frac{1}{2}ln\frac{2m_e c^2\beta^2\gamma^2 T_{max}}{I^2} - \beta^2 - \frac{\delta(\beta\gamma)}{2}) \tag{5.2}$$

Equation 5.2 is valid for values of $\beta\gamma$ between $\approx$ 0.1 and 1000. Here, z is the charge of the incident particle (in multiples of the elementary charge), Z the atomic number of the absorbing material, A the atomic mass in g mol^{-1} and K is a shorthand for $4\pi N_A r_e^2 m_e c^2$. N_A is the Avogadro's Number, r_e and m_e are the classical radius and the rest mass of the electron. c is the speed of light. T_{max} is the maximum possible energy transfer in a single collision (in MeV) and I the mean excitation energy in eV.
For muons, the Bethe–Bloch shape (with some additional effects for lower and higher energies) is shown in figure 5.4. In the Bethe-Bloch formula the $1/\beta^2$ term is dominant for low energies and the stopping power decreases with increasing energy and at a particle velocity β of about 0.96 ($\beta\gamma \approx$3) a minimum is reached. A particle with an energy loss corresponding to the minimum of the Bethe–Bloch formula is called a Minimum Ionizing Particle (MIP). For higher energies, the energy loss increases again, leading to the logarithmic relativistic rise. The function $\delta(\beta\gamma)$ describes the so-called density effect that suppresses the relativistic rise.
In silicon, the average energy needed to create an electron-hole pair is 3.65 eV, 3 times larger than Si band gap of 1.12 eV. This difference of energy generates phonons, which in the end will be degraded into thermal energy. A MIP penetrating into a detector is responsible of a uniform ionization along its path. A typical Silicon wafer has a thickness of 300 μm and the signal generated in it by a MIP is typically around 23000 e$^-$.
The Bethe-Bloch formula predicts the average value of the energy deposition loss distribution per unit path length, but is essentially not describing the behavior of a single particle because of the stochastic nature of energy losses. The distribution of the energy loss is instead modeled by a Landau distribution that properly includes the statistical fluctuations which occur in the number of collisions and a energy transfer in each collision. It also includes the rare but important effect of the so-called $\delta-$electrons generation which obtain enough energy by the interaction to become ionizing particles themselves. $\delta-$electrons are responsible for an asymmetry in the collected spectrum, with a longer tail toward higher energies, leading to a spectrum described by a Landau distribution having the most probable value, Δ_p, 30% below the average value. The Landau distribution is given by equation 5.3:

$$f_L(x,\Delta) = \frac{\varphi(\lambda)}{\xi}; \qquad \varphi(\lambda) = \frac{1}{2\pi j}\int_{r-j\infty}^{r+j\infty} e^{(u\ln(u)+\lambda u)}du \tag{5.3}$$

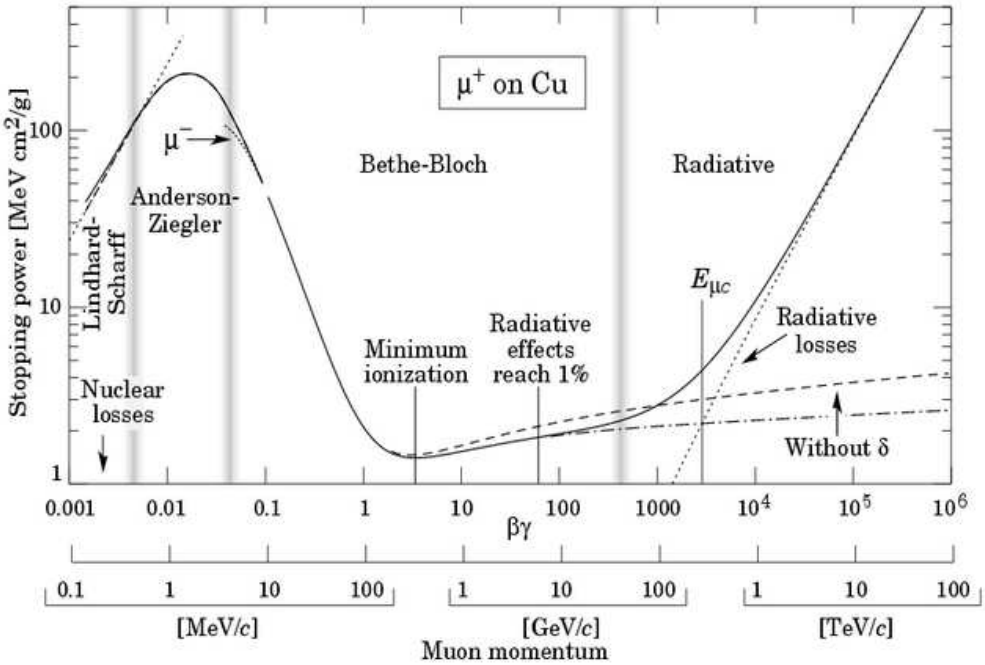

Figure 5.4.: dE/dx (stopping power or energy loss) for muons penetrating copper as a function of $\beta\gamma$ =p/(m_μc). The solid curve shows the total energy loss, with different components highlighted as dashed lines. The arrow labeled μ^- points to an effect that is specific to negatively charged particles [69].

where ξ is the mean energy loss defined by taking only the first term of Bethe-Block formula defined as $\xi = 0.1535\frac{z^2 Z}{A\beta^2}\rho x$.
r is an arbitrary real constant and the variable λ is:

$$\lambda = \frac{1}{\xi}(\Delta - \langle\Delta\rangle) - \beta^2 - \ln\left(\frac{\xi}{E_m}\right) - 1 + C_E$$

where C_E is the Euler constant. The Landau distributions for various thickness of silicon is shown in figure 5.5.

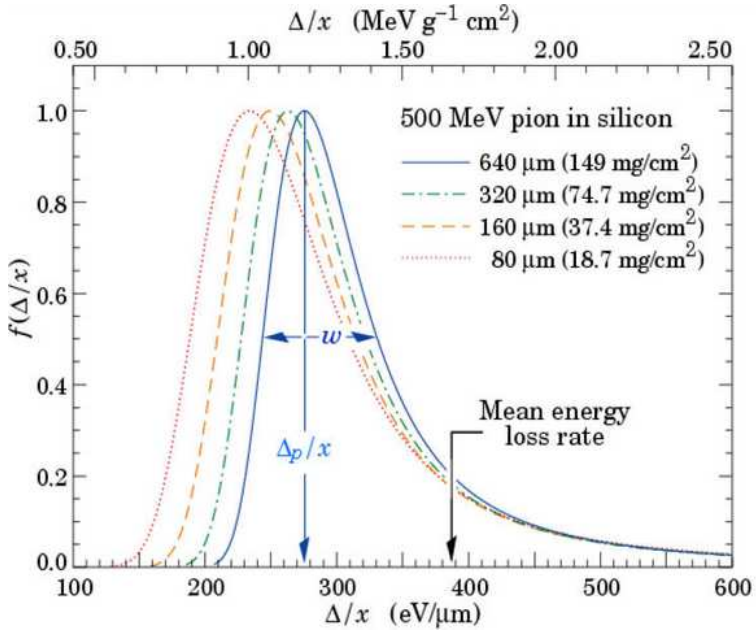

Figure 5.5.: Landau distributions for various thickness of silicon. For reference the ATLAS Pixel Detector sensors are 250 μm, instead the IBL ones are 230 (3D) and 200 (Planars) μm thick [69].

5.2.2. Pixel sensors and Front-Ends electronics

The Pixel Detector is composed by 2024 modules in total, for a total of 92 million pixels. Each module is made of a 16.4×60.8 mm^2 planar n-in-n silicon sensor tile , 250 μm thick, and is connected to 16 front-end (FE-I3) chips (with 2880 pixels each) and 1 Module Control Chip (MCC). In 2014 the Insertable B-Layer (IBL) [70] has been added to the Pixel Detector, it consists of 14 staves (64 cm long, 2 cm wide). Each IBL stave carries and provides cooling to 32 FE-I4 read-out chips, which are bump-bonded to silicon sensors. In the IBL two different silicon sensor technologies are used: planar n-in-n (200 μm thick) and 3D (230 μm thick) [70]. Each IBL stave is populated with planar pixel technology (12 double chip modules) in the central region and 3D technology (8 single chip modules) in the forward region.

When a MIP crosses a silicon pixel sensor $\approx$ 80 electron-hole pairs per micrometer of thickness are generated. The pre-amplifier, as figure 5.6 shows, generates a voltage signal which is proportional to the deposited charge. The feedback capacitor is discharged by a constant current. This causes a linear decrease of the pre-amplifier output signal. The discriminator compares the pre-amplifier output signal to a pre-set threshold, actual (analogical) threshold corresponds to 3500 e, and changes its output state, when the signal exceeds the threshold and when it drops below the threshold. Because of the linear discharge of the pre amplifier, the discriminator has an output signal whose length has an almost linear relation to the signal charge of the hit. Therefore the duration of the discriminator signal (Time Over Threshold) gives a measurement of the analogue pulse height. The output of the discriminator is connected to a fast digital readout operating with a clock of 40 MHz. The readout of the Atlas front end chip is based on a time stamp which is distributed to all the pixels. In case of a hit in one of the pixel, the pixel address, the time stamps of the leading edge and of trailing edge are written to the corresponding RAM cells within the pixel. In this way the

information produced by individual pixels after a hit includes: the address of the pixel, the time at which the hit occurred in units of 25 ns or BC, a measure of the charge of the hit given by the ToT which is calculated as the time difference between the leading and trailing edge of the discriminator output signal. There is an upper limitation of ToT called “Latency”, it is the ToT maximum measured.

When a charged particle crosses a pixels sensor, usually the charge is deposited in more than one pixel. This is due to the incident angle of the particle, to the diffusion of electrons and holes in the sensor and to drift of the charge generated by the particle track owing to magnetic field. Different scenarios of charged particles crossing a silicon sensor with incident angle ϕ are shown in figure 5.7. .

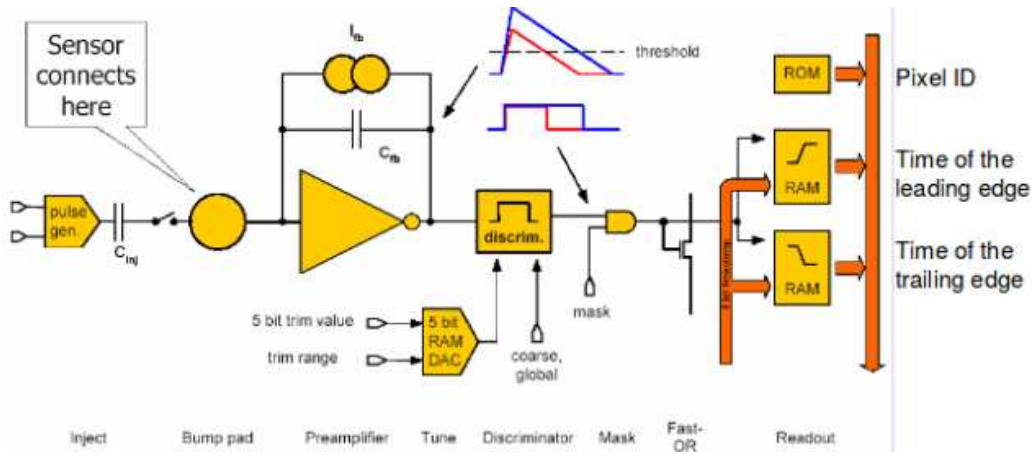

Figure 5.6.: Diagram showing the pixel cell electronics [71].

If two pixels have in common one corner, they are considered neighboring, so a single pixel can be surrounded by, at most, eight cells. A group of connected pixels is defined as a cluster. The information of all the pixels that composes the cluster is used to estimate the position using a linear approximation. The cluster measurements are refined during the fitting of the tracks by using the incident angle and predicted position of incidence on the pixel module of the track associated with the cluster.
The pixel modules can turn inactive due to several reasons[73] which results in changing the shape of the pixel clusters or losing some of them. All these problems affect the track reconstruction, the impact parameter measurement and the vertex performance. Therefore, I studied the impact on the b-tagging performance for such scenarios using Monte Carlo simulated events. Results are presented in chapter 9.

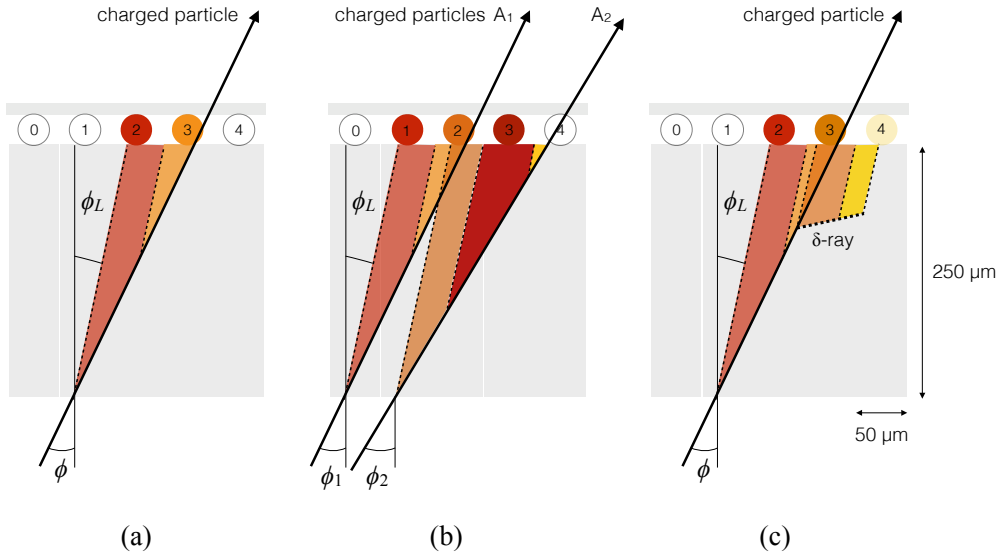

Figure 5.7.: Illustration of cluster sizes in the transverse direction for selected scenarios: (a) a single charged particle crossing the silicon sensor with incident angle, ϕ, producing a cluster with a width of two pixels. The charge drifts due to the electric and magnetic field in the direction of the Lorentz angle $_L$ to the surface. (b) a merged cluster produced by two close-by particles (A1, A2) that both deposit charge in the second pixel. The fourth pixel is not read-out as the charge is below the read-out threshold. (c) a large cluster created from a single charged particle due to a δ-ray produced in the silicon [72].

5.2.3. ToT calibration measurements

The ToT gives measure for the deposited charge and is determined by the pre-amplifier feedback current. The ToT is measured using a global current DAC per FE chip and a DAC in each pixel. If more charge is produced by a passing particle the signal will stay longer above the threshold. This explains the proportional relation between the ToT and the amount of charge which is produced. This relation is determined during calibration runs, where known charge is injected and the ToT is measured. The calibration ToT versus charge curve is parametrized and the parameters are kept in the data base with one curve per FE and not pixel by pixel (i.e.: Tuning for FE-I3: 19000 electrons=30 BC). Then a Gaussian smearing is added to account for differences of pixels belonging to the same FE and every pixel is calibrated per FE.
In figure 5.8 the ToT average versus the injected charge for each pixel of a module with a FE-I4 read-out chip is shown. The relationship between charge and ToT is parametrized by equation 5.4:

$$ToT = a_0 . \frac{(a_1 + Q)}{(a_2 + Q)} \tag{5.4}$$

where a_0, a_1, and a_2 are the parameters of the fit, Q is the deposited charged, and ToT is the average ToT over all the pixels in a front-end. The proportionality is not linear due to secondary order effects like time-walk (delay of the lower charge) and non constant discharge rate.

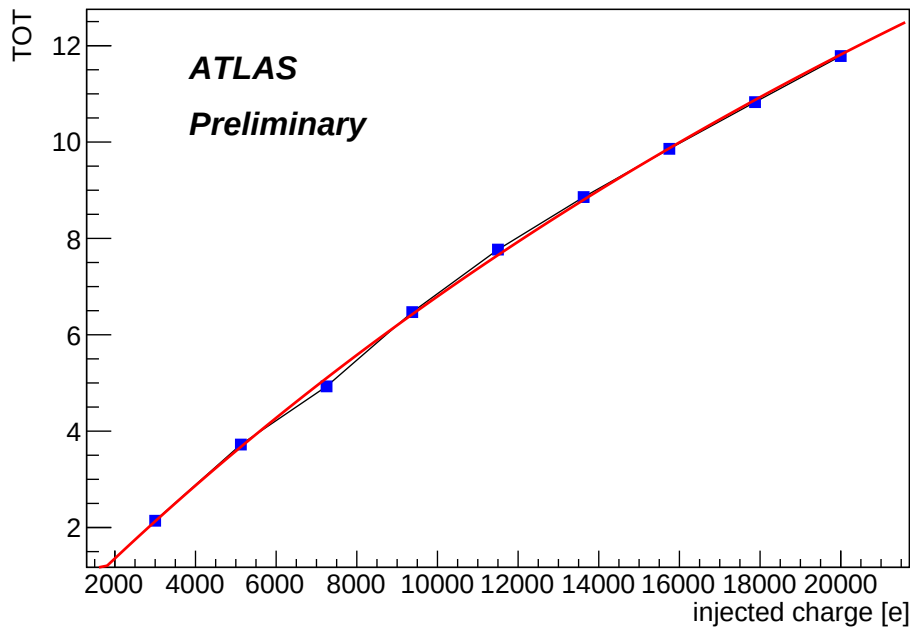

Figure 5.8.: ToT mean values vs injected charge for a FE-I4 module [74]. The mean values are obtained from a ToT scan, the fit is performed with a second order polynomial given in equation 5.4.

Calibration means tuning or determining the best operation parameters for the different parts of the detector mainly FE chips to satisfy some requirements such as detect very small

charges, very reliably and very fast. The problem of hits with small charge is that they suffer time walk which can push them to following BC. In Collision mode, only 1 BC is read for a given trigger. This means that delayed small charges are lost. Thus, there is a recovery FE mechanism, hit duplication, which permit that small hits ($<$ a given threshold) to be duplicated assigned to BC and BC-1.

According to the set threshold, the calibration of the FE-I3 is such that when a MIP crosses 250 μm of the sensor thickness, the ToT Landau peak is set at 18 BC for the B-layer and 30 BC for Layer 1 and 2. In IBL two types of sensors (planars and 3Ds) with different thickness (200 μm and 230 μm respectively) are present, and they are both calibrated to give a ToT Landau peak of 8 BC.

At high luminosity, the number of collision and particles produced will increase, hence the pixel detector specially the B-layer suffers from high occupency which is the number of hits per pixel per event. The main problematic layer is the B-layer being the closest layer as IBL with its special electronic system don't suffer from this issue.

The proposed solutions to reduce the B-layer high occupancy for Run2:

* Reduce the "Latency" with changing the calibration. For Run2, the Latency was decreased from 255 BC in Run1 to 150 BC, the ToT calibration from 30 BC to 18 BC as well (L0 offline ToT cut is defined as the L0 online cut scaled by 30/18).
* Turn off the hit duplication which leads to low charges hits loss.
* Increase the "Digital ToT" which is a Cut applied on the (analogical) ToT

I studied the impact of pixel digital ToT changes on the b-tagging algorithms performance. These studies are based on Monte Carlo simulations events and are presented in chapter 9.

5.3. Calorimeters

Calorimeters are usually designed to stop most of the particles coming from a collision, forcing them to deposit all of their energy within the detector. They typically consist of layers of "passive" and "absorbing" high-density material. The ATLAS calorimeter system, shown in figure 5.9, consists of an electromagnetic calorimeter that measures the energy of electrons and photons, and a hadronic calorimeter that measures the energy of charged and neutral hadrons. They are situated outside the solenoid magnet that surrounds the Inner Detector.

The electromagnetic calorimeter covers $|\theta| > 4.7^\circ$ ($|\eta| < 3.2$), and is divided into a barrel and two end-cap sections. It uses liquid argon as a sampling material and lead plates as absorbents. Its total thickness is about 24 radiation lengths in the barrel and about 26 in the end-caps. The constant term of the energy resolution has been measured to be about 1–3%.

The hadronic calorimeter surrounds the electromagnetic calorimeter and consists of a barrel and two end-cap sections. The barrel covers $|\theta| > 20.7^\circ$ ($|\eta| < 1.7$) and is divided into three sections. It uses scintillators as active material interleaved with steel absorbers. The end-caps cover $|\theta| > 0.9^\circ$ ($|\eta| < 4.9$) and are divided into two sections, called end-cap and forward. Both use liquid argon as the active material and copper and tungsten as absorbents. Its large angular coverage and total thickness of more than 10 hadronic interaction lengths are designed for high-energy jet measurements. Jet-energy scale uncertainties of order 1% or less have been measured.

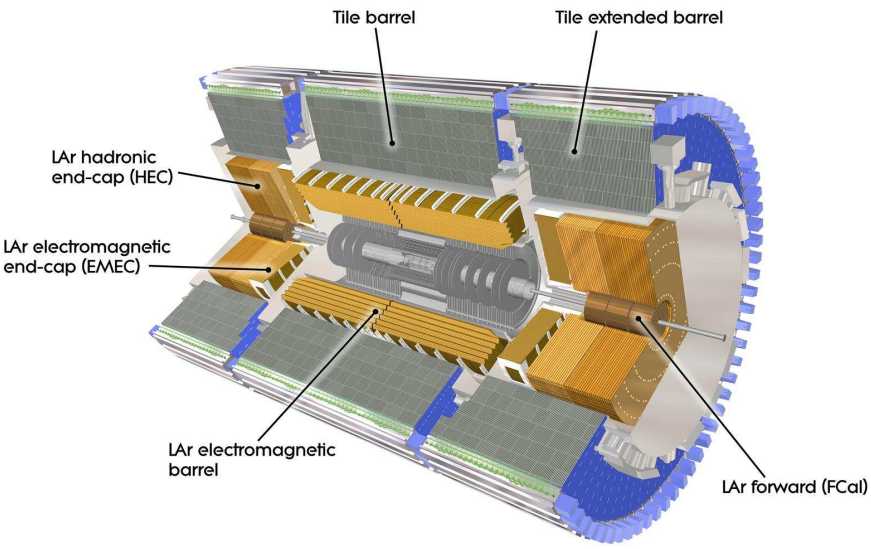

Figure 5.9.: Illustration of the ATLAS calorimeter system [66].

5.4. Muon spectrometer

The muon spectrometer (MS) forms the outer part of the ATLAS detector, its radius R is in the range between 4.5<R<11 m and its length is 46 m. Except neutrinos, high-energy muons are typically the only particles that penetrate through that region. The MS is designed to measure the trajectory of high-momentum muons, and to trigger events containing muons. It covers the region $|\theta|$ >7.7° ($|\eta|$ <2.7) and follows the geometry of the magnet system, as shown in figure 5.10. It provides, independently of the ID, momentum measurements of muons with a relative resolution up to 10% at $p_T = 1$ TeV and muon candidates can be identified in the p_T range between 3 GeV to 3 TeV.
The MS is formed by three concentric barrel layers at 5, 7.5 and 10 m that cover $|\theta|$ >40° ($|\eta|$ <1.0) and three end-cap disk-shaped planes perpendicular to the beam axis at $|z| = 7.4$, 10.5 and 21.5 m that cover 7.7° < $|\theta|$ <40° (1.0< $|\eta|$ <2.7).

The tracking detection is provided mainly by gas drift tube detectors (MDTs), except in the innermost layer of the forward direction where multi-wire proportional chambers (CSC) are used to better handle the higher particle fluency. The required resolution is achieved by optically monitoring the detectors alignment, with an accuracy of 30–60 μm; the achieved single-hit spatial resolution is 60–80 μm in the bending plane. The time resolution is about 700 ns for the MDTs and 7 ns for the CSCs.

Due to the response time of the MDTS, separate triggering capability is provided by gas avalanche detectors: resistible plate chambers (RCPs) in the barrel region and thin gap chambers (TGCs) in the end-cap region. Their design position resolution is about 1 cm and their time resolution is about 2 ns. The RCP and TGCs are an integral part of the trigger system that is explained in section 5.6.

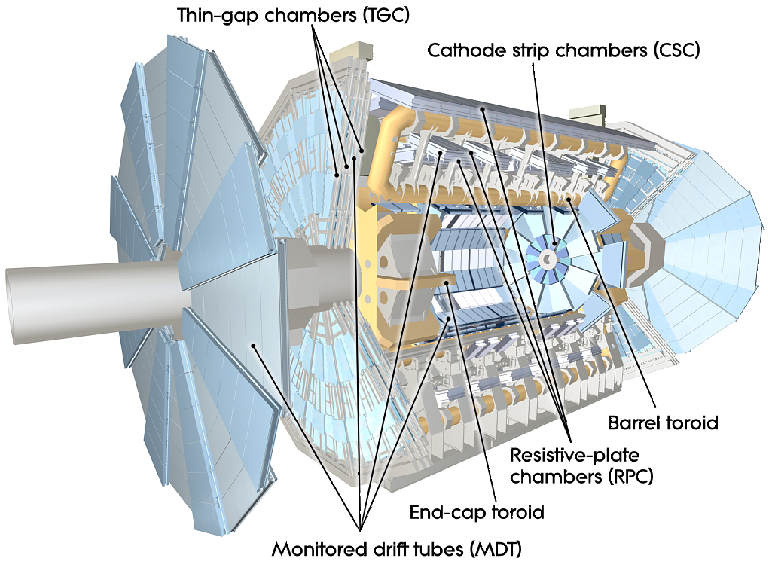

Figure 5.10.: Layout of the ATLAS muon spectrometer. The location of the barrel and end-cap Toroidal magnets is also show [66].

5.5. Forward detectors

The very forward region of ATLAS is occupied with a variety of sub-detectors that serve different purposes. These include: LUCID (Luminosity measurement using Cerenkov Integrating Detector) and BCM (Beam conditions monitor), a Cerenkov and a solid-state detector used to measure luminosity. To measure the luminosity, the ATLAS experiment looks at the number of interactions detected each time the proton beams cross. This is measured by the BCM and LUCID on either side of the interaction point. Luminosity also depends on the overlap of the beams at the collision point, a process that can only be measured by "van der Meer (vdM) scans". Thus, every year, the LHC has a series of special runs to perform vdM scans, named after the accelerator physicist Simon van der Meer who developed the technique at CERN in the 1970s. During these scans, the beams are separated, first vertically and then horizontally, so that the amount by which they overlap varies. When the beams only overlap by a small amount there are few interactions. As the overlap increases, so does the number of interactions. By knowing the separation of the two beams, ATLAS can calibrate the measurements taken by the BCM and LUCID [75].

The forward detectors also include

* ALFA (Absolute Luminosity For ATLAS), a Roman-pot detector used to measure elastic scattering which is challenging because elastically-scattered protons escape the interaction under very small angles of tens of micro-radiant.
* MBTS (Minimum Bias Trigger Scintillators), an array of scintillators used to trigger on minimum-bias events. Minimum Bias events are dominated by non diffractive inelastic interaction (soft interaction).
* ZDC (Zero Degree Calorimeter), a calorimeter used to measure neutron emission in heavy-ion collisions.

5.6. Trigger and data acquisition

The LHC delivers bunch crossings at 40 MHz, which results in a rate of inelastic interactions of about 1 GHz due to the pile-up of multiple proton–proton collisions in the same bunch crossing. Due to the resulting huge data volume, not all of these events can be recorded. The trigger system is a combination of hardware and software used to select events with potentially interesting signatures in real time, and to provide a rejection power of about 10^6 for minimum-bias interactions. It uses information provided by various sub-detectors. A "menu" of different algorithms process that information and decide if the event should be stored. The ATLAS trigger system consists of two levels: the first selection known as Level-1 trigger is entirely implemented in hardware. It uses about 7200 composed signals from the muon spectrometer and the calorimeter system. The Level-1 trigger selects signatures, called "objects", including high$-p_T$ muons or electrons, photons, jets, etc. The trigger logic can be programmed flexibly, such as by requiring different p_T thresholds or various objects in coincidence. The Level-1 trigger reduces the event rate to about 100 kHz with a latency of about 2μs. During this time the data of all channels of the detector are stored in pipelines at the front-end electronics.
The second trigger level is named high-level trigger (HLT) and is software based. It consists of a series of algorithms that use the full granularity of the detector within the "region of interest" defined by the Level-1 (i.e. $\eta\breve{}\phi$ region of objects). The HLT uses reconstruction algorithms that reach similar performance to that of offline analysis and reduces the output rate to about 1 kHz with a latency of about 10 ms. Typically, if an event is selected by an HLT algorithm, the corresponding data are stored to disk. However, to reduce the output rate of certain algorithms a "pre-scale" factor is applied. If the pre-scale factor applied is N, only 1 in N events are randomly selected to be stored. The HLT menu and the corresponding pre-scale factors are typically changed over time to accommodate the observed output rate. However, they are only changed at the end of "luminosity blocks" that are periods of time of about 1 minute.

6. Objects reconstruction

The starting point of any ATLAS physics analysis are the reconstructed and identified objects representing the observed characteristics of the particles resulting from the pp collisions and travelling through the detector. The following sections present an overview of particle identification in the ATLAS detector.

6.1. Tracks and primary vertex

Tracks above a certain p_T threshold are reconstructed offline within the full acceptance range of the ID, with multi-stage track identification algorithms. The inside-out algorithm reconstructs mostly particles produced in the primary p-p collisions. The tracks are seeded in the pixel detector (three seeds) and the hits from the neighboring SCT layers are added. The track candidates found in the silicon detectors are then extrapolated to include measurements in the TRT. The outside-in algorithm starts from segments reconstructed in the TRT and extends them inwards by adding silicon hits not yet used by inside-out tracking. It reconstructs secondary charged tracks (i.e. photon conversions, material interactions). Reconstructed tracks are selected by applying quality criteria for typical physics analyses:

* The loose tracks have $|p_T| >$ 400 MeV, $|\eta| <$2.5, number of silicon hits $\geq$7, number of shared modules $\leq$1, number of silicon holes $\leq$ 2, number of pixel holes $\leq$1.
* The tight primary tracks, in addition to the Loose selection requirements have number of silicon hits $\geq$ 9 if $|\eta| \leq$ 1.65, number of silicon hits $\geq$11 if $|\eta| \leq$ 1.65, at least one hit on the two innermost pixel layers, and no pixel holes.

The reconstructed tracks are specified by their azimuthal and polar angles, ϕ and θ, the charge over momentum ratio, q/p, and the impact parameters d_0 and z_0, the minimal transverse and longitudinal distance with respect to the center of the detector. These track parameters are used in the track to jet association as will be seen in section 8.2. The tracking efficiency for primary tracks in 2015 for tracks above 5 GeV remained high, as figure 6.1 shows: 90% for loose and 85% for tight primary selections.

Then, the proton–proton interaction vertices in an event are found by an iterative vertex finding algorithm [77]. Vertex candidates are fitted with a χ^2 fit, taking into account the compatibility of tracks with the vertex candidate. The initial vertex position is taken from the transverse beam position and the global maximum of the z-coordinates of all reconstructed tracks. Tracks not compatible with a vertex are removed and the fit is iterated. All rejected tracks are then used as an input to find further vertex candidates. The vertex with the highest sum of squared transverse momenta of all associated tracks is taken to be the primary interaction vertex. It is required to have at least two associated tracks with $p_T >$ 400 MeV. The secondary vertices reconstruction will be discussed in part III.

6.2. Jets

To cluster particles belonging to the same jet, the anti-k_t algorithm [78] with radius parameter R= 0.4 is used. The input is the positive-energy topological clusters (topoclusters) of the calorimeter cell energies. The uncertainty of the jet energy scale (JES) is the dominant

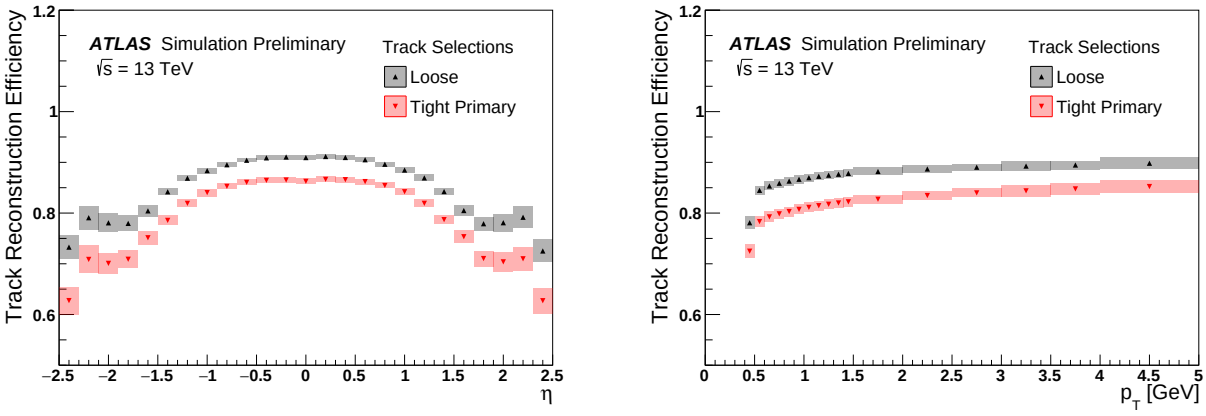

(a) (b)

Figure 6.1.: Track reconstruction efficiency in 2015 [76].

experimental uncertainty and an estimate can be derived by in situ measurements. The energy and direction of reconstructed jets are corrected by a EM+JES calibration scheme of the jet p_T and η. The first step is an offset pile-up correction derived from in-situ measurements to account for pile-up contribution to the topoclusters. The second step corrects the jet 4-vectors to move the jet origin from the ATLAS detector center to the primary vertex coordinates. Finally the energy and direction of reco-jets are corrected by constants derived from the comparison of the reco-jet kinematic to the one of truth-jet which denotes the jet formed from stable truth- particles generated in MC samples

6.3. Electrons and photons

The electron identification is based on a likelihood combining the electromagnetic calorimeter showers, tracking, track-cluster matching and TRT particle-identification to separate isolated electrons. Several input variables are used in particular, the number of IBL hits which serves for discriminating between electrons and converted photons. Three working points are defined cutting on the likelihood score, the loose, medium and tight working points. The combined reconstruction and identification efficiency in Z→ee events is shown in figure 6.2(a).

The photon identification uses the same ingredients as for electron but uses a set of cuts rather than a likelihood. Two working points are provided: loose and tight. The tight working point is separately tuned to differentiate converted and unconverted photons.

6.4. Taus

In ≈ 35% of the cases the τ-lepton will decay in a lepton and two neutrinos and in ≈ 65% of the cases the τ-lepton decays hadronically with an accompanying neutrino. The leptonically decaying taus would be identified as an electron or a muon associated to a track not pointing towards the primary vertex and with missing energy. However due to their short traveled

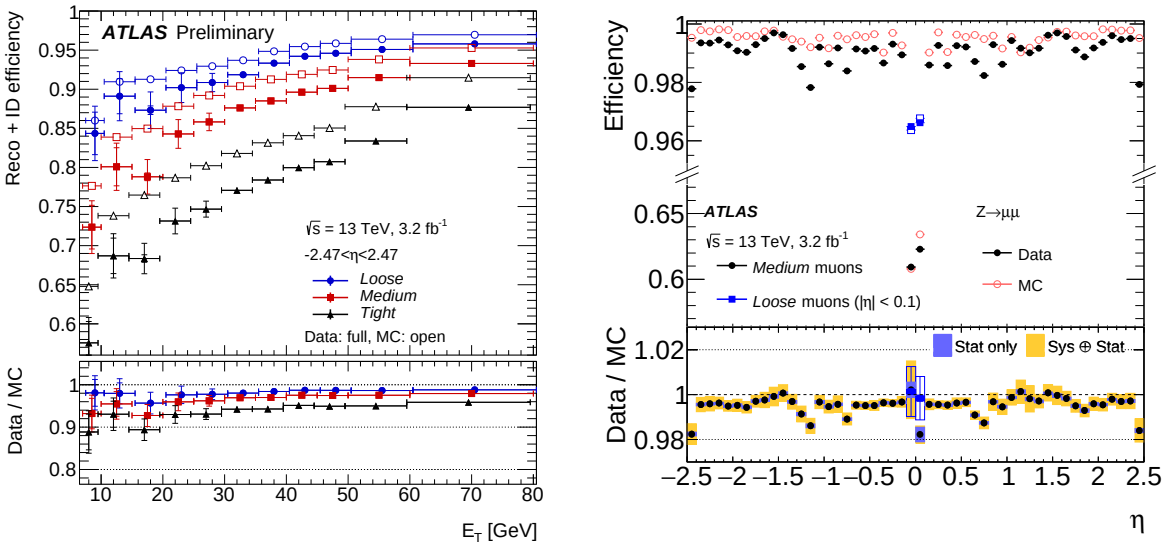

(a) (b)

Figure 6.2.: (a) Combined electron reconstruction and identification efficiency in Z→ee events as a function of the transverse energy E_T [79]. (b) Reconstruction efficiency of muons at the loose and medium identification working points as a function of η comparing Run2 data and simulations in Z→ $\mu\mu$ events [176].

distance, taus decaying to electrons or muons are very difficult to differentiate from prompt-leptons and are not reconstructed. The hadronically decaying taus are narrow jets with low track multiplicity. They are identified using boosted decision tree to distinguish them from q/g jets and electrons, the performance is evaluated using Z→ $\tau\tau$ candidates.

6.5. Muons

Muons are reconstructed using information from the ID, MS and calorimeter sub-detectors. Four types of muons are defined: combined (CB) muons, segment-tagged (ST) muons, stand-alone (SA) muons, and calorimeter-tagged (CT) muons. The CB muons are reconstructed by combining tracks in the MS to matched tracks in the ID. The ST muons are reconstructed from tracks in the ID matched to at least one local track segment in the MS. The SA muons are reconstructed only in the MS. The CT muons are reconstructed from tracks in the ID matched to an energy deposit in the calorimeter compatible with a minimum ionizing particle. To discriminate muon tracks coming from prompt muons against muon tracks induced by particles escaping the inner parts of the ATLAS detector an identification procedure is applied. Four identification working points are provided to the analyses using basic muon quality cuts: medium, loose, tight and high p_T muons. Figure 6.2(b) illustrates the outstanding performance of the muon reconstruction and identification, it shows the high muon identification efficiency.

6.6. Missing Transverse Energy

Physical missing energy is generated by particles escaping the detector. The initial partons energy being unknown the full missing energy computation is impossible. However since pp collisions are produced along the z -axis, initial partons can be assumed to have a negligible momentum in the transverse plane. The Missing Transverse Energy, noted MET or $\mathrm{E_T^{miss}}$, is then accessible requiring momentum conservation.

The $\mathrm{E_T^{miss}}$measurement is based on objects reconstructed in the EM and hadronic calorimeters as well as muons. For all physics objects a $\mathrm{E_T^{miss}}$term is computed as the vectorial negative sum of all transverse momenta. An additional term is added to account for soft emission using ID tracks matching the HS-PV and not associated to any physics object.

7. Production of Monte Carlo samples

7.1. Introduction

The large data set collected by ATLAS needs to be complemented with a sufficient number of Monte Carlo (MC) events for Standard Model measurements and new physics searches. MC events are used in data analysis in many different ways mainly to estimate the backgrounds, the selection efficiencies, to study systematic effects from detector or pile-up mis-modeling, or to verify data-driven background estimation methods.
The challenges encountered in MC production have different origins: one is the grid, which provides large number of uniform processing slots with limited running time, memory, local and global disk space. Another one are requirements from physics. On one side more MC events are always useful, which can be achieved by reducing running time. On the other side the produced MC events need to reflect accurately the conditions from data taking.
In this chapter we will review the ATLAS Monte Carlo production setup including the different production steps involved in full and fast detector simulation. This multi-step process shown in figure 7.1 includes the event generation, the detector simulation, the digitization and the reconstruction.

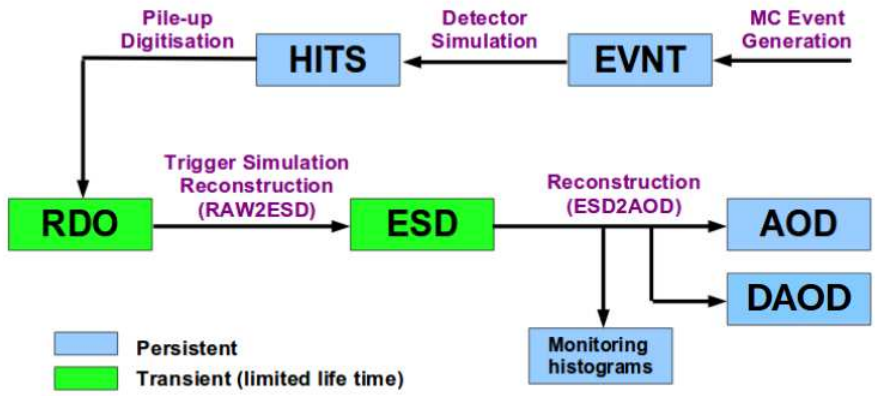

Figure 7.1.: ATLAS Monte Carlo Simulation Flow [80].

7.2. Monte Carlo production steps

7.2.1. Event generation

Event generation is the simulation of the interaction between the quarks and gluons in the colliding protons, the subsequent parton showering and hadronization and decays into stable particles. As the name indicates, the output of an event generator should be in the form of events. A typical hadronic event generator simulates the following sub-processes:

* Initially two protons are coming in on a collision course, each with a partonic flux given by the Parton Distribution Functions (PDFs).

* A collision between two partons, one from each side, gives the hard process of interest, characterized by the relevant matrix elements (MEs). These usually are leading order (LO) or next-to-LO (NLO), increasingly also next-to-NLO (NNLO).
* When short-lived "resonances" are produced in the hard process, such as the top, $W^{\pm}$, Z^0 or H^0, their decay has to be viewed as part of this process itself.
* A collision implies accelerated charges, and thereby bremsstrahlung. This can be described in terms of Parton Showers (PSs), usually split into Initial-State Radiation (ISR) and Final-State Radiation (FSR).
* Since PSs describe the same physics as higher-order MEs do, they must be combined consistently, with PSs adding multiple softer emissions not covered by the fixed-order hard MEs, without gaps or overlaps. This is called matching and merging (M&M), where matching is the procedure to obtain a smooth transition for a fixed parton multiplicity and merging the combination of several multiplicities, but often the two aspects are intertwined [81].
* Finally, the hadronization, the partons produced are combined in hadrons and unstable hadrons are further decayed to stable particles.

Around 30 different MC generators are in use in ATLAS. The standard multi-purpose MC generators, such as PYTHIA6 and 8 [82] [83], HERWIG, HERWIG++ [84] [85] and Sherpa [86], are fully integrated into the ATLAS software framework. Other MC generators, such as Alpgen and MC@NLO [87], provide only 4-vectors of the hard process. The hadronisation is done in the ATLAS framework using PYTHIA6, PYTHIA8, HERWIG or HERWIG++.

7.2.2. Detector simulation

The detector simulation is the calculation of how the particles from the generator interact with the detector material, how they shower into secondaries and how much energy they deposit in each sensitive element. At this step, all stable particles from the event generation are tracked through the ATLAS geometry. The ATLAS detector simulation is based on Geant4 [88], it has proven to be reliable and accurate for a wide range of particle types, energies and detector materials. Different approaches have been developed to speed up the detector simulation. One of these is improving the Calorimeter Simulation, being the most time-consuming part of the simulation step, because particles are stopped in the calorimeter followed by generation of secondary particle showers. The ATLAS Fast Calorimeter Simulation (FastCaloSim) uses a parameterisation based on the Geant4 simulation of single particles in a fine grid of particle energies and directions, which allows the bypassing of the shower generation step, directly obtaining the energy released in calorimeter cells. FastCaloSim in conjunction with Geant4 (referred to as ATLFASTII) allowed to reduce simulation time by a factor of 10 or more.

7.2.3. Digitization and reconstruction

The digitization turns the simulated energy deposits into a detector response, that similar to the raw data from the real detector, producing RDO files. At this step the response of the readout electronics is simulated. In addition, the effect of multiple pp interactions per bunch crossing (pile-up) is simulated. After this step, the MC processing steps are the same as for real data.

The simulated MC events are reconstructed in the same way as data recorded by the ATLAS detector. In addition, the trigger system is simulated. The main reconstruction process produces the Event Summary Data (ESD), which contains low level quantities as tracks and clusters and high level quantities as jet, electron, photon, muon and tau candidates. In a second, fast step the Analysis Object Data (AOD) is produced, which contains mainly high level information.

7.3. Production campaign

MC production is divided into campaigns, where the center-of-mass energy, geometry and conditions used in the production correspond to a running period of the LHC. Major campaigns correspond to the calendar year. Minor campaign versions usually reflect improvements in reconstruction software, trigger menu or pile-up simulation. In contrast to data taking and reprocessing campaigns, MC campaigns are run as long as MC events are needed for data analysis. In this thesis, the two MC campaigns used are MC15 and MC16.

Part III.

Identification of b-flavoured-jets

8. b-tagging in ATLAS in Run2

The identification of jets containing B-hadrons, called b-tagging, plays a significant role in many analysis at the LHC, both in searches for new physics and in further studies of the SM, in particular in the Higgs searches, as $h \to b\bar{b}$ dominates the total width (58%). The b-tagging in ATLAS relies on low level algorithms which extract the B-hadron properties discussed in section 8.1 from the tracks associated to the jets. The tracks association to jets procedure is presented in section 8.2, while section 8.3 describes the b-tagging algorithms and their respective performance. On the other hand, section 8.4 describes my studies of the treatment of V^0 for the IP3D b-tagging algorithm aiming to improve its performance.

8.1. B-hadrons properties

B-hadrons are rather unique in particle physics. They are heavy particles, with rest masses of $\approx$ 5-10 GeV/c^2, or roughly 5 to 10 times the proton's rest mass. B-hadrons are also long lived particles, with mean life-times of $\approx$ 1.6 ps. For comparison, the π^0 meson has a life time of $\approx 8.10^{-5}$ ps and the top quark has even shorter lifetime of $\approx 10^{-11}$ ps. Because of this long life-time, a B-hadron has a flight path, cτ, of $\approx$ 480-500 μm, τ being the B-hadrons's mean life-time and c is the speed of light. In other terms, a B-hadron will travel roughly half a mm before it decays. So a B-hadron with $p_T = 50$ GeV and mass= 5 GeV, will have a significant mean flight path $\beta\gamma c\tau$ and will travel on average about 3 mm in the transverse direction before decaying. Also, a B-hadron produces high number of charged particles per decay and there is $\approx$ 36% chance that a lepton will be produced during the decay process.

Hadrons are mainly produced in clustered collimated group within the detector, known as jets. What causes this clustering/jet is the fact that quarks/gluons cannot exist freely in nature, thus quarks, anti-quarks use some of their kinetic energy to pull other quarks/anti-quarks out of the vacuum to form hadrons, this is called hadronization. All this creates a jet. A b-jet is a jet having at least one B-hadron inside of it. Due to the hard fragmentation function of b-quarks , in contrast to light partons, the B-hadron receive in general $\approx$ 80% of the energy of the originating b-quark. The B-hadron energy is thus expected to contributes to 80% of the b-jet energy as shows figure 8.1(a).

Since a B-hadron has a long lifetime, and travels a measurable distance before decaying, the tracks formed by its decay products create a secondary vertex (SV) displaced from the primary interaction vertex (PV) as illustrated in figure 8.1(b). The tracks associated to the SV are characterized by a large invariant mass and large impact parameters (IP). IP stands for the distance from the point of closest approach of the track with respect to PV.

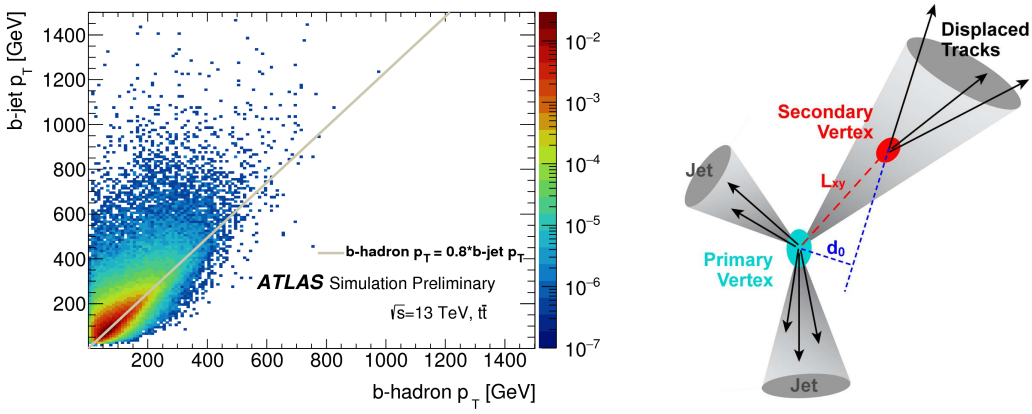

(a) (b)

Figure 8.1.: (a) The b-jet p_T as function of the B-hadron p_T. (b) A sketch of the b-jet decay products: displaced tracks and secondary vertex. Large impact parameter (d_0) tracks and a significant flight path length (L_{xy}) of the B-hadron are shown [89].

8.2. b-tagging ingredients

8.2.1. Tracks association to jet

Tracks are the most important input for b-tagging. The track-to-jet association is based on the angular distance between the jet and tracks, ΔR(track, jet). Since the decay products of high p_T particle are more collimated than the ones of low p_T particles, the cut value in the distance ΔR depends on the jet p_T as expressed by the equation 8.1, resulting in a smaller cone for jets at high p_T.

$$\Delta R\,(p_T) = a_0 + e^{a_1 + a_2 p_T} \tag{8.1}$$

where a_0 = 0.239, a_1 = -1.22 and a_2 = -1.64 $\cdot 10^{-5}$ (MeV^{-1}). The value of the coefficients a_i are optimized in order to collect on average 95% of the B-hadron decay products in the associated jet while minimizing the background track contamination (such as pile-up tracks described in 4.2). For a jet p_T of 20 GeV, the Δ R cut is 0.45 while for a jet with a p_T of 150 GeV the ΔR cut is 0.26 [90].

8.2.2. Events, jets and tracks selection

The determination of the position of the PV in each event is particularly important for b-tagging, since it defines the reference point with respect to which IP and vertex displacements are expressed. The PV is reconstructed using the adaptive multi-vertex finding algorithm, as described in section 6.1.

The tagging is performed on jets reconstructed by clustering energy deposits in the calorimeter with the anti-k_t algorithm (discussed in section 6.2) and a radius parameter of 0.4. Only jets with $p_T > 20$ GeV and $|\eta| < 2.5$ are considered. An algorithm referred to as the jet vertex tagger (JVT) [91], is used to reject jets from pileup. Jets with $p_T < 50$ GeV and $|\eta| < 2.4$ are rejected if they have a JVT output of less than 0.641.

Once associated with a jet, tracks are subject to specific requirements depending on each b-tagging algorithm. These requirements include cuts on the track p_T , the transverse and longitudinal impact parameters and number of hits in the pixel detector. The track selection depends on each specific b-tagging algorithm as shown in table 8.1. For the impact parameter based algorithm (IP2/3D), a tight selection is applied, while for the secondary vertex based algorithms (SSVF and JetFitter) a looser selection is used, relying on the secondary vertex reconstruction to provide additional purity.

Table 8.1.: The Run 2 track selection criteria for the main b-tagging algorithms.

Parameter	IP2/3D	SSVF	JetFitter
p_T (GeV)	> 1	> 0.7	> 0.5
$\|d_0\|$ (mm)	<1.0	<5.0	<7.0
$\|z_0 sin\theta\|$ (mm)	<1.5	<25	<10
Number of IBL hits	≥ 1	≥ 0	≥ 0
Number of pixel hits	≥ 1	≥ 1	≥ 1
Number of SCT hits	≥ 0	≥ 4	≥ 4
Number of pixel/SCT hits	≤ 7	≤ 7	≤ 7
Number of shared hits	≤ 1	≤ 1	≤ 1
Number of pixel holes	≤ 1	≤ 1	≤ 1
Number of pixel/SCT holes	≤ 2	≤ 2	≤ 2

8.2.3. Jet truth labeling

To estimate the b-tagging performance, it is necessary to know the truth flavour of the particles that jets originate from. To accomplish this, a procedure referred to as jet labeling is performed. Jets are matched to truth particles from the MC simulation with $p_T > 5$ GeV if the spatial distance between them is $\Delta R < 0.4$. The matching is done exclusively. If a B-hadron is found within the cone of $\Delta R < 0.4$ of a jet this jet is labeled as a b-jet. If no B-hadron is found, the matching algorithm searches for c-hadrons, and then, if a c-hadron is also not found, for τ-leptons. If none of these particles are found, the jet is labeled as a light jet.

8.2.4. Performance in simulation

The performance of a b-tagging algorithm characterizes its power to separate b-, c- and light-jets. Hence, it is represented as the efficiency with which a jet containing a true B-hadron is tagged by a b-tagging algorithm and the probability of mistakenly tagging a true c-jet or a true light-flavour parton (u-,d-,s-quark or gluon g) jet as a b-jet. These are referred to as b-jet tagging efficiency "ϵ_b", c-rejection "R_c" and light-rejection "R_u". R_u (R_c) is the inverse of the mis-tagging efficiency which is the fraction of jets labeled as light- (c-) jets and tagged as b-jets. The performance of the tagging algorithms is estimated in large samples of simulated $t\bar{t}$ events. The b-jets come from the top quark decays, they have average p_T, $\langle p_T \rangle = 57$ GeV.

8.2.5. Impact parameters definition

The tracks from B-hadron decay products tend to have large impact parameters which can be distinguished from tracks stemming from the PV as mentioned in section 8.1. The transverse impact parameter, d_0, is the distance of closest approach of the track to the PV point, in the r,ϕ projection, while the longitudinal impact parameter, z_0, is the difference between the z coordinate of the PV position and of the track at this point of closest approach in r-ϕ. Given that the decay point of the B-hadron must lie along its flight path, d_0 and z_0 are signed to further discriminate the tracks from B-hadron decay from tracks originating from the PV. d_0 and z_0 signs are expressed by the equations 8.2 and 8.3.

$$sign(d_0) = sign[(\vec{P_{jet}} \wedge \vec{P_{trk}}).(\vec{P_{trk}} \wedge (\vec{X_{PV}} - \vec{X_{trk}}))] \tag{8.2}$$

$$sign(z_0) = sign[(\eta_{jet} - \eta_{trk}).z_{0,trk}] \tag{8.3}$$

The sign is positive if the track intersects the jet axis in front of the PV, and negative if the intersection lies behind the PV. The experimental resolution generates a random sign for the tracks originating from the PV, while tracks from the b- and C-hadrons decay normally have a positive sign. Decays of V^0 e.g. K_s^0 and Λ^0 also produce tracks with positively signed impact parameters, enhancing the probability to identify light flavour jets as b-jets.

8.3. ATLAS Run 2 b-tagging algorithms

Several algorithms to identify jets containing B-hadrons are described in this section, ranging from those based on the presence of tracks with large impact parameters (section 8.3.1) or based on the reconstruction of an inclusive SV (section 8.3.2) to combined tagging algorithms making use of multi-variate (MV) discriminants (section 8.3.3).

8.3.1. Impact parameter based algorithms

IP2D and IP3D are tagging algorithms which exploit the impact parameters properties. IP2D relies on d_0 significance of tracks, $\frac{d_0}{\sigma_{d_0}}$), where σ_{d_0} is the uncertainty on the reconstructed d_0, while IP3D uses the z_0 significance ($\frac{z0}{\sigma_{z_0}}$) as well which makes it more powerful than IP2D but also less robust against pile-up.
These algorithms are based on a log-likelihood ratio (LLR) method in which for each track the measurement S=($\frac{d_0}{\sigma_{d_0}}$,$\frac{z0}{\sigma_{z_0}}$) is compared to pre-determined two-dimensional probability density functions (PDFs) obtained from simulation for the b- c- and light-jets hypotheses. The ratio of probabilities defines the track weight as expressed by equation 8.4.

$$W_{\text{IP3D}} = \log\left(\frac{p_b}{p_u}\right) \tag{8.4}$$

The probabilities p_b, p_u are the track template PDF for the b- and light-flavour jet flavour hypotheses. The jet weight is the sum of the per-track contributions (the track weight).
If no tracks are found in the jet, a negative value of -20 is assigned as the algorithm output [92]. The LLR formalism allows track categories to be used by defining different dedicated PDFs, for each of them. For the Run 2, the tracks are distributed into 14 categories depending on the track quality defined by the hits in the silicon layers. These categories are listed in

table 8.2. The transverse signed impact parameter significance of tracks in $t\bar{t}$ events for b-, c- and light-flavoured jets for the "Good category" is shown in figure 8.2(a), while figure 8.2(b) shows the log-likelihood ratio for IP3D.

Table 8.2.: Description of the Run2 track categories used by IP2D and IP3D

#	Description
0	No hits found in IBL and L0; some expected in both
1	No hits found in IBL and L0; some expected in IBL not in L0
2	No hits found in IBL and L0; some expected in L0 not in IBL
3	No hits found in IBL and L0; hits not expected in both
4	No hits found in IBL; some expected in IBL
5	No hits found in IBL; hits not expected in IBL
6	No hits found in L0; some expected in L0
7	No hits found in L0; hits not expected in L0
8	Shared hits found in both IBL and L0
9	Shared hits found in other layers
10	More than one shared SCT hits found
11	Split hits found in both IBL and L0
12	Split hits found in both IBL and L0
13	Good (not in any of the above categories)

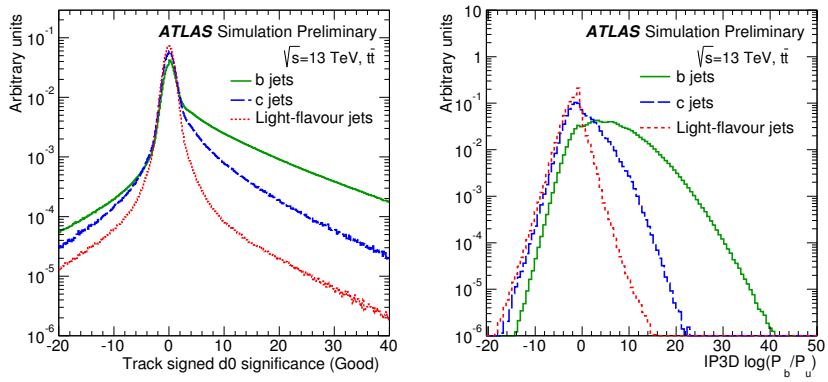

(a) (b)

Figure 8.2.: (a) The transverse signed impact parameter significance of tracks for b- (solid green), c- (dashed blue) and light-flavour (dotted red) jets for the "Good category". (b) The log-likelihood ratio for IP3D for b- c- and light jets .The MC sample used is $t\bar{t}$ [92].

8.3.2. Secondary vertex based algorithms

SSVF and JetFitter are vertex algorithms which aim at reconstructing the B-hadron displaced secondary vertex in the jet.

The SSVF algorithm reconstructs one secondary vertex per jet, using a selected set of the

tracks associated to the jet as mentioned in table 8.1. Tracks are first used to reconstruct two-track vertices.

Then, the vertex mass is used to reject vertices that are likely to originate from long lived particle decays (e.g: K_s^0, Λ^0) and photon conversions, while the position of the vertex in the r, ϕ projection is compared to a simplified description of the innermost pixel layers to reject secondary interactions in the detector material.

All tracks from the remaining two-track vertices are combined into a single inclusive vertex.

The flight length significance, shown in figure 8.3(a), is defined as the distance between the primary vertex and the inclusive secondary vertex divided by the measurement uncertainty and is the discriminating observable on which the SV tagging algorithm relies. The significance is signed with respect to the jet direction, in the same way as the transverse impact parameter of tracks is (see section 8.2.5).

SV1 is another tagging algorithm based on the same secondary vertex finding infrastructure, but it provides a better performance as it is based on a likelihood ratio formalism, like the one explained previously for the IP3D algorithm in section 8.3.1. Four of the vertex properties are exploited:

* The vertex mass shown in figure 8.3(b) which is the invariant mass of all charged-particle tracks used to reconstruct the vertex assuming that all tracks are pions.
* The ratio of the sum of the energies of these tracks to the sum of the energies of all tracks in the jet.
* The number of two-track vertices.
* In addition, the Δ R between the jet direction and the direction of the line joining the primary vertex and the secondary vertex is used in the LLR.

As is typical for secondary vertex tagging algorithms, the mistag rate is much smaller than for impact parameter-based algorithms, but the limited secondary vertex finding efficiency, of $\approx$ 70%, can be a drawback.

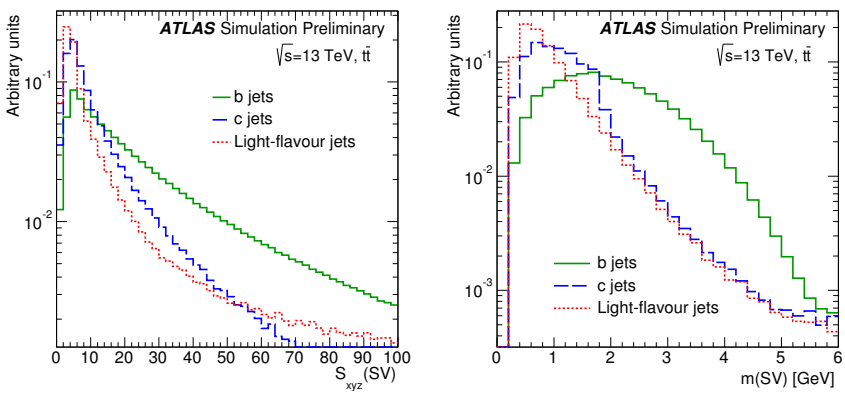

(a) (b)

Figure 8.3.: Properties of secondary vertices reconstructed by the SV algorithm for b-, c- and light-flavour jets in $t\bar{t}$ events: (a) the 3D decay length significance, (b) the invariant mass of tracks associated wih the vertex [92].

On the other hand, the JetFitter algorithm aims to reconstruct the full PV to b- to c-hadron cascade decay topology. It assumes that the PV and both b- and c-hadron decay vertices

are placed along one line, approximating the B-hadron path. A Kalman filter [93] is used to find such a common line and the positions of vertices on it. First, track candidates are used to build single-track vertices along the jet direction. Then vertices are merged two by two in decreasing order of probability to originate from the same vertex using a clustering algorithm. JetFitter allows to separate b- and c-hadron vertices even if only one track is attached to each of them and its secondary vertex reconstruction efficiency for b-jets, c-jets, and light-jets in $t\bar{t}$ simulated events is shown in figure 8.4.

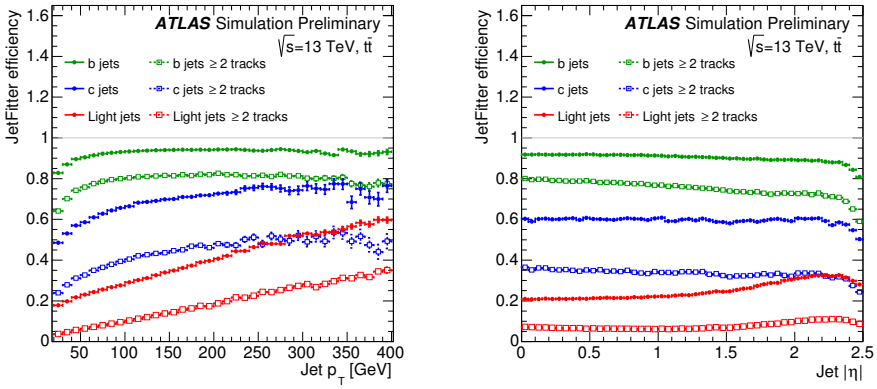

(a) (b)

Figure 8.4.: JetFitter secondary vertex reconstruction efficiency for b-jets, c-jets, and light-jets in $t\bar{t}$ simulated events at $\sqrt{s} = 13$ TeV as function of jet p_T (a) and jet $|\eta|$ (b) [1].

8.3.3. MVX algorithms

The reconstructed SV properties and the IPxD LLRs are combined in a multivariate-based algorithm (MVA) providing the final b-tagging discriminant. This final MVA provide the best separation between b-jets and other jet flavours. In Run 1, the output of the three taggers discussed above were used: IP3D output, SV1 output and JetFitterCombNN which is a neural network (NN) combining IP3D and JetFitter. “MV1” tagger is the name given to the NN trained exclusively against the light-jet background. An alternative, “MV1c”, tagger is also developed including c-jets in the training.

For Run 2, the MV1 was optimized. The IP3D LLRs are directly combined to the properties of the SSVF and JetFitter SVs in a Boosted Decision Tree (BDT) called “MV2” combining in total 24 input variables. Three alternatives of the MV2 taggers are available “MV2c00”, “MV2c10”, “MV2c20” differing on the fraction of c-jets included in the training. These fractions are respectively: 0%, 7% and 15% while the rest are light-jets. MV2c10 is the official/recommended algorithm for the physics analysis at Run2. The MV2c10 BDT output for b-, c- and light-flavour jets evaluated with $t\bar{t}$ events is shown in figure 8.5(a), while a comparison between MV2c20 and MV1 light jet rejection at 70% b-jet effiency as function of jet p_T is shown in figure 8.5(b).

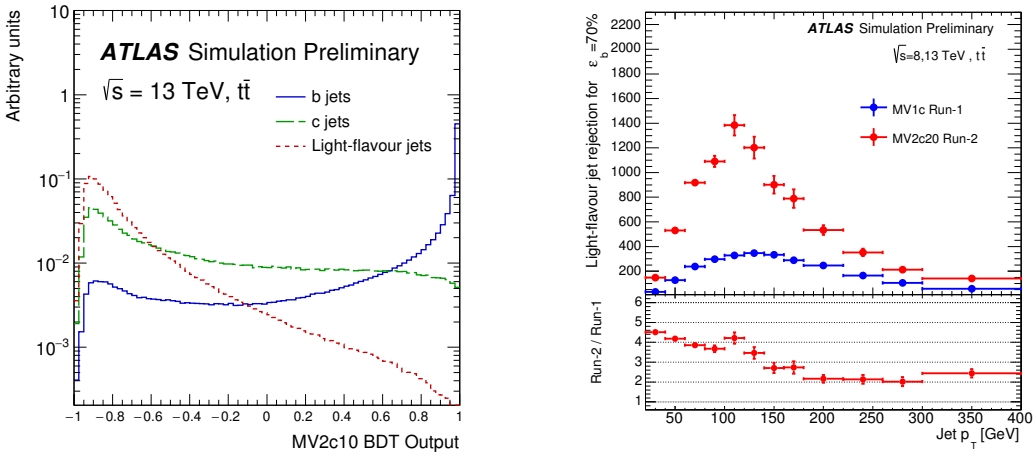

(a) (b)

Figure 8.5.: (a) MV2c10 BDT output for b- (solid blue), c- (dashed green) and light-flavour (dotted red) jets evaluated with $t\bar{t}$ events. (b) A comparison between MV2c20 and MV1 light jet rejection at 70% b-jet efficiency as function of jet p_T [1].

8.4. V^0-tracks reconstruction in jets

8.4.1. Motivation

V^0 are heavy, unstable particles, which decay into a pair of daughter particles. The most frequent are: Λ^0, $\bar{\Lambda}^0$, K_s^0. Being neutral, V^0 particles do not interact electromagnetically, and they do not create tracks in the detector. Instead of that, we detect their daughter particles which are charged and stable. K_s^0 decays to a π^+ and π^- with a branching fraction of $\approx$ 69.2%. The K_s^0 daughter, π^+ (π^-), decay to $\mu^+\nu_\mu$ ($\mu^-\bar{\nu}_\mu$) with branching fraction of $\approx$ 1. The other 30.8% of K_s^0 decay to 2 π^0, those decays are not very interesting, because the daughter particles are again neutral.
The V^0, decay to one positively and one negatively charged particle occurs via W^{*+} or W^{*-} Bosons as illustrated in figure 8.6. Due to this quark Flavour-Changing-Charged-Current, the V^0 particles have a relatively long lifetime as shown in table 8.3.

Table 8.3.: V^0 mean life time and flight path.

Particle	lifetime (s)	c.τ (cm)
Λ^0	$(2.631 \pm 0.020).10^{-10}$	7.9
$\bar{\Lambda}^0$	$(2.631 \pm 0.020).10^{-10}$	7.9
K_s^0	$(8.953\pm0.005).10^{-11}$	2.7
$\bar{K}_s^0$	$(8.953\pm0.005).10^{-11}$	2.7

As V^0 lifetime is close to the B-hadrons lifetime mentioned in section 8.1, tracks from V^0 decaying in light jets look like tracks from B-hadron decay, they acquire large impact parameters. Using these tracks in the IP3D jet weight computation, contributes to mistagging

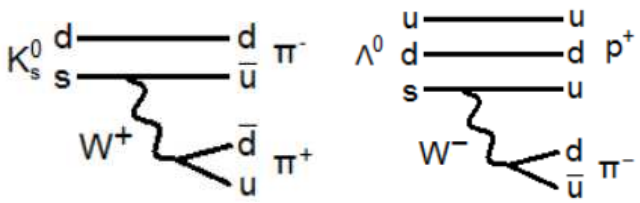

Figure 8.6.: Feynman diagrams of K_s^0, Λ^0 weak decays.

a light-jet as a b-jet. Thus, these tracks are flagged as "bad tracks" by SV1 as described in section 8.3.2 and rejected for IP3D weight computation. This introduce an inefficacy for tagging the true b-jets including V^0 correctly, as tracks from the V^0 decay in the b-jets are discarded. Therefore, I reconstructed the neutral-parent V^0-track and I studied the impact of using the newly reconstructed V^0-track on top of rejecting the 2 V^0 daughters tracks.

In data, a V^0 can be reconstructed if 2 "SV1 bad tracks" with opposite charges form a vertex of mass close to one of a known V^0 masses. Using the reconstructed vertex position and the momentum vector, a linear neutral track for the V^0 is drawn and used in the IP3D jet weight calculation. The impact parameters d_0 and z_0 of the new track are computed with respect to the PV. Their resolutions, $\sigma(d_0)$ and $\sigma(z_0)$, are computed as functions of the V^0 p_T and radius.

In this study, only the reconstruction of K_s^0 is done, being more frequent in b-jets than in light-jets. Using the truth information, the highest improvement on IP3D-b-tagging-performance expected is estimated. On the other hand, the efficiency of reconstructing the true/fake K_s^0 vertices using SV1 algorithm is computed. A sample of $t\bar{t}$ production from proton-proton collision at a center-of-mass energy of $\sqrt{s} = 13$ TeV generated with POWHEG plus PYTHIA 6 is used.

8.4.2. K_s^0-neutral-track reconstruction

A K_s^0 vertex is reconstructed if, in the same jet, 2 'SV1 bad tracks' with opposite charge forming a vertex with a mass close to the K_s^0 mass ($|M - 497.648| < 15$ MeV) are found. Figure 8.7 shows a comparison between the reconstructed and the corresponding true K_s^0: the p_T and the radius distributions look compatible between the two K_s^0.

The reco-K_s^0-track is drawn using the reconstructed K_s^0 vertex position (x,y,z) and momentum vector (p_x,p_y,p_z) as illustrated in figure 8.8. Its impact parameters, called $d_0^{experimental}$ and $z_0^{experimental}$, are computed in the usual way: the distance (d) between the point of closest approach (C) of the reco-K_s^0-track and the PV is calculated. $d_0^{experimental}$ is d projected into the transverse plane (x,y), while $z_0^{experimental}$ is the z-coordinate of the point C with respect to the PV. $d_0^{experimental}$ and $z_0^{experimental}$ are signed according to the formulas in section 8.3.1.

Similarly, the impact parameters of the true-K_s^0-track, d_0^{true} and z_0^{true}, are computed using the true K_s^0 momentum and position. A comparison between the experimental and true transverse impact parameters is presented in figure 8.7(c).

The difference between the experimental and true IPs (d_0, z_0) is used to estimate the resolution on $IP^{experimental}$: σ(IP^{experimental}) is taken as the standard deviation of the distribution of IP-difference fitted to a Gaussian.

Figure 8.9 shows the $d_0^{expermental}$ resolution dependence on K_s^0 p_T, K_s^0 decay radius and the

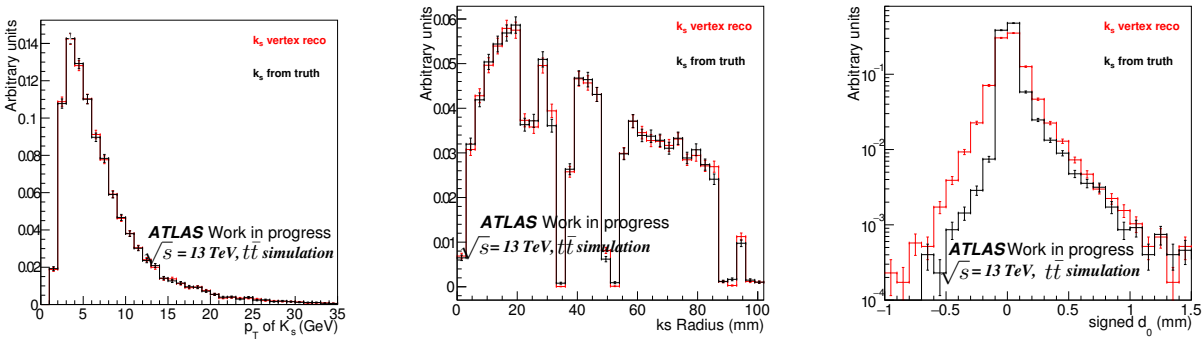

(a) p_T of K_s^0 (b) Radius of K_s^0 (c) d_0 of K_s^0

Figure 8.7.: Comparison between the reconstructed and the corresponding true K_s^0, p_T (a), radius (b) and d_0 (c).

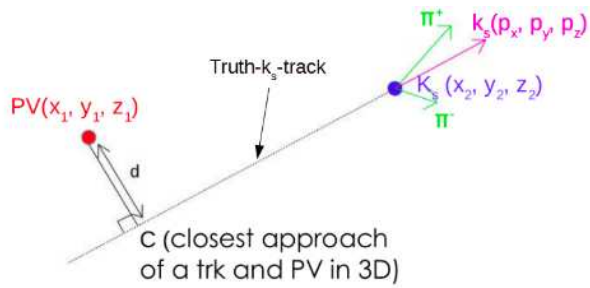

Figure 8.8.: The linear neutral K_s^0 'track' reconstructed using K_s^0 position and momentum vector.

angular separation between the K_s^0 decay products. The resolution improves with increasing K_s^0 p_T or decreasing K_s^0 radius. The opposite behavior of the resolution as function of K_s^0 p_T and Δ R(π^-,π^+) is due to the fact that the angular separation between the K_s^0 daughters decreases when K_s^0 p_T increases. However, the K_s^0 p_T and K_s^0 radius correlation is not obvious.

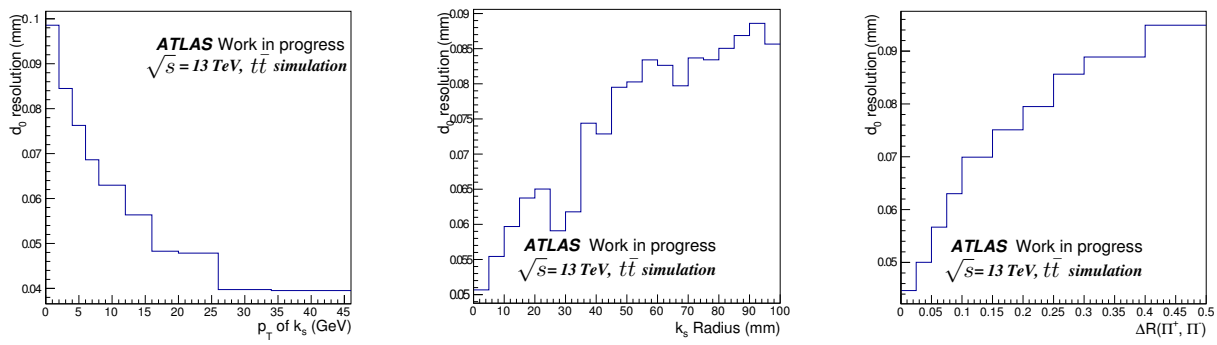

(a) (b) (c)

Figure 8.9.: The $d_0^{experimental}$ resolution as function of K_s^0 p_T (a), K_s^0 radius (b), and the angular separation between the K_s^0 daughters (c).

Thus, the IP resolutions are computed as functions of these 2 variables: K_s^0 p_T values are splitted into 3 ranges p_T < 5 GeV, $p_T \in$ [5, 10[GeV and $p_T \in$ [10, 100] GeV, while K_s^0 radius ranges used are R< 30 mm, R∈ [30, 50[mm and R∈ [50, 100] mm. The resolutions , $\sigma(d_0^{experimental})$ is computed for each of these 9 bins and presented in figure 8.10(a). , $\sigma(z_0^{expermental})$ is computed in the same way. The $d_0^{experimental}$ and $z_0^{experimental}$ significance distributions obtained, shown in figures 8.10(b) and 8.10(c), have good separation between the different jet flavours and have the same general behaviour as the 'Good' tracks IPs significance distributions mentioned in section 8.3.1. To test the effect of using the reco-K_s^0-track a new IP3D track category is created.

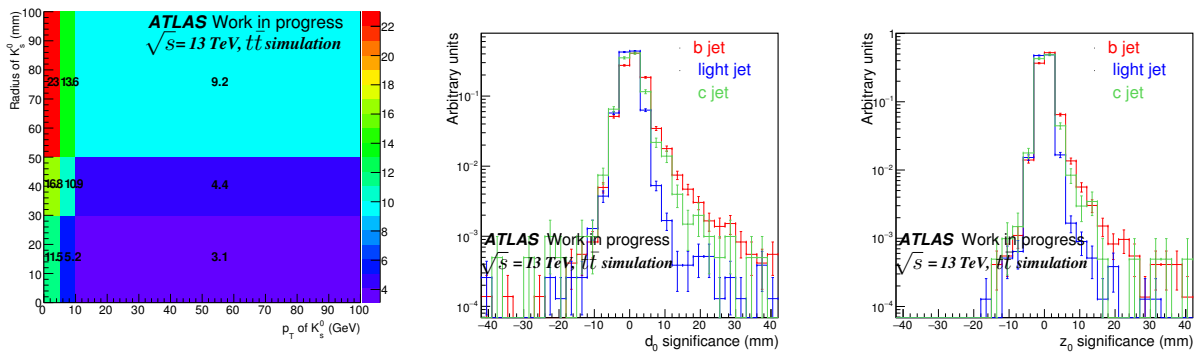

(a) (b) (c)

Figure 8.10.: $\sigma(d_0)$ in % for the bins chosen in K^0_s (p_T, Radius) (a). The IP significance of the reco-K^0_s-track: $\frac{d_0}{\sigma(d_0)}$ (b), $\frac{z_0}{\sigma(z_0)}$ (c).

8.4.3. K_s reconstruction efficiency

The K^0_s reconstruction efficiency is defined as the number of reconstructed K^0_s divided by the number of true K^0_s with 2 reconstructed $\pi^{\pm}$ tracks in the jet. The reconstruction efficiencies obtained for b, c and light-jets are 16.4% , 26% and 29% respectively. On the other hand among reconstructed K_s, 80% are true one, 8% are associated to a MC particle other than K_s and 12% are fakes (not matched to any MC particle).

To understand the reason for the low K^0_s reconstruction efficiency, a comparison between the true and the SV1 bad $\pi^{\pm}$ tracks from K^0_s versus the number of pixel hits and vsersus the p_T is presented in figures 8.11(b) and 8.11(c) respectively. As can be observed, around 29% of the true $\pi^{\pm}$ tracks from K^0_s don't have any pixel hits, while about 6% have p_T< 0.7 GeV. These tracks can't be reconstructed by SV1 as they don't obey the SV1 requirements mentioned in table 8.1. Figure 8.11(a) shows the K^0_s reconstruction efficiency as a function of K^0_s decay radius, for all jet flavours. As can be expected, the efficiency deteriorates when the K^0_s decay radius increases as the number of pixel hits will decreases.

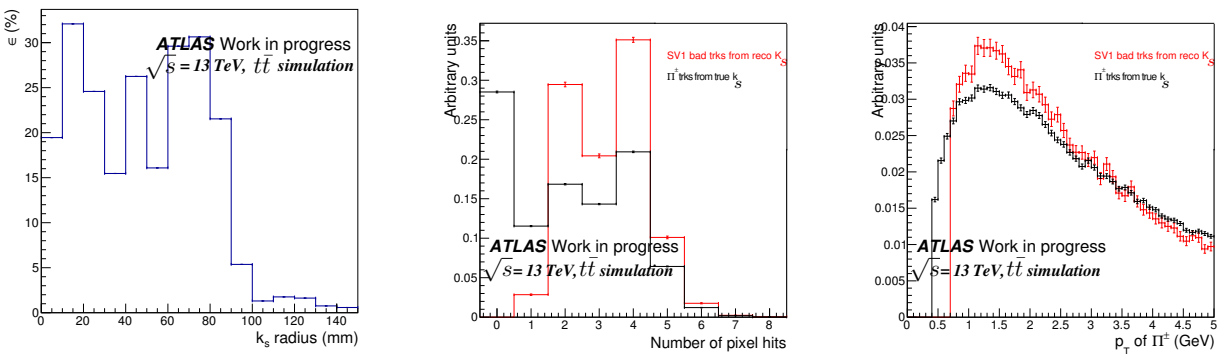

(a) (b) (c)

Figure 8.11.: The K_s^0 reconstruction efficiency as function of K_s^0 radius (a). Comparison between the true and the SV1 bad $\pi^{\pm}$ track from K_s^0 for the number of pixel hits (b) and for the p_T (c)

8.4.4. Impact on IP3D performance

The performance of the IP3D algorithm using the reco-K_s^0-track is shown in figure 8.12. The performance using the true-K_s^0-track is also shown to illustrate the maximal gain expected. As observed, at 70% b-jet efficiency, using the true-K_s^0-track instead of the true K_s^0 daughter $\pi^{\pm}$ tracks (red curve) gives an improvement of $\approx$ 16% with respect to the default IP3D performance (dark blue curve) where the SV1 bad tracks are rejected as described in section 8.3.1). Hence, 16% is the highest improvement for a perfect K_s^0-track reconstruction. However, using reco-K_s^0-track instead of the SV1 bad tracks (light blue) don't improve the performance. This is due to the small K_s^0 reconstruction efficiency discussed in section 8.4.3.

8.4.5. Conclusion and outlook

This study allowed to quantify the highest impact expected on the IP3D performance of using the mother-K_s^0-track instead of the $\pi^{\pm}$ daughter tracks. Also the K_s^0 reconstruction efficiency using the SV1 algorithm is estimated. No gain in IP3D performance is obtained using the SV1 reco-K_s^0-track due to the small SV1 K_s^0 reconstction efficiency obtained. Further studies can be done aiming to increase the K_s^0 reconstruction efficiency:

* To relax some SV1 cuts such as the number of pixel hits and the track p_T as discussed in section 8.4.3.
* To test other more appropriate algorithms which are able to reconstruct V^0.
* To look for the improvement with reconstructing other V^0 than K_s^0 like Λ^0, ...

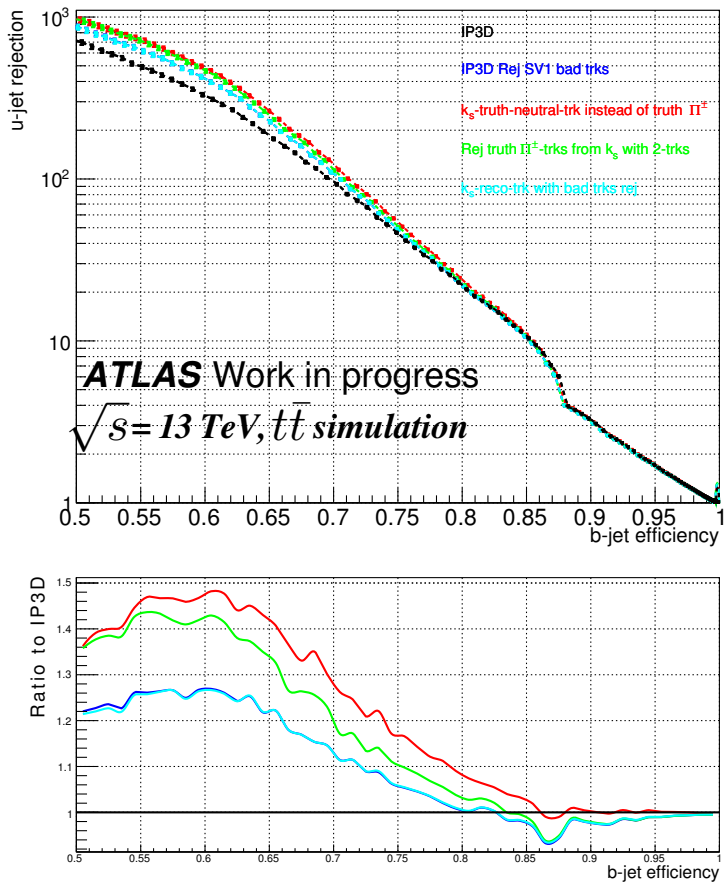

Figure 8.12.: The light jet rejection as a function of b-jet efficiency for IP3D default configuration, in dark blue. The IP3D performance using the reco- (in light blue) or the true- (in red) K_s^0-track instead of the K_s^0 daughter tracks are shown as well.

9. Robustness of b-tagging performance with various conditions of the pixel detector

9.1. Introduction

The typical resolution on position brought by the pixel detector is 10 μm in (r, ϕ) and 120 μm in Z (70 μm for IBL) [94]. This allows for a good accuracy on the measurement of impact parameters and a good secondary vertex reconstruction. However, the pixel detector modules can turn inactive due to several reasons [73] which results in changing the shape of the pixel clusters or losing some of them. All these problems affect the track reconstruction, the impact parameter measurement and the vertexing performance as discussed in section 5.2.2. Therefore, it is needed to quantify the impact on the b-tagging performance for such scenarios in order to define the threshold for good data in terms of fraction of non-functional modules.

Sections 9.5.1, 9.5.2 and 9.5.3 review my studies of the scenarios with pixel modules failures in the barrel layers I generated and the detailed expected impact on the b-tagging algorithms performance.

On the other hand, I studied the effect of increasing the pixels time over threshold (ToT) in the b-layer (L0), being one of the proposed solution to avoid the high occupancy due to the increase of the instantaneous luminosity in Run2 as discussed in section 5.2.2. The ToT change leads to hits loss which can affect badly the reconstruction of the tracks and the b-tagging performance as well. Sections 9.5.4 and L describe the impact on b-tagging algorithms performance of scenarios with different b-layer ToT minimal cut I generated.

9.2. Samples used

For this study, samples were re-digitized many times to test various configurations. To minimize the disk space and the process time required by the hits files, AFII samples (described in section 7.2.2) were used and two samples were selected in order to cover all the relevant jet p_T ranges.

First, a sample of $t\bar{t}$ events is used to study b-jets with medium p_T ($< p_T >=$ 57 GeV). The b-jets come from the top quark decays. The second sample provide light and b-jets with high momentum (jet p_T: 25-2000 GeV). It consists of a mix of three samples of Z'($\rightarrow b\bar{b}$) + Z'($\rightarrow q\bar{q}$) events with different Z' masses: 1, 2, and 5 TeV. "q" indicates any light flavour quark: u, d and s.

The hits samples from proton-proton collision at a center-of-mass energy of $\sqrt{s} = 13$ TeV used were generated with POWHEG [95] plus PYTHIA 6 [82] for $t\bar{t}$ events and PYTHIA 8 [83] for Z' mix events (see appendix J), then simulated using Geant4 [88].

The "ATLAS-R2-2015-03-01-00" geometry version was used for digitizing and reconstructing events to give an accurate description of the detector conditions for the Run 2 data-taking as described in section 7.2.3.

Jets are required to have a minimum p_T of 25 GeV and to be in a region with full tracking coverage, $|\eta| < 2.5$. Using information in the simulation, jets were labeled as b-, c- or light-jets as described in section 8.2.3.

Figures 9.1(a) and 9.1(b) show the p_T and η distributions of the true b-jets in the different samples used. Figure 9.1(c) shows the B-hadron decay radius distribution. This variable is correlated to the jet p_T: around 30% of the B-hadron in the Z' mix sample fly beyond the IBL before decaying.

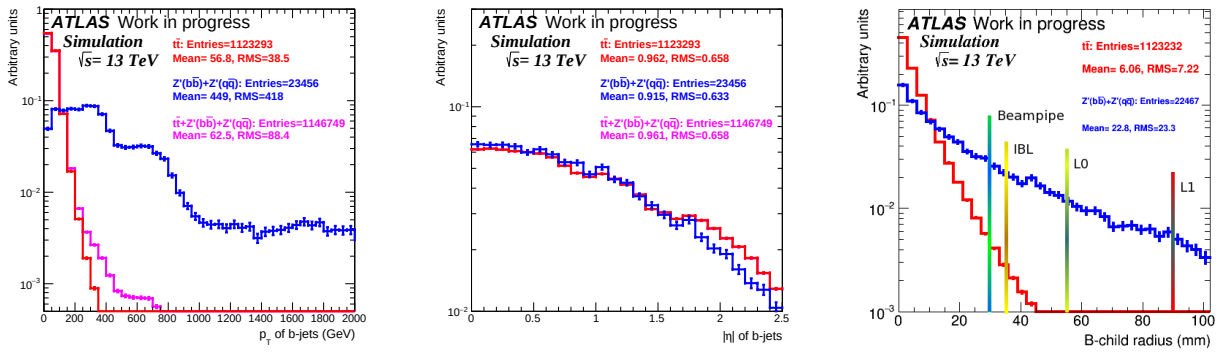

(a) p_T of b-jets (b) $|\eta|$ of b-jets (c) B-child radius

Figure 9.1.: p_T (a), $|\eta|$ (b) distributions of the b-jets and B-hadron decay radius distribution (c) in red for $t\bar{t}$, in blue for the Z' mix and in purple for all these samples merged together.

9.3. Baseline b-tagging performance

For the pixel dead modules study, the baseline configurations of $t\bar{t}$ and Z' mix samples were produced using the dead pixel map at the start of Run2 presented in table 9.1.

Table 9.1.: Fraction of dead modules per layers at the start of Run2.

Layer	Radius (mm)	Total number of Modules	Inactive modules	Fraction (%)
IBL	33	280	2	0.7
Layer-0	55	286	4	1.4
Layer-1	90	494	8	1.6
Layer-2	125	676	17	2.6

The baseline b-tagging performance for $t\bar{t}$ and Z' mix samples are shown in figure 9.2. As observed, the b-tagging performance depends on jet p_T. It degrades at very low jet p_T due to the multiple-scattering issue and at high jet p_T (Z' mix sample) as well, due to merging of tracks (pattern recognition), the detector inefficiency for very late decays and the increased track multiplicity from the fragmentation. The best b-tagging performance is at medium jet p_T ($t\bar{t}$ sample) where the effect of multiple-scattering is not important and there is no pattern recognition issue.

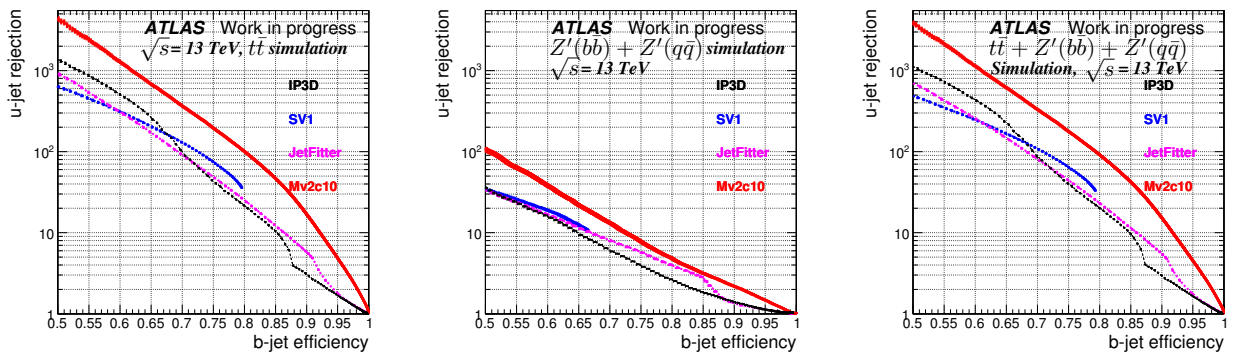

(a) $t\bar{t}$ sample (b) Z' mix samples (c) $t\bar{t}$ and Z' mix merged together

Figure 9.2.: The light-jet rejection as a function of the b-tagging efficiency for the baseline configuration produced using (a) $t\bar{t}$, (b) the Z' mix and (c) all these samples merged together. IP3D performance is shown in black, SV1 in blue, JetFitter in purple and MV2c10 in red.

Concerning the pixel time over threshold, the baseline configurations of $t\bar{t}$ and Z' mix samples were produced using ToT minimal cuts in L0 at 2 BC and 4 BC for the other pixel layers and EC as presented in the second line of table 9.4.

9.4. Configurations studied and impact on track categories

9.4.1. Dead pixel modules configurations

Scenarios of failures in IBL with a fraction y of dead modules up to 35% were produced. An extreme scenario with no IBL at all was needed to illustrate the maximal effect expected. The IBL scenarios produced from $t\bar{t}$ and Z' mix are detailed in table 9.2(a). Similar scenarios were produced for L0 (see table 9.2(b)). For each scenario, a new data base configuration with updated map of inactive modules is generated and used for digitizing and reconstructing the hits. Hence, for the track reconstruction the newly dead modules become places where a hit is not expected. Three scenarios with different fractions of inactive modules in L1 were also produced with $t\bar{t}$ and Z' mix samples and presented in table 9.3(a). Similar scenarios were produced for L2 as well (see table 9.3(b)).

Table 9.2.: Configurations, produced from $t\bar{t}$ or Z' mix samples, with a fraction y of dead modules for the two innermost layers: (a) IBL, (b) L0.

Sample	$t\bar{t}$	Z' mix
y(%)	{6, 9, 15, 25, 35, 100}	{35, 100}

(a)

Sample	$t\bar{t}$	Z' mix
y(%)	{6, 9, 15, 25, 35, 100}	{35, 100}

(b)

Table 9.3.: Configurations, produced from $t\bar{t}$ or Z' mix samples, with a fraction y of dead modules for the two outermost layers: (a) L1, (b) L2.

Sample	$t\bar{t}$	Z' mix
y(%)	{6, 9, 100}	{100}

(a)

Sample	$t\bar{t}$	Z' mix
y(%)	{6, 9, 100}	{100}

(b)

By comparing the different scenarios of pixel modules failures produced with respect to the baseline, the main differences appear in the:

* distribution of tracks into the 14 categories,
* z_0 and d_0 measurements,
* (good quality for IPxD) track multiplicity in jet,
* b-tagging algorithms discriminant distributions, which affect their performance.

We start by discussing in this section the first point while the last three points are detailed in section 9.5.1.3. Then, the impact on the performance of the four b-tagging algorithms IP3D, SV1, JetFitter and MV2c10 will be presented in sections 9.5.1, 9.5.2 and 9.5.3. To split tracks on the 14 IP3D Run2 categories, the hits in IBL and L0 are of particular importance, as is the knowledge of whether a hit was expected or not, based on the dead module maps. A track going through a dead module will be in the category "hit not expected and not found".

The IBL failure scenarios will increase the fraction of tracks in categories 2, 3 and 5 (the Run2 track categories are listed in table 8.2), while failures in L0 will increase the fraction of tracks in categories 1, 3 and 7. In both cases, this implies a degradation in IP2(3)D performance as the fraction of good tracks (category 13) decreases. Figure 9.3 illustrates the new distribution of tracks in these four categories for the scenarios with 35% of inactive modules in IBL (figures 9.3(a), 9.3(d)) and 35% of inactive modules in L0 (figures 9.3(b), 9.3(e)). Figure 9.3(a) shows a loss of 26% in the fraction of good tracks for $t\bar{t}$ while a slightly lower loss of 21% for the Z' mix is shown in figure 9.3(d) emphasizing the relatively more important role of the IBL for medium rather than high p_T jets. The same impact is seen for L0: a loss of 26% for $t\bar{t}$ (figure 9.3(b)) and 21% loss for the Z' mix (figure 9.3(e)). The complete distributions of tracks in categories are presented in appendix K for the various scenarios and samples.

The categories affected for L1 and L2 failure scenarios are categories 6, 9, 10. Categories 9 and 10 contain the tracks with shared hits which are clusters shared among more than one track, degrading track quality. Figures 9.3(c), 9.3(f) show the new distribution of tracks in these categories for L1 off and L2 off scenarios. Slightly higher effect is seen for Z' mix (figure 9.3(f)) compared with the $t\bar{t}$ sample (figure 9.3(c)). For the L1 totally off scenario, an additional 1.7% and 1.2% of IP tracks are going to categories 9 and 10 respectively for Z' mix sample, while for L2 off scenario it is 1.1% in category 9 and 1.7% in category 10.

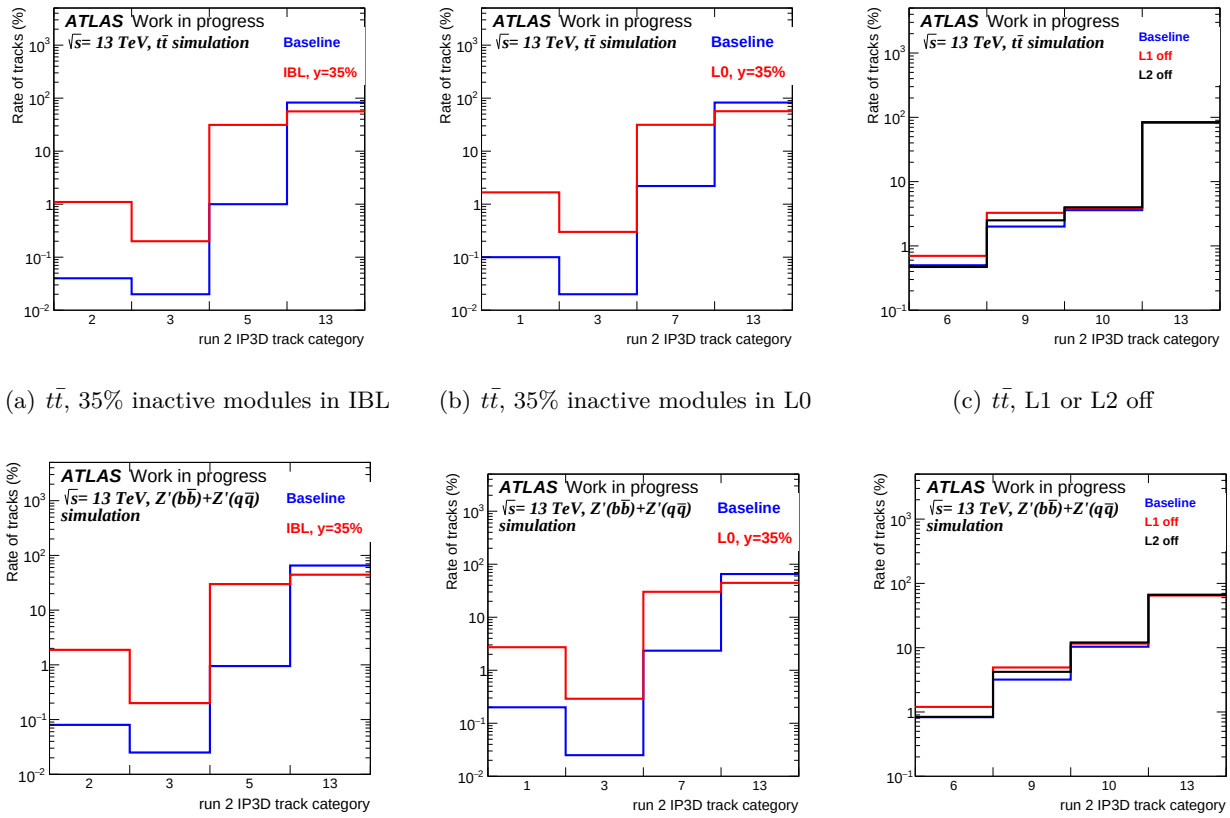

(a) $t\bar{t}$, 35% inactive modules in IBL (b) $t\bar{t}$, 35% inactive modules in L0 (c) $t\bar{t}$, L1 or L2 off

(d) Z' mix, 35% inactive modules in IBL (e) Z' mix, 35% inactive modules in L0 (f) Z' mix, L1 or L2 off

Figure 9.3.: Rate of tracks in the mostly affected track categories, in blue for the baseline and in red for the scenario with 35% of inactive modules in IBL (a) and (d), 35% of inactive modules in L0 (b) and (e), L1 off and in black for L2 off scenarios (c) and (f). $t\bar{t}$ sample is used for the upper plots and the Z' mix samples for the lower plots.

9.4.2. Pixel ToT configurations

Several scenarios with increased ToT minimal cut in L0 were produced. Among them two scenarios have L1(L2) ToT minimal cut increased as well. However, the end-cap (EC) minimal cut is fixed at 4 BC for all the configurations. Table 9.4 shows all the L0 scenarios produced from $t\bar{t}$ and Z' mix samples with their corresponding ToT minimal cut on L0 and L1(L2). The configurations produced have the same ToT calibration: ToT at the Minimal Ionizing Particle (MIP) on IBL at 10 BC and 30 BC for L0, L1, L2 and EC. As mentioned in section 5.2.3, due to the L0 calibration decrease from 30 BC to 18 BC, an L0 offline ToT cut is defined as the L0 online cut scaled by 30/18. Also, the configurations have the same Hit Duplication (explained in section 5.2.3) mode 'ON' for the L0, L1, L2 and for the EC. The baseline offline ToT minimal cut in L0 is 2 BC and the highest offline ToT minimal cut checked is 13 BC as shown in table 9.4. Two scenarios differing only on the L1(L2) ToT minimal cut were produced, this cut is increased from the baseline value at 4 BC to 6 BC. These two configurations serve to check the sensitivity of the b-tagging algorithms performance when increasing the outermost layers ToT minimal cut.

Table 9.4.: The Pixel ToT configurations with x and y representing respectively the ToT cuts (in BC) for L0 (offline) and the two outermost layers for $t\bar{t}$ and Z' mix samples. The baseline configuration has (x, y)= (2, 4) BC.

Sample	$t\bar{t}$	Z' mix
(x, y)	(2, 4)	(2, 4)
	(6, 4)	
	(6, 6)	
	(7, 6)	
	(8, 4)	
	(10, 4)	(10, 4)
	(13, 4)	(13, 4)

The scenarios listed in table 9.4 were produced using the MC15c configuration. One additional scenario on MC16a (discussed in section 7.3) configuration was produced. As shows the table 9.5, for the MC16a configuration the calibration is decreased for the IBL compared with the MC15c configurations, this leads to an increase in the high charge hits. For L0, L1, L2 and the EC the Hit Duplication is turned off, this induces a low charge hits loss. The similarities between MC16a and MC15c are the ToT at MIP for L0, L1, L2 and EC and the Latency. The only MC16a configuration is produced with a ToT minimal cut on L0 at 7 BC on L1, L2 at 6 BC.
The ToT minimal cut in EC applied is 6 BC which is larger than the cut applied for the MC15c configurations produced corresponding to 4 BC. Similarly to the scenarios of inactive pixel

Table 9.5.: Comparison between MC16a and MC15c configurations.

Configuration	MC16a	MC15c
ToT at MIP on IBL (BC)	8	10
Hit Duplication in L0, L1, L2, EC	OFF	ON
ToT minimal cut for EC (BC)	6	4

modules, by comparing the different MC15c with increased ToT minimal cut and the MC16a

scenarios produced with respect to the baseline, the main differences appear in the distribution of tracks into the 14 categories, consequently in z_0 and d_0 measurements, (good quality for IPxD) track multiplicity in jet and the b-tagging algorithms discriminant distributions which may affect the b-tagging algorithms performance.

As discussed in section 5.2.2, a pixel is fired when it measures a ToT larger than the ToT minimal cut. A pixel cluster is a group of fired pixels with common corner or edge. Using the properties of the pixel clusters in a layer, hits in this layer are localized. Therefore, increasing the L0 ToT minimal cut causes a decrease in the size (as shows table 9.6) or a loss (as shows table 9.7) of L0 pixel clusters.

Table 9.6.: The mean and the RMS of the L0 pixel clusters Z and (r, ϕ) size distributions for MC16a and for MC15c: baseline (2, 4), (6,4), (10,4) and (13,4) configurations.

Configuration	Baseline	MC16a	L0.ToT= 6	L0.ToT= 10	L0.ToT= 13
Z size mean [cells]	$2.02\pm1.7.10^{-3}$	$1.87\pm1.6.10^{-3}$	$1.90\pm1.6.10^{-3}$	$2.21\pm1.4.10^{-3}$	$1.65\pm1.5.10^{-3}$
Z size RMS [cells]	$1.08\pm1.2.10^{-3}$	$1.02\pm1.1.10^{-3}$	$1.03\pm1.1.10^{-3}$	0.89 ± 1.10^{-3}	0.88 ± 1.10^{-3}
(r, ϕ) size mean [cells]	$1.84\pm2.2.10^{-3}$	$1.73\ \pm1.6.10^{-3}$	$1.63\pm1.6.10^{-3}$	$1.39\pm1.2.10^{-3}$	$1.29\pm1.1.10^{-3}$
(r, ϕ) size RMS [cells]	$1.37\pm1.5.10^{-3}$	$0.99\pm1.1.10^{-3}$	$1.04\pm1.2.10^{-3}$	$0.77\pm0.9.10^{-3}$	$0.69\pm0.8.10^{-3}$

Table 9.7.: The fractions of tracks without any pixel cluster in L0 for MC16a and for MC15c: baseline (2, 4), (6,4), (10,4), (13,4) configurations. The fractions presented are within an error of 0.05%

Configuration	Baseline	MC16a	L0.ToT= 6	L0.ToT= 10	L0.ToT= 13
Tracks without pixel cluster in L0 (%)	12.6	12.7	13.16	15.45	20.6

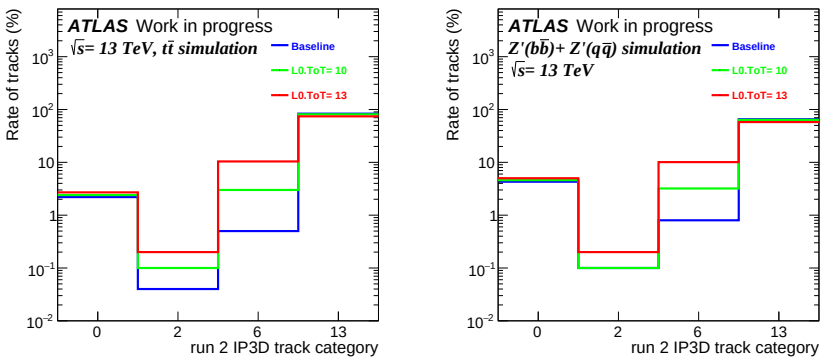

(a) (b)

Figure 9.4.: Rate of tracks in the four mostly affected track categories, in blue for the baseline and in red for the scenario with the highest L0 ToT cut (a) for the $t\bar{t}$ sample and (b) for the Z' mix sample.

Hence, the L0 scenarios will increase the fraction of tracks in categories 0, 2, 6, this implies a

degradation in IP2(3)D performance as the fraction of "good" tracks (category 13) decreases. The figures 9.4(a) and 9.4(b) illustrate the new distribution of tracks in these four categories for the MC15c scenarios: baseline, (10,4), (13,4). The complete distributions of tracks in categories are presented in appendix K. The figure 9.4(a) shows a loss of about 2% and 9.2% in the fraction of "good" tracks for (10,4) and (13,4) $t\bar{t}$ configurations respectively. Roughly speaking, the same impact is seen for the Z' mix (figure 9.4(b)) emphasizing that this effect is independent of track or jet p_T.

The impact on the performance of the four b-tagging algorithms IP3D, SV1, JetFitter and MV2c10 for the MC15c scenarios with increased ToT cut in L0 will be presented in section section 9.5.4, while the impact for the MC16a scenario can be found in appendix L.

9.5. b-tagging performance for the different layer configurations

9.5.1. IBL dead pixel modules configurations

Since the discriminating distributions (e.g. IP3D log-likelihood ratio, MV2c10 BDT output) are varying for each scenario (detailed in section 9.5.1.3), an operating point (OP) [a] doesn't correspond to the same b-jet efficiency in the baseline and in degraded scenarios. Therefore, the performance degradation for a scenario with respect to the baseline is presented in two different manners:

* By modifying the OP depending on each scenario to reach the same b-jet efficiency (ϵ_b), and comparing the light-jets rejection (R_u) at fixed ϵ_b. ROC curves, showing R_u vs ϵ_b, for the IBL scenarios are presented in section 9.5.1.1.
* Without modifying the OP (using the same 20.7 OP for scenarios and baseline), by assessing the relative degradation in terms of ϵ_b, R_u and R_c. Results for IBL scenarios are presented in section 9.5.1.2.

9.5.1.1. Integrated performance (R_u vs ϵ_b)

It is of interest to determine the degradation in the b-tagging performance obtained due to the increase in the fraction of inactive pixel modules in the IBL up to 35% for medium p_T ($t\bar{t}$ sample) and high p_T jets (Z' mix sample). This requires a comparison to be made between the IBL scenarios produced using different dead pixel maps and the baseline samples.

Figure 9.5 shows such a comparison between the baseline performance of four b-tagging algorithms: IP3D (9.5(a)), SV1 (9.5(b)) JetFitter (9.5(c)) and MV2c10 (9.5(d)) and their performance for the six IBL scenarios produced with the same $t\bar{t}$ sample.

The performance of the IP3D algorithm is the most affected compared with the three other b-tagging algorithms as it uses the fourteen PDF corresponding to the track categories listed in table 8.2. Indeed, as seen in figures 9.5(a) and 9.5(d), losing good tracks affects badly the IP3D performance and MV2c10 performance as well.

Comparing the IP3D algorithm performance for the scenario with 6% inactive modules in the IBL, the light-flavour jet rejection is degraded by 7% with respect to the baseline for a 75% b-jet efficiency. At 75% MV2c10 b-jet efficiency the loss in the light-jet rejection is about 5%. The degradation for the other IBL scenarios is represented in table 9.8.

[a] Operating points are defined by a single cut value on the discriminating variable of an algorithm, the cut is chosen to provide a specific b-jet efficiency on a simulated sample. They are defined for each release.

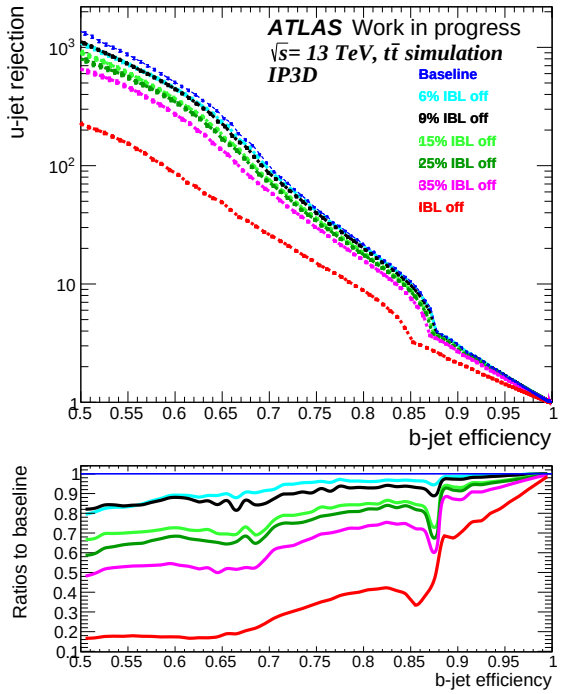

(a) IP3D

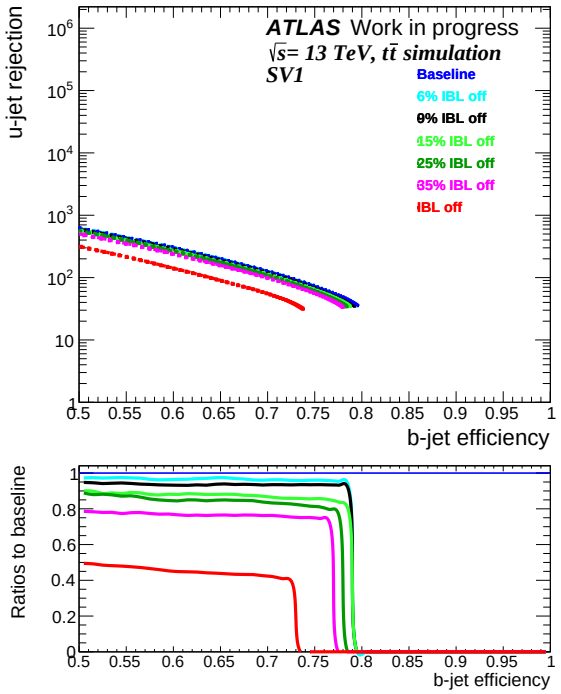

(b) SV1

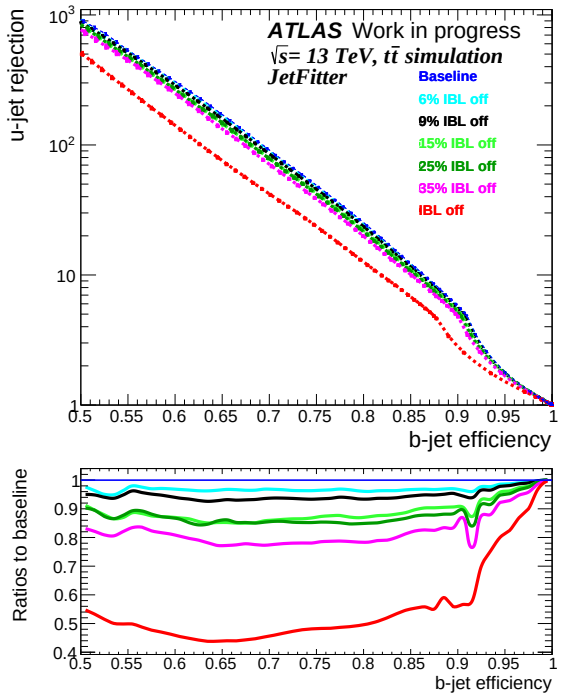

(c) JetFitter

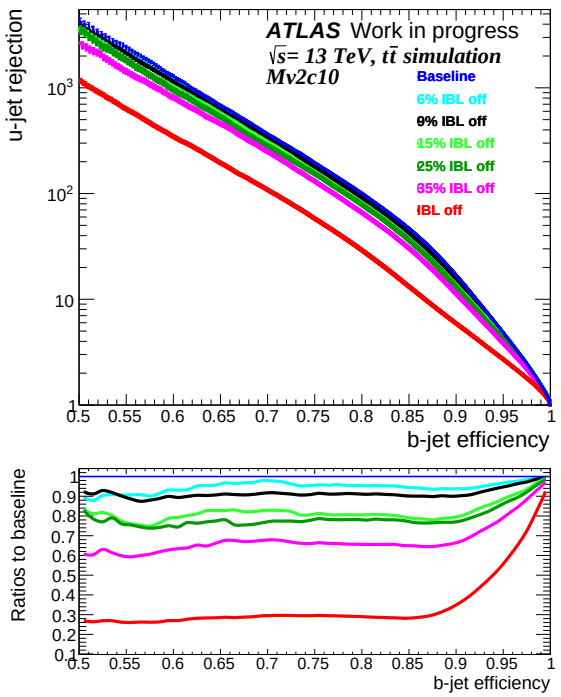

(d) Mv2c10

Figure 9.5.: The light jet rejection as a function of b-jet efficiency for the IP3D (a), SV1 (b), JetFitter (c) and MV2c10 (d) algorithms for IBL failure scenarios compared with the baseline in blue for $t\bar{t}$ sample.

Table 9.8.: The relative degradation in the light-jet rejection (%) for the IP3D and the MV2c10 taggers at a b-tagging efficiency of 75% for the six IBL scenarios produced using the $t\bar{t}$ sample.

IBL scenarios y(%)	6	9	15	25	35	100
R_u degradation for IP3D at $\epsilon_b = 75\%$	7	12	28	30	40	72
R_u degradation for MV2c10 at $\epsilon_b = 75\%$	5	9	20	25	38	70

The b-tagging algorithms based on secondary vertex properties SV1 and JetFitter are more robust because they don't use an explicit categorization of the tracks depending on the hit patterns in the pixel layers as is the case of the IP3(2)D algorithm. The degradation in the light-jet rejection for these algorithms at 60 % b-jet efficiency, depending on the IBL scenario, is presented in table 9.9.

Table 9.9.: The relative degradation in the light-jet rejection (%) for the SV1 and the JetFitter taggers at a b-tagging efficiency of 60% for the six IBL scenarios produced using the $t\bar{t}$ sample.

IBL scenarios y (%)	6	9	15	25	35	100
R_u degradation for SV1 at $\epsilon_b = 60\%$	2	5	10	15	20	50
R_u degradation for JetFitter at $\epsilon_b = 60\%$	5	7	14	15	20	55

Figure 9.6 shows the same comparison but for the Z' mix sample. The IBL is expected to improve the impact parameter resolution of tracks mostly at p_T up to 5-10 GeV (as discussed in section 9.5.1.3) and thus the improvement due to the addition of IBL is concentrated in the low to medium jet p_T region and not at high jet p_T. Therefore, the degradation in the light-jet rejection for the MV2c10 algorithm at 75% b-tagging efficiency for the scenario without IBL is only 5%, while, as table 9.8 shows, for the $t\bar{t}$ IBL off scenario the degradation is about 70%.

9.5.1.2. Impact using fixed operating points

In this section we will show the degradation in the b-tagging performance for a fixed OP (release 20.7 OP values were used) for each IBL failure scenario. Figure 9.7 shows the degradation in the performance for IP3D, SV1 and JetFitter algorithms for the operating points listed in table 9.10. Figure 9.8 shows the same for the MV2c10 algorithms at the three different operating points appearing in the same table. Each bin of the x-axis represents a scenario in IBL while the y-axis shows the degradation of the b-jet efficiency in red, the light jet rejection in blue and the c-jet rejection in green. The y axis positive values indicate a loss in the performance while negative values mean a gain and zero indicates no changes in the performance. The six plots of the figures 9.7 and 9.8 show a degradation in both the b-jet efficiency and the light jet rejection, however a gain in the c-jet rejection appeared. This gain can be explained by the fact that the B- and C-hadrons have close properties (high mass, long lifetime) thus the b-jet efficiency and the c-jet rejection (being the inverse of the c-jet efficiency) must behave in an opposite way. The middle plot of figure 9.8 shows the degradation for the MV2c10 tagger using the operating point at 0.6459, corresponding to 77% b-jet efficiency for the baseline. The last bin dedicated to the scenario with IBL entirely

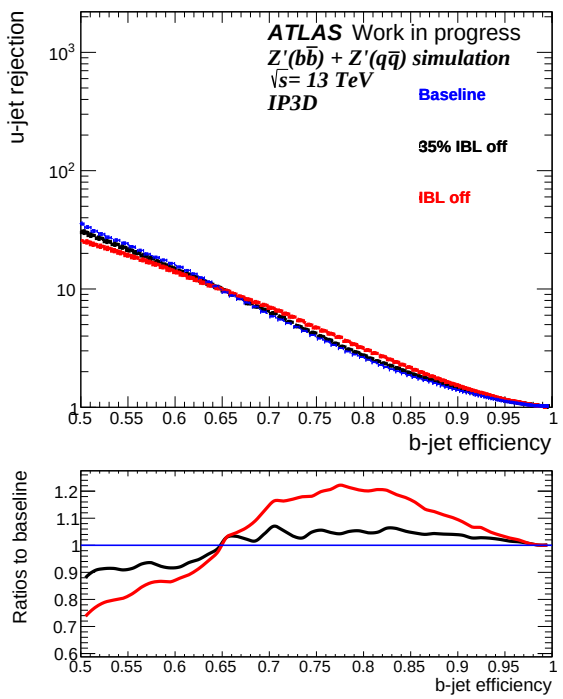

(a) IP3D

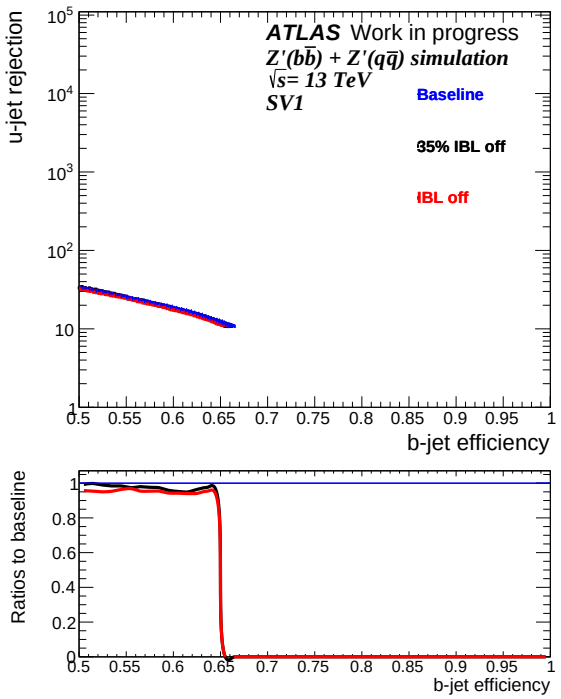

(b) SV1

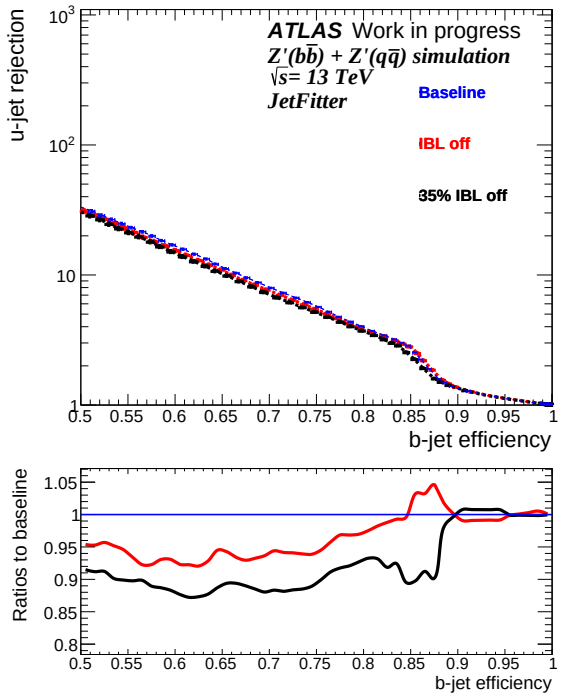

(c) JetFitter

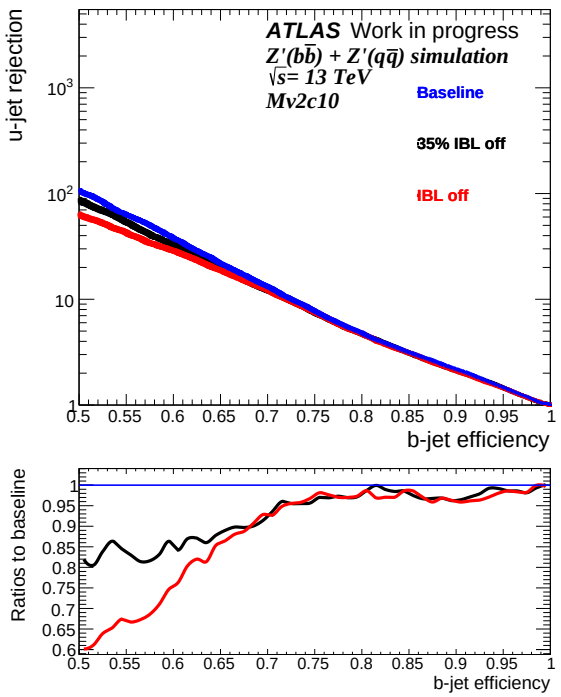

(d) Mv2c10

Figure 9.6.: The light jet rejection as a function of b-jet efficiency for the IP3D (a), SV1 (b), JetFitter (c) and MV2c10 (d) algorithms for IBL failure scenarios compared with the baseline in blue for the Z' mix sample.

off shows a 10% degradation in ϵ_B and 30% degradation in R_u and a gain of 12% in R_c (see table 9.11).

Table 9.10.: Release 20.7 operating points (for $t\bar{t}$ sample) checked.

	Cut Value	ϵ_b for the baseline (%)	R_u for the baseline(%)	R_c for the baseline (%)
IP3D	1.95268	75	44 ± 1	3.9 ± 0.1
SV1	4.00556	60	307 ± 16	9.2 ±0.2
JetFitter	-1.13082	75	192 ± 8	4.4 ± 0.1
MV2c10	0.8244	70	761 ± 63	8.8 ± 0.2
	0.6459	77	216 ± 10	4.7 ± 0.1
	0.1758	85	38 ± 1	2.7 ± 0.1

Table 9.11.: The b-jet efficiency, light jet rejection and c-jet rejection using the MV2c10 tagger operating point of 0.6459 for the baseline and the IBL off scenario.

Scenario	ϵ_b (%)	R_u	R_c
Baseline	77	215.9 ± 9.5	4.7 ± 0.1
IBL off	69	155.4 ± 9.7	5.3 ± 0.2

9.5.1.3. Study of the IBL role in multiple scattering and pattern recognition issues

Since the same events were used to produce the baseline and the various scenarios, it is possible to compare the baseline and the "IBL off" scenario on an event-by-event basis. For the same event, jets from both configurations were matched using a cut on ΔR at 0.1. The track with lowest (highest) p_T was selected in both jets. By comparing Run1 and Run2, the IBL improves the impact parameter resolution in both the transverse (d_0) and the longitudinal direction (z_0) [94]. This is because the IBL is installed at the smallest radius (33 mm) around the beam pipe and it is equipped with readout on the smallest pitch in Z direction (250 μm, it corresponds to 400 μm for the three other pixel layers) [96]. It is of interest to understand the impact of disabling the IBL without changing the ATLAS detector geometry (IBL is not removed).

The impact as function of track p_T was studied. A comparison of the d_0 and z_0 errors with and without IBL for both tracks are presented in appendix M. Clearly higher effect is seen for z_0 measurement and more specifically the track with lowest p_T. The same effect is presented in figure 9.9 showing $\rho = |d_0^{meas} - d_0^{truth}|$ the absolute value of $d_0(z_0)$ resolution which is the difference between the measured and the truth values.

The figure 9.10(c) shows the difference of z_0 error called 's' for the same track with and without IBL. Negative values indicate an increase in z_0 error without IBL. Similarly, figures 9.10(a) and 9.10(b) show respectively the difference of d_0 and z_0 resolutions with and without IBL. These three plots show clearly a longer negative tail for the track with lowest p_T compared with the track with highest p_T.

Indeed, compared to the high p_T tracks, the low p_T tracks are more subject to the multiple scattering, therefore, their directions are not well reconstructed. So when these low p_T tracks loose on top of this their closest hit to the PV in the IBL, they will be badly extrapolated and their impact parameter measurements will be badly measured as well.

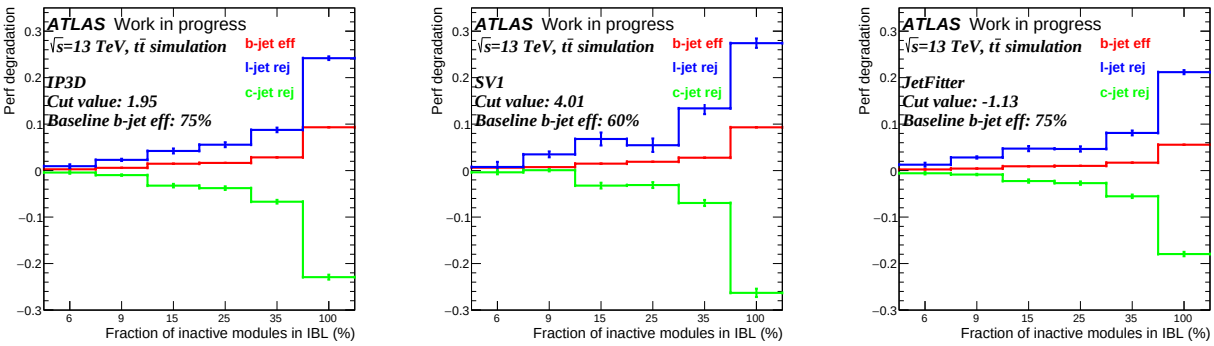

(a) (b) (c)

Figure 9.7.: The relative degradation in the performance for the six IBL failure scenarios using the 20.7 operating points for the IP3D (a), the SV1 (b) and the JetFitter (c) taggers. Sample used is $t\bar{t}$.

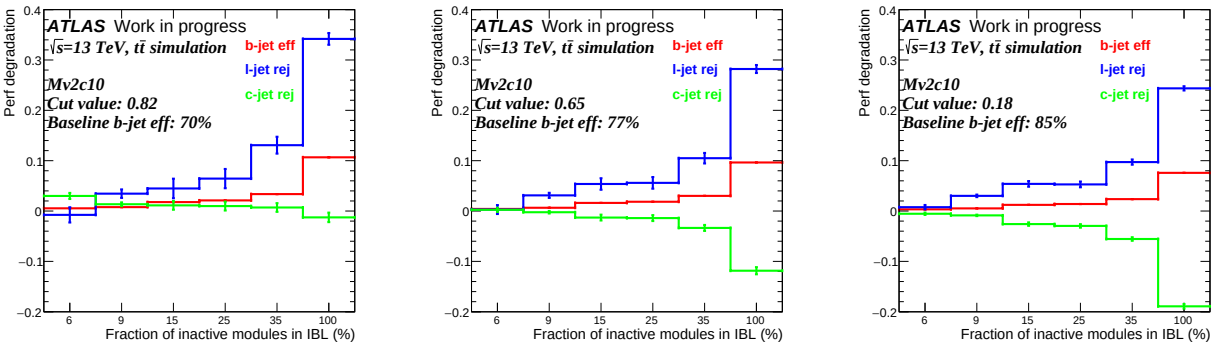

(a) (b) (c)

Figure 9.8.: The relative degradation in the performance for the six IBL failure scenarios using three different 20.7 operating points for the MV2c10 tagger. Sample used is $t\bar{t}$.

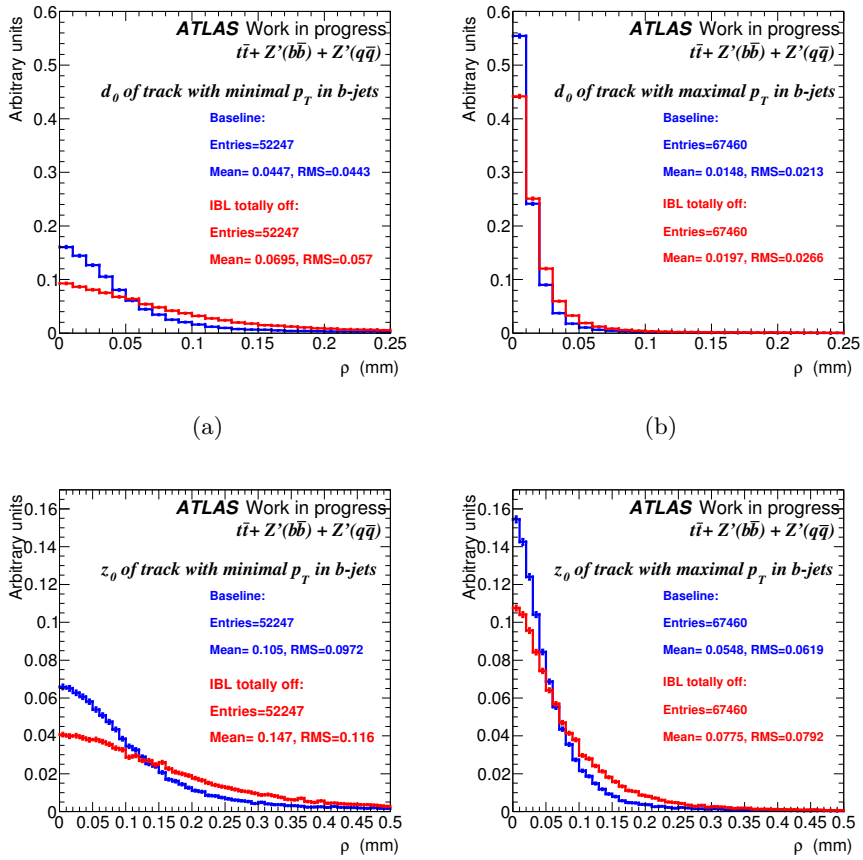

Figure 9.9.: Absolute value of (a) d_0 and (c) z_0 resolutions of the track with lowest p_T and (b), (d) for the track with highest p_T in b-jets, for the baseline (blue) and the scenario without IBL (red).

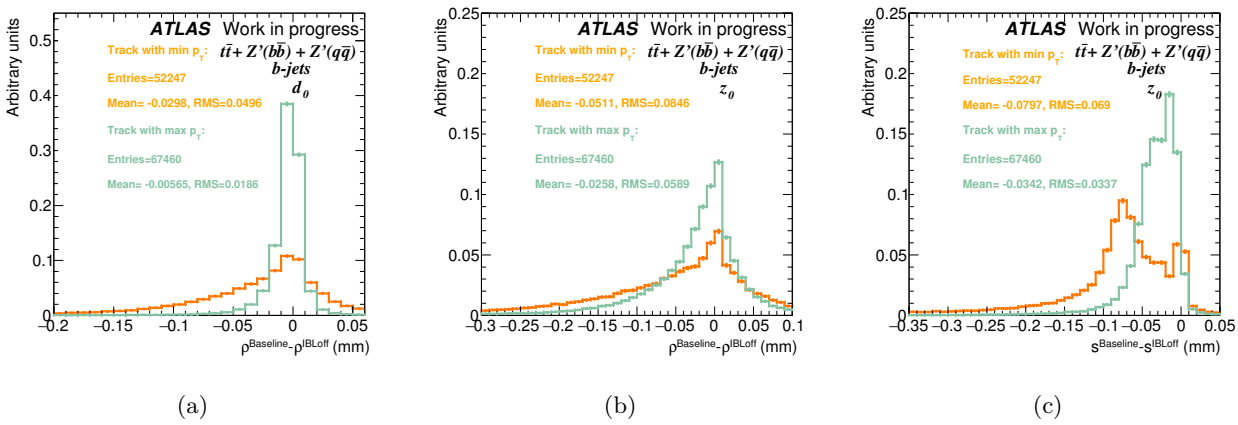

Figure 9.10.: The difference with and without IBL of the absolute value of d_0 resolution (a), z_0 resolution (b) and z_0 error (c) of track with lowest p_T (orange) and the track with highest p_T (green) in b-jets.

Effect on the IP3D b-tagger performance as a function of track and jet kinematics:

The individual track IP3D weight is changing due to the degradation in the track d_0 and z_0 measurements when disabling the IBL. As described previously in section 8.3.1, the track IP3D weight is computed as $W_{IP3D} = \log\left(\frac{p_b}{p_u}\right)$, where p_b, p_u are the track probability for the b- and light-flavour jet flavour hypotheses. The track IP3D weight distribution is shown in figure 9.11 for the lowest p_T and highest p_T tracks. Figures 9.11(a), 9.11(d) and 9.11(b), 9.11(e) show respectively the track weight distribution for the baseline and the scenario where IBL is totally disabled, while figures 9.11(c) and 9.11(f) show the track weight difference with enabled and disabled IBL.
Looking at the means, the high p_T tracks show a well discriminating weight distributions for the baseline which is not the case for low p_T tracks where a higher overlap between b- and light-jets appears. Due to the degradation in d_0 and z_0 measurements when disabling the IBL, for high p_T tracks, the weight changes from good to bad values, so the weight distributions show in this case an overlap between b- and light-jets and they are not anymore well discriminating. However, for low p_T tracks the weight changes from bad to worse, so the existing overlap between b- and the light-jets increases. Thus, the highest p_T tracks look more affected than the lowest p_T tracks in figures 9.11(c) and 9.11(f).
The impact of IBL off was studied as function of jet p_T as well. ROC curves (R_u vs ϵ_b) for three jet p_T ranges (low:]20, 50 GeV[, medium:]100, 140 GeV[, high: >300 GeV) are presented in figure 9.12 for the baseline and IBL off scenario. The highest effect due to IBL off appears for the low and medium p_T ranges: it is about 60% at 85% IP3D ϵ_b. The effect at high p_T is small, as explained before. The impact looks independent of jet η as shows figure 9.13.

Fraction and effect of loosing tracks with IBL totally off:

When the IBL is turned off, the track multiplicity in jet can change in particular the multiplicity of tracks selected by IP. For the mix of $t\bar{t} + Z'$ sample, 68% of b-jets are conserving their IP-tracks, 21% are loosing between 1 and 4 tracks and only 11% are gaining tracks. For light jets those numbers are: 73%, 18% and 9%. These b-jets loosing IP-tracks are more dense (higher number of IP-tracks), more boosted and have larger pseudorapidities as show figures 9.14 and 9.15.
Figure 9.16 shows the effect on the IP3D jet weight distribution for jets conserving (figures 9.16(a), 9.16(b) and 9.16(c)), loosing (figures 9.16(d), 9.16(e) and 9.16(f)) and gaining (figures 9.16(g), 9.16(h) and 9.16(i)) IP tracks. Left plot shows the baseline distributions, middle plot represents the distributions with IBL off. The right plot shows the difference of the weight for the same jet with and without IBL.
The log-likelihood ratio shown here is computed, as described previously in section 8.3.1, as ratio of the b- and light-flavour jet hypotheses. It is the sum of the per-track contributions (the track weight is shown previously in figure 9.11). If no tracks are found in the jet, a negative value of -20 is assigned as the algorithm output [92].
The jet P_b and P_u are computed as $\prod_{i=1}^{N} p_i$. In case of jet with P_b equal zero the W_{IP3D} is attributed to -30 while for P_u is zero it is assigned to 100. P_u (P_b) of a jet is equal zero if one of its track has a couple ($\frac{d_0}{\sigma(d_0)}$, $\frac{z_0}{\sigma(z_0)}$) without entries in the PDF used by IP3D. When turning

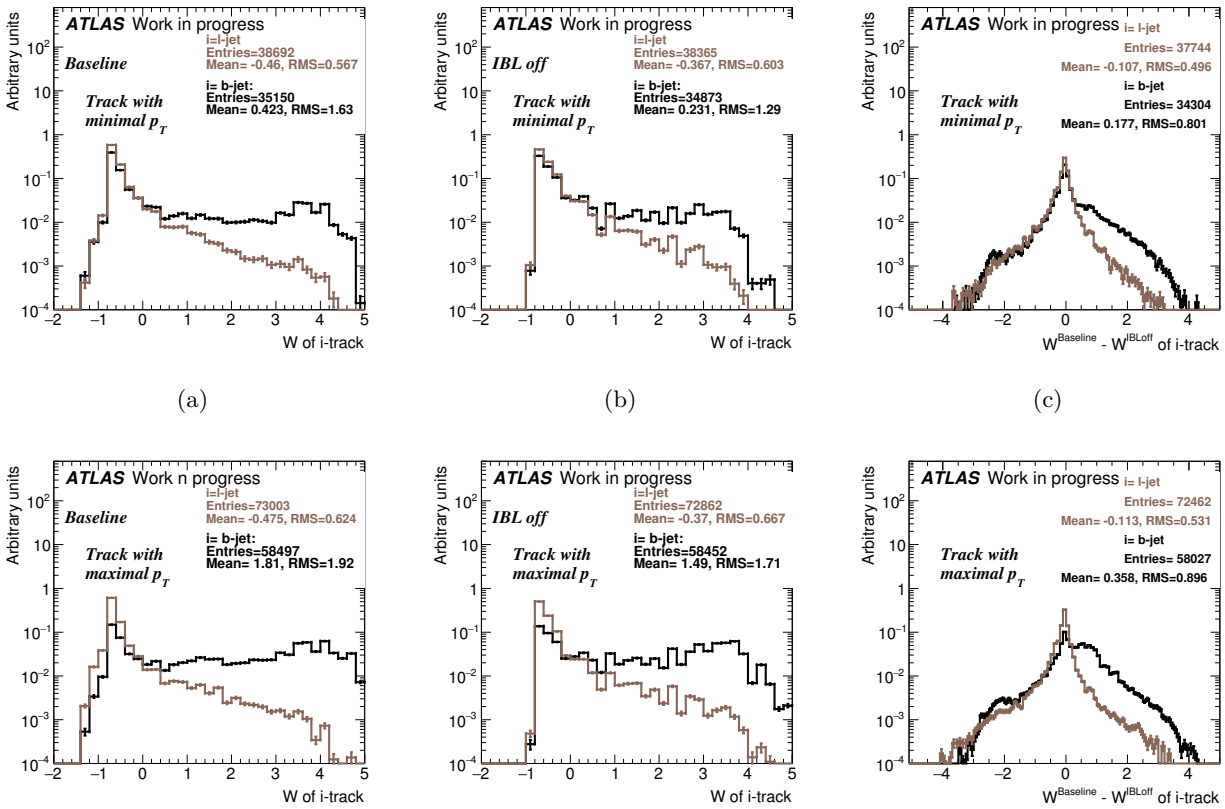

(a) (b) (c)

(d) (e) (f)

Figure 9.11.: The IP3D individual track weight distribution for the lowest p_T track in a jet (a), (b), (c) and the maximal p_T track in a jet (d), (e), (f) in b- (black) and light- (brown) jets.

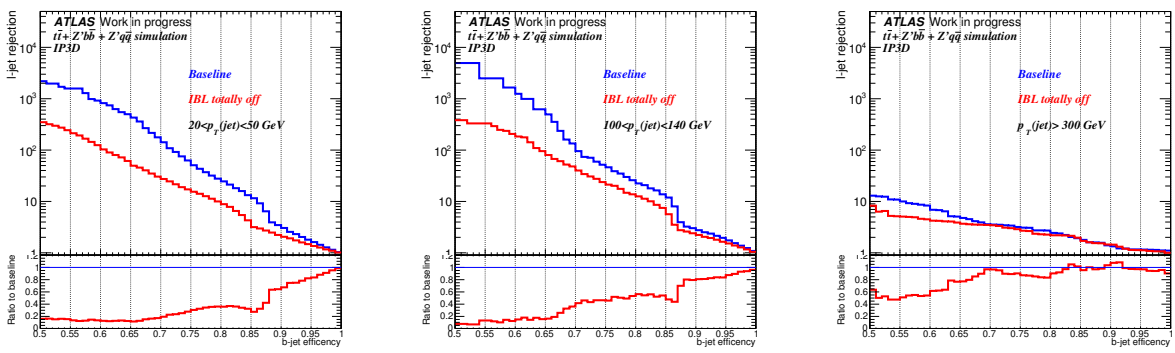

(a) (b) (c)

Figure 9.12.: IP3D light jet rejection vs b-jet efficiency as a function of jet p_T for IBL off (red) and the baseline (blue): (a) concerns only jets with p_T in]25, 50 GeV[range, (b) for]100, 140 GeV[and (c) for jets with $p_T >$ 300 GeV.

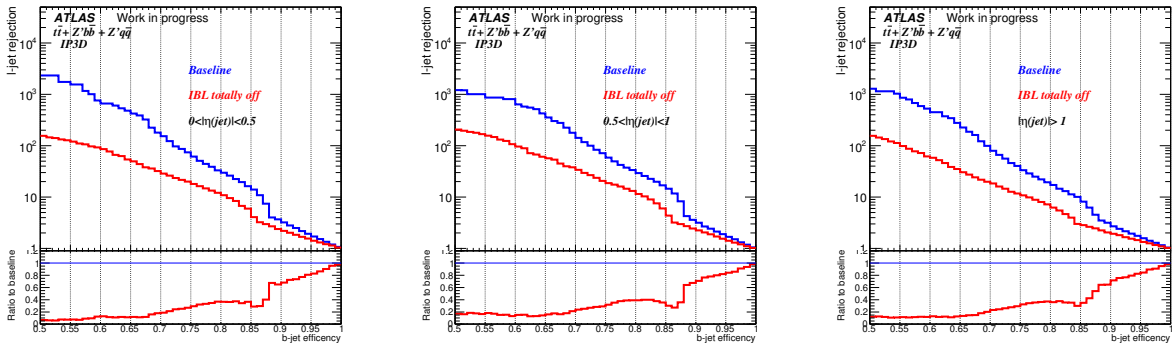

(a) (b) (c)

Figure 9.13.: IP3D light jet rejection vs b-jet efficiency as a function of jet η for IBL off (red) and the baseline (blue): (a) concerns only jets with η in [0, 0.5[range, (b) for [0.5, 1[while (c) contain jets with $\eta \geq 1$.

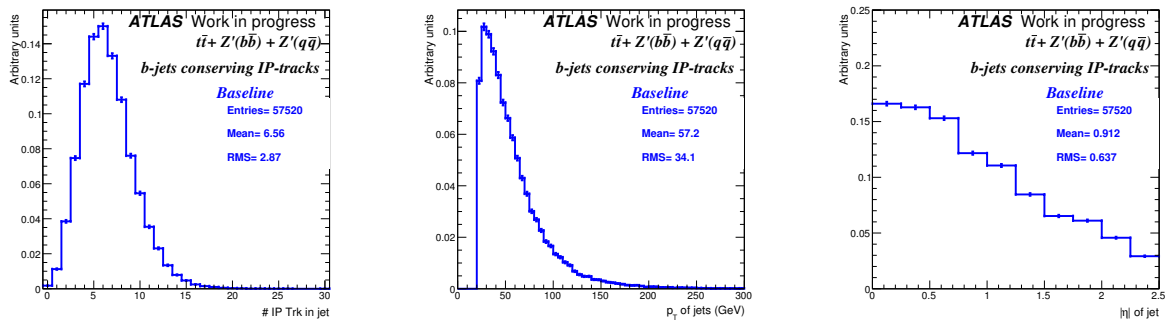

(a) (b) (c)

Figure 9.14.: (a) b-tagging quality track multiplicity, (b) p_T and (c) η distributions for b-jets conserving their tracks.

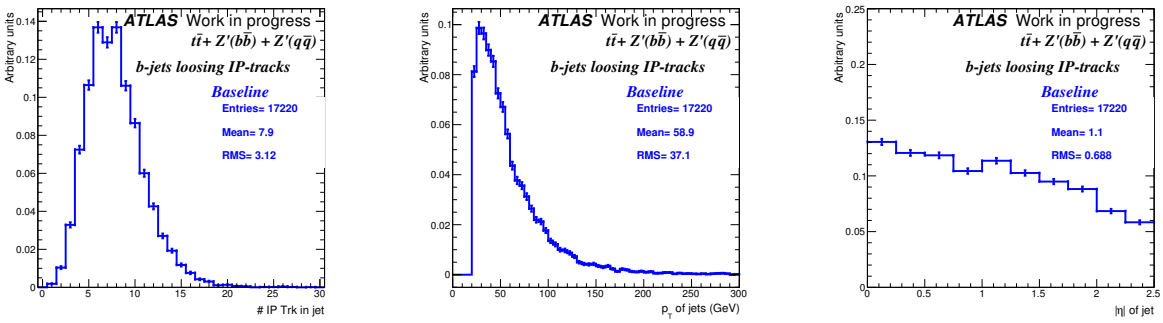

(a) (b) (c)

Figure 9.15.: (a) b-tagging quality track multiplicity, (b) p_T and (c) η distributions for b-jets loosing tracks.

off the IBL, an increase of jets with weights at -30 and 100 compared with the baseline is appearing and is due to the degradation in the impact parameters (d_0 and z_0) measurements.

The jets of figure 9.16(h) have the lowest spike at -20 as they are gaining tracks.

The jets loosing IP tracks in figure 9.16(e) have the highest peak at -20 as they may loose all their tracks.

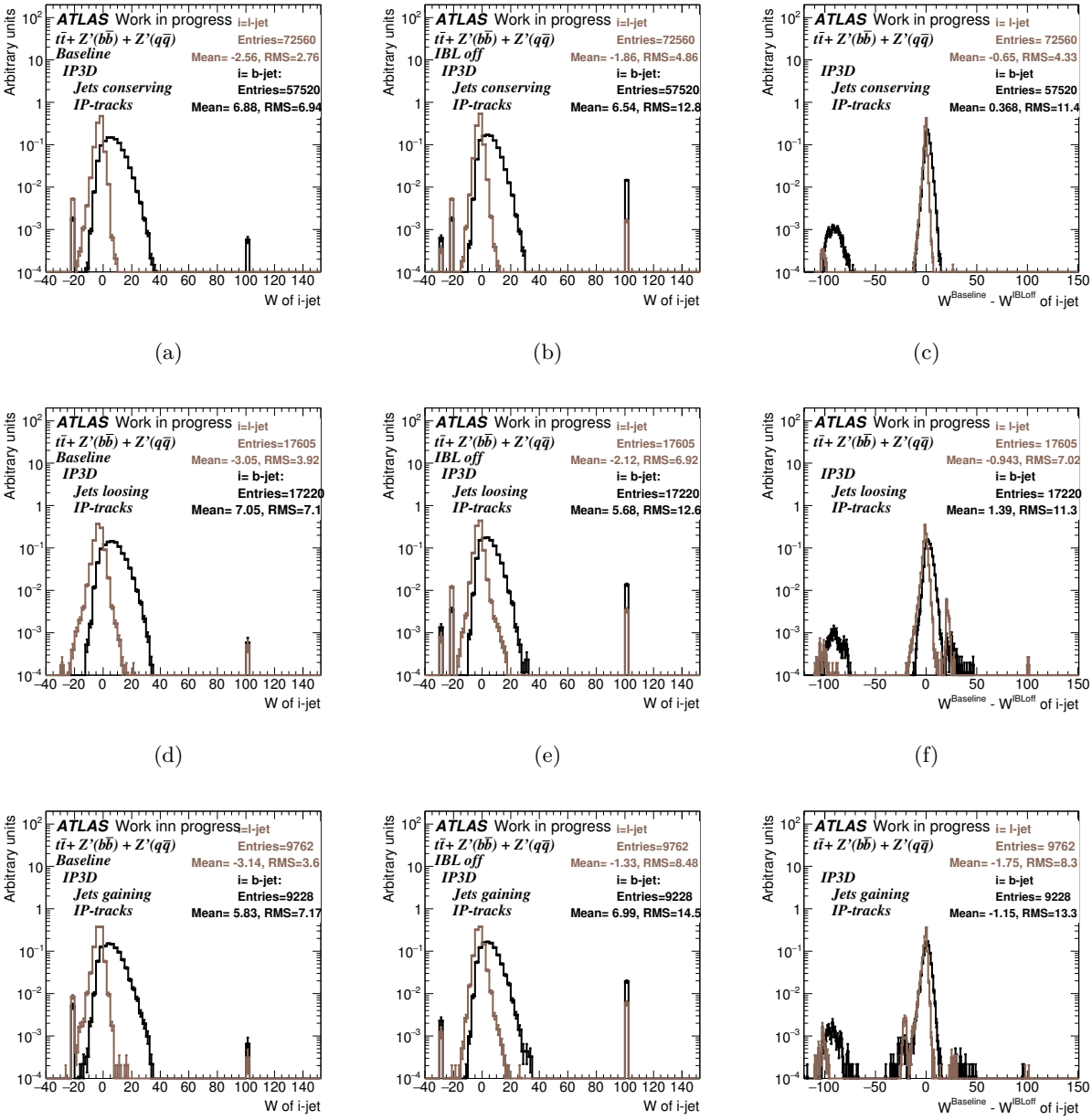

(a) (b) (c)

(d) (e) (f)

(g) (h) (i)

Figure 9.16.: The IP3D weight of b- (black) and light- (brown) jets conserving their IP-tracks (a), (b), (c), loosing (d), (e), (f) and gaining (g), (h), (i) IP-tracks. Left plots show the jet IP3D weight distribution for the baseline, the middle plots for the scenario without IBL and the right plots show the difference with and without IBL.

9.5.2. b-layer dead pixel modules configurations

This section is dedicated to the b-tagging performance evaluation for the L0 scenarios. Figures 9.17, 9.18 show the performance of the four tagging algorithms for the baseline and several L0 failure scenarios produced using $t\bar{t}$ and Z' mix samples respectively. The relative degradation in performance of the four algorithms at fixed b-jet efficiency for the L0 scenarios produced with $t\bar{t}$ sample is shown in tables 9.12 and 9.13. It is clear by comparing the fractions in these tables with those of the IBL scenarios presented in tables 9.8 and that the effect of the IBL is more important than L0 for jets with medium p_T in $t\bar{t}$ sample. However, for high p_T jets in Z' mix sample, the MV2c10 algorithm performance (figure 9.18(d)) without L0 shows a degradation higher than the case of the scenario with IBL off by a factor of two. In the case of Z' mix sample, this is presumably because a large fraction of the B-hadrons fly beyond the IBL before decaying, so for these boosted b-jets, the L0 role is more important than the IBL role.

Table 9.12.: The relative degradation in the light-jet rejection (%) for the IP3D and the MV2c10 taggers at a b-tagging efficiency of 75% for the six L0 scenarios produced using $t\bar{t}$ sample.

L0 scenarios y (%)	6	9	15	25	35	100
R_u degradation for IP3D at $\epsilon_b = 75\%$	4	8	10	18	22	42
R_u degradation for MV2c10 at $\epsilon_b = 75\%$	3	5	10	12	15	40

Table 9.13.: The relative degradation in light-jet rejection (%) for the SV1 and the JetFitter taggers at a b-tagging efficiency of 60% for the six L0 scenarios produced using $t\bar{t}$ sample.

L0 scenarios y(%)	6	9	15	25	35	100
R_u degradation for SV1 at $\epsilon_b = 60\%$	1	3	5	7	10	20
R_u degradation for JetFitter at $\epsilon_b = 60\%$	2	4	8	10	15	30

In the same way as in section 9.5.1.2, the degradation in the b-tagging performance for a fixed OP per L0 scenario using $t\bar{t}$ sample was checked. The figure 9.19 shows the degradation in the performance of IP3D, SV1 and JetFitter algorithms for the operating points listed in table 9.10 and figure 9.20 shows the same for MV2c10 algorithm at three different operating points appearing in the same table.

Each bin of the x-axis represents a scenario in L0 where the last bin is dedicated for the scenario with L0 totally off. The y-axis shows the degradation in the b-jet efficiency, R_u and R_c. For the four algorithms, the effect is smaller comparing with the results in section 9.5.1.2 for IBL scenarios. The light jet rejection is more affected than the b-jet efficiency which shows only 2% degradation for the scenario without L0 for a baseline MV2c10 b-jet efficiency of 77% presented in figure 9.20(b).

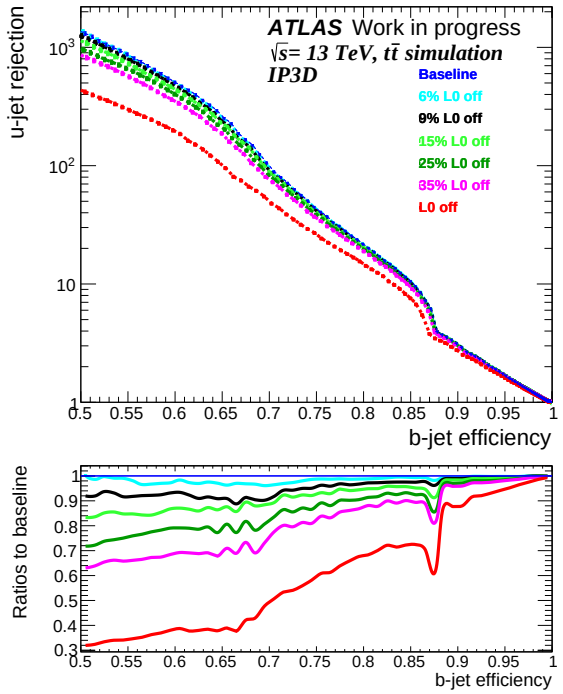

(a) IP3D

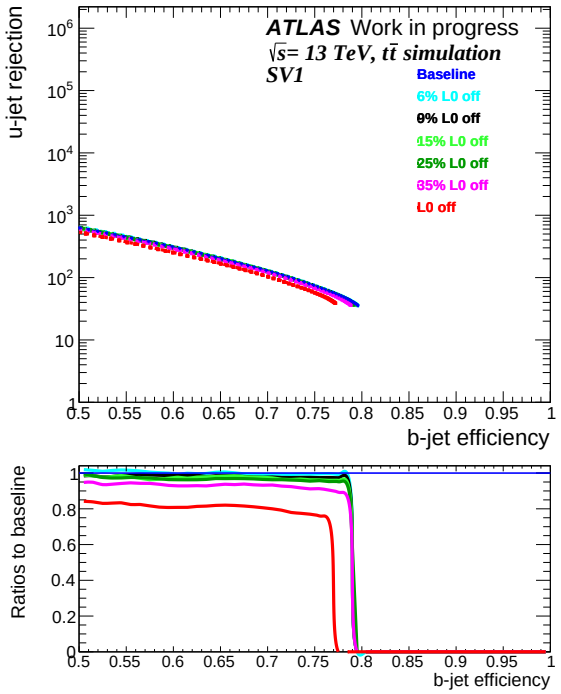

(b) SV1

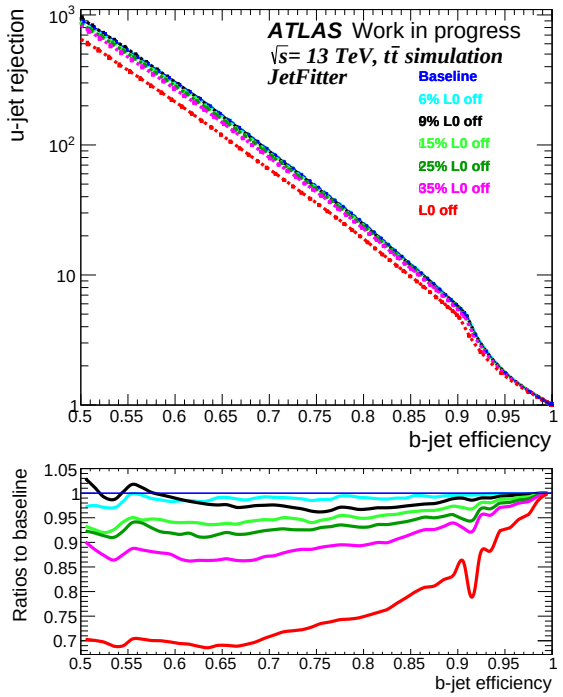

(c) JetFitter

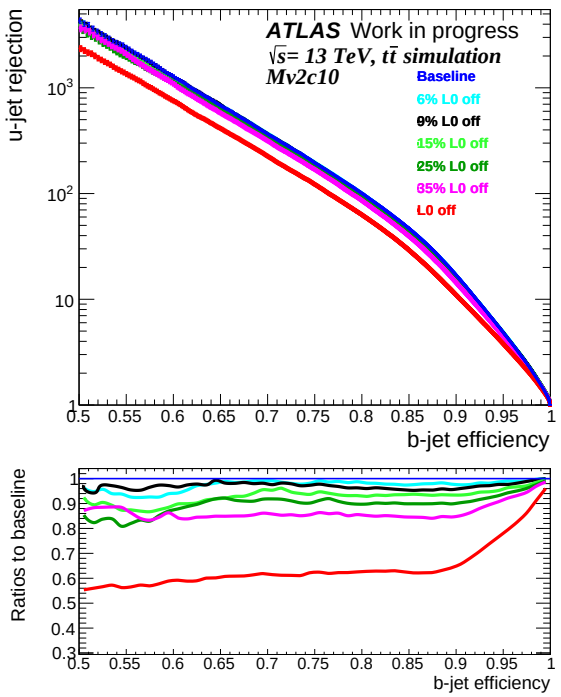

(d) Mv2c10

Figure 9.17.: The light jet rejection as a function of b-jet efficiency for the IP3D (a), SV1 (b), JetFitter (c) and MV2c10 (d) algorithms for L0 failure scenarios compared to the baseline in blue, for $t\bar{t}$ sample.

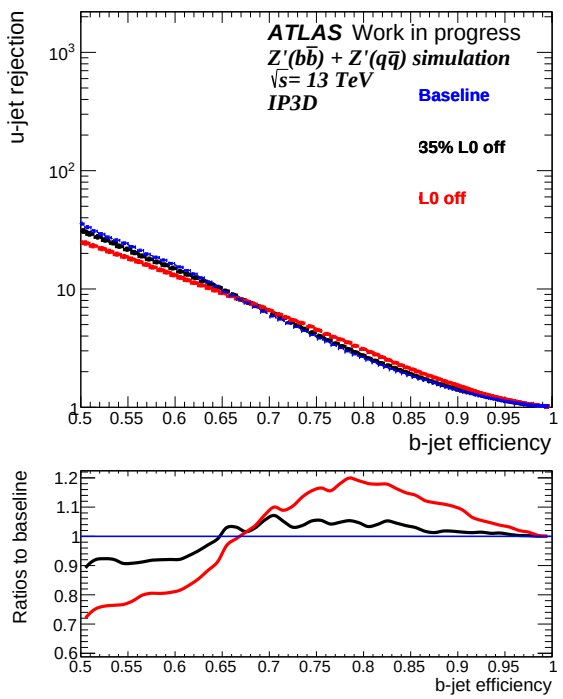

(a) IP3D

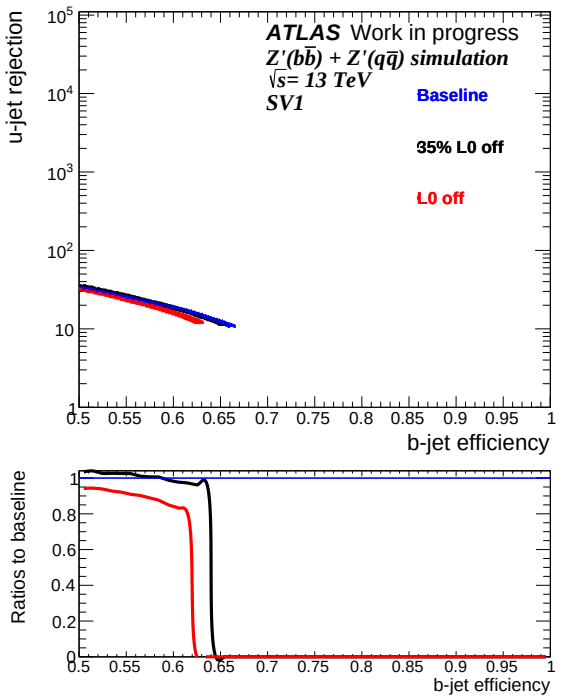

(b) SV1

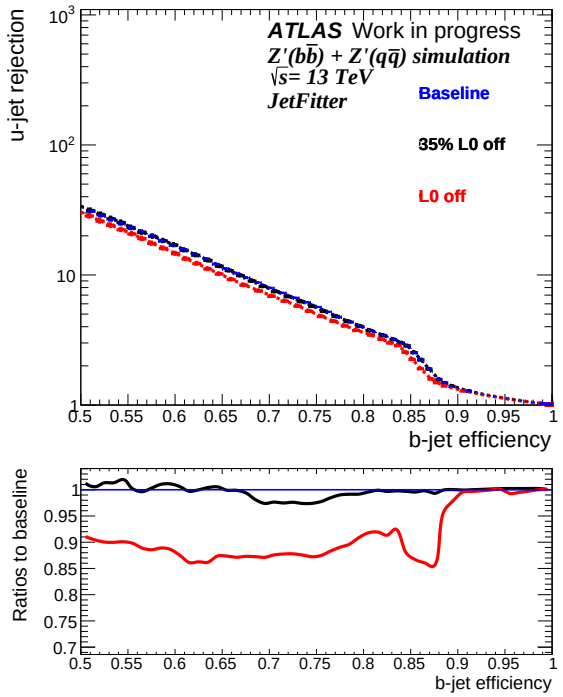

(c) JetFitter

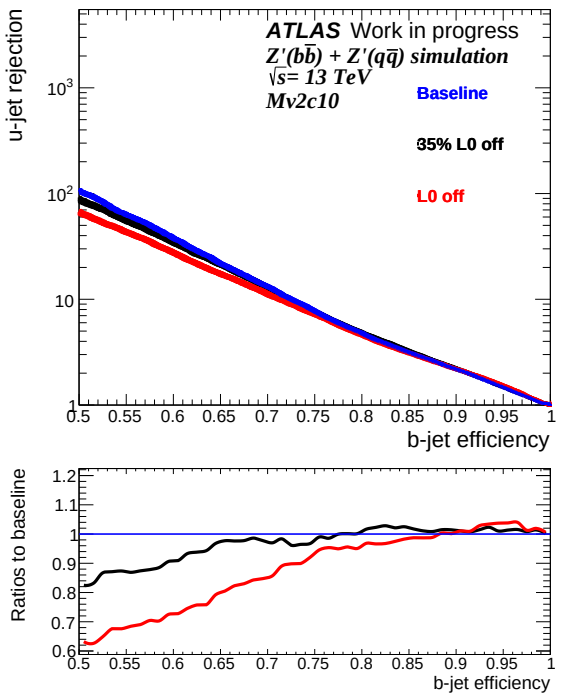

(d) Mv2c10

Figure 9.18.: The light jet rejection as a function of b-jet efficiency for the IP3D (a), SV1 (b), JetFitter (c) and MV2c10 (d) algorithms for L0 failure scenarios compared to the baseline in blue, for Z' mix sample.

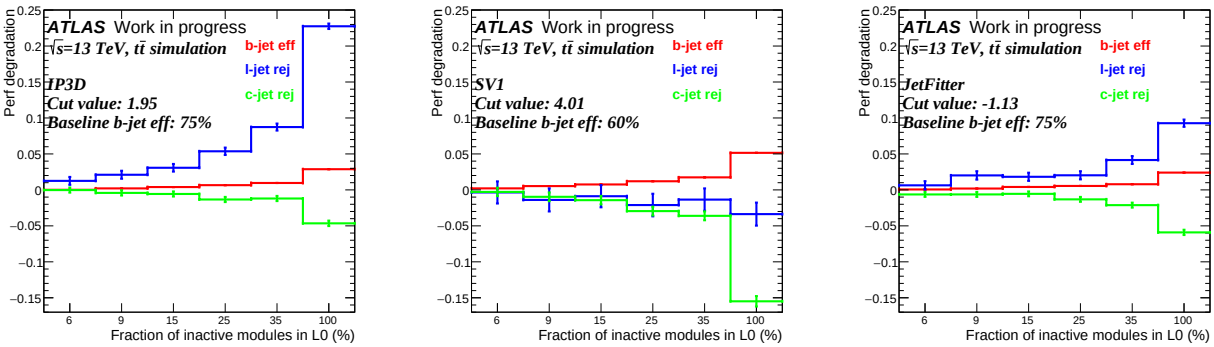

(a) (b) (c)

Figure 9.19.: The relative degradation in the performance for the six L0 failure scenarios using 20.7 OP for IP3D (a), SV1 (b) and JetFitter (c). Sample used is $t\bar{t}$.

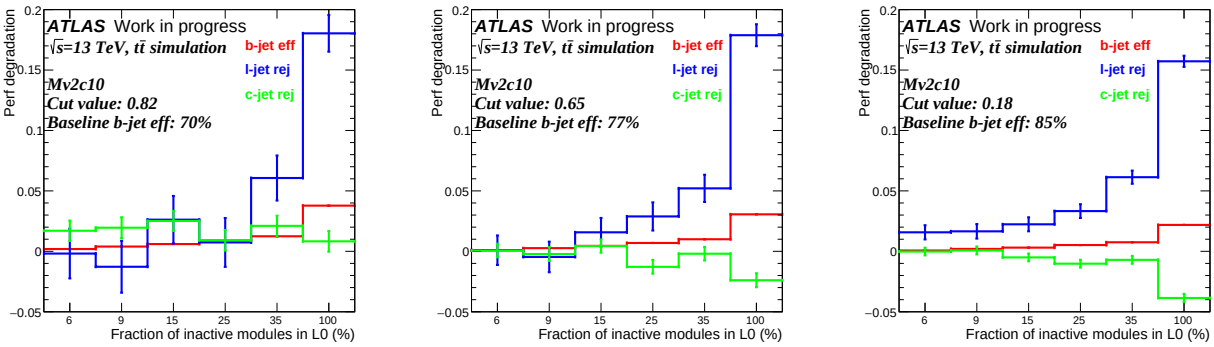

(a) (b) (c)

Figure 9.20.: The relative degradation in the performance for the six L0 failure scenarios using three different 20.7 OP for MV2c10 algorithm. Sample used is $t\bar{t}$.

9.5.3. Layer-1 and Layer-2 dead pixel modules configurations

As seen in the previous sections, the scenarios with disabled modules in the innermost layers to the interaction point (IBL, L0) show a higher degradation in the b-tagging performance for medium jet p_T ($t\bar{t}$ sample) compared to high jet p_T (Z' mix). In this section, the effect of increasing the fraction of inactive modules in the outermost layers (L1 and L2) is presented for $t\bar{t}$ (figure 9.21) and Z' mix samples (figure 9.22). SV1 algorithm shows an improvement in the light jet rejection for the scenario with L1 totally disabled for $t\bar{t}$ sample. This is an artifact of the internal cuts in the SV1 algorithm aimed at suppressing vertices beyond the IBL. For the $t\bar{t}$ sample the region outside of the IBL contains so few real vertices that they can't improve the b-tagging efficiency at all, while fake vertices there degrade the light jet rejection significantly. That's why it's better not to look for vertices at all outside of the IBL in the standard $t\bar{t}$ events. As expected, this improvement disappear when looking at high p_T jets ($p_T >$ 200 GeV) in the same $t\bar{t}$ events as shows figure 9.23(a).

Figures 9.23(b) and 9.23(c) show the radial distance distributions of the reconstructed secondary vertex (SV) in b- and light-jets respectively for the baseline and the various scenarios where one layer is totally disabled, for $t\bar{t}$ sample. A dip between L0 and L1 in case when L1 is completely off appears. It contributes to the suppression of vertices outside of the IBL.

The degradation in the light jet rejection for IP3D, JetFitter and MV2c10 algorithms at b-jet efficiency of 60% is presented in table 9.14 for L1 totally off and in table 9.15 for L2 totally off scenarios. Comparing the last two columns of both tables, it is clear that the effect is higher by about a factor of 2 for high p_T jets than for medium p_T jets for MV2c10. However, the MV2c10 light jet rejection degradation at medium p_T jets ($t\bar{t}$ sample) is not negligible about 28% for L1 totally off and 20% for L2 totally off at 60% b-jet efficiency.

Table 9.14.: The relative degradation in the light-jet rejection (%) for the IP3D, the JetFitter and the MV2c10 taggers at 60% b-tagging efficiency for the scenario with L1 totally off produced using $t\bar{t}$ sample (second column) and Z' mix sample (last column).

L1 totally off scenario	$t\bar{t}$	Z' mix
R_u degradation for IP3D at $\epsilon_b = 60\%$	20	26
R_u degradation for JetFitter at $\epsilon_b = 60\%$	20	34
R_u degradation for MV2c10 at $\epsilon_b = 60\%$	28	48

Table 9.15.: The relative degradation in the light-jet rejection (%) for the IP3D, the JetFitter and the MV2c10 taggers at 60% b-tagging efficiency for the scenario with L2 totally off produced using $t\bar{t}$ sample (second column) and Z' mix sample (last column).

L2 totally off scenario	$t\bar{t}$	Z' mix
R_u degradation for IP3D at $\epsilon_b = 60\%$	14	18
R_u degradation for JetFitter at $\epsilon_b = 60\%$	4	32
R_u degradation for MV2c10 at $\epsilon_b = 60\%$	20	47

Highly boosted B-hadrons in Z' mix sample are expected to decay beyond the IBL as seen in figure 9.1(c). Therefore, the degradation in the b-tagging performance was also studied as function of the B-hadron decay radius for Z' mix sample. As shows the figure 9.24(a), the

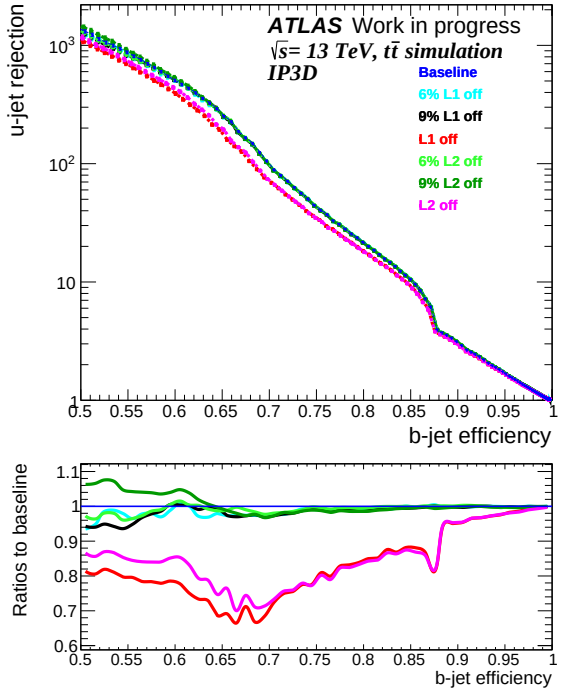

(a) IP3D

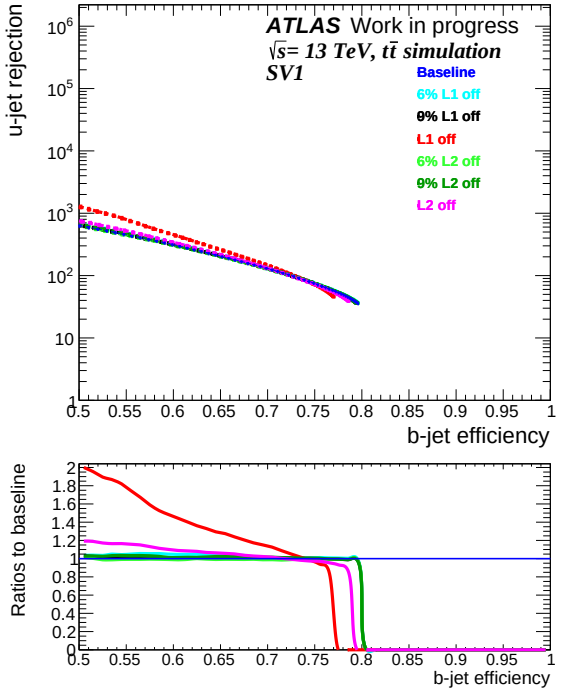

(b) SV1

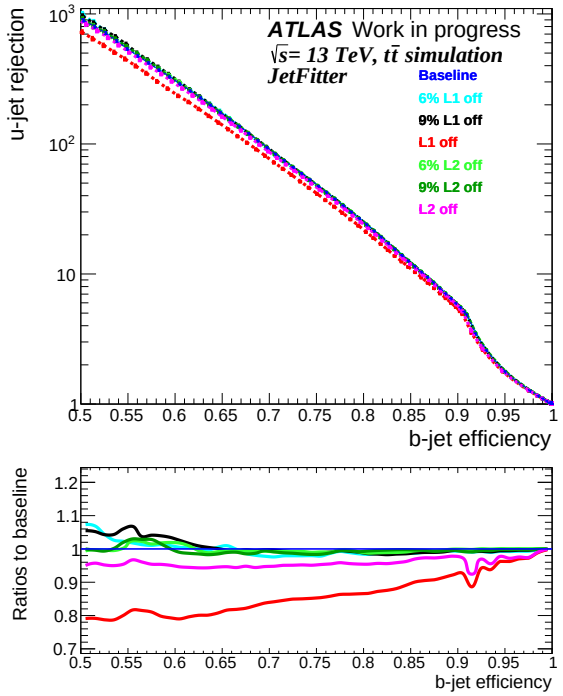

(c) JetFitter

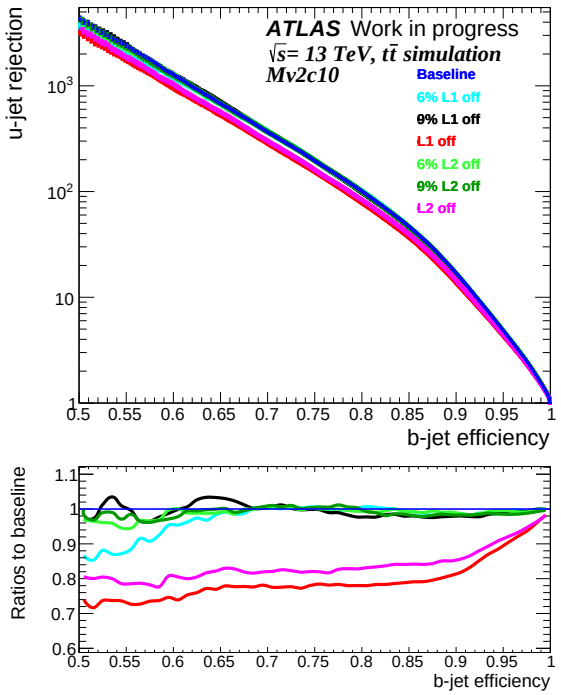

(d) Mv2c10

Figure 9.21.: The light jet rejection as a function of b-jet efficiency for the IP3D (a), SV1 (b), JetFitter (c) and MV2c10 (d) algorithms for L1 failure scenarios compared with the baseline in blue, for $t\bar{t}$ sample.

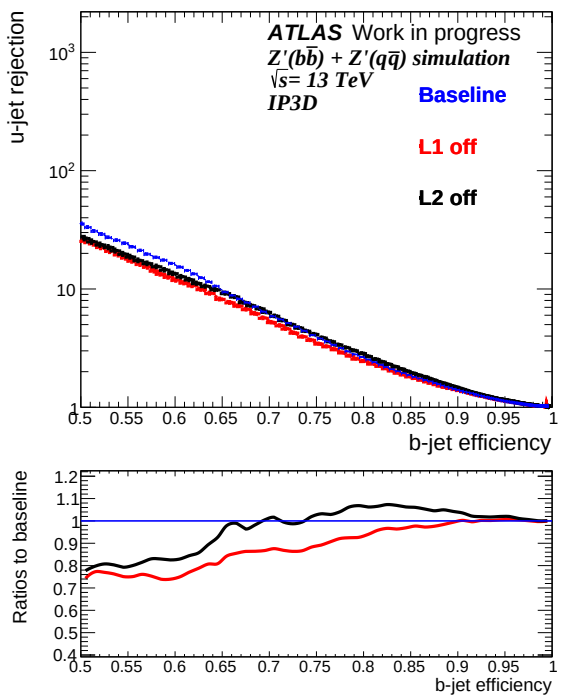

(a) IP3D

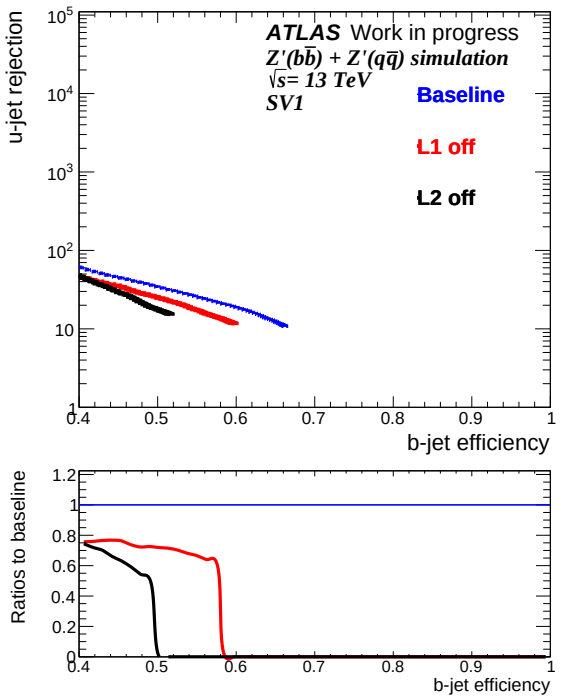

(b) SV1

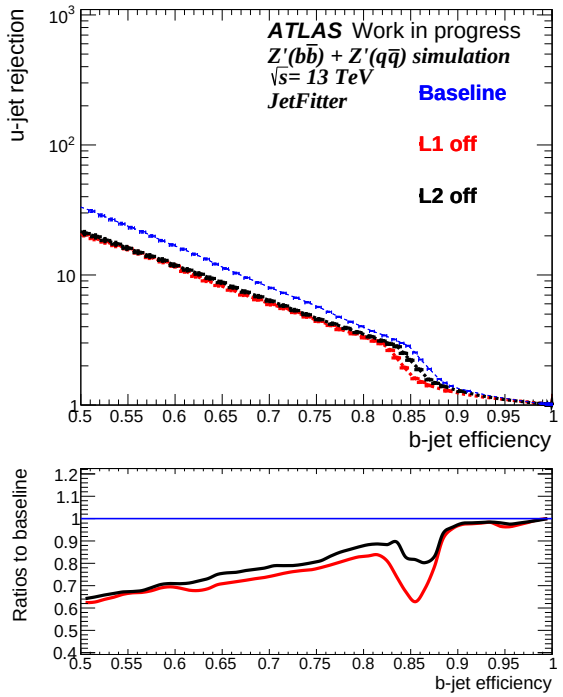

(c) JetFitter

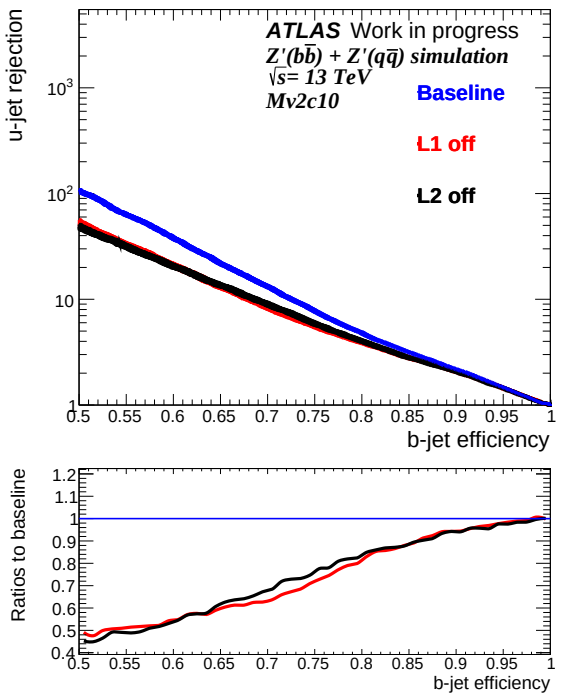

(d) Mv2c10

Figure 9.22.: The light jet rejection as a function of b-jet efficiency for the IP3D (a), SV1 (b), JetFitter (c) and MV2c10 (d) algorithms for L1 failure scenarios compared with the baseline in blue, for Z' mix sample.

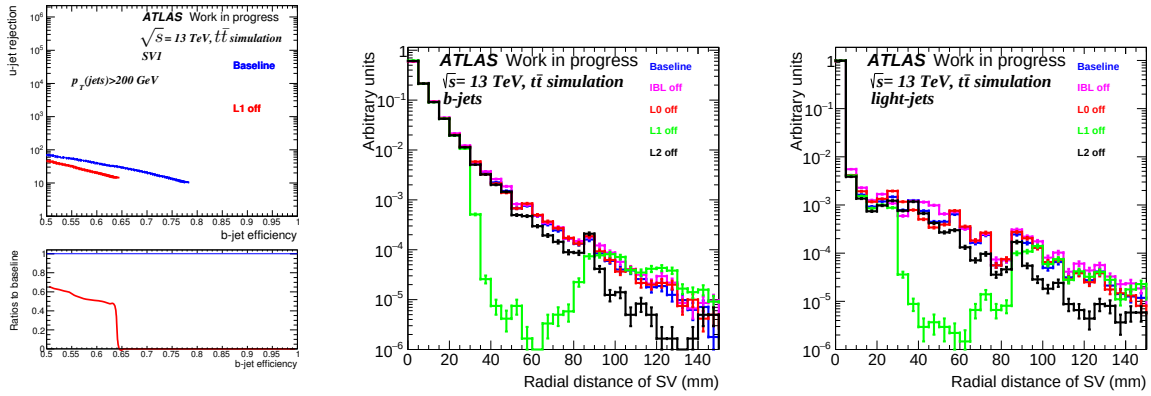

(a) (b) (c)

Figure 9.23.: (a) The SV1 performance for jets with $p_T >$ 200 GeV for the scenario with L1 totally off (red) and the baseline (blue) for $t\bar{t}$ sample. (b) The radial distance distributions of the reconstructed secondary vertex (SV) in b- and (c) in light-jets

performance degradation, in case of B-hadrons decaying inside the IBL, is the same for the four scenarios each with one different layer turned totally off. The degradation in the light jet rejection is about 20% for MV2c10 at 75% b-jet efficiency. However, the figure 9.24(b) illustrating the case where B-hadrons decay beyond the IBL (and inside L0) shows a higher degradation for the scenarios with L1 off or L2 off around 60% at ϵ_b=75%. For the scenario with L0 off the degradation is smaller about 20%.

Tracks coming from B-hadrons decaying between IBL and L0 behave like tracks in category 5 called 'hits not found in IBL and not expected' (show similar d_0 and z_0 significance). For the baseline these tracks are distributed in the 14 categories (listed in table 8.2) as hits are expected in IBL because IBL is active, however without IBL they only go to category 5. Therefore an important improvement in the light jet rejection for the scenario with IBL off with respect to the baseline appears in figure 9.24(b) and is due to the new distribution of tracks in the categories. The improvement with IBL off is not seen for $t\bar{t}$ sample as the tracks behave like tracks in 'hit not found in IBL hit expected' category (B-hadrons not boosted, they decay before IBL) while without IBL tracks becomes in category 5.

The figure 9.24(c) shows the MV2c10 performance of b-jets with B-hadrons decaying between L0 and L1. The scenarios IBL off, L0 off show a small improvement in the R_u with respect to the baseline of about 10%. A higher improvement is expected in scenario with both IBL and L0 are off because in this case tracks go to category 3 where no hits found in IBL and L0 and both are not expected which is the normal place of these tracks.

For $\bar{t}t$ sample, the degradation in the performance of IP3D algorithm using the same OP corresponding to a baseline $\epsilon_b = 75\%$ look similar for L1 and L2 scenarios as shows the figure 9.25(a). The same is seen for the three OP checked for MV2c10 algorithm by comparing the plots of figure 9.26. For Z' mix sample, the degradation of the IP3D, SV1 and JetFitter algorithms for the OP checked are shown in figure 9.27, while figure 9.28 shows the same for the three OP of MV2c10. For MV2c10 algorithm, L1 off and likewise L2 off scenarios show a high degradation in the b-jet efficiency around 10% while for the IBL off scenario the light jet rejection is the most affected.

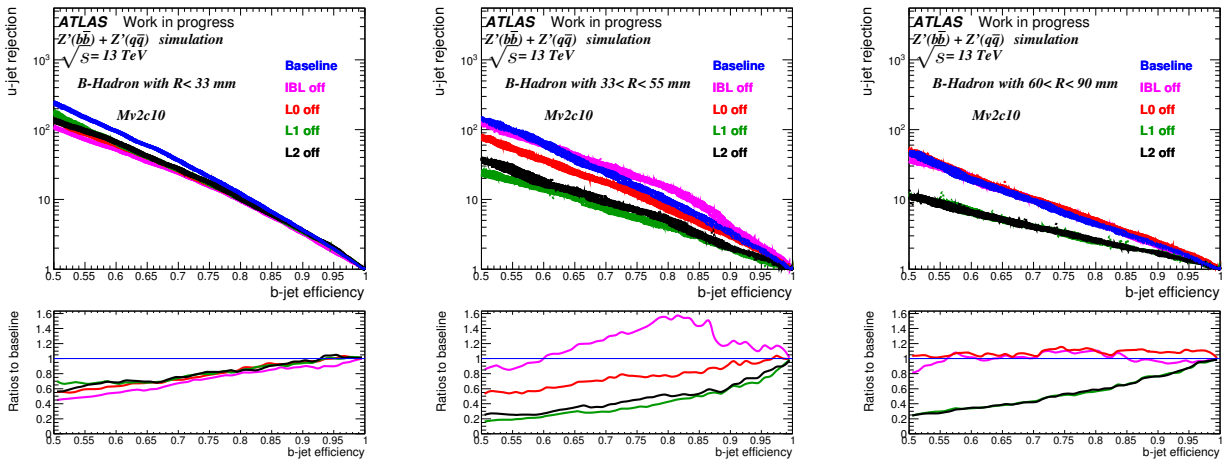

(a) (b) (c)

Figure 9.24.: MV2c10 light jet rejection as a function of b-jet efficiency for extreme scenarios IBL off (purple), L0 off (red), L1 off (green), L2 off (black) compared with the baseline in blue, for B-hadrons decaying before IBL (a) and before L0 (b), before L1 (c) in Z' mix sample.

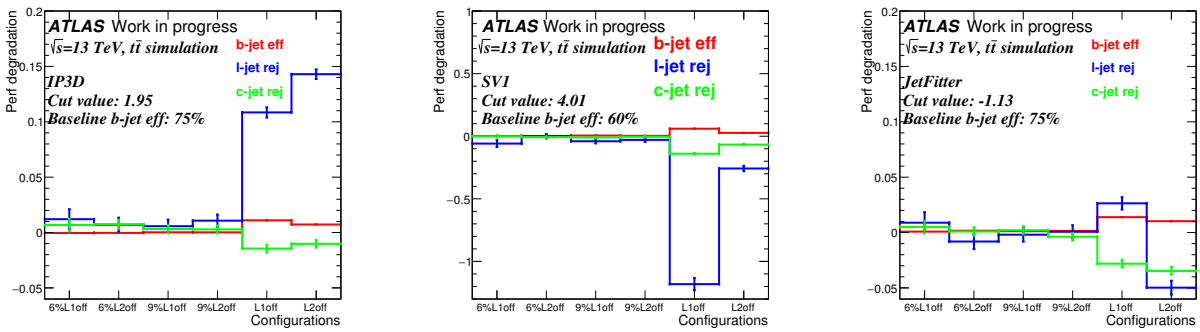

(a) (b) (c)

Figure 9.25.: The degradation in the performance for L1 failure scenarios using 20.7 OP for IP3D (a), SV1 (b) and JetFitter (c). Sample used is $t\bar{t}$.

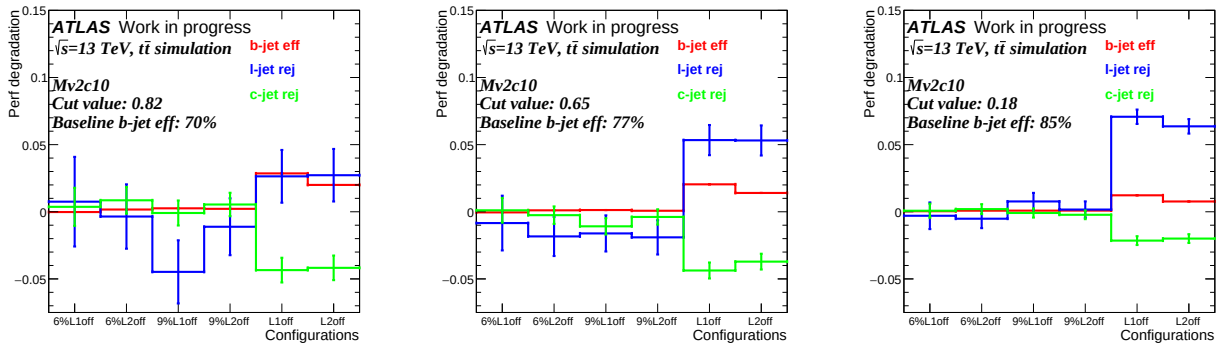

(a) (b) (c)

Figure 9.26.: The degradation in the performance for L1 failure scenarios using three different 20.7 OP for MV2c10 algorithm. Sample used is $t\bar{t}$.

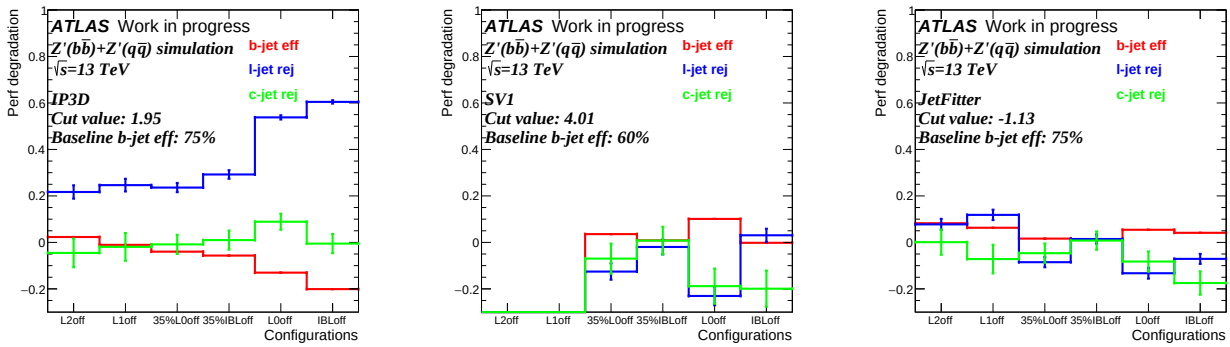

(a) (b) (c)

Figure 9.27.: The relative degradation in the performance using 20.7 OP for IP3D (a), SV1 (b) and JetFitter (c) for scenarios produced with Z' mix sample.

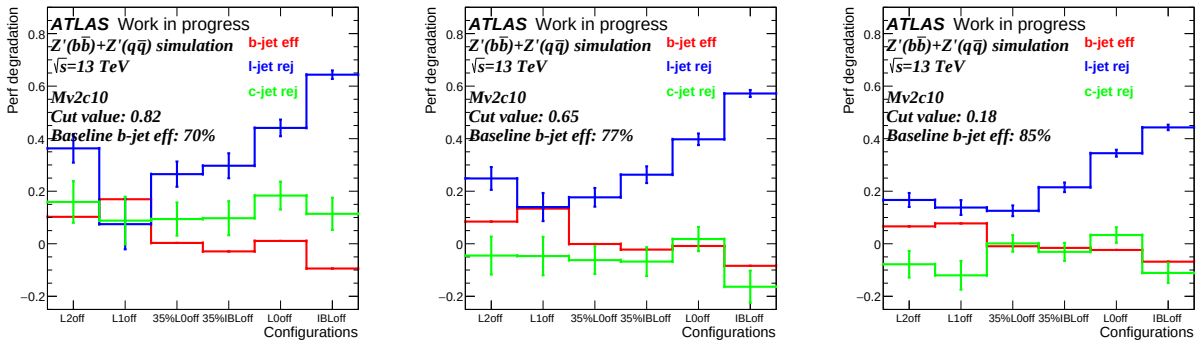

(a) (b) (c)

Figure 9.28.: The relative degradation in the performance using three different 20.7 OP for MV2c10 algorithm for scenarios produced with Z' mix sample.

9.5.4. b-layer pixel ToT configurations

In this section, the effect of increasing the L0 ToT minimal cut up to 13 BC on the b-tagging performance is presented for $t\bar{t}$ and Z' mix samples. Figure 9.29 shows a comparison between the baseline performance of the four b-tagging algorithms: IP3D (figure 9.29(a)), SV1 (figure 9.29(b)) JetFitter (figure 9.29(c)) and MV2c10 (figure 9.29(d)) and their performance for the six L0 scenarios produced with the same $t\bar{t}$ sample. As expected, the scenario with the highest ToT minimal cut in L0, at 13 BC, shows the highest decrease in performance.

Comparing the IP3D algorithm performance for the scenario with increased ToT minimal cut to 13 BC in L0, the light-flavour jet rejection is degraded by 30% with respect to the baseline for a 75% b-tagging efficiency. At fixed 75% MV2c10 b-tagging efficiency the loss in performance is about 15%. The degradation for the other L0 scenarios is represented in table 9.16.

Table 9.16.: The relative degradation in the light-jet rejection (%) for the IP3D and the MV2c10 taggers at 75 % b-tagging efficiency for the six L0 scenarios produced using $t\bar{t}$ sample. The x and y represent respectively the ToT cuts for the L0 (offline) and the two outermost layers.

L0 scenarios (x, y)	(6, 4)	(6,6)	(7, 6)	(8, 4)	(10,4)	(13,4)
R_u degradation for IP3D at $\epsilon_b = 75\%$	1	1	2	4	10	30
R_u degradation for MV2c10 at $\epsilon_b = 75\%$	0	1.5	2	5	7	15

The b-tagging algorithms based on secondary vertex properties SV1 and JetFitter are more robust because they don't use an explicit categorization of the tracks depending on the hit patterns in the pixel layers as is the case of IP3(2)D algorithm. The degradation in the light-jet rejection for these algorithms at 60 % b-jet efficiency, depending on the L0 scenario, is presented in table 9.17.

Table 9.17.: The relative degradation in the light-jet rejection (%) for the SV1 and the JetFitter taggers at 60 % b-tagging efficiency for the six L0 scenarios produced using $t\bar{t}$ sample. The x and y represent respectively the ToT cuts for L0 (offline) and the two outermost layers.

L0 scenarios (x, y)	(6, 4)	(6, 6)	(7, 6)	(8, 4)	(10, 4)	(13, 4)
R_u degradation for SV1 at $\epsilon_b = 60\%$	0	0	0	2	5	10
R_u degradation for JetFitter at $\epsilon_b = 60\%$	0	0	0	5	6	11

As show tables 9.16 and 9.17, increasing the offline ToT minimal cut in L0 to 7 doesn't affect any of the four b-tagging algorithms performance for the $t\bar{t}$ sample.

Figure 9.30 shows the same comparison for the light-jet rejection but for the Z' mix sample. The degradation in light-jet rejection for MV2c10 algorithm for the scenario with ToT minimal cut in L0 at 13 BC is about 10% at 75% b-jet efficiency.

Next, we checked the degradation in the b-tagging performance for a fixed OP for each L0 scenario. Figure 9.31 shows the degradation in performance for IP3D, SV1 and JetFitter algorithms for the operating points listed in table 9.10.

Figure 9.32 shows the same for the MV2c10 algorithms at the three different operating points appearing in the same table. Each bin of the x-axis represents a scenario in L0 with in-

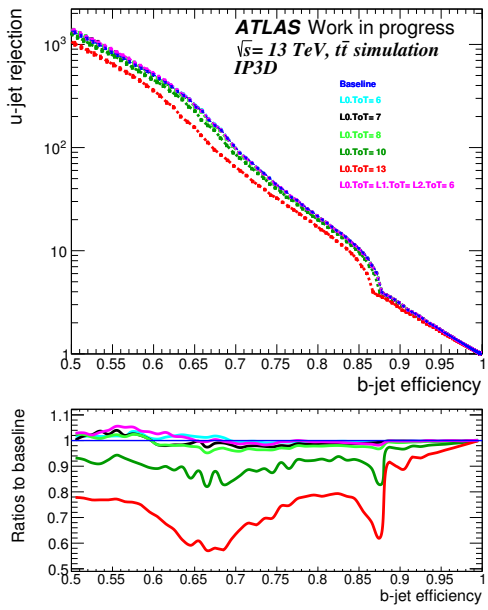

(a) IP3D

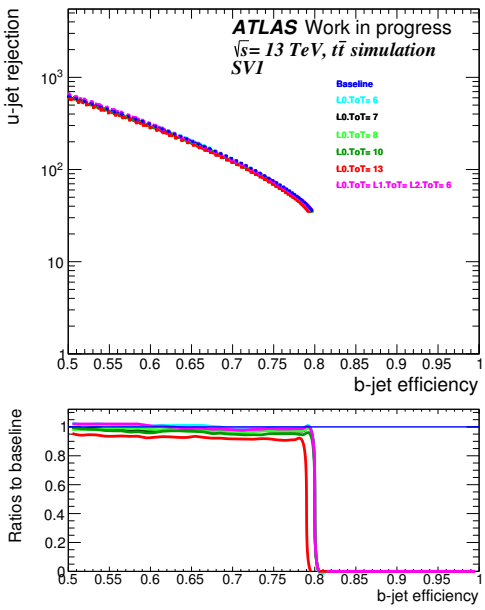

(b) SV1

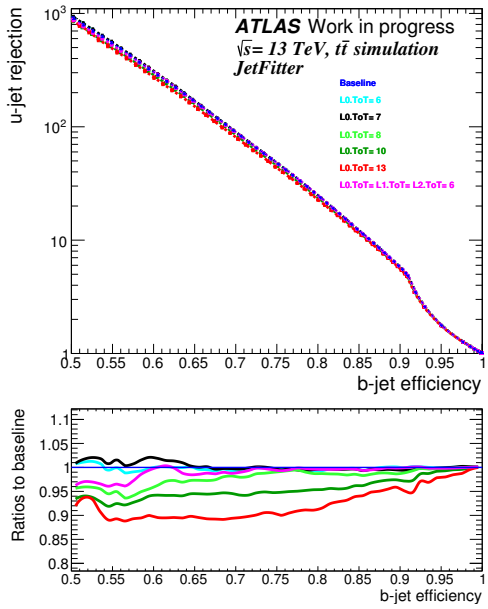

(c) JetFitter

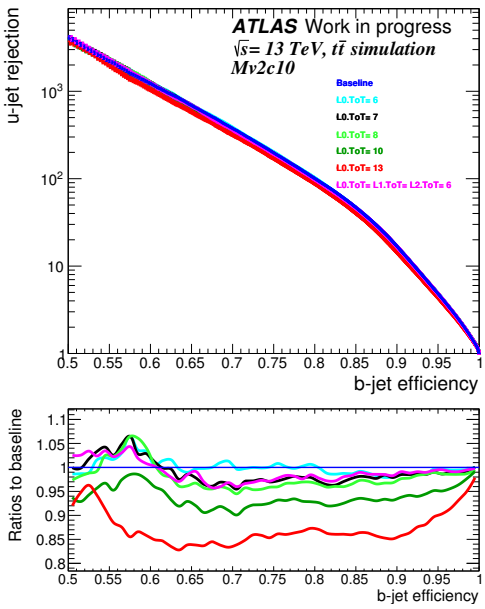

(d) Mv2c10

Figure 9.29.: The light jet rejection as a function of b-jet efficiency for the IP3D (a), SV1 (b), JetFitter (c) and MV2c10 (d) algorithms for MC15c L0 scenarios compared with the baseline in blue for $t\bar{t}$ sample.

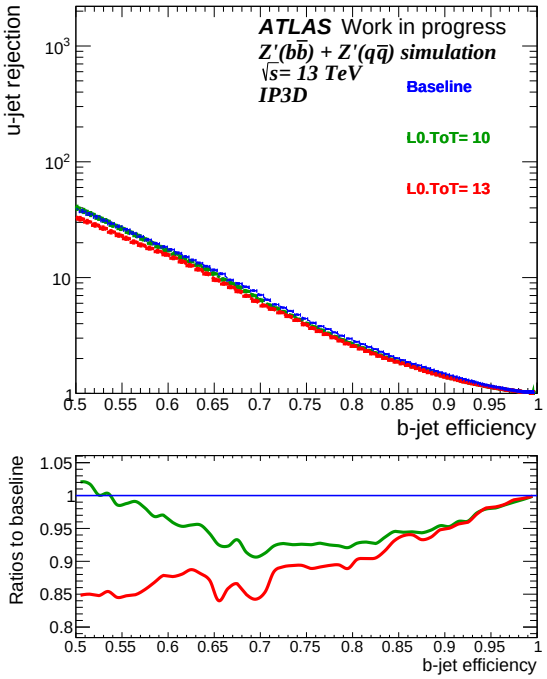

(a) IP3D

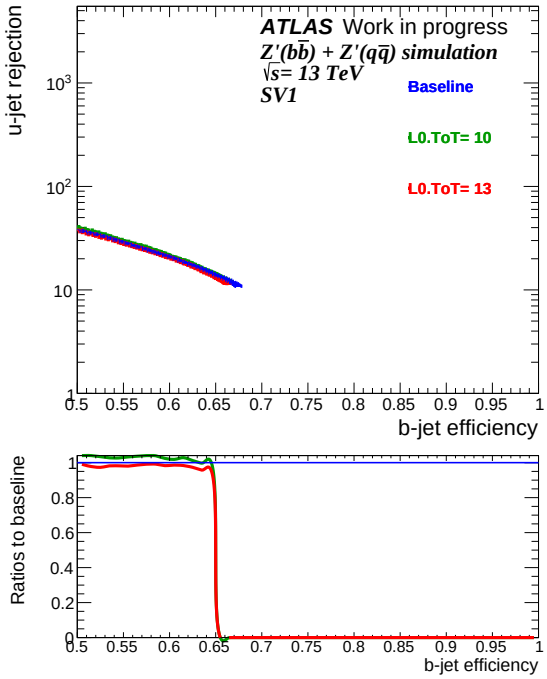

(b) SV1

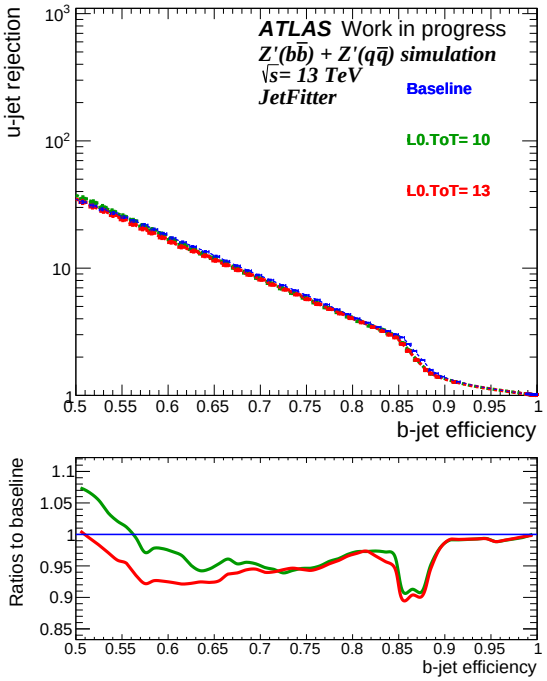

(c) JetFitter

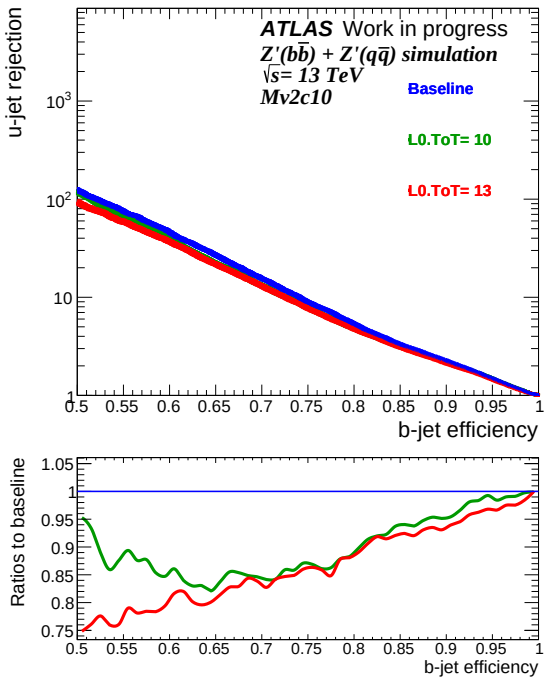

(d) Mv2c10

Figure 9.30.: The light jet rejection as a function of b-jet efficiency for the IP3D (a), SV1 (b), JetFitter (c) and MV2c10 (d) algorithms for L0 scenarios with ToT minimal cut at 13 BC, 10 BC compared with the baseline in blue for Z' mix sample.

creased offline ToT minimal cut while the y-axis shows the degradation of the b-jet efficiency in red, light jet rejection in blue and c-jet rejection in green.

Figure 9.32(b) shows the degradation for MV2c10 tagger using the OP at 0.65, corresponding to 77% b-jet efficiency for the baseline. The last bin dedicated to the scenario with the highest ToT minimal cut in L0, at 13 BC, shows a 2% degradation in ϵ_B.

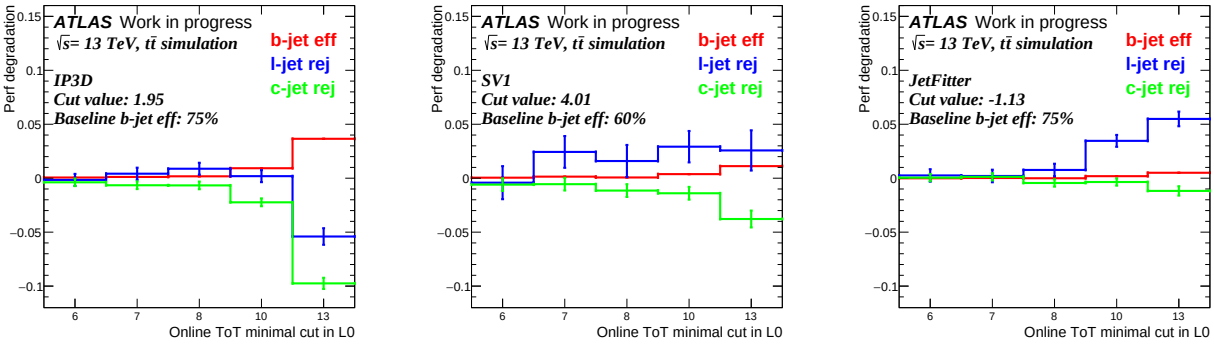

(a) (b) (c)

Figure 9.31.: The relative degradation in the performance for the five L0 scenarios using 20.7 OP for IP3D (a), SV1 (b) and JetFitter (c). The sample used is $t\bar{t}$.

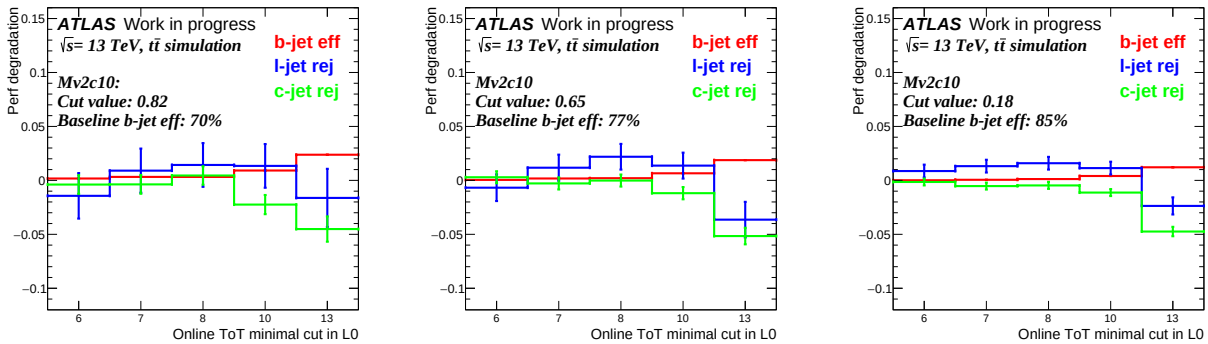

(a) (b) (c)

Figure 9.32.: The relative degradation in the performance for the five L0 scenarios using three different 20.7 OP for MV2c10 algorithm. The sample used is $t\bar{t}$.

Figures 9.33 and 9.35 show the degradation as function of jet p_T and η, for the scenarios with L0 ToT minimal cut at 10 BC respectively, while figures 9.34 and 9.36 show the same for the scenario with L0 ToT minimal cut at 13 BC. For the p_T dependence, comparing figures 9.33 and 9.34, the b-jet efficiency degradation (in red), for the first two bins (jets with $p_T <$ 100 GeV) look similar, however for the last bin dedicated to jets with $p_T >$ 100 GeV, the b-jet efficiency behaves differently, emphasizing that the high p_T jets are more affected by the increase of the ToT minimal cut in L0 as shows table 7.19(a). For the η dependence, comparing figures 9.35 and 9.36, central jets look more affected by the increase of the L0 ToT minimal cut as shows table 7.19(b). On the other hand, based on the figure 9.4, the

L0 scenarios on MC15c will increase the fraction of tracks namely in category 6, about 10% for the scenario with L0 ToT minimal cut at 13 BC, so another way to estimate the effect as function of η and p_T is to check the p_T and $|\eta|$ distributions of the excess of tracks in category 6. These distributions are shown in figures 9.37(a) and 9.37(b). The additional tracks tend to be centered ($|\eta|$ less than 1) with high p_T ($p_T > 4$ GeV). It is due to the fact that at high η the pixel cluster are larger as seen in figure 9.37(c), thus the hit resolution will not be affected by the increase of the ToT minimal cut. This was expected and go in line with the effect seen for centered and high p_T jets.

Table 9.18.: The b-jet efficiency degradation (in %) with respect to the baseline when increasing the L0 ToT minimal cut in function of jets p_T and $|\eta|$.

L0 ToT minimal cut (BC)	10	13
p_T: [0, 50[	0	1
p_T: [50, 100[	0	1
p_T: ≥ 100	1	4

(a) Degradation in function of jets p_T.

L0 ToT minimal cut (BC)	10	13
$\|\eta\|$: [0, 0.5[	0	4
$\|\eta\|$: [0.5, 1[	0	2
$\|\eta\| \geq 1$	0	0

(b) Degradation in function of jets $|\eta|$.

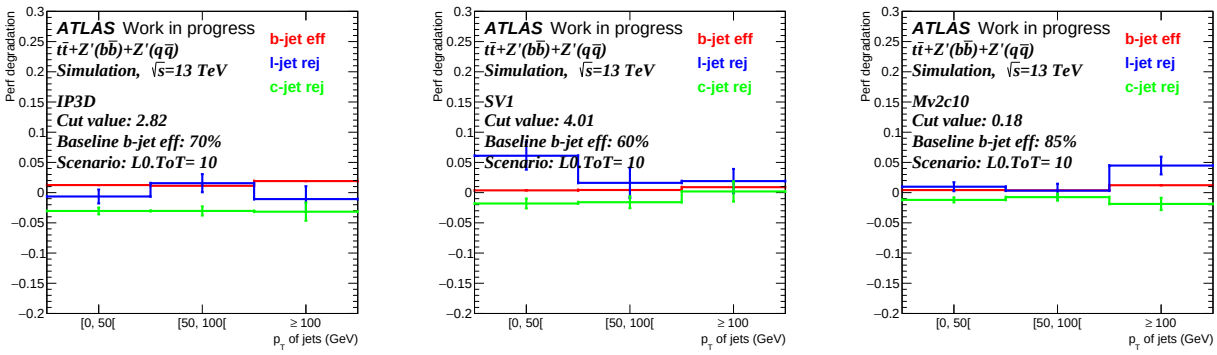

(a) (b) (c)

Figure 9.33.: The relative degradation in the performance for the L0 scenario with ToT cut at 10 using 20.7 OP as function of jet p_T, for IP3D using the OP corresponding to a baseline ϵ_b=70% (a), SV1 ϵ_b=60% (b) and MV2c10 at ϵ_b=85% (c). Sample used is $t\bar{t}$.

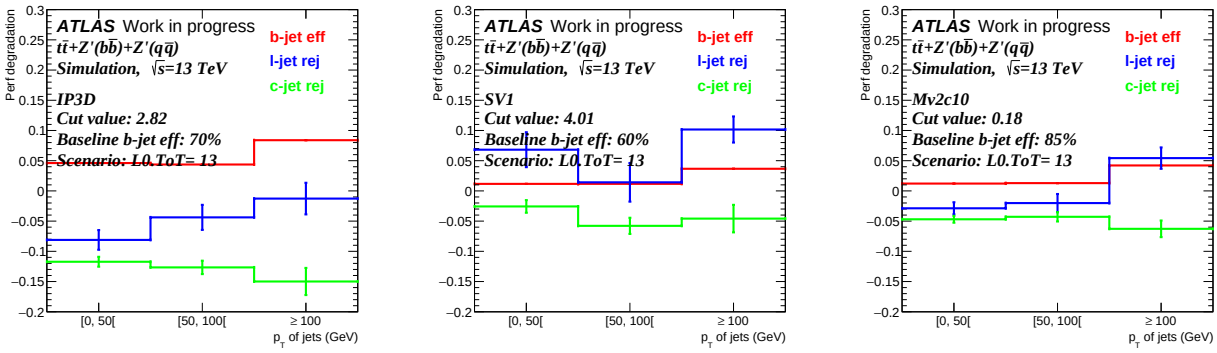

(a) (b) (c)

Figure 9.34.: The relative degradation in the performance for the L0 scenario with ToT cut at 13 using 20.7 OP as function of jet p_T, for IP3D using the OP corresponding to a baseline ϵ_b=70% (a), SV1 ϵ_b=60% (b) and MV2c10 at ϵ_b=85% (c). Sample used is $t\bar{t}$.

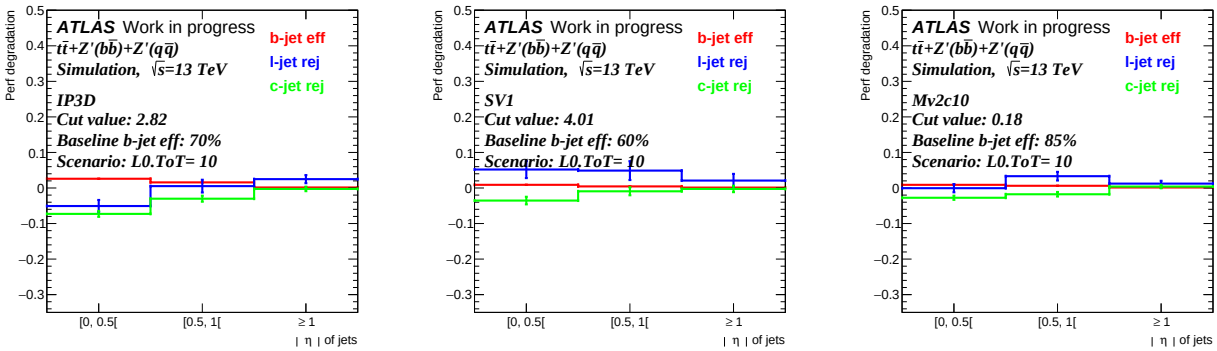

(a) (b) (c)

Figure 9.35.: The relative degradation in the performance for the L0 scenario with ToT cut at 10 using 20.7 OP as function of jet η, for IP3D using the OP corresponding to a baseline ϵ_b=70% (a), SV1 ϵ_b=60% (b) and MV2c10 at ϵ_b=85% (c). Sample used is $t\bar{t}$.

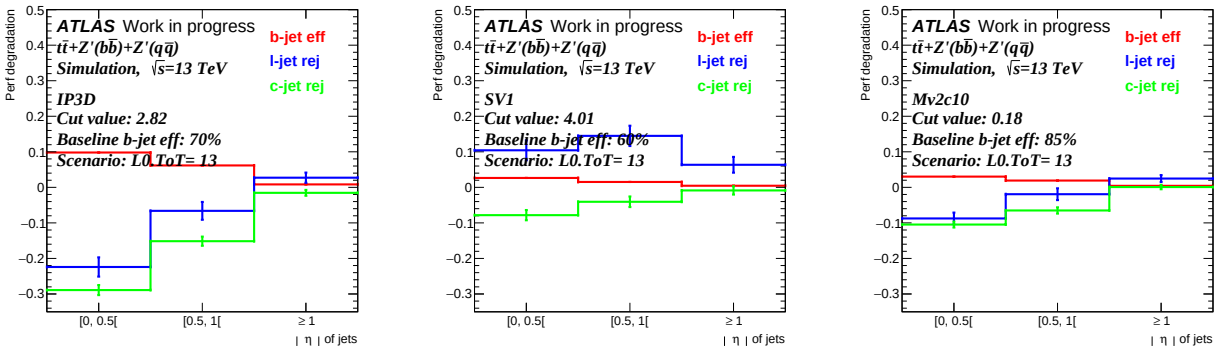

(a) (b) (c)

Figure 9.36.: The relative degradation in the performance for the L0 scenario with ToT cut at 13 using 20.7 OP as function of jet η, for IP3D using the OP corresponding to a baseline ϵ_b=70% (a), SV1 ϵ_b=60% (b) and MV2c10 at ϵ_b=85% (c). Sample used is $t\bar{t}$.

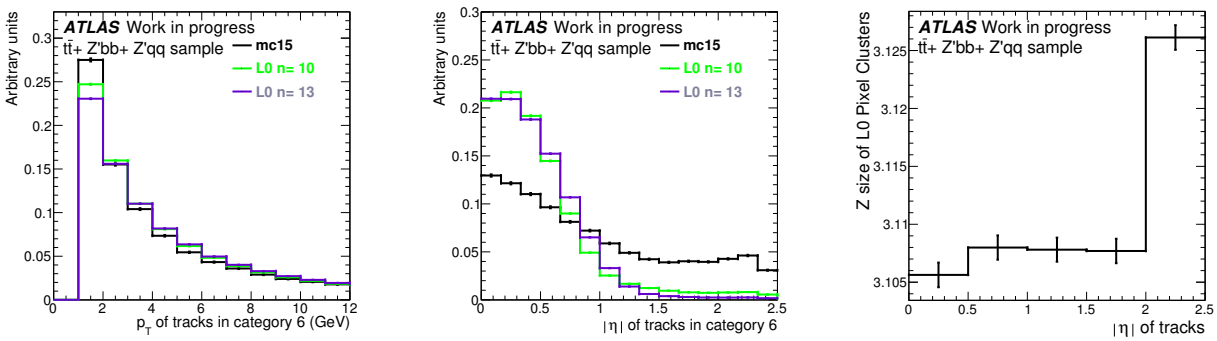

(a) (b) (c)

Figure 9.37.: Normalized p_T (a) and $|\eta|$ (b) distributions of tracks in category 6. (c) shows the Z size of L0 pixel clusters (in cells) as function of the $|\eta|$ of tracks.

9.6. Conclusions and outlook

The studies made on simulated data allow to quantify the impact on the b-tagging performance of both the increase in the fraction of pixel dead modules and the ToT minimal cut of the Run 2 pixel detector configuration. The effect was studied as a function of jet p_T and η using $t\bar{t}$, $Z'(b\bar{b})$ and $Z'(q\bar{q})$ merged samples. Further studies can be done:

* Investigate specific failures (e.g.: cooling loops, ROD) with dead half-staves in some parts of the detector.
* Re-tune the underlying reference histograms/PDF of the b-tagging algorithms (IP3D, MV2, etc) in this way part of the looses could be recovered and the decrease in performance will be much smaller compared with using the default reference histograms.
* Look for the effect on new/future b-tagging algorithms (e.g.: RNN) which are very sensitive to the track quality.

Part IV.

Search for electroweak production of chargino and neutralino in final states with 1 lepton, 2 b-jets and E_T^{miss}

10. Introduction

10.1. Search for Electroweak SUSY at LHC

The ATLAS and CMS experiments performed a large number of searches for SUSY during Run1/Run2 of the LHC and, in the absence of a significant excess in any channel, exclusion limits on the masses of SUSY particles were calculated in numerous scenarios, usually in the context of the MSSM. These scenarios include "high-scale" SUSY models such as mSUGRA or GMSB, both of which specify a particular SUSY-breaking mechanism as discussed previously in section 2.2. Most searches use the "simplified models" which permit the development of signature-based search strategies that, taken as an ensemble, have been shown to adequately cover the pMSSM. As discussed in section 2.4, these models allow us to efficiently address particular features of SUSY such as stop/sbottom production, electroweak production, compressed spectra, massive long-lived particles, R-parity violation, etc. without the need to embed these in a complete SUSY model. Early analyses were dominated by the searches for strongly interacting SUSY particles (gluinos, squarks) because of their large production cross sections (see figure 10.1).

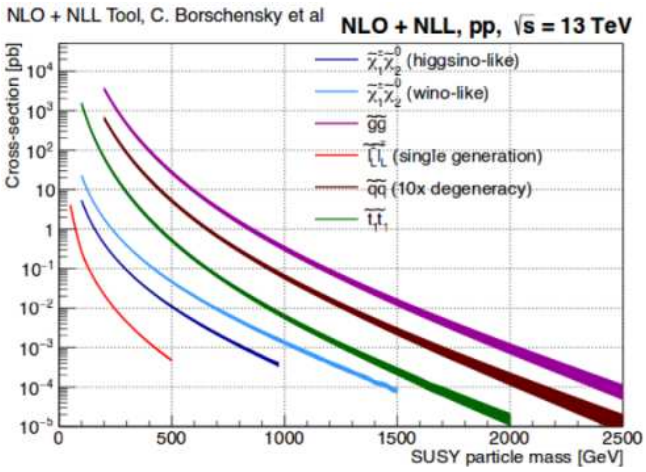

Figure 10.1.: NLO+NLL cross section for the production of sparticles at LHC at 13 TeV center-of-mass energy as a function of the average mass of the pair produced.

These studies resulted in very powerful constraints on the squarks and gluino masses, around 1- 1.8 TeV for a massless $\tilde{\chi}_1^0$ as figure 10.2 shows.

It also motivated the separate consideration of electroweak SUSY particle production, that is, direct production of particles that have no colour charge such as the charged sleptons, sneutrinos and the electroweakinos (charginos, neutralinos). On the experimental side, depending on the mechanism of SUSY breaking, it could be that strongly interacting squarks and gluinos are too massive to be produced at the LHC. In this case, the primary SUSY production mode is of charginos, neutralinos and sleptons, mediated by electroweak interactions, while on the theory side, weak-scale SUSY has long occupied a central place in the theoretical expectations for the LHC, as the addition of superpartners to SM particles near the scale of electroweak symmetry breaking solves the hierarchy problem. Given that the superpartners must be heavier than their SM counterparts, the SUSY cancellation of loops

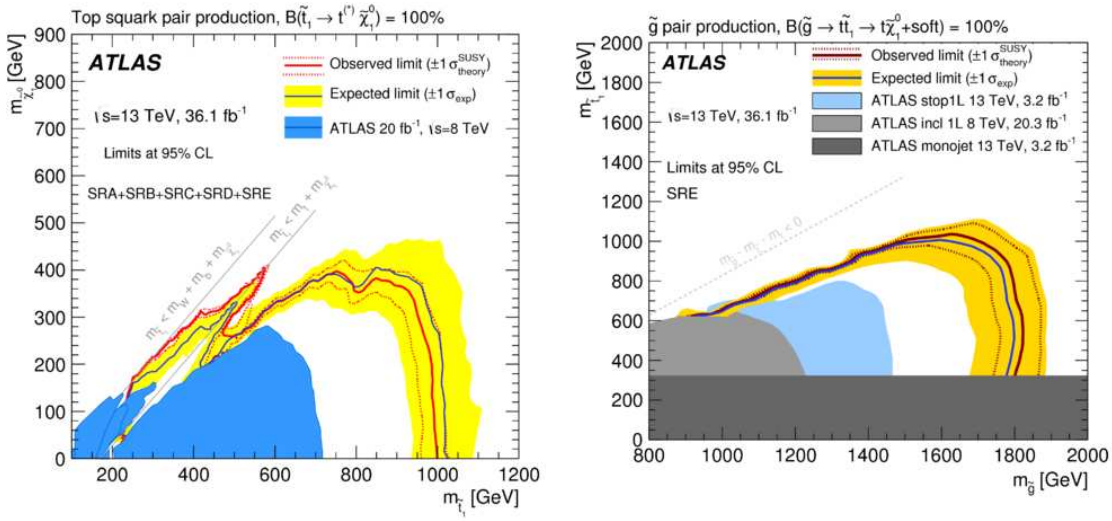

(a) (b)

Figure 10.2.: Exclusion contours on the scalar top (a) and gluino masses (b) for the final state with jets plus missing transverse momentum [97].

protecting the Higgs mass cannot be perfect. The heavier the superpartners, the more finely tuned the original bare mass must be against the loop contributions. For a reduced fine-tuning (theory will be "natural") electroweakinos, especially higgsinos, must be light.

Comparing with the SUSY strong production signatures, the SUSY electroweak productions yield a cleaner signal and can be less prone to systematic uncertainties, due to the fact that the electroweakinos decay to leptons, vector bosons or Higgs bosons and sleptons. The only hadronic activity in the event is due to bosonic decay products and initial-state radiation. Figure 10.3 shows the different electroweak direct production searches performed by ATLAS at Run2 with 2 or 3 leptons decay topologies with intermediate sleptons, chargino or neutralino, while in the next sections we focus on the searches for direct electroweak production of chargino and neutralino in final states with 1 lepton and a Higgs boson.

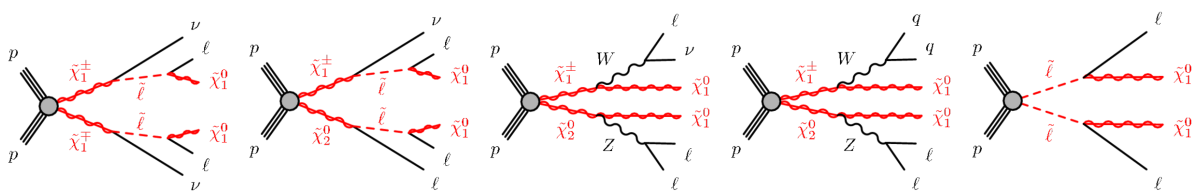

Figure 10.3.: Electroweak direct production with 2-leptons+ 0-jets, 2-leptons+ jets, 3-leptons decay topologies [98].

10.2. Chargino-neutralino pair production leading to Wh states with E_T^{miss}

Hereafter, we discuss the ATLAS search for electroweakinos $\tilde{\chi}_1^{\pm}, \tilde{\chi}_2^0$ pair-production, assuming a large higgsino $|\mu|$ parameter, so $\tilde{\chi}_1^{\pm}$ is a wino-like (see section 2.3.3.2) that interacts with fermions by gauge couplings and decays to a $W^{\pm}$ $+\tilde{\chi}_1^0$. The $\tilde{\chi}_2^0$ is considered as wino-like as well and decays to the lightest SUSY Higgs (h)+ $\tilde{\chi}_1^0$, while the $\tilde{\chi}_1^0$ is assumed to be bino-like interacting by g_1. This search is based on a simplified model where:

* The main $\tilde{\chi}_1^{\pm}$, $\tilde{\chi}_2^0$ production occurs via s-channel with $W^{*\pm}$ exchange as figure 10.4(a) shows, while the t-channel process shown in figure 10.4(b) is suppresed due to the high squark fixed mass. The s- and t- channels interfer and the t-channel, if not suppressed, would have a destructive interference which reduces the production cross section.

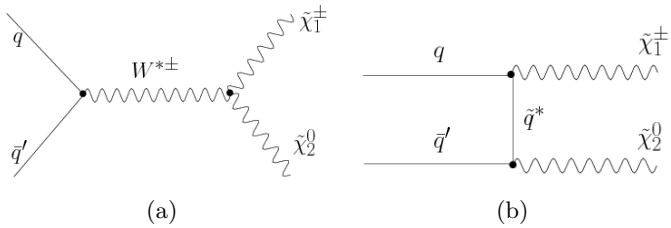

Figure 10.4.: Feynman diagrams for leading order (a) s-channel and (b) t-channel production of $\tilde{\chi}_1^{\pm}, \tilde{\chi}_2^0$.

* The $\tilde{\chi}_1^0$ is taken as the LSP and the Higgs boson is assumed to have SM properties with a mass of 125 GeV.
* Assuming that the $\tilde{\chi}_1^{\pm}$ and $\tilde{\chi}_2^0$ have the same masses, the model contains only 2 free parameters: $m_{\tilde{\chi}_1^{\pm},\tilde{\chi}_2^0}$ and $m_{\tilde{\chi}_1^0}$ with a constraint on the mass spliting:

$$\Delta M = m_{\tilde{\chi}_1^{\pm},\tilde{\chi}_2^0} - m_{\tilde{\chi}_1^0} > 125 \text{ GeV},$$

which is needed to produce an on-shell Higgs boson. Figure 10.5 shows the $\tilde{\chi}_1^{\pm}/\tilde{\chi}_2^0$, $\tilde{\chi}_1^0$ mass grid used for the Run2 analysis.

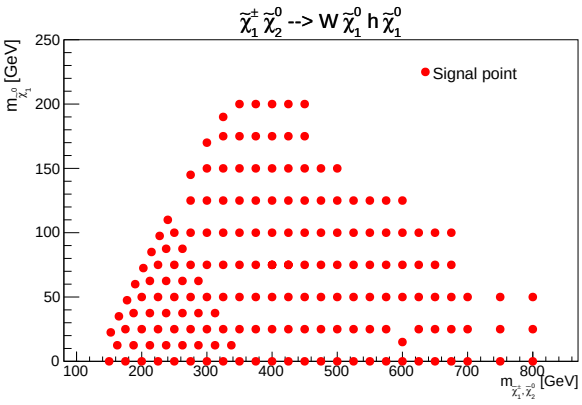

Figure 10.5.: The signal grid plotted in the ($m_{\tilde{\chi}_1^{\pm},\tilde{\chi}_2^0}$, $m_{\tilde{\chi}_1^0}$) plane [99].

* The $\tilde{\chi}_1^{\pm}$ and $\tilde{\chi}_2^0$ branching ratios, BR($\tilde{\chi}_2^0 \rightarrow$ h+ $\tilde{\chi}_1^0$) and BR($\tilde{\chi}_1^{\pm} \rightarrow$ W$^{\pm}$ +$\tilde{\chi}_1^0$), are fixed to 100%. However, the Higgs and W bosons branching fractions are assumed to be the same as in the SM.

The Run2 search targets hadronic and leptonic decays of the W boson, while for the Higgs boson, three decay modes are considered: Higgs boson decays to a pair of b-quarks, a pair of photons, a pair of W or Z bosons where at least one of the bosons decays leptonically. The four signatures considered are illustrated in figure 10.6.

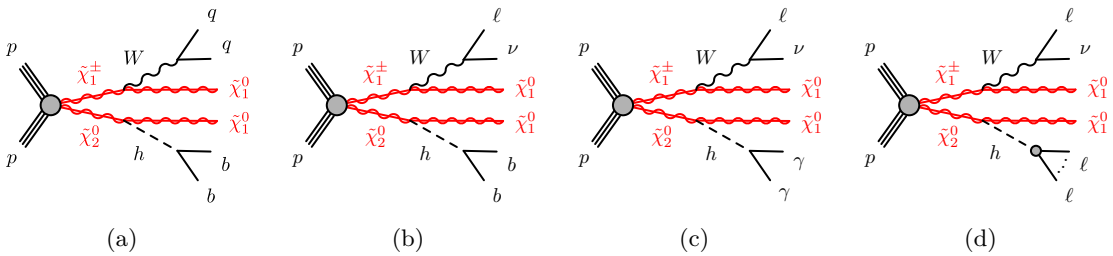

Figure 10.6.: Feynman diagrams for the direct production of $\tilde{\chi}_1^{\pm}, \tilde{\chi}_2^0$ and the four modes studied at Run2: (a) hadronic, $0\ell b\bar{b}$, (b) $1\ell b\bar{b}$, (c) $1\ell\gamma\gamma$ and (d) $\ell^{\pm}\ell^{\pm}$, 3ℓ leptonic channels. Leptons are either electrons or muons.

The dataset analysed corresponds to 36.1 fb^{-1} of proton–proton(pp) collisions data at $\sqrt{s}$ = 13 TeV collected by the ATLAS experiment during Run 2 of the LHC in 2015 and 2016. The full details about this Run2 ATLAS analysis can be found in Ref [100]. Previous searches for $\tilde{\chi}_1^{\pm}$, $\tilde{\chi}_2^0$ at the Run1 of the LHC targeting decays through the Higgs boson in leptonic signatures have been published by ATLAS [101] and CMS [102], while searches in the fully hadronic channel is done at Run2 for the first time.

The ATLAS Run1 analysis was based on 20.3 fb^{-1} of $\sqrt{s}$ = 8 TeV recorded during 2012. It was the first analysis using the Higgs boson to search for SUSY. However, no significant excess was observed with respect to SM expectation and exclusion limit at 95% C.L. were set at m$_{\tilde{\chi}_1^{\pm},\tilde{\chi}_2^0}$> 250 GeV for m$_{\tilde{\chi}_1^0}$ = 0 GeV [101]. The figure 10.7 shows the combination obtained using the result from the 3ℓ search in addition to the three channels $\ell^{\pm}\ell^{\pm}$, $1\ell\gamma\gamma$ and $1\ell b\bar{b}$ which looks the most sensitive at high $\tilde{\chi}_1^{\pm}$ masses.

In the next chapter, we focus on the Run2 $1\ell b\bar{b}$ analysis with the favoured Higgs decay mode to b-jets, with a BR(h$\rightarrow b\bar{b}$)= 58% (see section 1.4). The corresponding final states contain one lepton (e, μ), two jets originating from the fragmentation of b-quarks, b-jets, and large missing transverse momentum from ν and $\tilde{\chi}_1^0$ ($\vec{p}_T^{miss}$, its modulus is noted as E_T^{miss}) which should allow for good suppression of many standard model background processes. The main background processes with similar final states are $t\bar{t}$, W+jets. The Run 2 enhances the search sensitivity as table 10.1 shows presenting a comparison between Run 1 data analyzed and Run 2 data expected to be recordered until 2018. Clearly the gain in signal cross section (≈7 times) is higher than the gain in the cross section (≈4 times) of the main background process, $t\bar{t}$. The signal considered in this table has m$_{\tilde{\chi}_1^{\pm}}$ = 250 GeV.

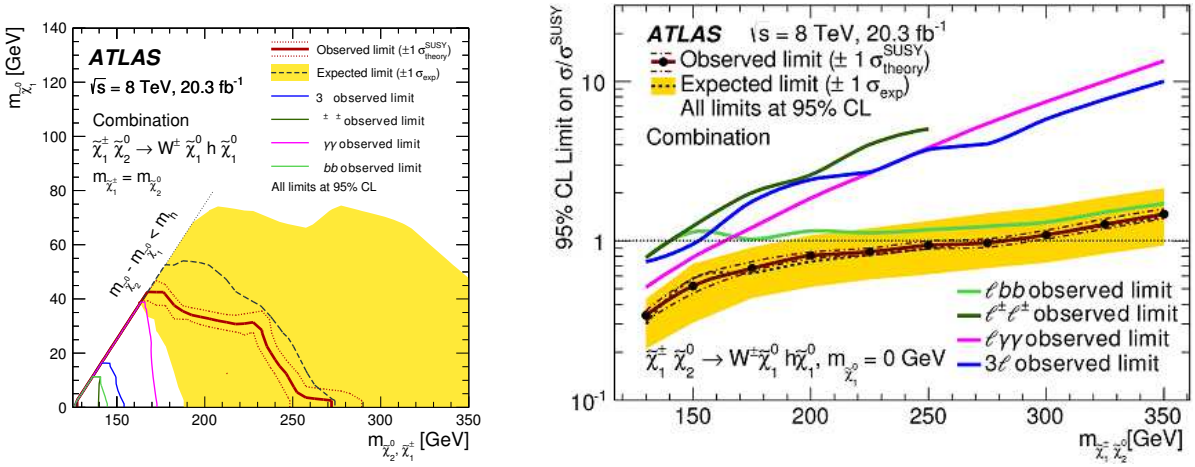

(a) (b)

Figure 10.7.: (a) Exclusion limits for the signal at 95% CL. Dashed blue represents the limit expected using the combined four different Higgs boson decay channels simulation and in red observed limit from Run1 ATLAS data. (b) The expected and observed cross-section exclusion as a function of the $\tilde{\chi}_1^{\pm}/\tilde{\chi}_2^0$ masses assuming m($\tilde{\chi}_1^0$)= 0 GeV [101].

Table 10.1.: Comparison between Run1 and Run2 for the signal with $m_{\tilde{\chi}_1^{\pm}}$ = 250 GeV and the main background process $t\bar{t}$ cross sections in pb.

	Run1 (2012)	Run2 (2015-2018)
Center of mass energy (TeV)	8	13
Integrated luminosity (fb^{-1})	20	100
signal cross section (pb)	0.1	0.7
$t\bar{t}$ cross section (pb)	0.25	0.83

11. One lepton, two b-jets and E_T^{miss} channel

11.1. Data-set and Monte Carlo samples

The raw data sample used in the $1\ell b\bar{b}$ analysis was recorded by the ATLAS detector during 2015 and 2016 in pp collisions at the LHC with a centre-of-mass energy of 13 TeV and a 25 ns proton bunch crossing interval. The application of data-quality requirements results in an integrated luminosity of 36.1 fb^{-1} consisting of the 3.2 fb^{-1} of data collected in 2015 and the 32.9 fb^{-1} in 2016. These preselection criteria are applied to ensure the quality of the data used, as the application of a Good Run List making sure that all detector subsystems were fully operational for all data runs used. Each event includes on average 13.7 and 24.9 inelastic pp collisions (pile-up) in the same bunch crossing in the 2015 and 2016 datasets, respectivly. In the next sections we describe the MC signal and background samples used in this analysis.

11.1.1. Signal models

The SUSY signal samples were generated with MADGRAPH5_aMC@NLO [103] using the leading order (LO) matrix elements $\tilde{\chi}_1^{\pm}\tilde{\chi}_2^0$ including the emission of up to two additional partons. The NNPDF23LO [104] parton distribution function (PDF) set was used. Then samples were interfaced to Pythia 6 [83] with the A14 [105] set of tuned parameters (tune) for the modeling of the parton showering (PS), hadronization and underlying event. The ME-PS matching was done using the CKKW-L algorithm [106]. The decays of the C-hadrons and B-hadrons were performed by EVTGEN program [107]. The signal cross sections, used to evaluate the signal yields, were calculated to next-to-leading order in the strong coupling constant , including the resummation of soft gluon emission at next-to-leading-logarithmic accuracy (NLO+NLL). The nominal cross section and the uncertainty are taken respectively from the centre and the spread of the cross section predictions using different PDF sets and their associated uncertainties, as well as from variations of factorisation and renormalisation scales, as described in Ref [108].

11.1.2. Standard model Monte Carlo

Background samples were simulated using different MC generator programs depending on the process. All background processes are normalized to the best available theoretical calculation for their respective cross-sections. The event generators, the accuracy of theoretical cross-sections, the underlying-event parameter tunes, and the PDF sets used for simulating the SM background processes are summarised in table 11.1. For all samples, except the ones generated using Sherpa, the EvtGen program [107] was used to simulate the properties of the bottom- and charm-hadron decays.

Hereafter, we describe the production of the most important background processes in this analysis, the $t\bar{t}$, W+jets and single top processes:

* Simulated $t\bar{t}$ events are generated using the POWHEG-BOX [95, 109], which implements the next-to-leading order matrix element for inclusive $t\bar{t}$ production and uses the CT10 [110] PDF set. Then samples were interfaced to PYTHIA-6 [111] for the

modeling of the parton showering (PS). The $t\bar{t}$ samples are normalized to their next-to-next-to-leading order cross-section including the resummation of soft gluon emission at next-to-next-to-leading-logarithmic accuracy.

* Simulated W+jets samples are produced using SHERPA-2.2.1 [86] with massive b-, c-quarks, and with up to four additional partons in the ME. These samples are normalized to their next-to-next-to-leading order QCD theoretical cross sections.
* Samples of single top quark backgrounds corresponding to the t-, s- and W t production mechanisms are generated with POWHEG-BOX using the CT10 PDF set and interfaced to PYTHIA-6. The leading-order cross-sections obtained from the generator is used for these samples.

Process	Generator + fragmentation/hadronization	Tune	PDF set	Cross-section order
$W/Z+$jets	SHERPA-2.2.1 [86]	Default	NNPDF3.0NNLO [104]	NNLO
$t\bar{t}$	POWHEG-BOX v2 [95, 109] + PYTHIA-6.428 [111]	PERUGIA2012 [112]	CT10 [110]	NNLO +NNLL
Single top	POWHEG-BOX v1 or v2 + PYTHIA-6.428	PERUGIA2012	CT10	NNLO +NNLL
Diboson WW, WZ, ZZ	SHERPA-2.2.1	Default	NNPDF3.0NNLO	NLO
Triboson	SHERPA	Default	CT10	NLO
$t\bar{t}+X$ $t\bar{t}W/Z$	MADGRAPH-2.2.2 [103] + PYTHIA-8.186 [83]	A14 [105]	NNPDF2.3	NLO
$t\bar{t}h$	MADGRAPH5_aMC@NLO-2.2.1 [113] + Herwig++-2.7.1	UEEE5 [114]	CT10	NLO
Wh, Zh	PYTHIA-8.186+EVTGEN [107]	A14	NNPDF2.3	LO

Table 11.1.: List of generators used for the different processes. Information is given about the underlying-event tunes, the PDF sets and the pQCD highest-order accuracy (LO, NLO, next-to-next-to-leading order, NNLO, and next-to-next-to-leading-log, NNLL) used for the normalization of the different samples.

11.2. Object definiton and event pre-selection

The selection cuts have been chosen carefully to allow for a maximal background suppression as well as a reasonable signal selection efficiency. As largely discussed in section 10.2, the signal is characterised by a large E_T^{miss}expected in the final state coming from the leptonic W decays and the two $\tilde{\chi}_1^0$, for this reason this analysis uses the E_T^{miss}trigger with data-taking period-dependent threshold. This trigger reaches the full efficiency for events with E_T^{miss}larger than 200 GeV.

11.2.1. Object definition

We are looking for final states containing one electron or muon, two b-jets, and missing transverse momentum. For tagging jets as originating from bottom quarks we use the MV2c10 multivariate b-tagging algorithm at the operating point corresponding to 77% b-tagging efficiency obtained in $t\bar{t}$ simulated events. The selection of these physics objects in the final state is performed in three steps: preselection, baseline selection and final signal selection. Particles have to pass kinematic requirements and identification criteria in the preselection: electrons have to satisfy $p_T > 10$ GeV within $|\eta| <2.47$ and loose identification criteria, muons have to satisfy the same p_T cut but within $|\eta| < 2.7$ and medium identification requirements, jets are required to have $p_T > 20$ GeV within $|\eta| < 2.8$.

The different physics objects are reconstructed independently and it is possible that the energy deposits in the detector are used by the different reconstruction algorithms. To resolve these ambiguities, the so called overlap removal is performed in several steps. In each step objects are removed if they are close in space to other objects using the angular distance variable ΔR. The overlap removal procedure is the following:

* remove non-btagged jets very near electrons (ΔR<0.2),
* remove electrons for events with $0.2 < \Delta R(e,j) < 0.4$,
* remove electrons near muons ($\Delta R < 0.01$),
* remove muons that lie $\Delta R < \min(0.4+(10\text{ GeV})/p_T^{\mu}, 0.4)$ from a jet,
* remove any jet reconstructed near muons ($\Delta R < 0.2$)

The objects that pass the overlap removal are called baseline objects while the signal objects have to pass, on top of the baseline selection criteria, tighter kinematic cuts and additional identification criteria in order to reject fake leptons. Those are either a lepton originating from semi-leptonic decays of B and C hadrons or a particle that is misidentified as lepton. For the signal jets, additional requirements are applied for those with $p_T < 60$ GeV and $|\eta| < 2.4$ using the jet vertex tagging algorithm in order to reject pile-up jets. A summary of the baseline criteria and signal selection requirements for electrons, muons and jets are shown in tables 11.2 and 11.3 respectively.

Table 11.2.: Cuts defining the baseline and signal electrons and muons.

Cut	p_T[GeV]	$\|\eta\|$	Quality	Isolation	Impact parameters [mm]
Baseline electron	> 10	< 2.47	LooseAndBLayerLLH	—	—
Signal electron	> 25	< 2.47	TightLLH	GradientLoose	$\|z_0^{PV}\| < 0.5$ $\|d_0^{PV}\|/\sigma(d_0^{PV}) < 5$
Baseline muon	> 10	< 2.7	Medium	—	—
Signal muon	> 25	< 2.7	Medium	GradientLoose	$\|z_0^{PV}\| < 0.5$ $\|d_0^{PV}\|/\sigma(d_0^{PV}) < 3$ $\|d_0^{PV}\| < 0.2$ (cosmic muon veto)

Table 11.3.: Summary of the jet selection criteria. The signal selection requirements are applied on top of the preselection.

	Algorithm	p_T cut [GeV]	$\|\eta\|$ cut
Baseline jet	anti-k_t ($R = 0.4$) EMTopo	> 20	< 2.8
Signal jet	JetVertexTagger @ ϵ =92% working point applied for jets with $p_T < 60$ GeV and $\|\eta\| < 2.4$	> 25	<2.8
Signal b-jet	MV2c10 @ Fixed cut $\epsilon_b = 77\%$ working point	> 25	<2.5

11.2.2. Event variables and pre-selection

First a preliminary selection is applied to clean the data from detector noise and non-collision background. Events are then selected if they pass some kinematic requirements for the objects described in the previous section and event variables presented below:

* N_{lep}^{base}, N_{lep}^{sig} which represent the number of baseline leptons and signal leptons per event respectively. To suppress the dileptonic $t\bar{t}$ events we require exactly one baseline lepton (e or μ) per event. The selected lepton must pass signal selection.
* N_{jet}^{sig}, N_{bjet} which represent the number of signal jets and b-jets per event respectively. An event has to contain exactly 2 or 3 signal jets where 2 must be b-tagged jets.
* $m_{b\bar{b}}$ is the invariant mass of the two b-jets in the event, and serves as a selection criterion for dijet pairs to be considered as Higgs boson candidates. At preselection m_{bb}>50 GeV is required.
* m_T^W is the transverse mass formed by the $E_T^{miss}$and the lepton in the event. It is defined as in equation 11.1.

$$m_T^W = \sqrt{2p_T^{\ell} E_T^{miss} \left(1 - \cos\left[\Delta\phi(\ell, \vec{p}_T^{miss})\right]\right)} \tag{11.1}$$

  This standard variable is able to provide an estimation of the invariant mass of the system "Y" composed by the $E_T^{miss}$and ℓ. From it's definition follows that $m_T^W \leq m_Y$, thus the turn off edge of it's distribution is a good estimator of the total invariant mass. It is particularly useful in the case where one of the two particles, produced in the decay of an heavy one, is invisible and is the only invisible particle in the event. For example in W$\rightarrow e/\mu\nu$ events, it gives a Jacobian peak with an edge at the W mass, but with the bulk of the distribution below the W mass. There is also a long tail above the W mass which arises from the boost of the W boson and the lepton p_T resolution. Thus, to reduce the W+jets and $t\bar{t}$ background processes, an $m_T^W > 40$ GeV is required at preselction.

  The $m_{b\bar{b}}$, m_T^Wcuts and the E_T^{miss}>100 GeV required at preselection reduce significantly the multi-jet final states arising from QCD interactions. In pure multi-jet event, the total transverse momentum should be perfectly balanced, due to the finite resolution of the calorimeter, but if the energy of one or more jets is mis-measured, this breaks the balancing of the event and, therefore, creates fake E_T^{miss}aligned with the mis-measured jet, thus the cut on $E_T^{miss}$is crucial to reduce this background process.
* Finally the contransverse mass variable, m_{CT}, is used to reduce the $t\bar{t}$ events. It was originally designed to measure the mass of pair produced heavy particles which decay identically and semi-invisibly. Its non-boost-corrected form is given by equation 11.2 [115]:

$$m_{CT}^2\left(v_1, v_2\right) = \left[\vec{E}_T\left(v_1\right) + \vec{E}_T\left(v_2\right)\right]^2 - \left[\vec{p}_T\left(v_1\right) - \vec{p}_T\left(v_2\right)\right]^2 \tag{11.2}$$

where v_1 and v_2 denote the visible particles or particle aggregates, in our case they are the b-quarks from the Higgs boson decay and are approximated as massless. Therefore, this formula reduces to equation 11.3.

$$m_{CT}^2\left(b_1, b_2\right) = 2p_T\left(b_1\right)p_T\left(b_2\right)\left(1 + \cos\Delta\phi_{bb}\right) \tag{11.3}$$

The m_{CT} distribution is expected to display an end-point in the limit of the visible particle being massless, given by equation 11.4.

$$m_{CT}^{\text{max}} = \frac{m_{\text{heavy}}^2 - m_{\text{invis}}^2}{m_{\text{heavy}}} \tag{11.4}$$

Adapting the $t\bar{t}$ background to this kinematic topology identifies $\mathrm{m_{heavy}} = \mathrm{m_{top}}$ and $\mathrm{m_{invis}} = \mathrm{m_W}$, resulting in a $m_{CT}^{\text{max}} \approx 135$ GeV. Throughout the analysis, the boost-corrected m_{CT}, which corrects for collinear boosts of the $t\bar{t}$ system in the transverse plane is used and the endpoint is shifted to 160 GeV due to the b-jet $\mathrm{p_T}$ resolution.

Concerning the signal, the events having highly-boosted $b\bar{b}$ resonances should correspond to high values of m_{CT} and thus preferentially pass the m_{CT} endpoint. We do not apply any m_{CT} cut at preselection however, this variable is used to define the signal enriched regions as will be seen in the next section.

Figure 11.1 shows the data/MC distributions for $m_{b\bar{b}}$, m_{CT}, m_{T}^{W} and $\mathrm{E_T^{miss}}$after applying the preselections with an increased lower $\mathrm{E_T^{miss}}$cut at 150 GeV. The data agree well with the SM background prediction from MC for all distributions.

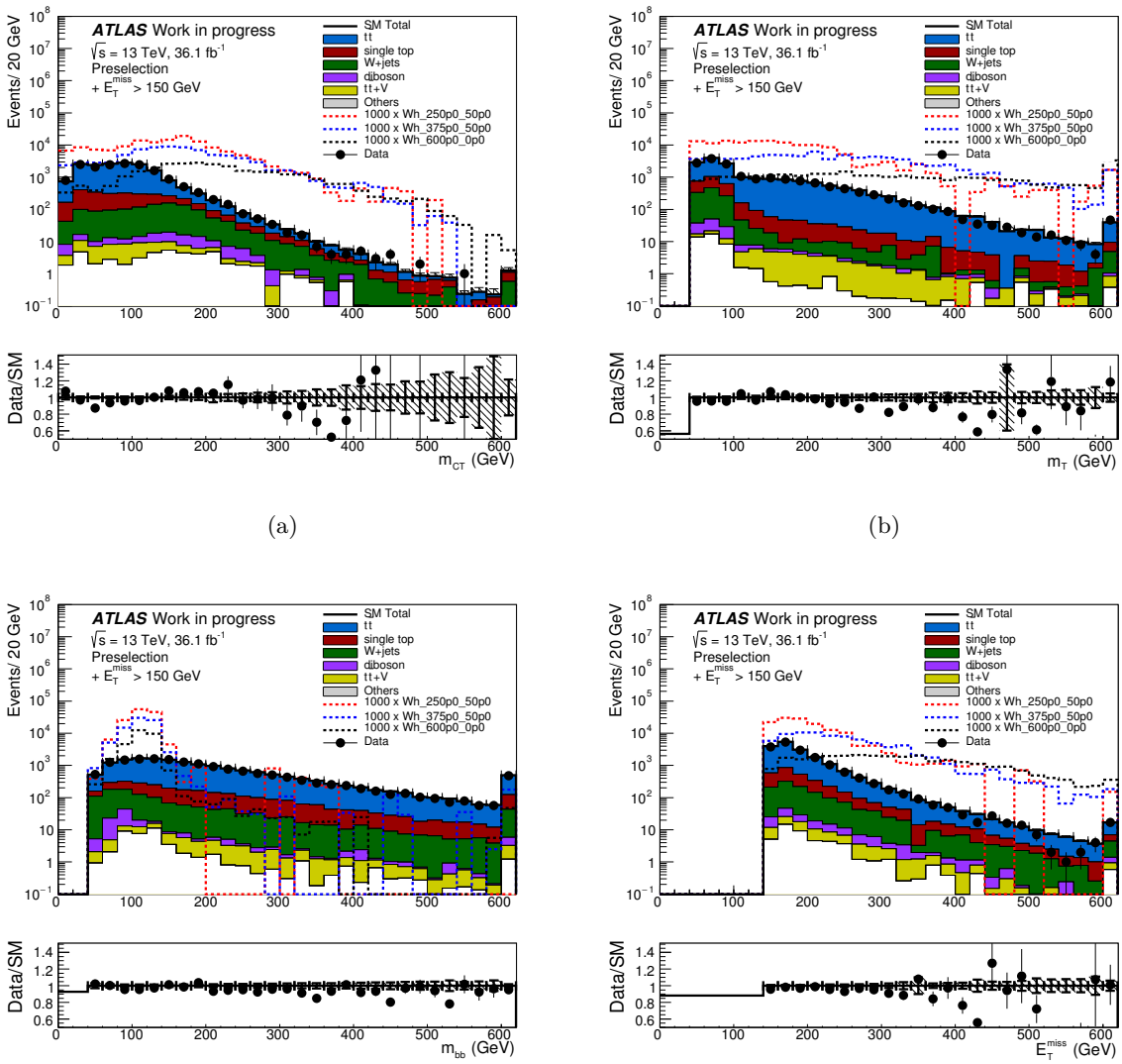

(a) (b)

(c) (d)

Figure 11.1.: Distributions of (a) m_{CT}, (b) m_{T}^{W}, (c) $m_{b\bar{b}}$ and (d) $\mathrm{E}_{\mathrm{T}}^{\mathrm{miss}}$for data and the expected background events passing the preselections with an increased lower $\mathrm{E}_{\mathrm{T}}^{\mathrm{miss}}$cut at 150 GeV. The lower panel shows the ratio between observed data and expected SM background processes. The red, blue and black dashed lines correspond to the bench mark signal model with $(\mathrm{m}_{\tilde{\chi}_1^{\pm},\tilde{\chi}_2^0}, \mathrm{m}_{\tilde{\chi}_1^0})$= (250, 50), (375, 50) and (600, 0) GeV respectively, where cross-section are multipled by 1000 for shape illustration. Uncertainties are statistical only.

11.3. Signal selection

The sensitivity to the $1\ell b\bar{b}$ signal depends on two parameters: it obviously decreases when increasing $\tilde{\chi}_1^{\pm}$ mass because of the exponentially falling signal cross-section as figure 10.1 shows, and it increases when increasing the mass splitting between $\tilde{\chi}_1^{\pm}$ and $\tilde{\chi}_1^0$, as larger ΔM

implies larger phase space for both the W and the Higgs bosons in the respective decays of the $\tilde{\chi}_1^{\pm}$ and $\tilde{\chi}_2^0$. Also, when increasing the $\tilde{\chi}_1^{\pm}$ mass, the W boson, Higgs boson and the LSP will acquire larger phase space, but at very high $\tilde{\chi}_1^{\pm}$ masses, compared to the exponentially falling signal cross section this effect is negligible. Therefore, we split the phase space of the search into three categories: small ΔM (125 GeV to about 150 GeV), medium ΔM (150 GeV to 250 GeV) and large ΔM (larger than 250 GeV). To separate these signal regions (SRs) we use the m_T variable because we found that it shows the highest correlation to the ΔM. As figure 11.2(a) shows, the m_T increases linearly when increasing the ΔM, consequently, the 3 orthogonal SRs were defined using the following transverse mass bins:

* SRML containing events with $100 < m_T^W < m_T^{low}$, optimised for small ΔM,
* SRMM within $m_T^{low} < m_T^W < m_T^{high}$, optimised for intermediate ΔM,
* SRMH with $m_T^W \geq m_T^{high}$ GeV, optimised for large ΔM.

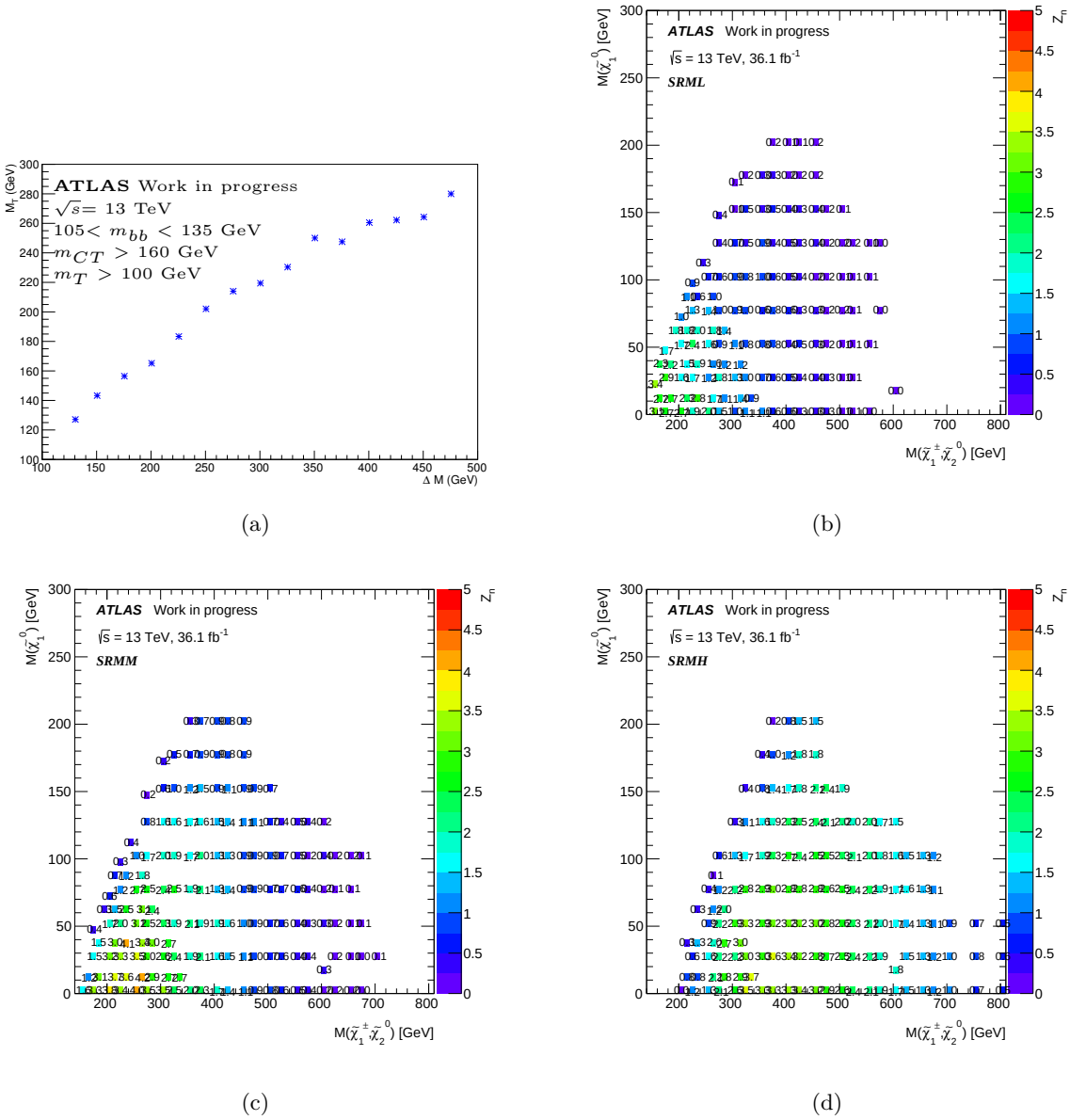

Figure 11.2.: (a) The m_T mean values corresponding to ΔM of the signal points. For the points with equal ΔM, the m_T mean value of the highest $m_{\tilde{\chi}_1^\pm}$ point is shown. (b) The expected significance, Z_N, for SRLM, (c) SRMM and (d) SRMH regions.

On top of the m_T cuts, common cuts on $m_{b\bar{b}}$, m_{CT} and E_T^{miss} are required for the 3 signal regions. To choose the best $m_{b\bar{b}}$ window, the m_{bb} distribution is fitted to a 1-sided 'Crystal-ball' function [116] that describes the non-gaussian tail of the $m_{b\bar{b}}$ resonance shape. This function is often used to model lossy processes like the reconstructed invariant mass of a resonance from the energies and momenta of its decay products where some fraction of the energies and momenta are lost to detection. It consists of a power law tail stitched to a Gaussian core and has 4 parameters: $\overline{x}$, σ, α and n. The power law parameter n appears in

the formula shown in equation 11.5 as n^n.

$$f(x;\alpha,n,\overline{x},\sigma) = \begin{cases} exp\left(-\frac{1}{2}\left(\frac{x-\overline{x}}{\sigma}\right)^2\right) & if \ \ \frac{x-\overline{x}}{\sigma} > -\alpha \\ \left(\frac{n}{|\alpha|}\right)^n exp\left(-\frac{|\alpha|^2}{2}\right)\left(\frac{n}{|\alpha|} - |\alpha| - \frac{x-\overline{x}}{\sigma}\right)^{-n} & else \end{cases} \tag{11.5}$$

The fit results in a most probable value (M.P.V.) of ≈ 120 GeV and a width of ≈15 GeV as figure 11.3 shows. Therefore, the central $m_{b\bar{b}}$ bin of 105–135 GeV is used, this bin contains about 70% of the signal events.

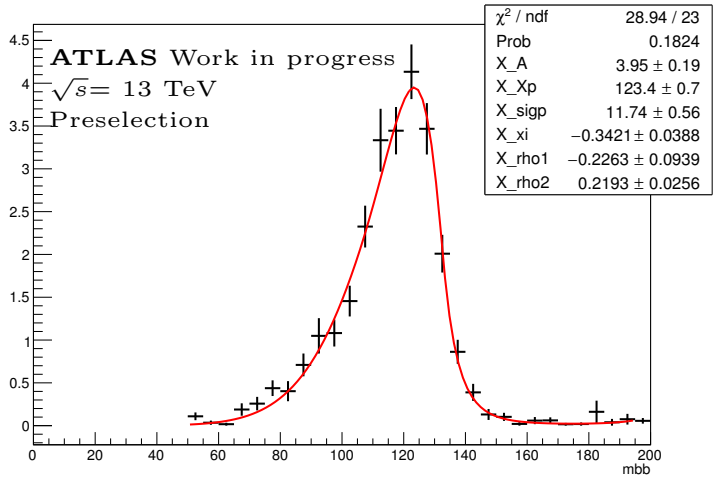

Figure 11.3.: Full m_{bb} distribution at preselection, for the signal point (450, 0) GeV fitted to a Crystal-ball function.

Concerning the m_{CT}, a lower cut at 160 GeV is applied, it corresponds to the $t\bar{t}$ background upper endpoint decribed in the previous section. Finally the choice of the E_T^{miss}>200 GeV cut and the m_T^{edge} values, m_T^{low}= 140 GeV and m_T^{high}= 200 GeV, are optimized in each region together based on expected significance (Z_N) corresponding to an integrated luminosity of 36.1 fb^{-1}. The significance is calculated using the RooStats::NumberCountingUtils package [117], including the MC statistical uncertainties as well as a flat 30% systematic uncertainty on the total background event count. The Z_N is set to "-1" when the signal yield is less than 3.

Figure 11.4 shows the distributions of the m_T amd E_T^{miss} variables with all other cuts in the region applied, except the plotted quantity (the "N-1" plots), while the figures 11.4(a) and 11.4(b) show the significance dependence on the choice of m_T^{low} and m_T^{high} respectively.

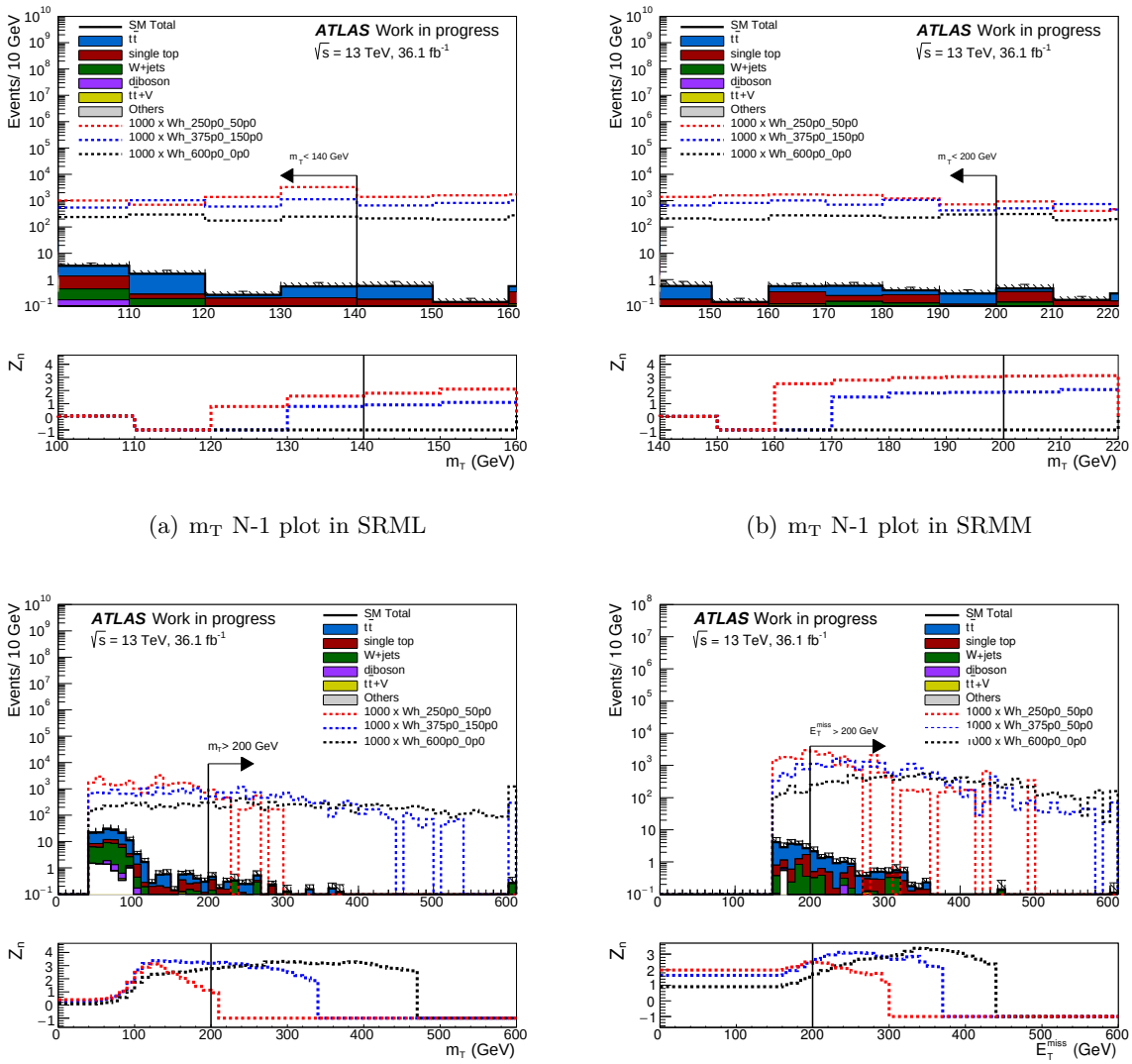

(a) m_T N-1 plot in SRML

(b) m_T N-1 plot in SRMM

(c) m_T N-1 plot in SRMH

(d) E_T^{miss} N-1 plot in SR inclusive

Figure 11.4.: The m_T and E_T^{miss} N-1 distributions for the (250, 50), (375, 50) and (600, 0) signal points. The bottom pad shows a the expected significance when cutting on the value on the x-axis.

The precise definition of the SRs is reported in table 11.4 while the expected significance obtained in these three SRs are shown in figure 11.2.

11.4. Background estimation

The contributions from the $t\bar{t}$, single top (corresponding to the Wt channel) and W+ jets background in SRs are estimated from MC simulation, but with yields that are normalized to data in dedicated control regions (CRs). The contribution from multijet production, where the lepton is misidentified as a jet or comes from a heavy-flavour hadron decay or photon

Variable	SRML	SRMM	SRMH
N_{lepton}		$=1$	
p_{T}^{ℓ} [GeV]		> 25	
N_{jet} ($p_{\text{T}} > 25$ GeV)		$=2$ or 3	
$N_{b-\text{jet}}$		$= 2$	
$\text{E}_{\text{T}}^{\text{miss}}$ [GeV]		> 200	
m_{CT} [GeV]		> 160	
m_{T}[GeV]	$\in [100, 140]$	$\in [140, 200]$	> 200
$m_{b\bar{b}}$ [GeV]		$\in [105, 135]$	

Table 11.4.: Summary of the event selection for signal regions of the $1\ell b\bar{b}$ channel.

conversion, is found to be negligible after preselection. The remaining sources of background (single top t- and s-channels, Z+ jets, diboson, Z h, and W h, triboson and $t\bar{t}$+ V/h production), including their total yields, are estimated directly from MC simulation predictions. This section describes the CRs used to estimate the $t\bar{t}$, W+jets and Wt background processes, as well as validation regions (VRs) in data to validate the data-driven background estimation methods. Orthogonal to the signal regions, these regions are defined as close as possible to the signal regions to minimise extrapolations in kinematic observables ($m_{b\bar{b}}$, m_{CT}) as shown in figure 11.5.

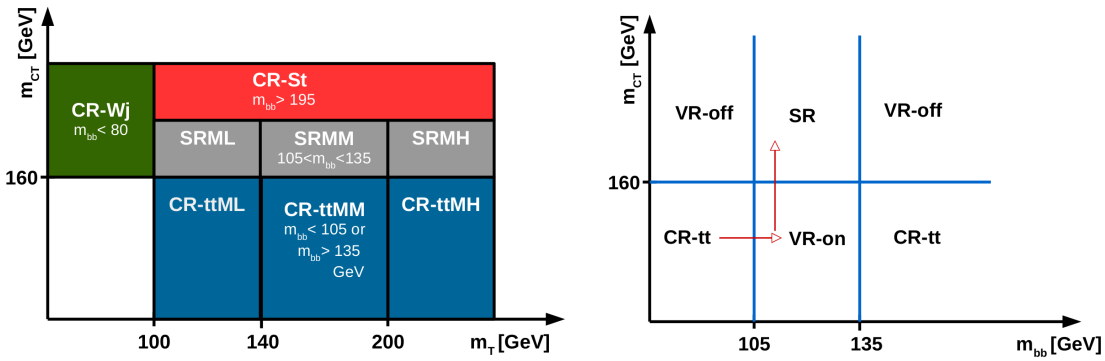

(a) (b)

Figure 11.5.: Shown are (a) the three SRs and the five CRs used in the analysis in the (m_{T} , m_{CT}) plan, (b) the SR, the $t\bar{t}$ CRs and the VRs in between in the (m_{bb} , m_{CT}) plan. A lower $\text{E}_{\text{T}}^{\text{miss}}$ cut at 200 GeV is required for all these regions except for VR-off, where this cut is relaxed to 180 GeV.

11.4.1. Background control regions

Three sets of CRs, CR-tt, CR-St and CR-Wj, are designed to estimate the $t\bar{t}$, W t and W+ jets background processes, respectively. The $t\bar{t}$ CRs are defined by reverting the signal selections on m_{CT} and $m_{b\bar{b}}$. Three $t\bar{t}$ CRs are used denoted as CR-ttML, CR-ttMM and CR-ttMH corresponding to the 3 SRs and having the same m_{T}^{W}, $\text{E}_{\text{T}}^{\text{miss}}$cuts as in the signal selections. These control regions are dominated by $t\bar{t}$ as figure 11.6(a) shows and have low signal contamination: the highest signal containation in these regions are 4.8%, 2% and 1.1% respectively.

The CR-Wj contains events with 40<m_{T}^{W}<100 GeV and $m_{b\bar{b}}$ < 80 GeV, while the same cuts on the $\mathrm{E}_{\mathrm{T}}^{\mathrm{miss}}$and m_{CT} as in the signal regions are applied. The upper threshold of the $m_{b\bar{b}}$ has been chosen to maximise the purity of W+jets events and keeping enough statistics. The CR-Wj expected background composition is shown in figure 11.6(c) while the highest signal contamination is ≈ 4.4%.

Last, for the CR-St the high $m_{b\bar{b}}$ > 195 GeV sideband is used, this lower threshold has been chosen to maximise the purity of single top events but also keeping enough statistics. Due to limited statistics, a single bin of m_{T}^{W} > 100 GeV is used, and the same cut on $\mathrm{E}_{\mathrm{T}}^{\mathrm{miss}}$and as in the signal selection are applied. The expected background composition in this region is shown in figure 11.6(b) while the highest signal contaminations is ≈ 4.3%.

The data agree well with the SM predictions in the 5 CRs, an example of comparision between data and the expected background from simulation is shown in figure 11.7 pesenting the distribution of m_{CT} in the inclusive CR-tt (defined using m_{T}^{W} >100 GeV) and the distribution of m_{T}^{W}in CR-Wj. Considering only statistical uncertainties, the data-to-simulation yield factor for all background is found to be between 1.02 ±0.14 and 0.89 ± 0.04 for CR-tt, 1.26 ± 0.19 for CR-Wj and 1.18 ± 0.18 for CR-St.

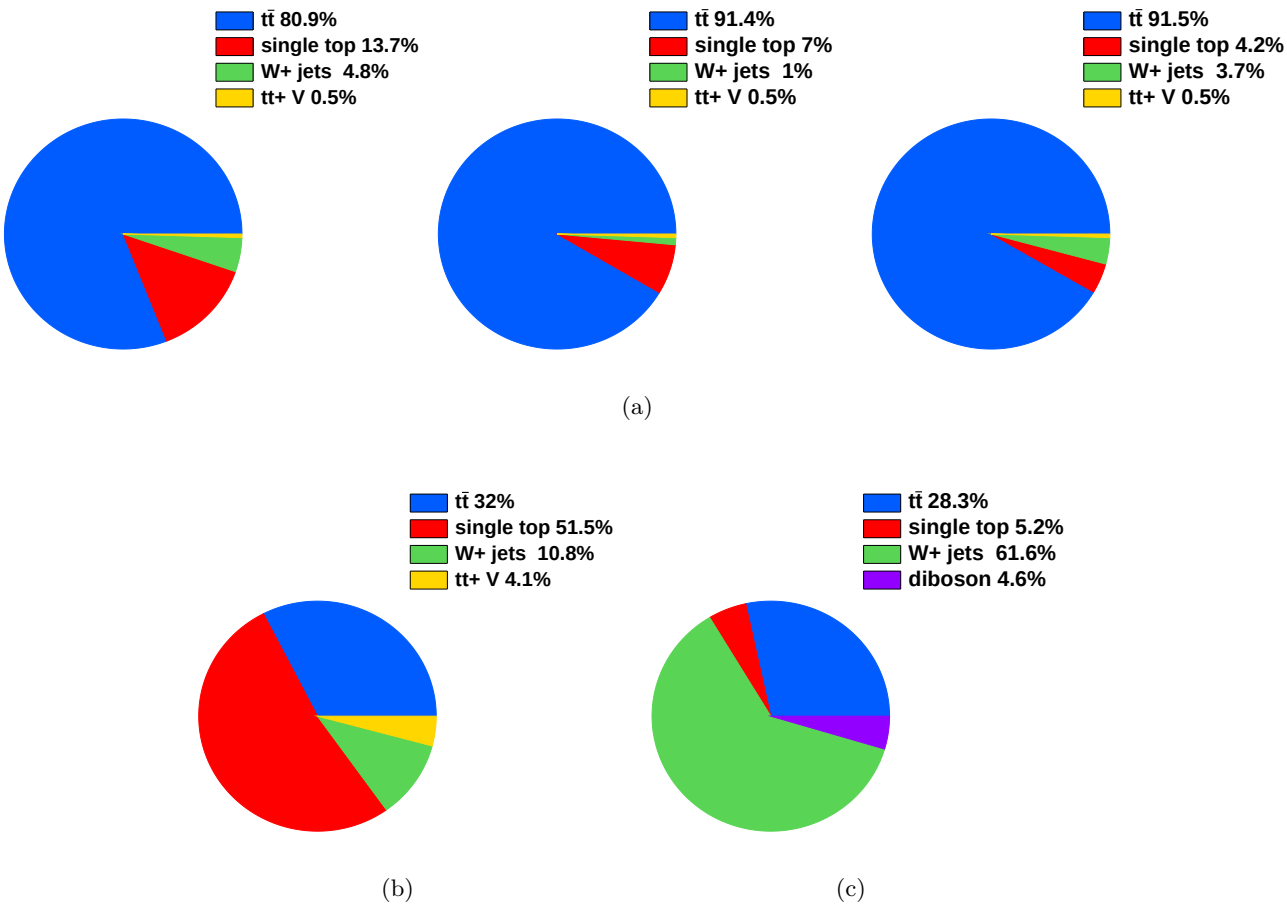

Figure 11.6.: Expected background compositions and the highest signal contamination in (a) CR-tt Low, Med and High, (b) CR-St and (c) CR-Wj control regions.

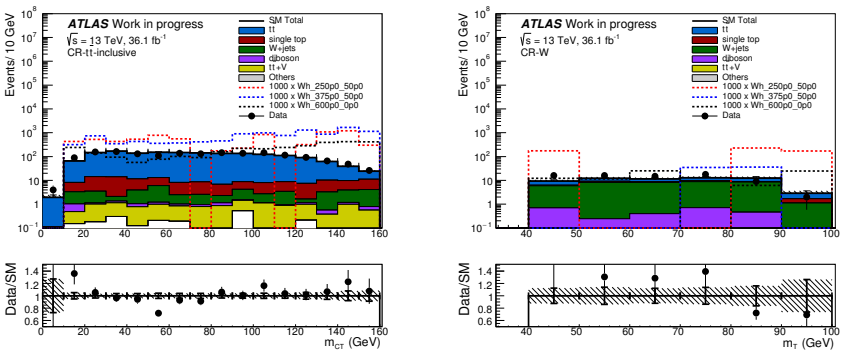

(a) (b)

Figure 11.7.: Distributions of (a) m_{CT} in the inclusive CR-tt and (b) m_{T}^{W} in CR-Wj, comparing data with the expected backgrounds from simulation. The lower panel shows the ratio between observed data and expected SM background. Uncertainties are statistical only.

11.4.2. Background validation regions

To validate the background predictions and kinematic variables used in the extrapolation between CRs and SRs, two sets of validation regions are chosen:

* VR-onpeak regions are defined as the 3 CR-tt regions but requiring 105<$m_{b\bar{b}}$ <135 GeV. They are dominated by the $t\bar{t}$ events as figure 11.8(a) shows and have low signal contamination of ≈ 10%.
* VR-offpeak requires m_{CT} > 160 GeV, $m_{b\bar{b}}$ < 95 GeV or in the range 145-195 GeV and $\mathrm{E}_{\mathrm{T}}^{\mathrm{miss}}$lower cut relaxed to 180 GeV to reduce the signal contamination. These regions are dominated by $t\bar{t}$ and single top as figure 11.8(b) shows.

The m_{bb} off peak VR-offML has low signal contamination of ≈ 15%, however the VR-offMM and VR-offMH, have non negligeable signal contamination, ∼ 20%, for some mass points outside the Run-1 exclusion as figure 11.9 shows. Thus, some additional studies were done to first show that the measured fraction of the signal outside the $m_{b\bar{b}}$ peak is compatible with the expected one; second, to ensure that this non-negligeable signal contamination in these sidebands is covered by the systematic uncertainty on the background. These studies are documented in appendix N.

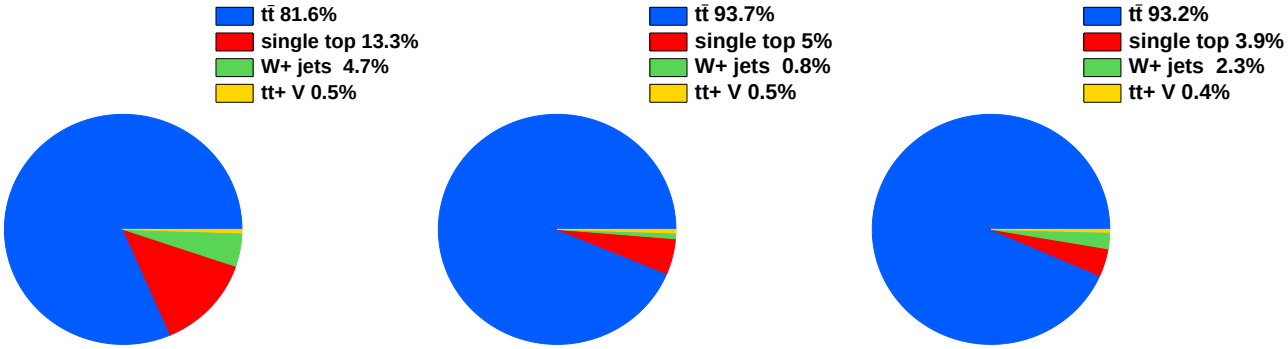

(a)

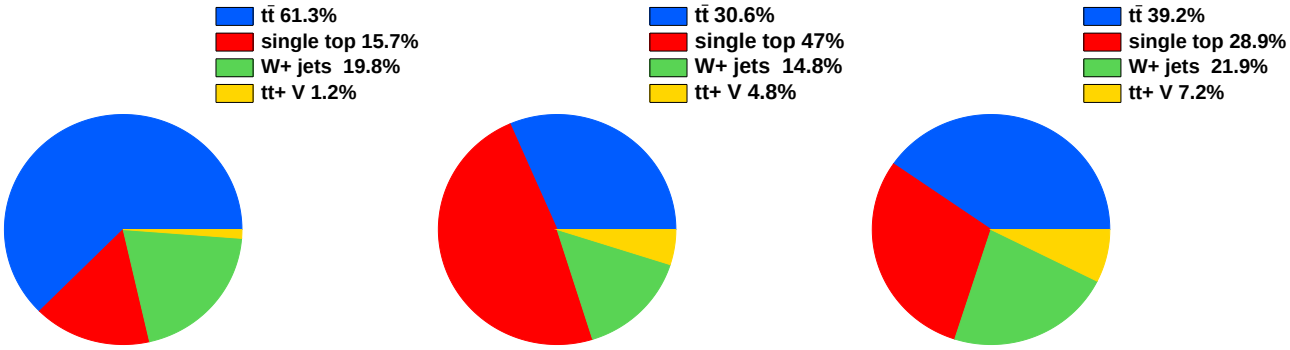

(b)

Figure 11.8.: Expected background compositions in (a) VR-onpeak and (b) VR-offpeak regions.

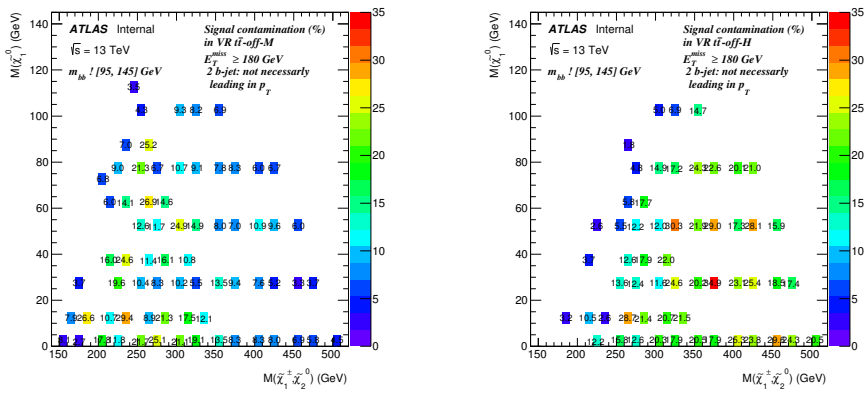

(a) (b)

Figure 11.9.: The signal contamination in % in the offpeak sideband validation regions: VR-offMM (a) and VR-offMH (b).

11.4.3. Truth composition of $t\bar{t}$ in CR/VR/SRs

The semileptonic/dileptonic $t\bar{t}$ composition at the truth level in the CRs, VRs and SRs is presented in table 11.5. It shows that the dileptonic (with no hadronic tau) $t\bar{t}$ dominates in all regions except in SRML and VR-offML.

Table 11.5.: The truth composition of the $t\bar{t}$ events in control, validation and signal regions.

$t\bar{t}$ composition	Semi-leptonic		Di-leptonic	
	e/μ/non had-tau (%)	had-tau (%)	e/μ/non had-tau(%)	had-tau (s)(%)
CR-ttML	40.6 $\pm$1.72	0	52.8 $\pm$ 1.82	6.66 $\pm$ 0.86
CR-ttMM	0.54 $\pm$0.17	0	87.5 $\pm$ 0.86	12 $\pm$ 0.74
CR-ttMH	0.07 $\pm$0.02	0.02 $\pm$ 0.01	76.6 $\pm$ 0.42	23.3 $\pm$ 0.40
VR-offML	75.5 $\pm$5.32	0	17 $\pm$ 4.78	7.55 $\pm$ 3.08
VR-offMM	5 $\pm$ 5.64	0	80 $\pm$ 8.29	15 $\pm$ 6.75
VR-offMH	0	0	81.6 $\pm$ 6.32	18.4 $\pm$ 6.32
VR-onML	27.9 $\pm$4.24	0	66.7 $\pm$ 4.97	5.44 $\pm$ 2.19
VR-onMM	0	0	86.8 $\pm$ 2.01	13.2 $\pm$ 2.01
VR-onMH	0.15 $\pm$ 0.11	0	76.5 $\pm$ 1.08	23.4 $\pm$ 1.02
SRML	96.2$\pm$3.77	0	3.85 $\pm$ 3.77	0
SRMM	12.5 $\pm$11.7	0	62.5 $\pm$ 17.1	25 $\pm$ 15.3
SRMH	0	0	66.7 $\pm$ 11.6	33.3 $\pm$ 11.6

In terms of jets, the $t\bar{t}$+ 1 light-jet dominates. Moreover, we checked the number of truth heavy flavor jets (nHF) and the number of truth light flavor jets (nLF) variations from the CRs to VRs(off, on) and SRs using the $t\bar{t}$ samples (see appendix O). We found similar distributions of HF and LF jets numbers in all regions. The low m_T regions are where we see the biggest deviation, but these regions have low statistics and these deviations are covered by statistics uncertainties. Figure 11.10 shows the mean HF/LF numbers as function of m_{CT} (upper plots), m_{bb} (bottom plots) for the $t\bar{t}$ events in control, validation and signal regions. We observe a slight increase in the number of HF with increasing m_{CT}, however the dependence of HF/LF numbers on m_{bb} looks less important.

11.5. Systematic uncertainties

Besides the statistical uncertainty coming from the finite number of events in the MC samples, the signal and background estimation is also affected by systematic uncertainties that can be categorized into two sources, experimental and theoretical: the experimental uncertainties are due to the finite precision of the calibration of the reconstructed objects and the non-perfect description of the experimental conditions, for example luminosity or pile-up; while theoretical uncertainties arise from the imperfect modelling of the processes in MC generators. The dominant experimental and theoretical uncertainties on the various signal regions are detailled in the next sections.

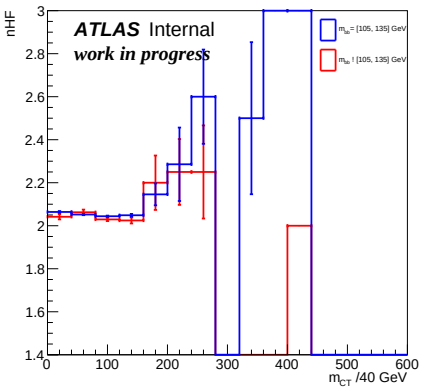

(a) nHF dependence on m_{CT}

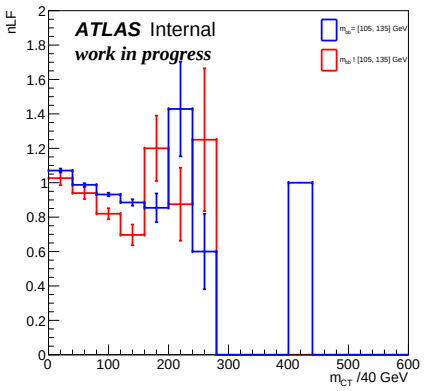

(b) nLF dependence on m_{CT}

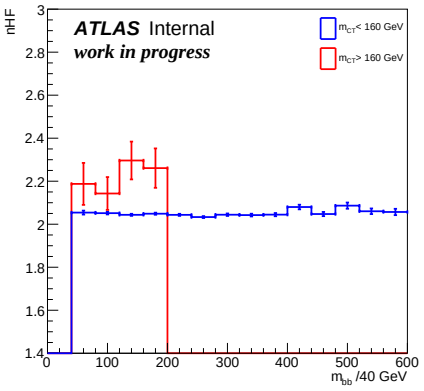

(c) nHF dependence on $m_{b\bar{b}}$

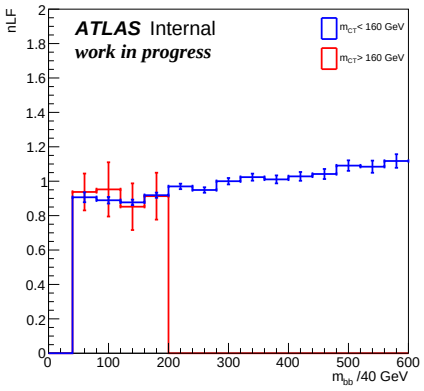

(d) nLF dependence on $m_{b\bar{b}}$

Figure 11.10.: The truth number of heavy and light flavors jets as function of m_{CT}, m_{bb} of the $t\bar{t}$ events in control, validation and signal regions.

11.5.1. Experimental uncertainties

The experimental uncertainties considered for this analysis are:

* Jet Enery Resolution (JER) uncertainty which affects the endpoint of the m_{CT} distribution and thus influences the efficiency of the m_{CT} requirement. It has a significant role in this analysis, accounting for nearly 20% systematic uncertainty in the SRMM region.
* Jet Energy Scale (JES) uncertainty which is the uncertainty on the final jet energy calibration. It is a correction relating the calorimeter's response to the true jet energy, it contributes up to 4.7% in SRMM.
* Uncertainties from the modelling of the b-tagging efficiencies and the mis-tag rates are sub-dominant for this channels because of the two b-tagged jets requirement, its maximal value is 10.5% in SRLM.
* Uncertainties related to the lepton efficiencies, for electrons, the uncertainties originate from the e/gamma resolution and scale and from the electron reconstruction efficiency. Similarly, for muons the uncertainties originate from the muon resolution and reconstruction efficiency, the isolation and the momentum scale. Its maximal value is 2.9% in SRMM.
* $\mathrm{E_T^{miss}}$soft term uncertainty due to the imperfections in the calibrations of hard objects which do also affect the $\mathrm{E_T^{miss}}$value. Their associated uncertainties (mainly JES and JER) are propagated to the $\mathrm{E_T^{miss}}$, its maximal value is 2.7% in SRLM.
* Uncertainty due to pileup re-weighting considered as two-sided variation in the event weights. This contributes up to 9% in SRML.
* Uncertainty in the combined 2015+2016 integrated luminosity which is 3.2%.

11.5.2. Signal theoretical uncertainties

The theoretical uncertainties on the signal samples cross sections that mainly affect the signal yields are calculated using the so-called "U-L prescription" [118]. Two sources of uncertainty are considered:

* the QCD renormalisation and factorisation scales, assumed equal here,
* the PDF uncertainties based upon two PDF sets CTEQ66 [119] and MSTW2008nlo90cl [120] while the signal samples were produced as described previously in section 11.1.1 using the NNPDF23LO [104] (nominal) PDF set including 101 members ($\mathrm{N_{mem}}$).

The table 11.6 presents the $(m_{\tilde{\chi}^{\pm}}, m_{\tilde{\chi}_1^0})$= (500, 0) GeV signal yields in SRML corresponding to 101 nominal PDF members, it shows that the choice of the PDF may affect also the signal acceptance. Therefore, a study was performed to check this impact using the truth samples of 3 signal mass points with low, medimum and high Δ M respectively: $(m_{\tilde{\chi}^{\pm}}, m_{\tilde{\chi}_1^0})$= (240, 110), (250, 0), (500, 0) GeV. We apply the same method used for the cross section uncertainties, "U-L prescription" which consists on combining 2 PDFs: CTEQ6.6 with $\mathrm{N_{mem}}$= 45 and MSTW2008nlo90cl with $\mathrm{N_{mem}}$=41. Following this method, the mean and systematic uncertainty on the product efficiency times acceptance (Eff $\times$ Acc) are given by equation 11.6:

$$\begin{aligned} \text{Mean} = \frac{\mathrm{U+L}}{2}, \quad \text{Uncert} = \frac{U-L}{2} \\ \mathrm{U} = \mathrm{Max}\left[\left(\mathrm{CTEQ_0} + \mathrm{CTEQ_{up}}\right), (\mathrm{MSTW_0} + \mathrm{MSTW_{up}})\right] \\ \mathrm{L} = \mathrm{Min}\left[(\mathrm{CTEQ_0} - \mathrm{CTEQ_{down}}), (\mathrm{MSTW_0} - \mathrm{MSTW_{down}})\right] \end{aligned} \tag{11.6}$$

where $\mathrm{CTEQ_0}$ (σ^0) is the (Eff $\times$ Acc) obtained using CTEQ central member (k=0) and $\mathrm{CTEQ_{up/down}}$ are its symmetric uncertainties computed as:

$$\mathrm{CTEQ_{up}} = \mathrm{CTEQ_{down}} = \frac{1}{2}\sqrt{\sum_{\mathrm{k=1}}^{\frac{\mathrm{N_{mem}}}{2}} (\sigma^{2*\mathrm{k}-1} - \sigma^{2*\mathrm{k}})^2}$$

. Similarly for $\mathrm{MSTW_0}$ is the (Eff $\times$ Acc) using MSTW central member, however, $\mathrm{MSTW_{up/down}}$ are the asymmetric uncertainties calculated as:

$$\mathrm{MSTW_{up}} = \sqrt{\sum_{\mathrm{k=1}}^{\frac{\mathrm{N_{mem}}}{2}} \max[\sigma^{2*\mathrm{k}-1} - \sigma^0, \sigma^{2*\mathrm{k}} - \sigma^0, 0]^2}$$

$$\mathrm{MSTW_{down}} = \sqrt{\sum_{\mathrm{k=1}}^{\frac{\mathrm{N_{mem}}}{2}} \max[\sigma^0 - \sigma^{2*\mathrm{k}-1}, \sigma^0 - \sigma^{2*\mathrm{k}}, 0]^2}$$

The resulting (Eff $\times$ Acc) means and systematic uncertainties, per signal region, for the 3 signal points are presented in table 11.7. Second line of each region is showing the uncertainty as fraction(%) of the mean, it is around 10% and it is the same order as the the errors on the cross sections.

Table 11.6.: The raw number of the signal ($m_{\tilde{\chi}^\pm}, m_{\tilde{\chi}_1^0}$)= (500, 0) GeV events in SRML corresponding to the 101 nominal PDF members.

k=0: 195	k=1: 199	k=2: 195.3	k=3: 190.1	k=4: 198.1	k=5: 169.9	k=6: 188.1	k=7: 207.8	k=8: 205.9	k=9: 193.6
k=10: 192	k=11: 190.3	k=12: 173	k=13: 216.6	k=14: 188.4	k=15: 193.9	k=16: 190	k=17: 202.5	k=18: 202.4	k=19: 188.1
k=20: 179.3	k=21: 190	k=22: 198.4	k=23: 174.2	k=24: 190.8	k=25: 212.7	k=26: 189.3	k=27: 182.6	k=28: 204.3	k=29: 183.9
k=30: 180.1	k=31: 198.1	k=32: 197.3	k=33: 191.1	k=34: 202.7	k=35: 194	k=36: 212.3	k=37: 196.8	k=38: 189.8	k=39: 197.6
k=40: 188.2	k=41: 208.1	k=42: 202.9	k=43: 190	k=44: 227.7	k=45: 218.2	k=46: 187.3	k=47: 192.7	k=48: 196.7	k=49: 199.2
k=50: 183.8	k=51: 192.2	k=52: 188.8	k=53: 194.6	k=54: 216.3	k=55: 178	k=56: 192.5	k=57: 200	k=58: 202.9	k=59: 190.4
k=60: 194.6	k=61: 200.1	k=62: 197.1	k=63: 191.5	k=64: 188.9	k=65: 203.6	k=66: 194	k=67: 184	k=68: 201.3	k=69: 189.7
k=70: 182.7	k=71: 191.7	k=72: 182.1	k=73: 195	k=74: 204.1	k=75: 196.8	k=76: 193.2	k=77: 194.2	k=78: 197.3	k=79: 181.8
k=80: 167	k=81: 198.5	k=82: 197.8	k=83: 198.8	k=84: 193.3	k=85: 186.1	k=86: 202	k=87: 184.8	k=88: 227.1	k=89: 185.7
k=90: 179.2	k=91: 203.4	k=92: 202.4	k=93: 199.8	k=94: 224.2	k=95: 184.1	k=96: 197.7	k=97: 187.4	k=98: 197.1	k=99: 191.2
k=100: 210.9									

Table 11.7.: The (Eff $\times$ Acc), mean$\pm$ Uncert$_{sys}$ in %, per signal region for 3 signal points. Second line of each signal region is showing the uncertainty as fraction(%) of the mean.

Region	(240, 110)	(250, 0)	(500, 0)
SRML	$(5.7\pm0.5)10^{-2}$	$(2.9\pm0.2)10^{-1}$	$(7.3\ \pm0.6)10^{-1}$
	8.8	6.9	8.2
SRMM	$(2.6\ \pm0.2)10^{-2}$	$(3.7\ \pm0.3)10^{-1}$	$(14\pm1)10^{-1}$
	7.7	8.1	7.1
SRMH	0	$(2.3\ \pm0.2)10^{-1}$	$(54.9\pm4.6)10^{-1}$
	0	8.7	8.4

11.5.3. Background theoretical uncertainties

The theoretical systematic uncertainties are due to the imperfect modelling of the processes in MC generators, they are determined by varying the MC generator parameters, such as the renormalisation and factorisation scales, the model used for the parton showering or the extent of the emission of additional partons in the initial or final states. Depending on the MC generator, the theoretical uncertainties are propagated by either event weights accounting for a variation of a parameter by its uncertainty or by generating new MC events where the theoretical parameter of interest is varied by its uncertainty. Further uncertainties arise from the uncertainty in the total cross-section of the predicted backgrounds. As the $t\bar{t}$, W+jets ans Wt yields are determined in dedicated CRs, uncertainties in those processes only affect the extrapolation from the control into the signal region (and amongst the various control regions). Therefore, no cross-section uncertainty is considered and transfer factors representing the ratio of the predicted yields between the SR and the corresponding CR(x) defined in equation 11.7 are used to evaluate the various systematic uncertainties.

$$\mathrm{TF}^{\mathrm{process}} = \frac{\mathrm{N}_{\mathrm{SR}}}{N_{\mathrm{CR(process)}}} \tag{11.7}$$

The systematic uncertainty on a transfer factor is given by comparing transfer factors derived using variation samples to ones derived using a 'nominal' sample as equation 11.8 shows.

$$\Delta\mathrm{TF}^{\mathrm{Process}}_{\mathrm{Syst}} = \frac{\mathrm{TF}^{\mathrm{Variation}} - \mathrm{TF}^{\mathrm{Nominal}}}{\mathrm{TF}^{\mathrm{Nominal}}} \tag{11.8}$$

Where statistically-independent samples are used for the evaluation of the nominal and variation transfer factors, a statistical component for each uncertainty is also derived as defined in equation 11.9.

$$\Delta TF^{Process}_{Stat} = \frac{TF^{Variation} - TF^{Nominal}}{TF^{Nominal}} \tag{11.9}$$

To derive the systematic uncertainty due to a particular variation, the systematic and statistical components of the TF are then added in quadrature. Theory uncertainties for $t\bar{t}$ processes are dominant for this channel, ranging from 15-20%. For the $t\bar{t}$ and single top processes, generator uncertainties are calculated by comparing Powheg + Pythia6 (nominal samples) to Sherpa 2.2.1, and the parton shower models are tested using Powheg + Pythia 6 compared to Powheg+ Herwig++. Scale variations are evaluated by varying the hdamp parameter between m_{top} and $2\times m_{\mathrm{top}}$, and the renormalization and factorization scales up and down by a factor of two. The uncertainties on the extent of the radiation of additional partons in the initial or final states (ISR/FSR) are estimated by two dedicated $t\bar{t}$ simulations where the amount of radiation emitted in the initial or final state was set to half or twice the value of the nominal sample, respectively. Systematic uncertainties on the contributions from single top production also account for the impact of interference terms between single-resonant and double-resonant top production.

The $Z+$jets and $W+$jets modelling uncertainties are estimated using the nominal SHERPA 2.2.1 samples by considering different merging (CKKW-L) and resummation scales, PDF variations from the NNPDF30NNLO replicas, as well as variations of the renormalization and factorization scales.

For the diboson background process, the uncertainty on the cross-section is considered. For

the tt+ V background uncertainties we include the scale and PDF uncertainties.

11.6. Fitting procedure

The expected SM background in each SR are estimated with a profile likelihood [121] named as "background-only" fit. The purpose of this fit is to estimate the total background in SRs and VRs, without making assumptions on any signal model. Therefore, it only uses the background samples and it assumes that the CRs are free of signal contamination. The fit is only performed in the CR(s), and the dominant background processes are normalized to the number of observed event in these regions after subtracting the other background components. Thus, these background predictions are independent of the observed number of events in each SR and VR which allows for an unbiased comparison between the predicted and observed number of events in each region. The fit uses for each SR, the number of events observed in its associated CR and the number of events predicted by simulation in each region for all background processes. These numbers are both described by Poisson statistics. The correlations in the systematic uncertainties described in the previous section that are common between SRs and CRs are treated as nuisance parameters in the fit and are modeled by Gaussian probability density functions. The product of the various probability density functions forms the likelihood, which the fit maximizes by adjusting the background normalization and the nuisance parameters. Then the normalization factors are derived from the fit. For background processes without a defined CR, contributions are estimated using the MC. The normalization factors are found to be between 0.9 $\pm$ 0.2 and 1.15$\pm$ 0.13 for the three SRs $t\bar{t}$ estimates, 1.15$^{+0.71}_{-1.05}$ for Wt and 1.4$\pm$0.5 for W+ jets, where the uncertainties include statistical and systematic.

The observed yields compared to the background estimates before and after the scale factors are applied for the three SRs are shown in table 11.8 a good agreement is found between data and SM predictions for 2 of the signal regions while the signal region SRMM shows a mild excess of about 2 σ.

Next to obtain the 95% CL upper limit on the number of events in a "beyond the Standard Model prediction" for each SR, we use "the model-independent signal" fit. The fit in the SR proceeds in the same way as the background-only fit, except that the number of events observed in the signal region is added as an input to the fit. When normalized by the integrated luminosity of the data sample, these results can be interpreted as upper limit on the visible cross section of new physics, σ_{vis} which is defined here as the product of acceptance, reconstruction efficiency and production cross section.

11.7. Results

The observed yields compared to the background estimates, after applying the background-only fit scale factors, for all SRs presented in table 11.8 shows a no significant excess above the SM expectation in any of the signal regions.

This can also be seen in figure 11.11 presenting the postfit, unblinded distributions of the m_{CT} and $\mathrm{E}_{\mathrm{T}}^{\mathrm{miss}}$variables of the SRMH and SRMM respectively. Concerning the VRs, figure 11.12 shows the VRs yields which match the background estimation as well.

Therefore, upper limits on contributions from new physics are estimated using the model-independent fits. Table 11.9 summarizes the observed and expected 95% CL upper limits

SR channel	SRML	SRMM	SRMH
Observed events	6	7	5
Fitted bkg events	5.7 ± 2.3	2.8 ± 1.0	4.6 ± 1.2
Fitted triboson_Sherpa221 events	0.0 ± 0.0	0.0 ± 0.0	0.0 ± 0.0
Fitted VH events	0.0 ± 0.0	0.0 ± 0.0	0.0 ± 0.0
Fitted Z+jets events	0.08 ± 0.04	0.0 ± 0.0	0.0 ± 0.0
Fitted $t\bar{t}$ V events	0.098 ± 0.035	0.32 ± 0.09	0.54 ± 0.14
Fitted ttH events	0.025 ± 0.011	0.029 ± 0.010	0.037 ± 0.018
Fitted singletop events	$1.4^{+1.4}_{-1.4}$	$0.8^{+0.9}_{-0.8}$	1.2 ± 1.1
Fitted diboson events	$0.12^{+0.15}_{-0.12}$	0.051 ± 0.032	0.075 ± 0.020
Fitted wjets_Sherpa221 events	0.6 ± 0.4	0.24 ± 0.12	1.6 ± 0.6
Fitted $t\bar{t}$ events	3.4 ± 2.9	1.4 ± 1.0	1.1 ± 0.6
MC exp. SM events	5.8 ± 2.9	2.5 ± 1.1	4.0 ± 1.0
MC exp. triboson_Sherpa221 events	0.0 ± 0.0	0.0 ± 0.0	0.0 ± 0.0
MC exp. VH events	0.0 ± 0.0	0.0 ± 0.0	0.0 ± 0.0
MC exp. Z+jets events	0.08 ± 0.04	0.0 ± 0.0	0.0 ± 0.0
MC exp. $t\bar{t}$ V events	0.098 ± 0.035	0.32 ± 0.09	0.54 ± 0.14
MC exp. ttH events	0.025 ± 0.011	0.029 ± 0.010	0.037 ± 0.019
MC exp. singletop events	1.3 ± 0.8	0.7 ± 0.6	1.1 ± 0.4
MC exp. diboson events	$0.12^{+0.15}_{-0.12}$	0.051 ± 0.032	0.075 ± 0.020
MC exp. wjets_Sherpa221 events	0.42 ± 0.25	0.16 ± 0.06	1.09 ± 0.27
MC exp. $t\bar{t}$ events	3.8 ± 2.7	1.2 ± 0.8	1.2 ± 0.6

Table 11.8.: Background-only fit results for the SRML, SRMM and SRMH regions, for an integrated luminosity of 36.1 fb^{-1}. Nominal MC expectations (normalised to MC cross-sections) are given for comparison. The uncertainties shown are the statistical plus systematic.

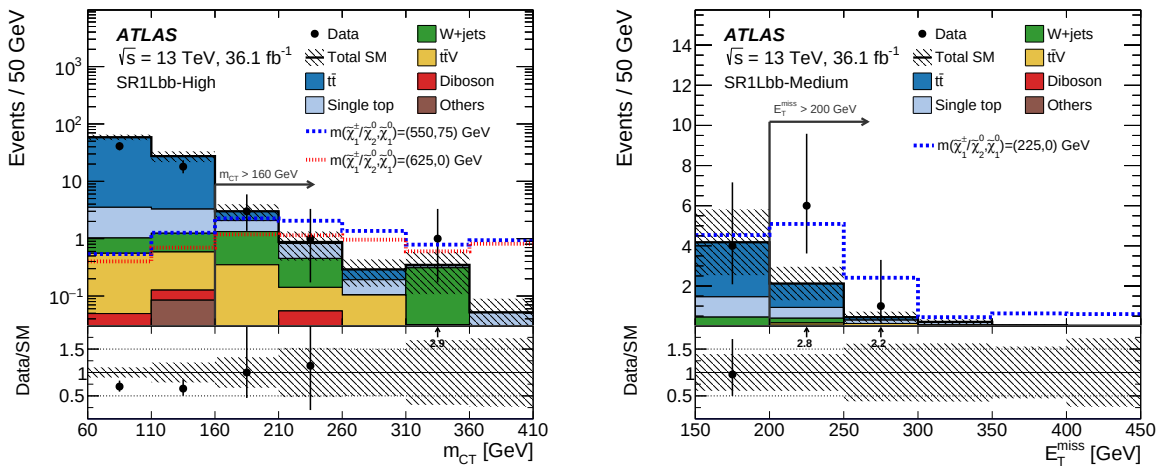

(a) (b)

Figure 11.11.: Data and SM predictions in SRs for (a) m_{CT} in SRMH and (b) $\mathrm{E_T^{miss}}$in SRMM. All SRs selections but the one on the quantity shown are applied. The statistical and systematic uncertainties are included in the uncertainty band.

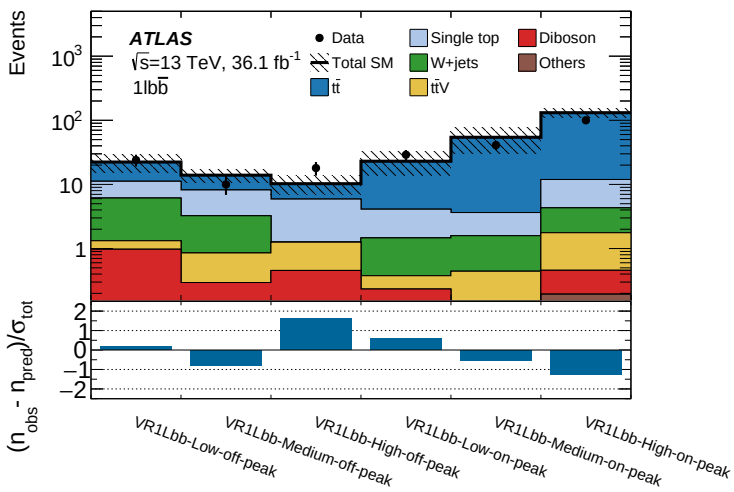

Figure 11.12.: Comparison of the predicted background with the observed numbers of events in the validation regions. The normalization of the background processes is obtained from the fit to the CRs. The upper panel shows the observed number of events and the predicted background yield. The statistical and systematic uncertainties are included in the uncertainty band. The lower panel shows the pulls in each VR.

on the number of BSM events and on the observed visible cross-section, for the 3 SRs. The expected number is obtained by setting the nominal event yield in each SR to the background expectation, while the observed number is obtained by using the actual event yield. p_0-values, which represents the probability of the SM background alone to fluctuate to the observed number of events or higher, are also shown. The smaller the p_0-value the more likely for the background-only hypothesis to be incorrect.

Table 11.9.: The observed 95% CL upper limits on the visible cross sections σ_{vis}, the observed (S^{95}_{obs}) and expected (S^{95}_{exp}) 95% CL upper limits on the number of signal events with $\pm 1\sigma$ excursions of the expectation, and the discovery p-value (p_0), truncated at 0.5.

	σ_{vis} [fb]	S^{95}_{obs}	S^{95}_{exp}	p_0-value
SRML	0.23	8.3	$8.0^{+3.3}_{-2.2}$	0.46
SRMM	0.28	10.0	$5.6^{+2.9}_{-1.7}$	0.04
SRMH	0.18	6.4	$6.1^{+3.1}_{-1.9}$	0.44

11.8. Interpretation

The results have been used to set exclusion limits at the 95% confidence level (CL) on the common mass of the $\tilde{\chi}_1^{\pm}$ and $\tilde{\chi}_2^0$ for various values of the $\tilde{\chi}_1^0$ mass in the simplified model considered in the analysis. The CLs method [122] is used to derive the confidence level of the exclusion for a particular signal model, then signal models with a CLs value below 0.05 are excluded at 95% CL. Figure 11.13(a) shows the expected and observed exclusion where a statistical combination of the results of the three $1\ell bb$ signal regions is performed, while figure 11.13(b) shows a comparison of the expected and observed exclusions for each analysis channel studied. Because of the high branching ratio of the Higgs boson into b-quark pairs, the sensitivity of the $1\ell bb$ and the $0\ell bb$ channels is the best at medium and high masses of the chargino and next-to-lightest neutralinos. Consequentely the $1\ell bb$ channel excludes the mass up to 540 GeV for a massless neutralinos, while the $0\ell bb$ channel which benefits also from the high hadronic W boson branching ratio gives a tighter limit at 680 GeV.

11.9. Conclusion and outlook

The search for $\tilde{\chi}_1^{\pm}$, $\tilde{\chi}_2^0$ production in events with one lepton, two b-jets, and missing transverse momentum is presented. The analysis uses 36.1 fb^{-1} of proton–proton collision data collected by the ATLAS experiment in 2015 and 2016 at $\sqrt{s}$= 13 TeV at the LHC. No evidence of new physics is observed and new tighter limits are placed on the $\tilde{\chi}_1^{\pm}$, $\tilde{\chi}_2^0$ production, with significant improvements over previous searches: $\tilde{\chi}_1^{\pm}$, $\tilde{\chi}_2^0$ masses up to 540 GeV for a massless neutralino $\tilde{\chi}_1^0$ are excluded at 95% C.L.

More generally, the SUSY searches, using the dataset recorded by the ATLAS detector in 2015 and 2016 with the integrated luminosity of 36.1 fb^{-1}, have not been successful. However,

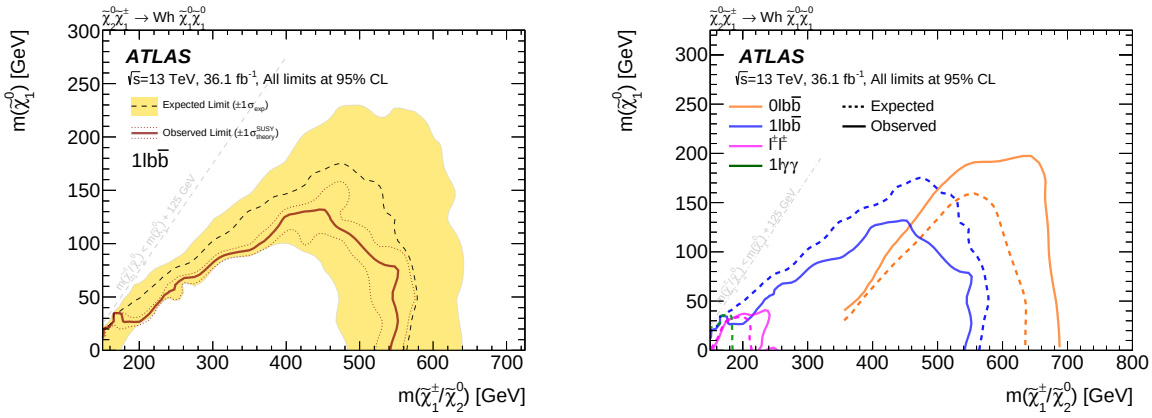

(a) (b)

Figure 11.13.: The expected and observed exclusion limits as a function of the $\tilde{\chi}_2^0/\tilde{\chi}_1^\pm$ masses and $\tilde{\chi}_1^0$ mass for (a) $1\ell bb$ channel, (b) all channels. Only the expected exclusion is shown for the $1\ell\gamma\gamma$ channel since the observed exclusion does not appear due to the small excess observed.

there is still hope that SUSY signals might show up with the future LHC data. A summary plot of the SUSY searches at ATLAS using the 36.1 fb^{-1} data, showing their maximum reach in mass is presented in figure 11.14. Signals could be seen in the "Compressed SUSY spectra" searches where the current limits are weaker, as figure 11.14 shows. Contrary to the chargino-neutralino search presented in this thesis which has $\Delta M = m_{\tilde{\chi}_1^\pm,\tilde{\chi}_2^0} - m_{\tilde{\chi}_1^0} > 125$ GeV, the "Compressed SUSY spectra" scenario has ΔM much smaller of order of few GeV.

Moreover, these current limits are the results of the simplified models searches which focus on one decay chain with fixed branching ratio, however, the complete picture is obtained by the pMSSM coverage, where the actual limits may be weakened when considering the decay to different final states. Certainly we need higher luminosity and eventually higher energy to progress on the SUSY searches.

At the end of Run2 in 2018, an integrated luminosity of 148.5 fb^{-1} has been recorded. Then, the LHC will be upgraded to rerun in 2021 at 14 TeV until 2023. During this Run3, 300 fb^{-1} of data are expected which is one order of magnitude more than the dataset analysed in this thesis. After 2023, we will benefit from the high luminosity LHC (HL-LHC) upgrade where the integrated luminosity by the end of Run5 is expected to reach 3000 fb^{-1}. With more data from these future runs, the reach in mass is expected to increase significantly.

With 3000 fb^{-1} of data, for the chargino-neutralino electroweak pair production leading to Wh in $1\ell bb + E_T^{miss}$ scenario we discussed in this thesis we could reach chargino limits up to 1300 GeV and neutralino up to 650 GeV or equivalently chargino discovery potential up to 950 GeV and neutralino discovery potential up to 250 GeV [124]. These results are obtained by re-optimizing the search using the multivariate analysis method as figure 11.15 shows.

On the other hand, the increase in the data volume expected by the LHC futur runs, offer us the possibility to search for new supersymmetric signals with smaller cross sections. Such as the chargino-neutralino productions through VBF processes which could also provide the same final states plus addtional light jets. A representative Feynman diagram is shown in figure 11.16(a). The corresponding cross sections calculated at $\sqrt{s}$ =13 TeV, are shown in figure 11.16(b). Contrary to the non-VBF process cross sections presented in figure 10.1,

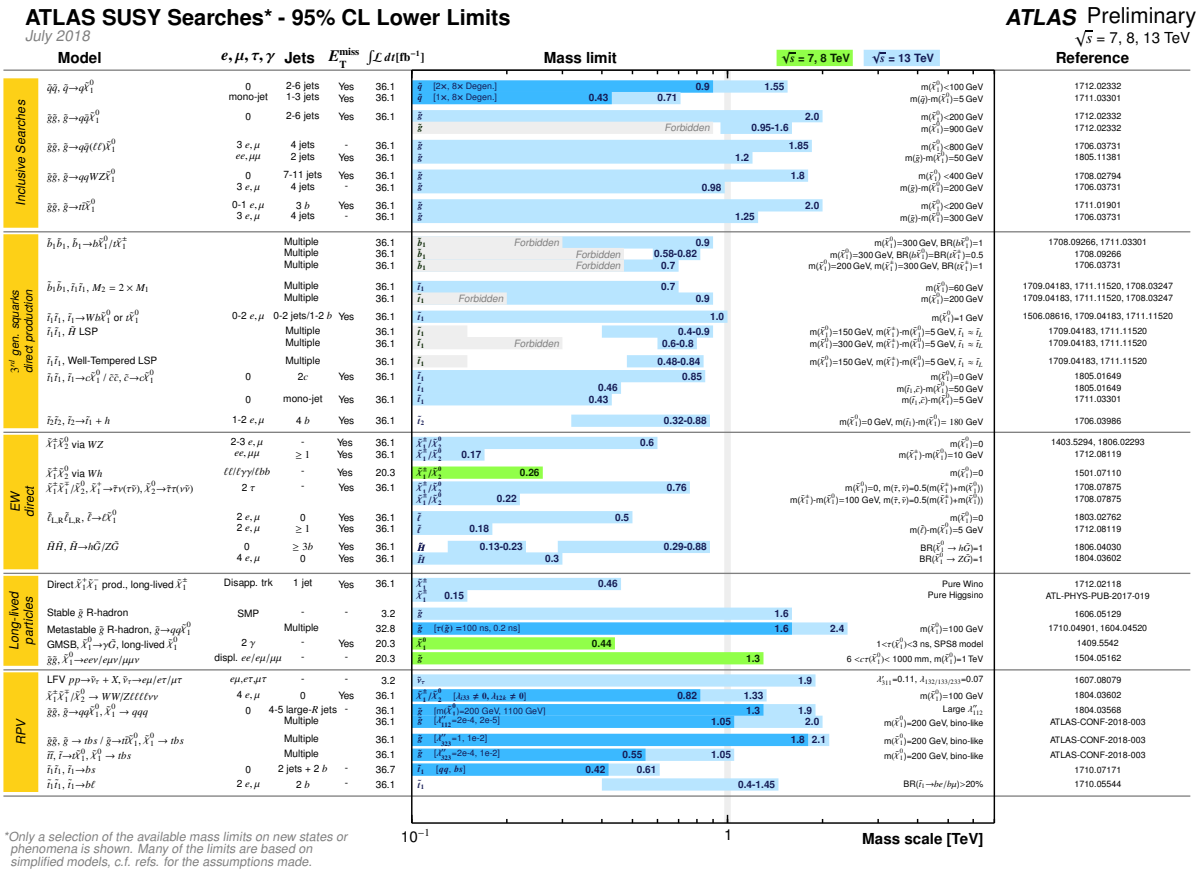

Figure 11.14.: Maximum mass reach of the ATLAS searches for SUSY [123].

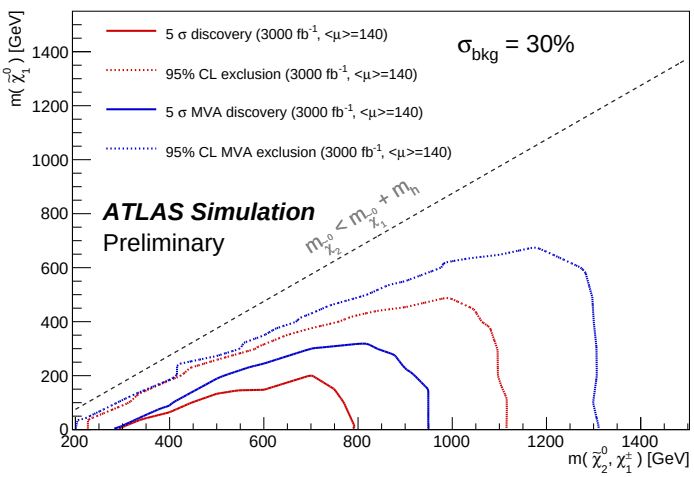

Figure 11.15.: Expected 95% exclusion and discovery contours for the 3000 fb^{-1} luminosity scenario in the $(m_{\tilde{\chi}_1^\pm}, m_{\tilde{\chi}_1^0})$ plane for the Wh-mediated simplified model, comparing the cut and count and MVA approaches [124].

the VBF cross sections shown in figure 11.16(b) are already multiplied by the Higgs to bb and W to lepton branching ratios, corresponding to 0.58 and 0.32 respectively. Also they are calculated at LO and not NLO+ NLL like the non-VBF cross sections. Taking all of that into account and by comparing the cross sections for the signal point ($m_{\tilde{\chi}_1^\pm}$, $m_{\tilde{\chi}_1^0}$)= (600, 0) GeV, the VBF process cross section seems to be one order of magnitude smaller than the non-VBF process cross section.

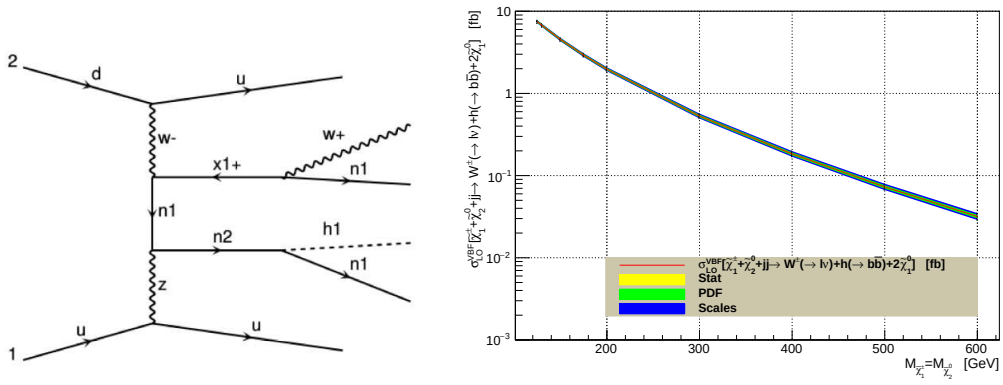

(a) (b)

Figure 11.16.: Chargino-neutralino pair production via VBF process at the LHC (a) Feynman diagram where x1+, n1, n2 and h1 denote the $\tilde{\chi}_1^+$, $\tilde{\chi}_1^0$, $\tilde{\chi}_2^0$ and the SM higgs respectively, (b) cross section at LO at $\sqrt{s}$ =13 TeV.

Part V.

Conclusion

In this concluding chapter, I summarize the contributions of this thesis. Three main parts were addressed in this thesis. First the search for electroweak production of supersymmetric $\tilde{\chi}_1^{\pm}$ +$\tilde{\chi}_2^0$ →W($\ell+\nu$)+h(bb)+$\tilde{\chi}_1^0$ using the 36.1 fb^{-1} of data collected by ATLAS at LHC Run2 with $\sqrt{s}$= 13 TeV was presented. It's the continuation of the search that pioneered in Run1 through the first usage of a Higgs boson as a tag to search for SUSY. The presence of b-jets in the final state requires adapting and improving the b-tagging algorithms for the ATLAS Run2. This second aim also serves as my qualifcation ATLAS authorship project which is mandatory to become a qualified ATLAS author.

The project concerns the optimisation of b-jets identification in Run2 data taking. More specifically, I studied the impact of several modifications related to the pixel tracker of ATLAS (Run2 conditions) on the b-tagging performance. Namely, varying the fraction of inactive modules and the pixel time over threshold. Such studies are very important and needed to better operate the pixel detector during the Run2 data taking. On the inactive modules study, scenarios inspired from the existing data quality granularity and flags were produced and studied.The aim of this study was to define the threshold for good data in terms of fraction of non-operant modules. So, Monte carlo samples with up to 35% inactive modules for the 4 pixel layers were produced and the b-tagging performances were compared with the default Run2 ATLAS detector configuration. The degradation in b-tagging performance versus jet kinematics variables p_T and η was studied as well. Also, changing the pixels time over threshold (ToT) on b-tagging was investigated. Increasing the pixels ToT in b-layer is one of the proposed solution to avoid the high occupency due to the increase of the luminosity in Run2. The Monte carlo samples with b-layer ToT cut up to 13 BC were produced and the b-tagging performances were compared to the default configuration with b-layer ToT cut at 4 BC. The degradation in b-tagging performance versus jet kinematics variables pt and eta was studied. In parallel, I studied the optimization of tracking-related variables and of track classification for impact parameter-based b-tagging algorithms (IP2D/IP3D).

Concerning the analysis, I mainly worked on the production of the MC samples, the SR, CR and VR definition, truth studies and signal theory uncertainties. About the strategy, we splitted the phase space of the search into three regions optimized for the signal with low $\tilde{\chi}_1^{\pm}$, $\tilde{\chi}_1^0$ mass splitting ΔM , medium ΔM and high ΔM. To separate these signal regions we used the m_{T}^{W} variable. We designed other regions to control each of the main backgrounds: $t\bar{t}$, single top and W+jets. Apart from the m_{T}^{W}, some standard variables were used to separate signal from background, such as the invariant mass of the two b-jets in the event $m_{b\bar{b}}$, which serves as a selection criterion for dijet pairs to be considered as Higgs boson candidates. We also use the contransverse mass, m_{CT}, variable mainly to reduce the $t\bar{t}$. However, no evidence of new physics is observed and new tighter limits are placed on the $\tilde{\chi}_1^{\pm}$, $\tilde{\chi}_2^0$ production, with significant improvements over previous searches: $\tilde{\chi}_1^{\pm}$, $\tilde{\chi}_2^0$ masses up to 540 GeV for a massless neutralino $\tilde{\chi}_1^0$ are excluded at 95% C.L.

The third goal was to improve Suspect3, which is a SUSY spectrum generator and one of the theory tools that will serve to interpret all the LHC Run2 simplified SUSY searches results. Suspect3 calculates SUSY mass spectra and couplings, currently, as all equivalent tool on the market, Suspect3 uses inputs at the electroweak scale such as M_Z , M_t , α_s, the soft

SUSY breaking parameters as the top trilinear coupling A_t to calculate the SUSY masses and couplings. My task on this front was to add a few options trading-off some soft-SUSY breaking parameters from the Higgs and stop sectors currently used as inputs, for the well measured Higgs boson mass. First, I computed the free parameter A_t for a given Higgs boson mass using a simplified expression of the radiative corrections to the Higgs boson mass.

Next, I used the state-of-the-art radiative corrections (full 1-loop and leading 2-loop RC) while implementing the A_t inversion within a newer version of Suspect3. Similarly to the simplified case, an iterative procedure was initially used to compute A_t where the first guess is the result of the simplified routine. However, I encountered some difficulties with this inversion because the full 1-loop RC of the Higgs mass have several A_t dependencies which have to be developed. An improved, approach where cubic dependencies on A_t from the loops have been identified, and the implementation of a more sophisticated iteration procedure taking into account repulsive or attractive fixed-points, has allowed to solve the problem and to lead to very good convergence of the inversion, taking the Higgs mass as input and A_t as output. The two-loop contributions have been also included and found to lead to good convergence as well.

Bibliography

[1] ATLAS Collaboration,
"Expected performance of the ATLAS b-tagging algorithms in Run-2,"
tech. rep. ATL-PHYS-PUB-2015-022, CERN, 2015,
URL: https://cds.cern.ch/record/2037697 (cit. on pp. 9, 115, 116).

[2] F. Halzen and A. Martin,
Quarks and leptons: an introductory course in modern particle physics,
Wiley, New York, USA, 1984 (cit. on pp. 34, 41–43).

[3] R. P. Feynman, *Space-Time Approach to Quantum Electrodynamics*,
Physical Review **76** (1949) p. 770 (cit. on p. 35).

[4] G. 't Hooft and M. J. G. Veltman,
Regularization and Renormalization of Gauge Fields, Nucl. Phys. **B44** (1972) p. 189
(cit. on p. 36).

[5] P. W. Higgs, *Broken Symmetries and the Masses of Gauge Bosons*,
Phys. Rev. Lett. **13** (1964) p. 508 (cit. on p. 37).

[6] P. Higgs, *Broken symmetries, massless particles and gauge fields*,
Physics Letters **12** (1964) p. 132 (cit. on p. 37).

[7] F. Englert and R. Brout, *Broken Symmetry and the Mass of Gauge Vector Mesons*,
Phys. Rev. Lett. **13** (9 1964) p. 321 (cit. on p. 37).

[8] J. Goldstone, A. Salam, and S. Weinberg, *Broken Symmetries*,
Phys. Rev. **127** (1962) p. 965 (cit. on p. 37).

[9] S. L. Glashow, *Partial Symmetries of Weak Interactions*,
Nucl. Phys. **22** (1961) p. 579 (cit. on p. 39).

[10] A. Salam, *Weak and Electromagnetic Interactions*,
Conf. Proc. **C680519** (1968) p. 367 (cit. on p. 39).

[11] S. L. Glashow, J. Iliopoulos, and L. Maiani,
Weak Interactions with Lepton-Hadron Symmetry, Phys. Rev. **D2** (1970) p. 1285
(cit. on p. 40).

[12] Patrignani, C. *et al.* (Particle Data Group), *Review of Particle Physics*,
Chin. Phys. **C40** (2016) p. 100001 (cit. on pp. 41, 42, 53).

[13] T. van Ritbergen and R. G. Stuart,
On the precise determination of the Fermi coupling constant from the muon lifetime,
Nucl. Phys. **B564** (2000) p. 343, arXiv: hep-ph/9904240 [hep-ph] (cit. on p. 41).

[14] D. M. Webber, "A New part-per-million measurement of the positive muon lifetime
and determination of the Fermi Constant,"
Particles and fields. Proceedings, Meeting of the Division of the American Physical Society, DPF 2011, Providence, USA, August 9-13, 2011,
arXiv: 1109.6689 [hep-ex] (cit. on p. 41).

[15] C. Rubbia, *The Discovery of the W and Z bosons*, Phys. Rept. **239** (1994) p. 241
(cit. on p. 42).

[16] E. Radermacher, *The Experimental Discovery of the Intermediate Vector Bosons W^+, W^- and Z^0 at the CERN $p\bar{p}$ Collider*, Prog. Part. Nucl. Phys. **14** (1985) p. 231 (cit. on p. 42).

[17] D. J. Gross and F. Wilczek, *Ultraviolet Behavior of Nonabelian Gauge Theories*, Phys. Rev. Lett. **30** (1973) p. 1343 (cit. on p. 43).

[18] H. D. Politzer, *Reliable Perturbative Results for Strong Interactions?* Phys. Rev. Lett. **30** (1973) p. 1346 (cit. on p. 43).

[19] D. LHC Higgs Cross Section Working Group Florian et al., *Handbook of LHC Higgs Cross Sections: 4. Deciphering the Nature of the Higgs Sector*, (2016), arXiv: 1610.07922 [hep-ph] (cit. on p. 44).

[20] LHC Higgs Cross Section Working Group, S. Heinemeyer, C. Mariotti, et al., *Handbook of LHC Higgs Cross Sections: 3. Higgs Properties*, (CERN, Geneva, 2013), arXiv: 1307.1347 [hep-ph] (cit. on p. 44).

[21] ATLAS Collaboration, *Observation of a new particle in the search for the Standard Model Higgs boson with the ATLAS detector at the LHC*, Physics Letters B **716** (2012) p. 1 (cit. on p. 45).

[22] ATLAS Collaboration, "Observation of H→ $b\bar{b}$ decays and VH production with the ATLAS detector," tech. rep. ATLAS-CONF-2018-036, CERN, 2018, URL: http://cdsweb.cern.ch/record/2630338 (cit. on p. 45).

[23] ATLAS and CMS Collaborations, *Measurements of the Higgs boson production and decay rates and constraints on its couplings from a combined ATLAS and CMS analysis of the LHC pp collision data at $\sqrt{s} = 7$ and 8 TeV*, JHEP **08** (2016) p. 045, arXiv: 1606.02266 [hep-ex] (cit. on p. 46).

[24] S. P. Martin, *A Supersymmetry primer*, (1997) p. 1, [Adv. Ser. Direct. High Energy Phys.18,1(1998)], arXiv: hep-ph/9709356 [hep-ph] (cit. on pp. 48, 52–54, 56, 57).

[25] F. Quevedo, S. Krippendorf, and O. Schlotterer, *Cambridge Lectures on Supersymmetry and Extra Dimensions*, (2010), arXiv: 1011.1491 [hep-th] (cit. on p. 48).

[26] R. Haag, J. T. Lopuszanski, and M. Sohnius, *All Possible Generators of Supersymmetries of the s Matrix*, Nucl. Phys. **B88** (1975) p. 257, [,257(1974)] (cit. on p. 48).

[27] Borut Bajc, *A short introduction to supersymmetry*, (2011), URL: http://www-f1.ijs.si/~bajc/susy.pdf (cit. on p. 49).

[28] J. Wess and B. Zumino, *A Lagrangian Model Invariant Under Supergauge Transformations*, Phys. Lett. **49B** (1974) p. 52 (cit. on p. 51).

[29] E. Witten, *Constraints on Supersymmetry Breaking*, Nucl. Phys. **B202** (1982) p. 253 (cit. on p. 52).

[30] E. Witten, *Dynamical Breaking of Supersymmetry*, Nucl. Phys. **B188** (1981) p. 513 (cit. on p. 52).

[31] A. Djouadi et al.,
"The Minimal supersymmetric standard model: Group summary report," *GDR (Groupement De Recherche) - Supersymetrie Montpellier, France, April 15-17, 1998*, arXiv: hep-ph/9901246 [hep-ph] (cit. on pp. 52, 57).

[32] L. Hall, J. Lykken, and S. Weinberg,
Supergravity as the messenger of supersymmetry breaking,
Phys. Rev. D **27** (10 1983) p. 2359,
URL: https://link.aps.org/doi/10.1103/PhysRevD.27.2359 (cit. on pp. 52, 61).

[33] M. Guchait, *Exact solution of the neutralino mass matrix*,
Zeitschrift für Physik C Particles and Fields **57** (1993) p. 157, ISSN: 1431-5858,
URL: https://doi.org/10.1007/BF01555748 (cit. on p. 56).

[34] ATLAS Collaboration, *Summary of the ATLAS experiment's sensitivity to supersymmetry after LHC Run 1 - interpreted in the phenomenological MSSM*,
Journal of High Energy Physics **10** (2015), arXiv: 1508.06608 [hep-ex]
(cit. on pp. 58–60).

[35] A. Djouadi, J.-L. Kneur, and G. Moultaka, *SuSpect: A Fortran code for the supersymmetric and Higgs particle spectrum in the MSSM*,
Comput. Phys. Commun. **176** (2007) p. 426, arXiv: hep-ph/0211331 [hep-ph]
(cit. on pp. 61, 64).

[36] A.Djouadi,J-L.Kneur,G.Moultaka,M.Ughetto,D.Zerwas, *SuSpect3*, (2012),
URL: http://suspect.in2p3.fr/suspect3-LH.pdf (cit. on p. 61).

[37] B. C. Allanach, *SOFTSUSY: a program for calculating supersymmetric spectra*,
Comput. Phys. Commun. **143** (2002) p. 305, arXiv: hep-ph/0104145 [hep-ph]
(cit. on p. 61).

[38] W. Porod, *SPheno, a program for calculating supersymmetric spectra, SUSY particle decays and SUSY particle production at e+ e- colliders*,
Comput. Phys. Commun. **153** (2003) p. 275, arXiv: hep-ph/0301101 [hep-ph]
(cit. on p. 61).

[39] W. Porod and F. Staub,
SPheno 3.1: Extensions including flavour, CP-phases and models beyond the MSSM,
Comput. Phys. Commun. **183** (2012) p. 2458, arXiv: 1104.1573 [hep-ph]
(cit. on p. 61).

[40] N. Arkani-Hamed, J. March-Russell, and H. Murayama, *Building models of gauge mediated supersymmetry breaking without a messenger sector*,
Nucl. Phys. **B509** (1998) p. 3, arXiv: hep-ph/9701286 [hep-ph] (cit. on p. 61).

[41] J. A. Bagger, T. Moroi, and E. Poppitz, *Anomaly mediation in supergravity theories*,
JHEP **04** (2000) p. 009, arXiv: hep-th/9911029 [hep-th] (cit. on p. 61).

[42] P. Z. Skands et al., *SUSY Les Houches accord: Interfacing SUSY spectrum calculators, decay packages, and event generators*, JHEP **07** (2004) p. 036,
arXiv: hep-ph/0311123 [hep-ph] (cit. on pp. 61, 65).

[43] B. C. Allanach et al., *SUSY Les Houches Accord 2*,
Comput. Phys. Commun. **180** (2009) p. 8, arXiv: 0801.0045 [hep-ph]
(cit. on p. 61).

[44] A. Djouadi, M. M. Muhlleitner, and M. Spira, *Decays of supersymmetric particles: The Program SUSY-HIT (SUspect-SdecaY-Hdecay-InTerface)*, Acta Phys. Polon. **B38** (2007) p. 635, arXiv: hep-ph/0609292 [hep-ph] (cit. on p. 61).

[45] W. Celmaster and R. J. Gonsalves, *Renormalization-prescription dependence of the quantum-chromodynamic coupling constant*, Phys. Rev. D **20** (6 1979) p. 1420, URL: https://link.aps.org/doi/10.1103/PhysRevD.20.1420 (cit. on p. 65).

[46] W. Siegel, *Supersymmetric dimensional regularization via dimensional reduction*, Physics Letters B **84** (1979) p. 193, ISSN: 0370-2693, URL: http://www.sciencedirect.com/science/article/pii/037026937990282X (cit. on p. 65).

[47] D. Capper, D. Jones, and P. V. Nieuwenhuizen, *Regularization by dimensional reduction of supersymmetric and non-supersymmetric gauge theories*, Nuclear Physics B **167** (1980) p. 479, ISSN: 0550-3213, URL: http://www.sciencedirect.com/science/article/pii/0550321380902448 (cit. on p. 65).

[48] D. M. Pierce, J. A. Bagger, K. T. Matchev, et al., *Precision corrections in the minimal supersymmetric standard model*, Nucl. Phys. **B491** (1997) p. 3, arXiv: hep-ph/9606211 [hep-ph] (cit. on pp. 65, 67, 68, 74).

[49] D. J. Castano, E. J. Piard, and P. Ramond, *Renormalization group study of the Standard Model and its extensions. 2. The Minimal supersymmetric Standard Model*, Phys. Rev. **D49** (1994) p. 4882, arXiv: hep-ph/9308335 [hep-ph] (cit. on p. 66).

[50] V. Barger, M. S. Berger, and P. Ohmann, *Supersymmetric grand unified theories: Two-loop evolution of gauge and Yukawa couplings*, Phys. Rev. D **47** (3 1993) p. 1093, URL: https://link.aps.org/doi/10.1103/PhysRevD.47.1093 (cit. on p. 66).

[51] B. de Carlos and J. A. Casas, *One loop analysis of the electroweak breaking in supersymmetric models and the fine tuning problem*, Phys. Lett. **B309** (1993) p. 320, arXiv: hep-ph/9303291 [hep-ph] (cit. on p. 66).

[52] R. Arnowitt and P. Nath, *Loop corrections to radiative breaking of electroweak symmetry in supersymmetry*, Phys. Rev. D **46** (9 1992) p. 3981, URL: https://link.aps.org/doi/10.1103/PhysRevD.46.3981 (cit. on p. 67).

[53] A. Dedes, G. Degrassi, and P. Slavich, *On the two loop Yukawa corrections to the MSSM Higgs boson masses at large tan beta*, Nucl. Phys. **B672** (2003) p. 144, arXiv: hep-ph/0305127 [hep-ph] (cit. on pp. 69, 78).

[54] G. Degrassi, P. Slavich, and F. Zwirner, *On the neutral Higgs boson masses in the MSSM for arbitrary stop mixing*, Nucl. Phys. **B611** (2001) p. 403, arXiv: hep-ph/0105096 [hep-ph] (cit. on pp. 69, 78).

[55] H. E. Haber, R. Hempfling, and A. H. Hoang, *Approximating the radiatively corrected Higgs mass in the minimal supersymmetric model*, Z. Phys. **C75** (1997) p. 539, arXiv: hep-ph/9609331 [hep-ph] (cit. on p. 71).

[56] B. C. Allanach, A. Djouadi, J. L. Kneur, et al., *Precise determination of the neutral Higgs boson masses in the MSSM*, JHEP **09** (2004) p. 044, arXiv: hep-ph/0406166 [hep-ph] (cit. on p. 79).

[57] L. R. Evans and P. Bryant, *LHC Machine*, J. Instrum. **3** (2008) S08001. 164 p, This report is an abridged version of the LHC Design Report (CERN-2004-003), URL: https://cds.cern.ch/record/1129806 (cit. on p. 83).

[58] ATLAS Collaboration, *ATLAS: technical proposal for a general-purpose pp experiment at the Large Hadron Collider at CERN*, LHC Tech. Proposal, CERN, 1994, URL: http://cds.cern.ch/record/290968 (cit. on p. 84).

[59] CMS Collaboration, *Technical proposal*, LHC Tech. Proposal, Cover title : CMS, the Compact Muon Solenoid : technical proposal, CERN, 1994, URL: http://cds.cern.ch/record/290969 (cit. on p. 84).

[60] ALICE Collaboration, *ALICE: Technical proposal for a Large Ion collider Experiment at the CERN LHC*, LHC Tech. Proposal, CERN, 1995, URL: http://cds.cern.ch/record/293391 (cit. on p. 84).

[61] LHCb Collaboration, *LHCb : Technical Proposal*, Tech. Proposal, CERN, 1998, URL: http://cds.cern.ch/record/622031 (cit. on p. 84).

[62] CERN, "Taking a closer look at LHC," tech. rep., URL: http://www.lhc-closer.es/taking_a_closer_look_at_lhc/1.home (cit. on p. 84).

[63] ATLAS Collaboration, "Luminosity Public Results Run2," tech. rep., CERN, URL: https://twiki.cern.ch/twiki/bin/view/AtlasPublic/LuminosityPublicResultsRun2#Luminosity_summary_plots_for_AN2 (cit. on p. 86).

[64] O. B. G. Apollinari, *High Luminosity LHC Project Description*, CERN-ACC-2014-0321, URL: https://cds.cern.ch/record/1974419 (cit. on pp. 86, 87).

[65] "Physics at a High-Luminosity LHC with ATLAS," *Proceedings, 2013 Community Summer Study on the Future of U.S. Particle Physics: Snowmass on the Mississippi (CSS2013): Minneapolis, MN, USA, July 29-August 6, 2013*, arXiv: 1307.7292 [hep-ex], URL: http://www.slac.stanford.edu/econf/C1307292/docs/submittedArxivFiles/1307.7292.pdf (cit. on p. 86).

[66] ATLAS Collaboration, *The ATLAS Experiment at the CERN Large Hadron Collider*, Journal of Instrumentation **3** (2008) S08003, URL: http://stacks.iop.org/1748-0221/3/i=08/a=S08003 (cit. on pp. 88, 90, 98, 99).

[67] *ATLAS magnet system: Technical Design Report, 1*, Technical Design Report ATLAS, CERN, 1997, URL: https://cds.cern.ch/record/338080 (cit. on p. 89).

[68] C. Leroy and P.-G. Rancoita, *Silicon Solid State Devices and Radiation Detection*, WORLD SCIENTIFIC, 2012, eprint: https://www.worldscientific.com/doi/pdf/10.1142/8383, URL: https://www.worldscientific.com/doi/abs/10.1142/8383 (cit. on p. 91).

[69] Stefano Meroli, "Energy Loss Distribution of charged particles in silicon layers," tech. rep., URL: http://meroli.web.cern.ch/Lecture_StragglingFunction.html (cit. on pp. 92, 93).

[70] M. Capeans, G. Darbo, K. Einsweiller, et al., "ATLAS Insertable B-Layer Technical Design Report," tech. rep. CERN-LHCC-2010-013. ATLAS-TDR-19, 2010, URL: https://cds.cern.ch/record/1291633 (cit. on p. 93).

[71] ATLAS Collaboration, *ATLAS pixel detector electronics and sensors*, Journal of Instrumentation **3** (2008) P07007, URL: http://stacks.iop.org/1748-0221/3/i=07/a=P07007 (cit. on p. 94).

[72] G. Aad et al., *A neural network clustering algorithm for the ATLAS silicon pixel detector*, JINST **9** (2014) P09009, arXiv: 1406.7690 [hep-ex] (cit. on p. 95).

[73] G. Mullier, *The upgraded Pixel Detector of the ATLAS experiment for Run-2 at the Large Hadron Collider*, Journal of Instrumentation **11** (2016) p. C02061, URL: http://stacks.iop.org/1748-0221/11/i=02/a=C02061 (cit. on pp. 94, 123).

[74] ATLAS Collaboration, "Pixel detector and IBL 2015 Plots," tech. rep., URL: https://twiki.cern.ch/twiki/bin/view/AtlasPublic/ApprovedPlotsPixel#Pixel_detector_and_IBL_2015_Plot (cit. on p. 96).

[75] S. Grinstein, *The ATLAS Forward Proton Detector (AFP)*, Nucl. Part. Phys. Proc. **273-275** (2016) p. 1180 (cit. on p. 99).

[76] ATLAS Collaboration, "Early Inner Detector Tracking Performance in the 2015 data at $\sqrt{s}$ = 13 TeV," tech. rep. ATL-PHYS-PUB-2015-051, CERN, 2015, URL: http://cdsweb.cern.ch/record/2110140 (cit. on p. 102).

[77] ATLAS Collaboration, "Performance of primary vertex reconstruction in proton-proton collisions at $\sqrt{s}$=7 TeV in the ATLAS experiment," tech. rep. ATLAS-CONF-2010-069, CERN, 2010, URL: https://cds.cern.ch/record/1281344 (cit. on p. 101).

[78] M. Cacciari, G. P. Salam, and G. Soyez, *The anti- k t jet clustering algorithm*, Journal of High Energy Physics **2008** (2008) p. 063, URL: http://stacks.iop.org/1126-6708/2008/i=04/a=063 (cit. on p. 101).

[79] "Electron efficiency measurements with the ATLAS detector using the 2015 LHC proton-proton collision data," tech. rep. ATLAS-CONF-2016-024, CERN, 2016, URL: https://cds.cern.ch/record/2157687 (cit. on p. 103).

[80] *Update of the Computing Models of the WLCG and the LHC Experiments*, CERN, 2014, URL: https://cds.cern.ch/record/1695401/ (cit. on p. 105).

[81] S. Höche, F. Krauss, M. Schönherr, et al., *QCD matrix elements + parton showers: The NLO case*, JHEP **04** (2013) p. 027, arXiv: 1207.5030 [hep-ph] (cit. on p. 106).

[82] T. Sjöstrand, S. Mrenna, and P. Z. Skands, *PYTHIA 6.4 Physics and Manual*, JHEP **0605** (2006) p. 026, arXiv: hep-ph/0603175 (cit. on pp. 106, 123).

[83] T. Sjöstrand, S. Mrenna, and P. Z. Skands, *A Brief Introduction to PYTHIA 8.1*, Comput. Phys. Commun. **178** (2008) p. 852, arXiv: 0710.3820 [hep-ph] (cit. on pp. 106, 123, 166, 167).

[84] M. Bahr et al., *Herwig++ Physics and Manual*, Eur. Phys. J. **C58** (2008) p. 639, arXiv: 0803.0883 [hep-ph] (cit. on p. 106).

[85] J. Bellm, S. Gieseke, D. Grellscheid, et al., *Herwig 7.0/Herwig++ 3.0 release note*, The European Physical Journal C **76** (2016) p. 196, ISSN: 1434-6052, arXiv: 1512.01178 [hep-ph] (cit. on p. 106).

[86] T. Gleisberg, S. Hoeche, F. Krauss, et al., *Event generation with SHERPA 1.1*, JHEP **0902** (2009) p. 007, arXiv: 0811.4622 [hep-ph] (cit. on pp. 106, 167).

[87] S. Frixione and B. R. Webber, *Matching NLO QCD computations and parton shower simulations*, JHEP **0206** (2002) p. 029, arXiv: hep-ph/0204244 [hep-ph] (cit. on p. 106).

[88] A. Rimoldi and A. Dell'Acqua, *The Full detector simulation for the ATLAS experiment: Status and outlook*, eConf **C0303241** (2003) TUMT001, arXiv: physics/0306086 [physics] (cit. on pp. 106, 123).

[89] ATLAS Collaboration, "Optimisation and performance studies of the ATLAS b-tagging algorithms for the 2017-18 LHC run," tech. rep. ATL-PHYS-PUB-2017-013, CERN, 2017, URL: http://cds.cern.ch/record/2273281 (cit. on p. 110).

[90] R. Zaidan, "A search for a charged Higgs boson in the $H^+ \to t\bar{b}$ channel and b-tagging algorithms with the ATLAS experiment at the LHC.," Theses: Université de la Méditerranée - Aix-Marseille II, 2009, URL: https://tel.archives-ouvertes.fr/tel-00546131 (cit. on p. 110).

[91] K. G. Tomiwa, *Performance of Jet Vertex Tagger in suppression of pileup jets and E_T^{miss} in ATLAS detector*, Journal of Physics: Conference Series **802** (2017) p. 012012, URL: http://stacks.iop.org/1742-6596/802/i=1/a=012012 (cit. on p. 110).

[92] ATLAS Collaboration, "Optimisation of the ATLAS b-tagging performance for the 2016 LHC Run," tech. rep. ATL-PHYS-PUB-2016-012, CERN, 2016, URL: http://cds.cern.ch/record/2160731 (cit. on pp. 112–114, 137).

[93] *Vertex reconstruction and track bundling at the LEP collider using robust algorithms*, Computer Physics Communications 96 **189-208** (1996), URL: https://web-docs.gsi.de/~ikisel/reco/Methods/Fruehwirth-LEP-CPC96-1996.pdf (cit. on p. 115).

[94] ATLAS Collaboration, "ATLAS Inner Tracker Performance at the beginning of the LHC Run-2," tech. rep. ATL-INDET-PROC-2016-002, CERN, 2016, URL: https://cds.cern.ch/record/2147407/ (cit. on pp. 123, 134).

[95] S. Frixione, P. Nason, and C. Oleari, *Matching NLO QCD computations with Parton Shower simulations: the POWHEG method*, JHEP **0711** (2007) p. 070, arXiv: 0709.2092 [hep-ph] (cit. on pp. 123, 166, 167).

[96] ATLAS Collaboration,
"IBL Efficiency and Single Point Resolution in Collision Events,"
tech. rep. ATL-INDET-PUB-2016-001, CERN, 2016,
URL: https://cds.cern.ch/record/2203893 (cit. on p. 134).

[97] M. Aaboud et al., *Search for a scalar partner of the top quark in the jets plus missing transverse momentum final state at $\sqrt{s}$=13 TeV with the ATLAS detector*, JHEP **12** (2017) p. 085, arXiv: 1709.04183 [hep-ex] (cit. on p. 162).

[98] A. Sopczak, *SUSY (ATLAS)*, (2017), [EPJ Web Conf.182,20212(2018)], arXiv: 1712.10165 [hep-ph] (cit. on p. 162).

[99] D. Bogavac, A. Cervelli, J. Lorenz, et al., "Search for chargino and neutralino production in final state with one lepton, two b-jets consistent with a Higgs boson, and missing transverse momentum at $\sqrt{s} = 13$ TeV with the ATLAS detector,"
tech. rep. ATL-COM-PHYS-2017-381, CERN, 2017,
URL: https://cds.cern.ch/record/2259593 (cit. on p. 163).

[100] M. D'Onofrio, D. Miller, A. De Santo, et al.,
"Search for chargino and neutralino production in final state with a Higgs boson, and missing transverse momentum at $\sqrt{s} = 13$ TeV with the ATLAS detector,"
tech. rep. ATL-COM-PHYS-2018-486, CERN, 2018,
URL: https://cds.cern.ch/record/2316315 (cit. on p. 164).

[101] G. Aad et al.,
Search for direct pair production of a chargino and a neutralino decaying to the 125 GeV Higgs boson in $\sqrt{s} = 8$ TeV pp collisions with the ATLAS detector,
Eur. Phys. J. **C75** (2015) p. 208, arXiv: 1501.07110 [hep-ex]
(cit. on pp. 164, 165).

[102] A. M. Sirunyan et al., *Combined search for electroweak production of charginos and neutralinos in proton-proton collisions at $\sqrt{s} = 13$ TeV*, JHEP **03** (2018) p. 160, arXiv: 1801.03957 [hep-ex] (cit. on p. 164).

[103] J. Alwall, R. Frederix, S. Frixione, et al.,
The automated computation of tree-level and next-to-leading order differential cross sections, and their matching to parton shower simulations, JHEP **07** (2014) p. 079, arXiv: 1405.0301 [hep-ph] (cit. on pp. 166, 167).

[104] R. D. Ball et al., *Parton distributions with LHC data*,
Nucl. Phys. B **867** (2013) p. 244, arXiv: 1207.1303 [hep-ph]
(cit. on pp. 166, 167, 182).

[105] ATLAS Collaboration, "ATLAS Run 1 Pythia8 tunes,"
tech. rep. ATL-PHYS-PUB-2014-021, 2014,
URL: https://cds.cern.ch/record/1966419 (cit. on pp. 166, 167).

[106] L. Lönnblad and S. Prestel,
Merging Multi-leg NLO Matrix Elements with Parton Showers,
JHEP **03** (2013) p. 166, arXiv: 1211.7278 [hep-ph] (cit. on p. 166).

[107] D. J. Lange, *The EvtGen particle decay simulation package*,
Nucl. Instrum. Meth. A **462** (2001) p. 152 (cit. on pp. 166, 167).

[108] C. Borschensky, M. Kramer, A. Kulesza, et al., *Squark and gluino production cross sections in pp collisions at $\sqrt{s}$ = 13, 14, 33 and 100 TeV*,
Eur. Phys. J. C **74** (2014) p. 3174, arXiv: 1407.5066 [hep-ph] (cit. on p. 166).

[109] S. Alioli, P. Nason, C. Oleari, et al., *A general framework for implementing NLO calculations in shower Monte Carlo programs: the POWHEG BOX*, JHEP **1006** (2010) p. 043, arXiv: 1002.2581 [hep-ph] (cit. on pp. 166, 167).

[110] H.-L. Lai, M. Guzzi, J. Huston, et al., *New parton distributions for collider physics*, Phys. Rev. D **82** (2010) p. 074024, arXiv: 1007.2241 [hep-ph] (cit. on pp. 166, 167).

[111] T. Sjöstrand, S. Mrenna, and P. Z. Skands, *PYTHIA 6.4 Physics and Manual*, JHEP **05** (2006) p. 026, arXiv: hep-ph/0603175 [hep-ph] (cit. on pp. 166, 167).

[112] P. Z. Skands, *Tuning Monte Carlo Generators: The Perugia Tunes*, Phys. Rev. D **82** (2010) p. 074018, arXiv: 1005.3457 [hep-ph] (cit. on p. 167).

[113] J. Alwall, R. Frederix, S. Frixione, et al., *The automated computation of tree-level and next-to-leading order differential cross sections, and their matching to parton shower simulations*, JHEP **07** (2014) p. 079, arXiv: 1405.0301 [hep-ph] (cit. on p. 167).

[114] S. Gieseke, C. Rohr, and A. Siodmok, *Colour reconnections in Herwig++*, Eur. Phys. J. C **72** (2012) p. 2225, arXiv: 1206.0041 [hep-ph] (cit. on p. 167).

[115] G. Polesello and D. R. Tovey, *Supersymmetric particle mass measurement with the boost-corrected contransverse mass*, JHEP **03** (2010) p. 030, arXiv: 0910.0174 [hep-ph] (cit. on p. 169).

[116] J. E. Gaiser, "Charmonium Spectroscopy From Radiative Decays of the J/ψ and ψ'," PhD thesis: SLAC, 1982, URL: http://www-public.slac.stanford.edu/sciDoc/docMeta.aspx?slacPubNumber=slac-r-255.html (cit. on p. 173).

[117] K. CRANMER, "STATISTICAL CHALLENGES FOR SEARCHES FOR NEW PHYSICS AT THE LHC," *Statistical Problems in Particle Physics, Astrophysics and Cosmology* p. 112, eprint: https://www.worldscientific.com/doi/pdf/10.1142/9781860948985_0026, URL: https://www.worldscientific.com/doi/abs/10.1142/9781860948985_0026 (cit. on p. 174).

[118] M. Kramer, A. Kulesza, R. van der Leeuw, et al., *Supersymmetry production cross sections in pp collisions at $\sqrt{s} = 7$ TeV*, (2012), arXiv: 1206.2892 [hep-ph] (cit. on p. 182).

[119] P. M. Nadolsky, H.-L. Lai, Q.-H. Cao, et al., *Implications of CTEQ global analysis for collider observables*, Phys. Rev. **D78** (2008) p. 013004, arXiv: 0802.0007 [hep-ph] (cit. on p. 182).

[120] A. D. Martin, W. J. Stirling, R. S. Thorne, et al., *Parton distributions for the LHC*, Eur. Phys. J. **C63** (2009) p. 189, arXiv: 0901.0002 [hep-ph] (cit. on p. 182).

[121] M. Baak, G. J. Besjes, D. Côte, et al., *HistFitter software framework for statistical data analysis*, Eur. Phys. J. **C75** (2015) p. 153, arXiv: 1410.1280 [hep-ex] (cit. on p. 185).

[122] T. Junk, *Confidence level computation for combining searches with small statistics*, Nucl. Instrum. Meth. **A434** (1999) p. 435, arXiv: hep-ex/9902006 [hep-ex] (cit. on p. 188).

[123] ATLAS Collaboration,
Summary plots from the ATLAS Supersymmetry physics group, (2018), URL: https://atlas.web.cern.ch/Atlas/GROUPS/PHYSICS/CombinedSummaryPlots/SUSY/ (cit. on p. 190).

[124] ATLAS Collaboration, "Prospect for a search for direct pair production of a chargino and a neutralino decaying via a W boson and the lightest Higgs boson in final states with one lepton, two b-jets and missing transverse momentum at the high luminosity LHC with the ATLAS Detector,"
tech. rep. ATL-PHYS-PUB-2015-032, CERN, 2015,
URL: http://cdsweb.cern.ch/record/2038565 (cit. on pp. 189, 190).

[125] C. ATLAS, "Letter of Intent for the Phase-II Upgrade of the ATLAS Experiment," tech. rep. CERN-LHCC-2012-022. LHCC-I-023, Draft version for comments: CERN, 2012, URL: https://cds.cern.ch/record/1502664.

[126] O. S. Brüning, P. Collier, P. Lebrun, et al., *LHC Design Report*, CERN, 2004, URL: https://cds.cern.ch/record/782076.

[127] J. Stirling, "Parton Luminosity and Cross-section plots," tech. rep., URL: http://www.hep.ph.ic.ac.uk/%5C~%7B%7Dwstirlin/plots/plots.html.

[128] ATLAS Collaboration,
"Summary plots from the ATLAS Standard Model physics group," tech. rep., URL: https://atlas.web.cern.ch/Atlas/GROUPS/PHYSICS/CombinedSummaryPlots/SM/.

[129] A. Team,
"Computer-generated diagram of an LHC dipole. Schéma d'un dipôle du LHC," 1998, URL: https://cds.cern.ch/record/39731.

[130] R. Alemany-Fernandez, E. Bravin, L. Drosdal, et al.,
Operation and Configuration of the LHC in Run 1, (2013),
URL: https://cds.cern.ch/record/1631030.

[131] R. Bruce, G. Arduini, H. Bartosik, et al., "LHC Run 2: Results and Challenges," tech. rep. CERN-ACC-2016-0103, CERN, 2016,
URL: https://cds.cern.ch/record/2201447.

[132] TOTEM Collaboration, "TOTEM, Total Cross Section, Elastic Scattering and Diffraction Dissociation at the LHC: Technical Proposal,"
tech. rep. CERN-LHCC-99-007. LHCC-P-5, CERN, 1999,
URL: http://cds.cern.ch/record/385483.

[133] LHCf Collaboration, *The LHCf detector at the CERN Large Hadron Collider*, Journal of Instrumentation **3** (2008) S08006,
URL: http://stacks.iop.org/1748-0221/3/i=08/a=S08006.

[134] ATLAS Collaboration, "Electron efficiency measurements with the ATLAS detector using the 2012 LHC proton-proton collision data,"
tech. rep. ATLAS-CONF-2014-032, CERN, 2014,
URL: https://cds.cern.ch/record/1706245.

[135] T. Davidek, M. Volpi, and T. Zenis, "Response of the ATLAS Tile Calorimeter to Hadrons in Stand-Alone Testbeam Data," tech. rep. ATL-TILECAL-PUB-2009-004. ATL-COM-TILECAL-2009-002, The note has been updated using comments received by both referees.: CERN, 2009, URL: https://cds.cern.ch/record/1161351.

[136] ATLAS Collaboration, "The Expected Performance of the ATLAS Inner Detector," tech. rep. ATL-PHYS-PUB-2009-002. ATL-COM-PHYS-2008-105, CERN, 2008, URL: https://cds.cern.ch/record/1118445.

[137] ATLAS Collaboration, "Studies of the ATLAS Inner Detector material using $\sqrt{s}$ =13 TeV *pp* collision data," tech. rep. ATL-PHYS-PUB-2015-050, CERN, 2015, URL: https://cds.cern.ch/record/2109010.

[138] ATLAS Collaboration, "ATLAS public web page," tech. rep., URL: http://atlas.cern/resources/multimedia.

[139] ATLAS Collaboration, "Event Displays from Collision Data public page," tech. rep., URL: https://twiki.cern.ch/twiki/bin/view/AtlasPublic/EventDisplayRun2Collisions.

[140] ATLAS Collaboration, "Alignment of the ATLAS Inner Detector with the initial LHC data at $\sqrt{s}$ = 13 TeV," tech. rep. ATL-PHYS-PUB-2015-031, CERN, 2015, URL: https://cds.cern.ch/record/2038139.

[141] N. Nikiforou, "Performance of the ATLAS Liquid Argon Calorimeter after three years of LHC operation and plans for a future upgrade," *Proceedings, 3rd International Conference on Advancements in Nuclear Instrumentation Measurement Methods and their Applications (ANIMMA 2013): Marseille, France, June 23-27, 2013*, 2013, arXiv: 1306.6756 [physics.ins-det], URL: https://inspirehep.net/record/1240499/files/arXiv:1306.6756.pdf.

[142] ATLAS Collaboration, *Readiness of the ATLAS Liquid Argon Calorimeter for LHC Collisions*, Eur. Phys. J. **C70** (2010) p. 723, arXiv: 0912.2642 [physics.ins-det].

[143] G. W. Wilburn, A. Mattillion, G. Facini, et al., "Tile Calorimeter Cell Energy Distribution Using 2015 Collision Data at $\sqrt{s}$ = 13 and 0.9 TeV," tech. rep. ATL-COM-TILECAL-2016-003, CERN, 2016, URL: https://cds.cern.ch/record/2131164.

[144] ATLAS Collaboration, *Commissioning of the ATLAS Muon Spectrometer with Cosmic Rays*, Eur. Phys. J. **C70** (2010) p. 875, arXiv: 1006.4384 [physics.ins-det].

[145] P. Nason, *A New method for combining NLO QCD with shower Monte Carlo algorithms*, JHEP **0411** (2004) p. 040, arXiv: hep-ph/0409146.

[146] F. Cascioli, P. Maierhofer, and S. Pozzorini, *Scattering Amplitudes with Open Loops*, Phys. Rev. Lett. **108** (2012) p. 111601, arXiv: 1111.5206 [hep-ph].

[147] T. G. Cornelissen, N. Van Eldik, M. Elsing, et al., "Updates of the ATLAS Tracking Event Data Model (Release 13)," tech. rep. ATL-SOFT-PUB-2007-003. ATL-COM-SOFT-2007-008, CERN, 2007, URL: https://cds.cern.ch/record/1038095.

[148] ATLAS Collaboration,
"Particle Identification Performance of the ATLAS Transition Radiation Tracker,"
tech. rep. ATLAS-CONF-2011-128, CERN, 2011,
URL: https://cds.cern.ch/record/1383793.

[149] T. Cornelissen, M. Elsing, S. Fleischmann, et al.,
"Concepts, Design and Implementation of the ATLAS New Tracking (NEWT),"
tech. rep. ATL-SOFT-PUB-2007-007. ATL-COM-SOFT-2007-002, CERN, 2007,
URL: https://cds.cern.ch/record/1020106.

[150] ATLAS Collaboration, "Reconstruction of primary vertices at the ATLAS experiment in Run 1 proton–proton collisions at the LHC,"
tech. rep. arXiv:1611.10235. CERN-EP-2016-150, CERN, 2016,
URL: https://cds.cern.ch/record/2235651.

[151] ATLAS Collaboration,
"The Optimization of ATLAS Track Reconstruction in Dense Environments,"
tech. rep. ATL-PHYS-PUB-2015-006, CERN, 2015,
URL: https://cds.cern.ch/record/2002609.

[152] ATLAS Collaboration,
"Comparison of the impact parameter resolution in Run 1 and Run 2," tech. rep.,
URL:
https://atlas.web.cern.ch/Atlas/GROUPS/PHYSICS/PLOTS/IDTR-2015-007/.

[153] ATLAS collaboration, *Muon reconstruction efficiency and momentum resolution of the ATLAS experiment in proton–proton collisions at* $\sqrt{s} = 7$ *TeVin* 2010,
The European Physical Journal C **74** (2014) p. 3034, ISSN: 1434-6052,
URL: http://dx.doi.org/10.1140/epjc/s10052-014-3034-9.

[154] ATLAS collaboration, *Muon reconstruction performance of the ATLAS detector in proton–proton collision data at* $\sqrt{s} = 13$ *TeV*,
The European Physical Journal C **76** (2016) p. 292, ISSN: 1434-6052,
URL: http://dx.doi.org/10.1140/epjc/s10052-016-4120-y.

[155] ATLAS Collaboration, "Electron and photon reconstruction and identification in ATLAS: expected performance at high energy and results at 900 GeV,"
tech. rep. ATLAS-CONF-2010-005, CERN, 2010,
URL: https://cds.cern.ch/record/1273197.

[156] W. Lampl, S. Laplace, D. Lelas, et al.,
"Calorimeter Clustering Algorithms: Description and Performance,"
tech. rep. ATL-LARG-PUB-2008-002. ATL-COM-LARG-2008-003, CERN, 2008,
URL: https://cds.cern.ch/record/1099735.

[157] ATLAS collaboration, "Expected electron performance in the ATLAS experiment,"
tech. rep. ATL-PHYS-PUB-2011-006, CERN, 2011,
URL: https://cds.cern.ch/record/1345327.

[158] ATLAS Collaboration, "Photon identification in 2015 ATLAS data,"
tech. rep. ATL-PHYS-PUB-2016-014, CERN, 2016,
URL: https://cds.cern.ch/record/2203125.

[159] ATLAS Collaboration, *Jet energy measurement with the ATLAS detector in proton-proton collisions at $\sqrt{s} = 7$ TeV*,
The European Physical Journal C **73** (2013) p. 2304, ISSN: 1434-6052,
URL: http://dx.doi.org/10.1140/epjc/s10052-013-2304-2.

[160] ATLAS Collaboration,
"Tagging and suppression of pileup jets with the ATLAS detector,"
tech. rep. ATLAS-CONF-2014-018, CERN, 2014,
URL: https://cds.cern.ch/record/1700870.

[161] ATLAS Collaboration, "Jet Calibration and Systematic Uncertainties for Jets Reconstructed in the ATLAS Detector at $\sqrt{s} = 13$ TeV,"
tech. rep. ATL-PHYS-PUB-2015-015, CERN, 2015,
URL: https://cds.cern.ch/record/2037613.

[162] ATLAS Collaboration,
"Tau Reconstruction and Identification Performance in ATLAS,"
tech. rep. ATLAS-CONF-2010-086, CERN, 2010,
URL: https://cds.cern.ch/record/1298857.

[163] "Performance of missing transverse momentum reconstruction for the ATLAS detector in the first proton-proton collisions at at $\sqrt{s}$= 13 TeV,"
tech. rep. ATL-PHYS-PUB-2015-027, CERN, 2015,
URL: https://cds.cern.ch/record/2037904.

[164] "Technical Design Report for the ATLAS ITk Pixel Detector,"
tech. rep. ATL-COM-ITK-2017-073, CERN, 2017,
URL: https://cds.cern.ch/record/2296611.

[165] E. B. for the LHC team, *LHC Report: LHC hit the target!. Dernières nouvelles du LHC : l'accélérateur a atteint son objectif !* (2016) p. 4,
URL: https://cds.cern.ch/record/2212514.

[166] M. Cacciari, G. P. Salam, and G. Soyez, *The catchment area of jets*,
Journal of High Energy Physics **2008** (2008) p. 005,
URL: http://stacks.iop.org/1126-6708/2008/i=04/a=005.

[167] M. Cacciari and G. P. Salam, *Pileup subtraction using jet areas*,
Physics Letters B **659** (2008) p. 119, ISSN: 0370-2693, arXiv: 0707.1378 [hep-ph],
URL:
http://www.sciencedirect.com/science/article/pii/S0370269307011094.

[168] D. J. Lange, *The EvtGen particle decay simulation package*,
Nuclear Instruments and Methods in Physics Research Section A: Accelerators, Spectrometers, Detectors and Associated Equipment **462** (2001) p. 152,
BEAUTY2000, Proceedings of the 7th Int. Conf. on B-Physics at Hadron Machines,
ISSN: 0168-9002, URL:
http://www.sciencedirect.com/science/article/pii/S0168900201000894.

[169] J. Pumplin, D. R. Stump, J. Huston, et al., *New Generation of Parton Distributions with Uncertainties from Global QCD Analysis*,
Journal of High Energy Physics **2002** (2002) p. 012,
URL: http://stacks.iop.org/1126-6708/2002/i=07/a=012.

[170] H.-L. Lai, M. Guzzi, J. Huston, et al., *New parton distributions for collider physics*, Phys. Rev. D **82** (7 2010) p. 074024, URL: https://link.aps.org/doi/10.1103/PhysRevD.82.074024.

[171] L. Breiman, J. Friedman, C. Stone, et al., *Classification and Regression Trees*, The Wadsworth and Brooks-Cole statistics-probability series, Taylor & Francis, 1984, ISBN: 9780412048418, URL: https://books.google.fr/books?id=JwQx-WOmSyQC.

[172] A. L. Jeremy G. Siek Lie-Quan Lee, *Boost Graph Library, The: User Guide and Reference Manual*, Addison-Wesley Professional, 2001, URL: http://www.boost.org/doc/libs/1_65_1/libs/graph/doc/index.html.

[173] A. Banfi, G. P. Salam, and G. Zanderighi, *Accurate QCD predictions for heavy-quark jets at the Tevatron and LHC*, Journal of High Energy Physics **2007** (2007) p. 026, URL: http://stacks.iop.org/1126-6708/2007/i=07/a=026.

[174] R. E. Ticse Torres, "Search for the Higgs boson in the $ttH(H \to bb)$ channel and the identification of jets containing two B hadrons with the ATLAS experiment.," Theses: Centre de Physique des Particules de Marseille, 2016, URL: https://tel.archives-ouvertes.fr/tel-01516435.

[175] T. Liu, L. Wang, and J. M. Yang, *Pseudo-goldstino and electroweakinos via VBF processes at LHC*, JHEP **02** (2015) p. 177, arXiv: 1411.6105 [hep-ph].

[176] G. Aad et al., *Muon reconstruction performance of the ATLAS detector in proton–proton collision data at $\sqrt{s}$ =13 TeV*, Eur. Phys. J. **C76** (2016) p. 292, arXiv: 1603.05598 [hep-ex] (cit. on p. 103).

J. Data sets used for the study of the robustness of b-tagging performance with various conditions of the pixel detector

$t\bar{t}$ sample used: mc15_13TeV.410000.PowhegPythiaEvtGen_P2012_ttbar _hdamp172p5_nonallhad.simul.HITS.e3698_a766

Table 0.10.: Z'($b\bar{b}$) dataSets names of the HITS samples for the different Z' masses values.

Mass (TeV)	Data set names
$m = 1$	mc15_13TeV.301922.Pythia8EvtGen_A14NNPDF23LO_Zprimebb1000. simul.HITS.e3889_a766/
$m = 2$	mc15_13TeV.301926.Pythia8EvtGen_A14NNPDF23LO_Zprimebb2000. simul.HITS.e3889_a766/
$m = 5$	mc15_13TeV.301930.Pythia8EvtGen_A14NNPDF23LO_Zprimebb5000. simul.HITS.e3889_a766/

Table 0.11.: Z'($q\bar{q}$) dataSets names of the HITS samples for the different Z' masses values.

Mass (TeV)	Data set names
$m = 1$	mc15_13TeV.304767.Pythia8EvtGen_A14NNPDF23LO_Zprimeqq1000. simul.HITS.e4674_a766
$m = 2$	mc15_13TeV.304771.Pythia8EvtGen_A14NNPDF23LO_Zprimeqq2000. simul.HITS.e4674_a766
$m = 5$	mc15_13TeV.304775.Pythia8EvtGen_A14NNPDF23LO_Zprimeqq5000. simul.HITS.e4674_a766

K. Rate of tracks in the fourteen categories for the pixel configurations studied

Table 0.12.: Rate (%) of tracks in the fourteen categories for the baseline and the IBL scenarios produced with $t\bar{t}$ sample. y represents the fraction of inactive module in IBL.

Category	Baseline	y=6%	y=9%	y=15%	y=25%	y=35%	y=100%
0	2.3	2.2	2.1	1.9	1.8	1.5	0
1	0.1	0.06	0.07	0.07	0.05	0.06	0
2	0.04	0.2	0.3	0.6	0.7	1	3
3	0.02	0.4	0.06	0.1	0.6	0.2	2
4	2.5	2.4	2.3	2.1	2	1.7	0
5	1	5	8	17	18	31	95
6	0.5	0.5	0.5	0.4	0.4	0.3	0
7	2	1	1.5	1.5	1	1.4	0
8	0.02	0.01	0.02	0.02	0.01	0.01	0
9	2	1.9	1.9	1.7	1.7	1.4	0
10	3.6	3.4	3.3	2.9	2.9	2.4	0
11	1.1	1.09	1.06	0.9	0.9	0.7	0
12	1.8	1.7	1.6	1.5	1.4	1.2	0
13	83	80	77	69	68	56	0

Table 0.13.: Rate (%) of tracks in the fourteen categories for the baseline and the L0 scenarios produced with $t\bar{t}$ sample. y represents the fraction of inactive module in L0.

Category	Baseline	y=6%	y=9%	y=15%	y=25%	y=35%	y=100%
0	2.3	2.1	2	1.9	1.7	1.5	0
1	0.1	0.3	0.5	0.7	1	2	5
2	0.04	0.04	0.04	0.04	0.04	0.03	0
3	0.02	0.05	0.1	0.1	0.2	0.3	1
4	2.5	2.4	2.3	2.1	1.9	1.7	0
5	1	0.9	0.87	0.83	0.7	0.6	0
6	0.5	0.5	0.48	0.46	0.42	0.4	0
7	2	5	10	14	22	31	94
8	0.02	0.02	0.02	0.01	0.01	0.01	0
9	2	1.9	1.8	1.75	1.6	1.4	0
10	4	3.3	3.1	3	2.7	2.3	0
11	1	0.99	0.94	0.87	0.8	0.7	0
12	1.8	1.6	1.5	1.4	1.3	1	0
13	83	81	76	73	65	57	0

Table 0.14.: Rate (%) of tracks in the fourteen categories for the baseline and the L1 (L2) scenarios produced with $t\bar{t}$ sample. y represents the fraction of inactive module in L1 (L2).

Category	Baseline	L1, y=6%	L1, y=9%	L1, y=100%	L2, y=6%	L2, y=9%	L2, y=100%
0	2.3	2.17	2.15	1.6	2.15	2.13	1
1	0.1	0.08	0.08	0.06	0.08	0.08	0.05
2	0.04	0.04	0.04	0.04	0.04	0.04	0.03
3	0.02	0.02	0.02	0.02	0.02	0.02	0.02
4	2.5	2.46	2.47	2.42	2.47	2.46	2.4
5	1	1	0.96	0.91	0.96	0.96	0.92
6	0.5	0.52	0.51	0.7	0.51	0.51	0.48
7	2.2	1.58	1.57	1.54	1.57	1.57	1.54
8	0.02	0.02	0.02	0.02	0.02	0.02	0.02
9	2	2.01	1.98	3	1.98	1.98	2.5
10	3.6	3.44	3.44	3.9	3.44	3.46	4
11	1.1	1.04	1.04	1.1	1.04	1.03	1.03
12	1.8	1.7	1.7	1.5	1.7	1.7	1.6
13	83	84.02	84.08	82.9	84.08	84.1	84.13

Table 0.15.: Rate (%) of tracks in the fourteen categories for the baseline and the scenarios produced with Z' mix sample. y represents the fraction of inactive module.

Category	Baseline	IBL, y=35%	IBL, y=100%	L0, y=35%	L0, y=100%	L1, y=100%	L2, y=100%
0	4.3	3	0	2.9	0	3	2.3
1	0.2	0.1	0	3	8	0.1	0.09
2	0.09	2	5.5	0.06	0	0.08	0.06
3	0.03	0.2	2	0.3	0.9	0.01	0.01
4	4.17	2.9	0	2.8	0	3.9	3.7
5	1	30	93	0.7	0	0.85	0.87
6	0.8	0.57	0	0.59	0	1.2	0.8
7	2	1	0	30	91	1.54	1.53
8	0.01	0.01	0	0.01	0	0.02	0.03
9	3	2.34	0	2.32	0	5	4
10	11	7.4	0	7.3	0	11.6	12
11	4.7	3.4	0	3.2	0	5	4.7
12	4	2.4	0	2.38	0	3	3.2
13	65	44.4	0	44.5	0	65	66

Table 0.16.: Rate (%) of tracks in the fourteen categories for the baseline and the scenarios with the highest L0 ToT cuts produced with $t\bar{t}$ sample.

Category	Mc15c	L0 n=10	L0 n=13
0	2.19	2.36	2.63
1	0.11	0.114	0.115
2	0.04	0.076	0.17
3	0.03	0.03	0.03
4	2.45	2.38	2.25
5	0.95	0.91	0.80
6	0.5	3.1	10.44
7	2.31	2.35	2.37
8	0.017	0.015	0.016
9	1.94	1.93	1.9
10	3.37	3.20	2.96
11	1.02	0.74	0.64
12	1.64	1.60	1.46
13	83.4	81.1	74.22

Table 0.17.: Rate (%) of tracks in the fourteen categories for the baseline and the scenarios with the highest L0 ToT cuts produced with Z' mix sample.

Category	Mc15c	L0 n=10	L0 n=13
0	4.28	4.55	5.03
1	0.21	0.20	0.21
2	0.09	0.12	021
3	0.03	0.03	0.03
4	4.2	4.07	3.88
5	0.95	0.92	0.81
6	0.82	3.22	10.1
7	2.38	2.37	2.39
8	0.02	0.014	0.015
9	3.20	3.37	3.42
10	10.21	10	9.19
11	4.7	3.72	3.28
12	3.48	3.67	3.49
13	65.4	63.74	57.94

L. MC16a configuration

This section is dedicated to the b-tagging performance evaluation for the MC16a scenario. Figure 0.17 shows the performance of the four tagging algorithms for the baseline and the MC16a scenario produced using $t\bar{t}$ samples.

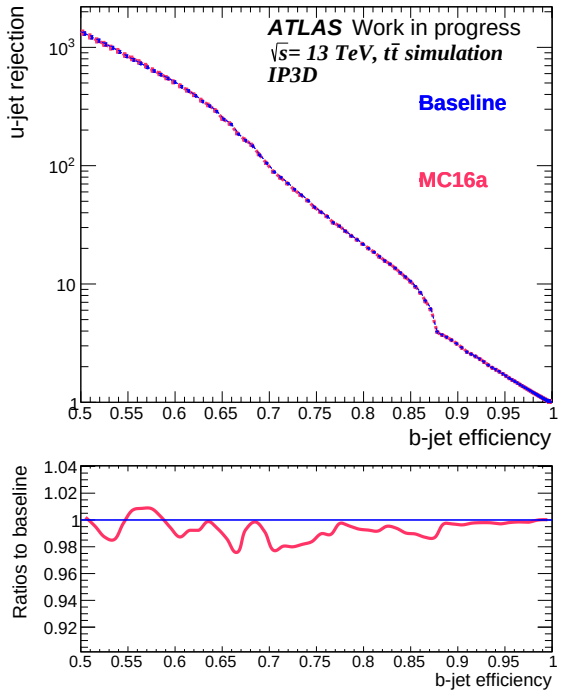

(a) IP3D

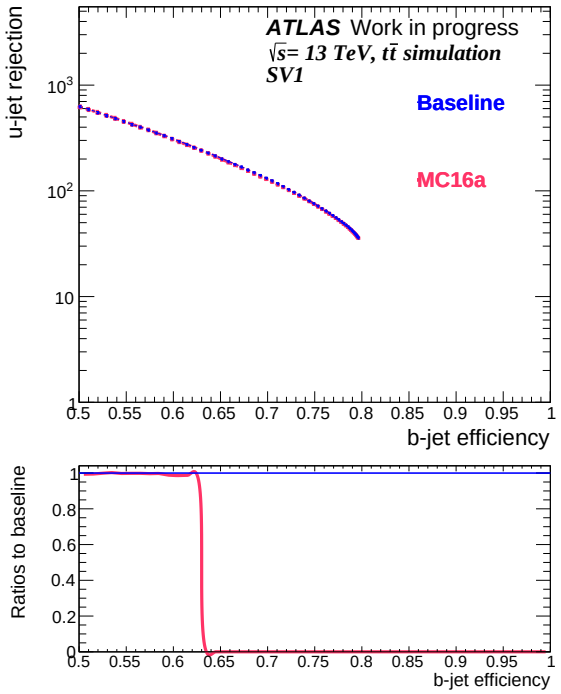

(b) SV1

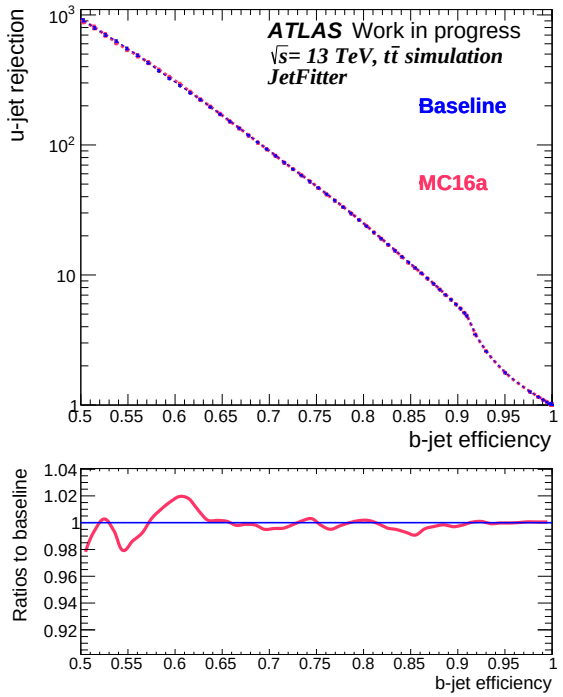

(c) JetFitter

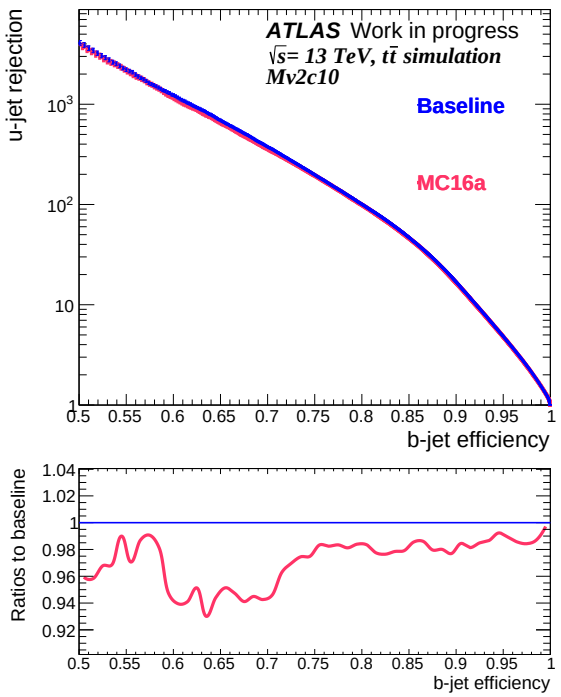

(d) Mv2c10

Figure 0.17.: The light jet rejection as a function of b-jet efficiency for the IP3D (a), SV1 (b), JetFitter (c) and MV2c10 (d) algorithms for MC16a configuration compared with the MC15c baseline in blue for $t\bar{t}$ sample.

M. Additional plots on b-tagging

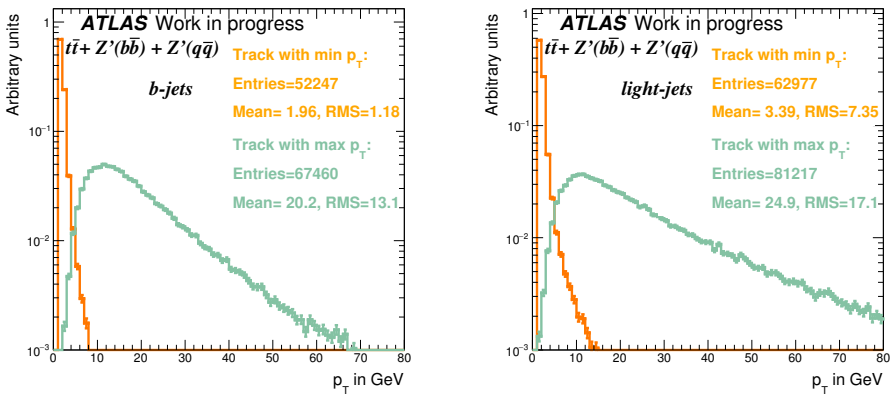

(a) (b)

Figure 0.18.: p_T distribution of the track with lowest p_T (orange) and the track with highest p_T (green) in b-jets (a) and light jets (b).

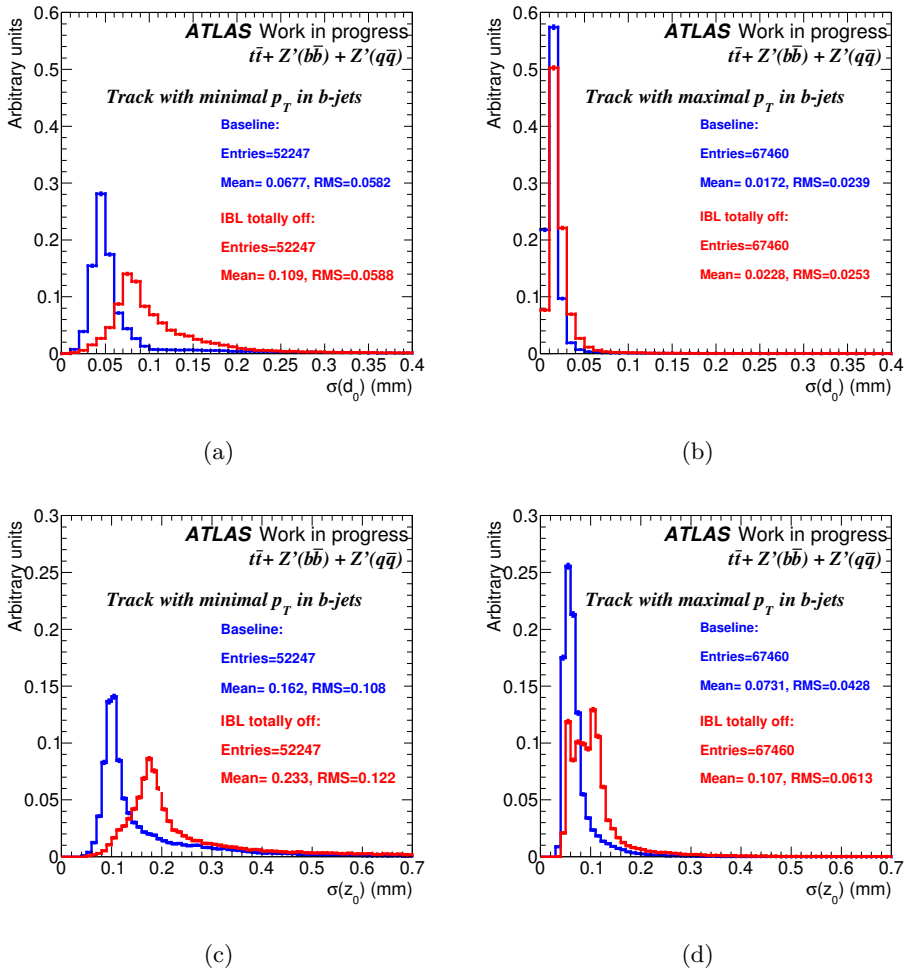

Figure 0.19.: (a) d_0 and (c) z_0 error distributions of the track with lowest p_T while (b) and (d) show the same for the track with highest p_T, in the b-jet in blue with IBL and in red fwithout IBL

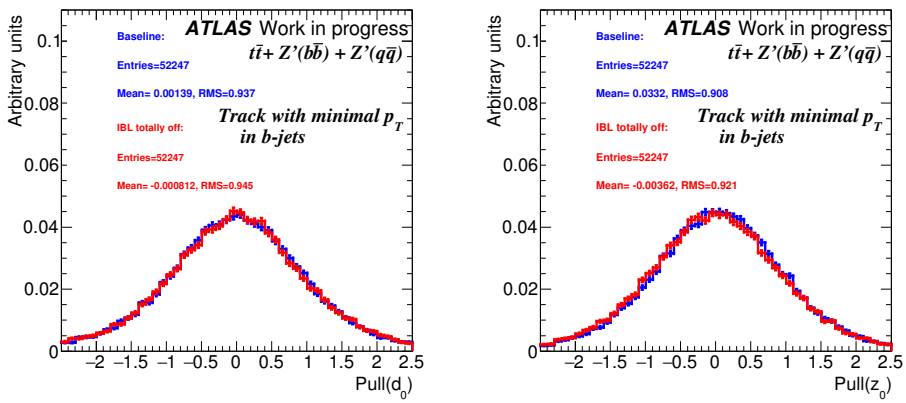

(a) (b)

Figure 0.20.: The pull (a) d_0 and (b) z_0 distribution for the track with the lowest p_T in the b-jet, in blue with IBL and in red for scenario without IBL.

N. Signal Contamination in VR-offMM and VR-offMH

The m_{bb} off peak VR, VRMMoff and VRHMoff, have non negligeable signal contamination, $\sim$ 20%, for some mass points outside the Run-1 exclusionIn this appendix, we present some additional studies to first show that the measured fraction of the signal outside the m_{bb} peak is compatible with the expected one; second, to ensure that this non-negligeable signal contamination in these side bands is covered by the systematic uncertainty of the background.

Figure 0.21 (Figure 0.22) shows the expexted numbers of signal events in VRMMoff (VRHMoff) and their statistical uncertainties, for the signal points having a contamination higher than 15% in VRMMoff (VRHMoff). Obviously, the signal contamination calculation in these 2 VRs suffers from large statistical uncertainties i.e. for the mass point (237,12) GeV, we expect in VRMMoff 2.8$\pm$1.7 events, the statistical uncertainty represents 60% of the number of expected events.

On the other hand, to better estimate the fraction of signal in and out the m_{bb} peak, we looked at the contributions in the 3 SR for the points having contamination higher than 15% in VRMMoff (VRHMoff). These contributions are shown in Figure 0.23 (0.24). To match the VROff cuts, we relaxed the SR E_T^{miss} cut to 180 GeV, m$_{bb}$ = [95,145] GeV. For the majority of the points the contribution in the corresponding SR is $\sim$ 8 times the number of events expected in the VRoff.

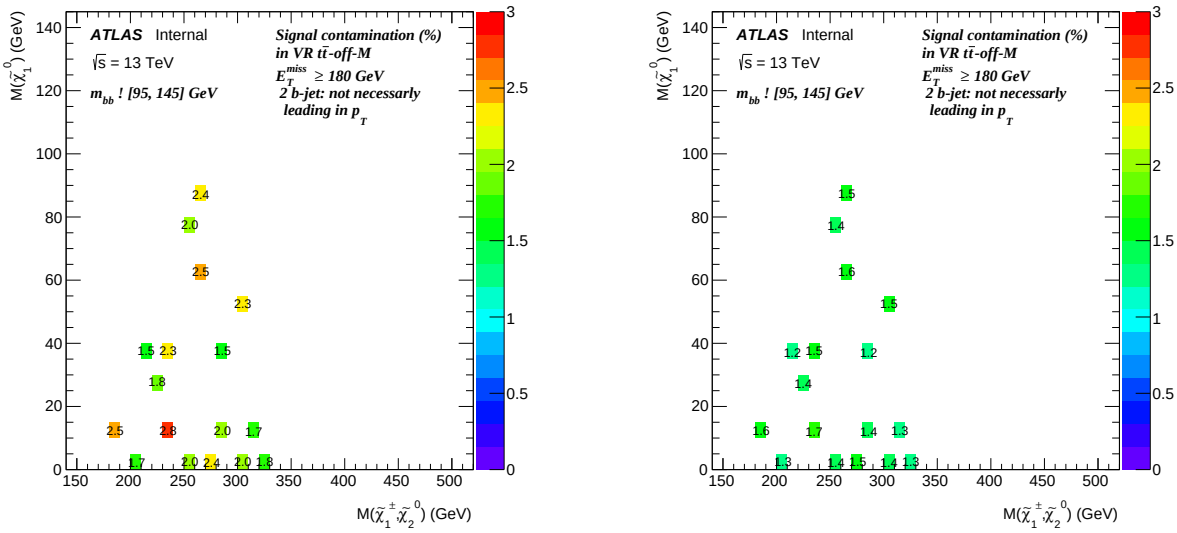

(a) Expexted number of signal in VRMMoff

(b) Statistical uncertainties on these numbers

Figure 0.21.: For the signal points having contamination in VRMMoff > 15%: the expexted numbers of signal events in VRMMoff (a), their statistical uncertaities (b).

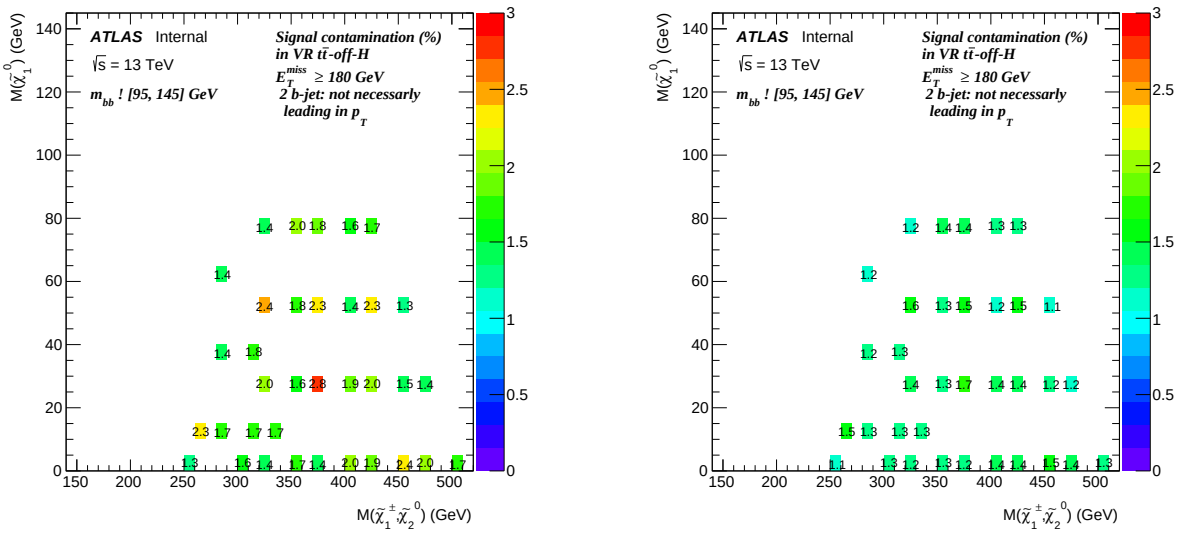

(a) Expexted number of signal in VRHMoff

(b) Statistical uncertainties on these numbers

Figure 0.22.: For the signal points having contamination in VRHMoff > 15%: the expexted number of signal events in VRHMoff (a), their statistical uncertainties (b).

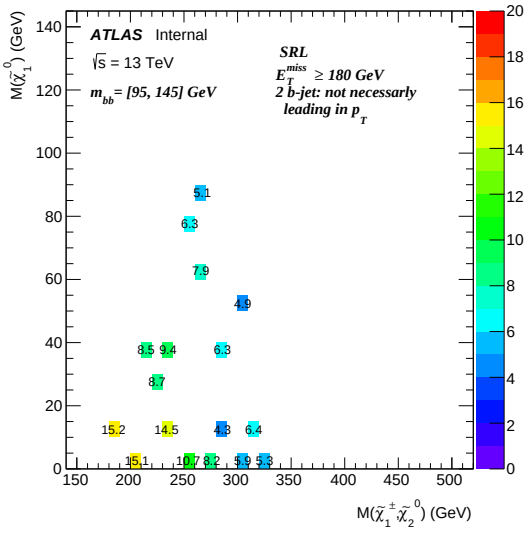

(a) Low: $100 < m_T < 140$

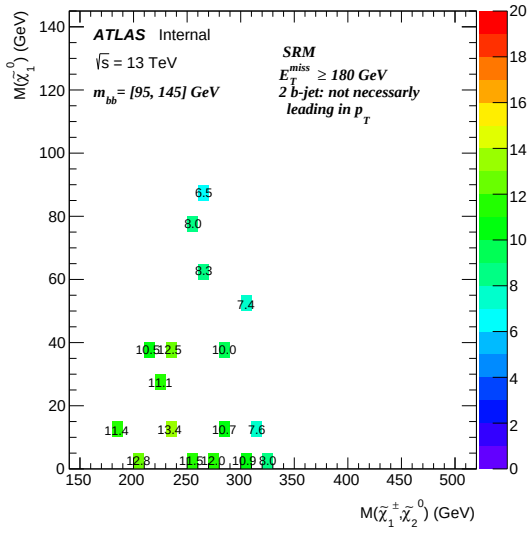

(b) Medium: $140 < m_T < 200$

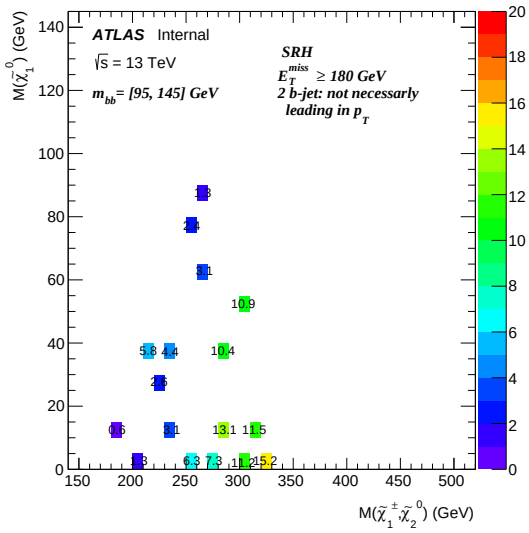

(c) High: $m_T > 200$

Figure 0.23.: Signal points having contamination in VRHMoff > 15%: Expexted number of signal in SRLM (a), Expexted number of signal in SRMM (b), Expexted number of signal in SRHM (c).

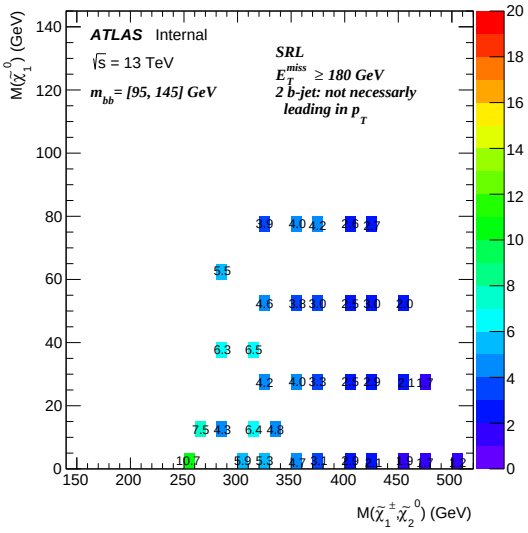

(a) Low: $100 < m_T < 140$

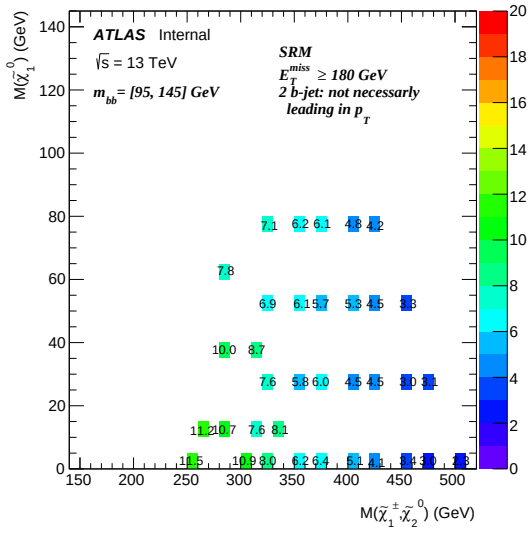

(b) Medium: $140 < m_T < 200$

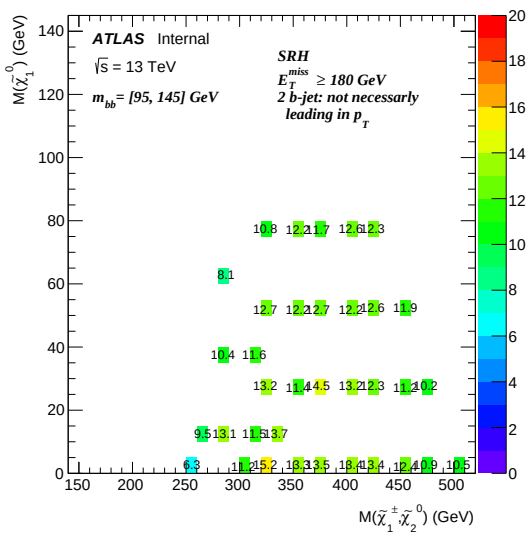

(c) High: $m_T > 200$

Figure 0.24.: Signal points having contamination in VRHHoff $> 15\%$: Expexted number of signal in SRLM (a), Expexted number of signal in SRMM (b), Expexted number of signal in SRHM (c).

We also checked the full m_{bb} distributions of the 6 signal points having the highest contaminations: (237,12), (262,62) and (312,12) GeV in VRMMoff and (375,25), (450,0), (250,0) GeV in VRHMoff. We apply here the VRoff-inclusive cuts: m_{CT} >160 GeV, $E_T^{miss} > 180$ GeV, m_T >100 GeV, $m_{bb} > 50$ GeV. The full m_{bb} distributions fitted to a bukin function in m_{bb} =[50,195] GeV range are shown in Figures 0.25 and 0.27. These Figures show that the events outside m_{bb} =[95,145] are in the tails of the distribution.

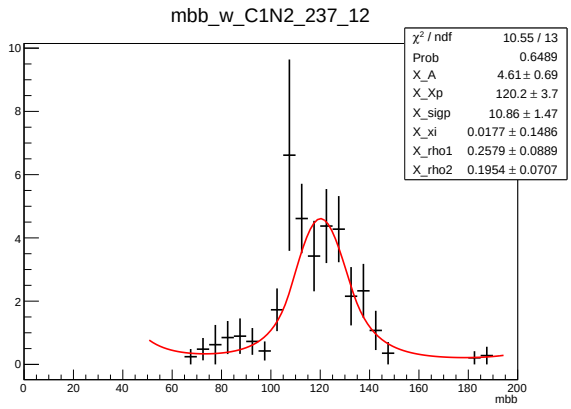

(a) Signal point (372, 12) GeV

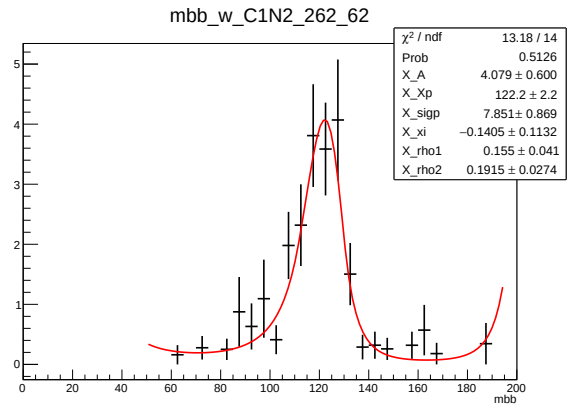

(b) Signal point (262, 62) GeV

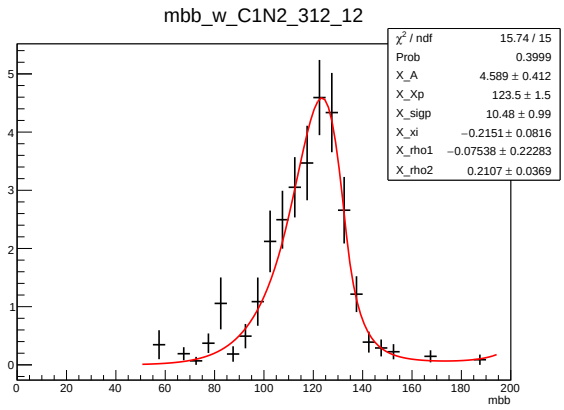

(c) Signal point (312, 12) GeV

Figure 0.25.: Full m_{bb} distributions, of the 3 signal points having the highest contamination in VRMMOff: Signal point (372, 12) GeV (a), Signal point (262, 62) GeV (b), Signal point (312, 12) GeV (c).

Figures 0.26 and 0.28 show the full m_{bb} distributions for the same signal points but at preselection, so E_T^{miss} and m_T cuts were relaxed here to get more statistics: $E_T^{miss} > 100$ GeV, m_T >40 GeV and using the same m_{CT} >160 GeV. These full m_{bb} distributions serve to calculate the fraction of events out the m_{bb} peak ($m_{bb} \notin$ [95,145]) for the 6 signal points at Preselection, and with tighter m_T and E_T^{miss} cuts. These fractions are summarized in table 0.18. Uncertainties shown are only statistical. At preselection, the fitted m_{bb} distribution is used to estimate this fraction. However, with tighter m_T and E_T^{miss} cuts, the original m_{bb} is used. The fractions obtained are $\sim$ 10% to 15%, compatible between the 6 signal points. We remind that our m_{bb} window does not contain the full Higgs boson peak, the side band region can contain 15%.

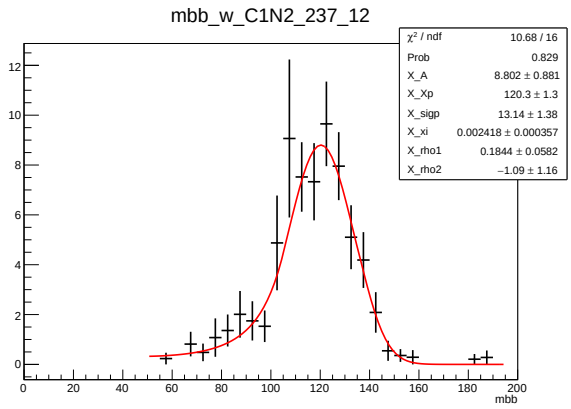

(a) Signal point (312, 12) GeV

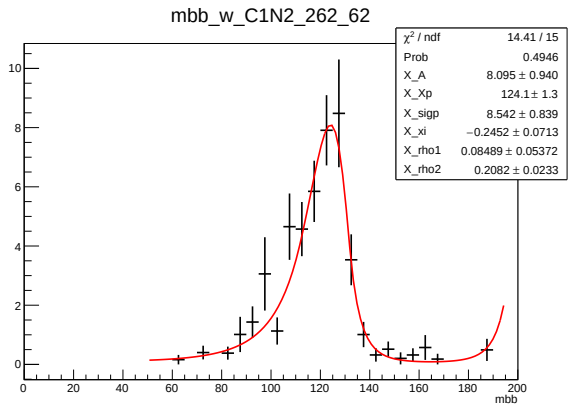

(b) Signal point (312, 12) GeV

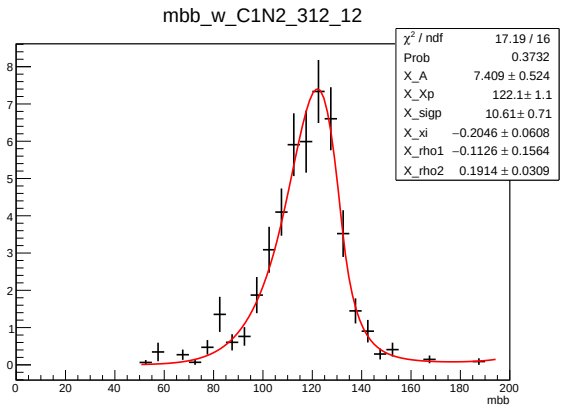

(c) Signal point (312, 12) GeV

Figure 0.26.: Full m_{bb} distributions at preselection, of the 3 signal points having the highest contamination in VRMMOff: Signal point (372, 12) GeV (c), Signal point (262, 62) GeV (b), Signal point (312, 12) GeV **??**.

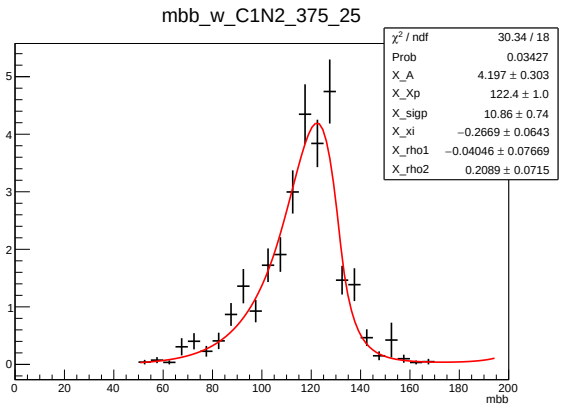

(a) Signal point (275, 25) GeV

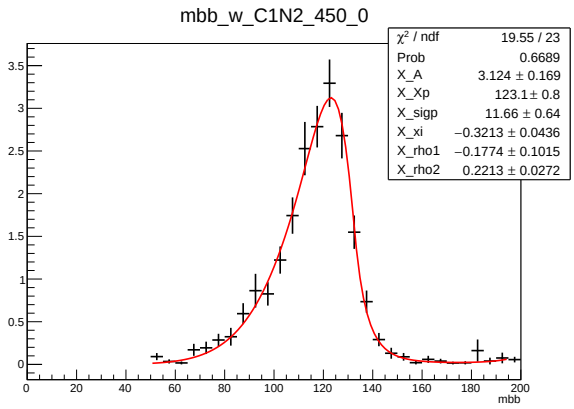

(b) Signal point (450, 0) GeV

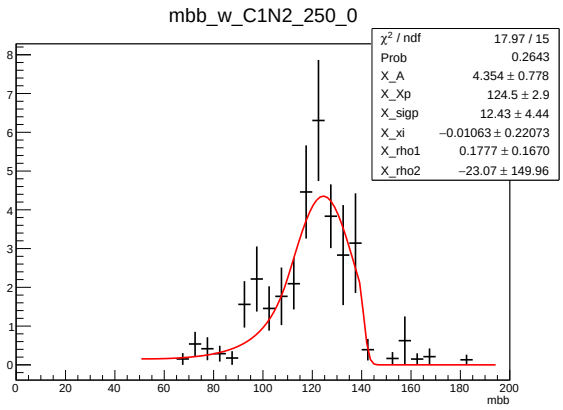

(c) Signal point (250, 0) GeV

Figure 0.27.: Full m_{bb} distributions, of the 3 signal points having the highest contamination in VRHMOff: Signal point (375, 25) GeV (a), Signal point (450, 0) GeV (b), Signal point (250, 0) GeV (c).

Table 0.18.: Fraction (%) of events having mbb $\notin$ [95,145] for the 6 sig pts at Preselection, and with tighter m_T and E_T^{miss} cuts Errors shown are only stat errors.

Fraction (%)	(237,12)	(262,12)	(312,12)	(375,25)	(450,0)	(250,0)
Preselection	12.2 ±1.8	15.4±2.4	9.9±2.01	13±2.4	12±2.9	9.2±1.7
Presel $+m_T$ >100 $+E_T^{miss}$ > 180 GeV	15±2.6	17±3.5	13±2.8	16.5±3.1	16.6±3.6	14±2.7

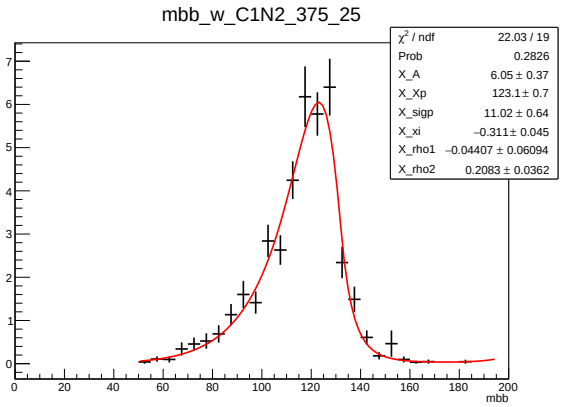

(a) Signal point (375, 25) GeV

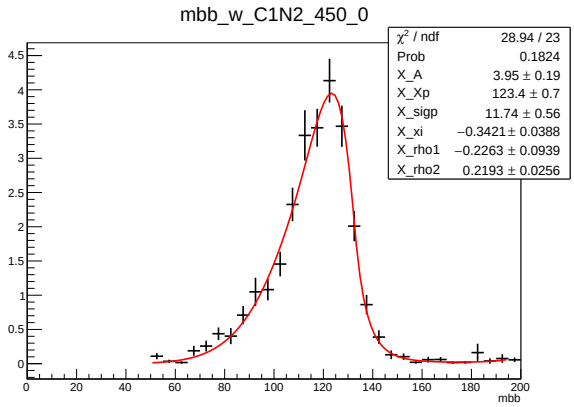

(b) Signal point (450, 0) GeV

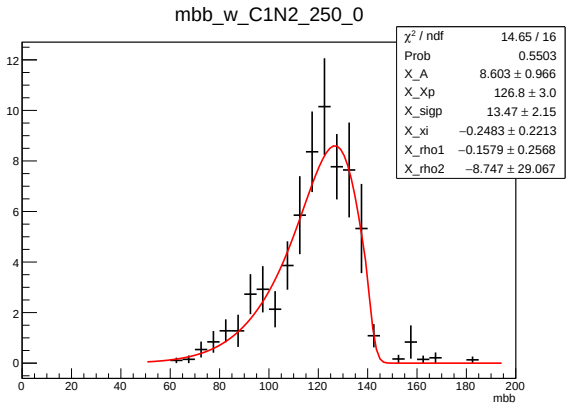

(c) Signal point (250, 0) GeV

Figure 0.28.: Full m_{bb} distributions at preselection, of the 3 signal points having the highest contamination in VRHMOff: Signal point (375, 25) GeV (a), Signal point (450, 0) GeV (b), Signal point (250, 0) GeV (c).

Last, referring to the the total background uncertainties in the VRoff; we have > 50% total background uncertainties. This ensures that the >20% signal contamination are well within the systematic uncertainty, which makes these regions insensitive.

O. Truth composition of $t\bar{t}$ in CR/VR/SRs

The truth composition in terms of heavy flavor was studied as well. We checked the number of truth heavy flavor jets(nHF) and the number of truth light flavor jets (nLF) variations from the CR to VR(off, on) and SR using the $t\bar{t}$ samples. The nHF is the sum of the number of truth b-jets and the number of truth c-jets, nLF is the sum of the number of truth light-jets and the number of truth hadronic tau. Figure 0.29 shows a comparison of the nHF (left) and nLF (right) normalized distributions for the different low (upper plots), medium (middle plots) and high (bottom plots) regions. We observe similar distributions HF/LF jets numbers in all regions. The low m_T regions are where we see the biggest deviation, but these regions have low statistics and these deviations are covered by statistics uncertainties. Figure 11.10 shows the mean HF/LF numbers as function of m_{CT} (upper plots), m_{bb} (bottom plots) for the $t\bar{t}$ events in control, validation and signal regions. We observe a slight increase in the number of HF with increasing m_{CT}, however the dependence of HF/LF numbers on m_{bb} looks less important.

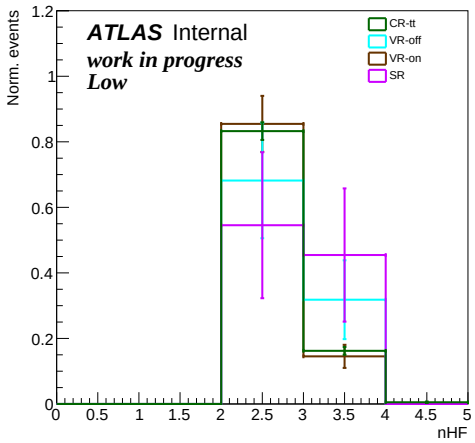

(a) nHF in regions

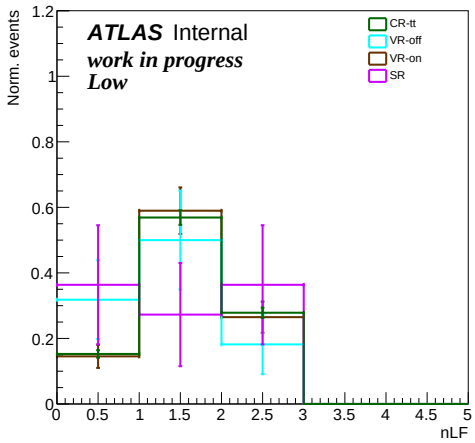

(b) nLF in regions

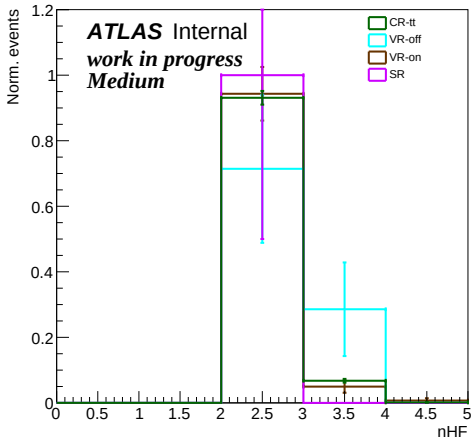

(c) nHF in regions

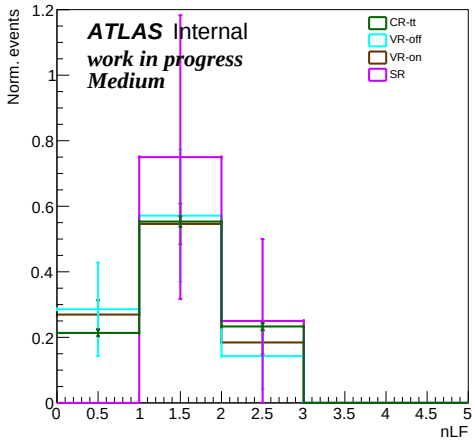

(d) nLF in regions

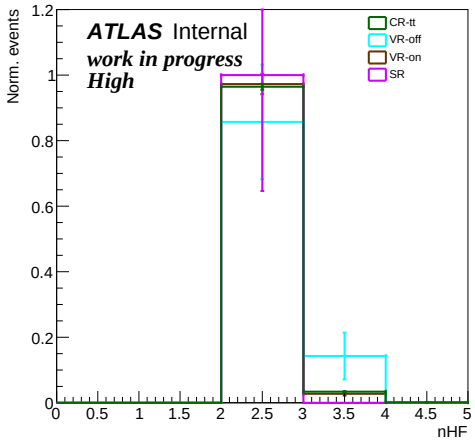

(e) nHF in regions

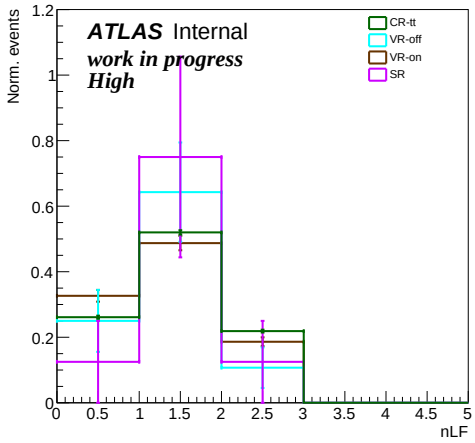

(f) nLF in regions

Figure 0.29.: The truth number of heavy and light flavors jets of the $t\bar{t}$ events in control, validation and signal regions.